Factors Controlling Variability in the Oxidative Capacity of the Troposphere on Interannual to Interglacial Time Scales

Factors controlling variability in the oxidative capacity of the troposphere on interannual to interglacial time scales

A dissertation presented
by
Lee Thomas Murray
to
The School of Engineering and Applied Sciences

in partial fulfillment of the requirements
for the degree of
Doctor of Philosophy
in the subject of
Engineering Sciences

Harvard University
Cambridge, Massachusetts
May 2013

Factors controlling variability in the oxidative capacity of the troposphere on interannual to interglacial time scales

Abstract

This thesis explores the natural forces controlling variability of the tropospheric oxidants on interannual to glacial-interglacial time scales. The oxidants (primarily OH and ozone) determine the lifetime of many trace gases of human interest, including air pollutants and long-lived greenhouse gases such as methane. The oxidants respond to meteorological conditions, precursor emissions (natural and anthropogenic), and surface and overhead stratospheric boundary conditions, all of which have changed since the Last Glacial Maximum (LGM; 21ka). This dissertation first examines in mechanistic detail the effect of variability in the lightning source of nitrogen oxides (NO_x) precursors on interannual variability (IAV) of the oxidants in the recent past. An optimized technique is presented to constrain the lightning NO_x source in the GEOS-Chem global chemical transport model (CTM) to time-varying satellite data from the Lightning Imaging Sensor. This constraint improves the ability of the CTM to reproduce observed IAV in 9-year (1998-2006) hindcasts of tropical ozone and OH. IAV in ozone and OH is more sensitive to lightning than to biomass burning, despite greater IAV in NO_x from the latter source. The sensitivity of OH to lightning reflects positive chemical feedbacks on ozone production, HO_x recycling, and loss frequencies. This dissertation next introduces an offline-coupled climate-biosphere-chemistry framework for determining oxidant levels at and since the LGM. Detailed simulations of tropospheric composition are performed by GEOS-Chem driven by meteorological fields from the GISS ModelE general circulation model, land cover from the BIOME4-TG global terrestrial equilibrium vegetation model, and fire emissions from the LMfire model. Time slice simulations are presented for the present day, preindustrial, and two different possible representations of the LGM climate. Sensitivity of the results to uncertainty in lightning and biomass burning emissions is tested. Though well-buffered, all simulations find net

reduced oxidative capacities relative to the present day. The most important parameters for controlling tropospheric oxidants over glacial-interglacial periods are changes in overhead ozone, tropospheric H_2O, and lightning. The results are discussed in the context of the ice-core record, particularly for methane.

Contents

Listing of figures

List of Tables

Citations to Previously Published Work

Chapters 2 has appeared previously as:

> Murray, L. T., D. J. Jacob, J. A. Logan, R. C. Hudman, and W. J. Koshak (2012), Optimized regional and interannual variability of lightning in a global chemical transport model constrained by LIS/OTD satellite data, *J Geophys Res-Atmos*, 117(D20307), doi:10.1029/2012JD017934.

To the memory of my grandmothers:

Helen Murray (1916-2008) and Annabelle Tyran (1924-2011)

Acknowledgments

I am deeply grateful for the contribution of many individuals to this work.

Daniel Jacob welcomed me into his research group when I was only a sophomore. His dedication to his students is why I remained at Harvard for my Ph.D. He has been an incredible advisor, and is a scientist that I deeply respect and hope to emulate in my professional career.

I have also had the privilege of being advised by both Jennifer Logan and Loretta Mickley, whose additional expertise and perspectives have been invaluable. Further mentorship from Rynda Kay, a senior grad student when I was an undergrad, was instrumental to my early development and confidence as an atmospheric chemist.

I am constantly amazed at the brilliance and collegiality of the 85+ individuals that have comprised the Harvard Atmospheric Chemistry Modeling Group since I joined in May 2004. In particular, I thank my officemates Bess Corbitt, Kevin Wecht, and Eloïse Marais, and housemate Helen Amos, for friendship and stimulating conversations. I am further thankful to all the faculty, staff, and students who made SEAS and the EPS department my home for the past decade.

My NASA GSRP advisor Bill Koshak was very helpful in my working with the LIS satellite. I have greatly enjoyed my role as an initial member of the ICECAP science team (along with Loretta Mickley, Becky Alexander, Eric Sofen, and Jed Kaplan), and look forward to future studies of paleo-chemistry with them.

The stresses of graduate school were made manageable with an incredible support group of friends. In addition to those already named, I would like to especially thank Doug McClure, Hilary Close, Katie Sullivan, Josh Rissmiller, Justin Tokarksi, Mackenzie Smith, Matt Jakubik, and Max Boehlke.

I would like to thank my family for their steadfast support and encouragement of my early scientific inclinations. Lastly, I would like to thank my fiancé Tom, who has provided constant support, concern, and love.

Chapter 1

Overview

The tropospheric oxidants are the cleansing agents of Earth's atmosphere. Of these, four stand out for their abundance and reactivity: the hydroxyl radical (OH), ozone, hydrodgen peroxide, and the nitrate radical. Their collective burden defines the *oxidative capacity* of the troposphere [*Thompson*, 1992].

The oxidative capacity determines the lifetime before removal of many trace gases of importance for human health and climate, including air pollutants and long-lived greenhouse gases such as methane and hydrogenated halocarbons [*Shindell et al.*, 2007; *Fiore et al.*, 2012]. Furthermore, tropospheric ozone itself is an important air pollutant at the surface [*EPA*, 2006] and greenhouse gas [*IPCC*, 2007], the oxidants influence aerosol in ways relevant for public health and climate [*Liao et al.*, 2003; *Tie et al.*, 2005; *Leibensperger et al.*, 2011], and oxidative stresses perturb ecosystems [*Collins et al.*, 2010; *Sitch et al.*, 2007]. The oxidants are strongly and non-linearly coupled to one another, and respond to meteorological conditions, changes in precursor emissions, and surface and stratospheric boundary conditions [e.g., *Holmes et al.*, 2013; *Spivakovsky et al.*, 2000; *Lelieveld et al.*, 2002; *Ehhalt*, 1999]. The stiff and non-linear coupling of the oxidants in the chemistry-climate-biosphere system allows their influence to operate at modes well beyond their individual chemical lifetimes.

Recent multi-model studies show that global models of atmospheric chemistry are relatively mature, and reproduce large-scale spatial and seasonal patterns of the oxidants as observed or implied by observational constraints [*Young et al.*, 2013; *Stevenson et al.*, 2006; *Shindell et al.*, 2006a; *Voulgarakis et al.*, 2013; *Fiore et al.*, 2009; *Prather et al.*, 2012]. Much less attention has been given toward the ability of global 3D models to reproduce oxidant variability on time scales longer than a year or two. However, those that have indicate large uncertainties [e.g., *Naik et al.*, 2012; *Young et al.*, 2013].

Understanding the mechanisms for oxidant variability and reproducing observed changes across the recent past is important if we are to predict how oxidants may change in response to future anthropogenic perturbations, and the associated climate and health consequences of those changes. Meanwhile, understanding how oxidants may have changed over even longer time scales (e.g., since the Last Glacial Maximum, 19-23k years ago) is important for putting recent anthropogenic changes into context.

Therefore, the motivation of this thesis has been to identify and reduce uncertainties in the key parameters that control variability in the oxidative capacity of the past on interannual to glacial-interglacial time scales. To that end, I use as my primary tool the GEOS-Chem 3D global chemical transport model (CTM; http://www.geos-chem.org) to bridge the gap between observational constraints and proxies, the tropospheric oxidants, and the underlying physical mechanisms.

1.1 Research questions and methods

1.1.1 Interannual variability in lightning

Nitrogen oxides ($NO_x \equiv NO + NO_2$) produced by lightning make a major contribution to the global production of tropospheric ozone and OH [*Schumann and Huntrieser*, 2007]. However, lightning distributions inferred from standard convective parameterizations in global chemical

transport models (CTMs) fail to reproduce observations from the Lightning Imaging Sensor (LIS) and the Optical Transient Detector (OTD) satellite instruments [*Christian et al.*, 2003; *Tost et al.*, 2007]. As I began this thesis work, global models had begun to constrain their lightning distributions to the satellite climatology, but there was uncertainty in the community as to the best spatial scale over which to do this. However, if constraining lightning over some large-scale coherent regions could provide equal improvements to tropical ozone as earlier work using native model resolution [*Sauvage et al.*, 2007a], then the hope was that these regions might provide sufficient sampling statistics to use LIS to constrain interannual changes for the first time.

My work therefore addressed the following questions:

- Can spatiotemporally-sparse observations of lightning from satellite be used to constrain IAV in lightning for global models?
- How has tropical lightning activity changed in the past decade?

I answered these questions by using satellite observations of tropical lightning activity from the Lightning Imaging Sensor and Optical Transient Detector within the GEOS-Chem CTM, and evaluated with tropical columns of ozone and NO_2 from the Aura satellite and ozonesondes.

1.1.2 Interannual variability in the oxidative capacity

Observations of the interannual variability (IAV) of tropical ozone [*Ziemke et al.*, 2001] and recent confidence in time series of OH anomalies deduced from methyl chloroform data [*Montzka et al.*, 2011] offer a new opportunity to examine the factors controlling IAV of the oxidative capacity. Lightning NO_x is known to be an important precursor for determining seasonal and spatial patterns of tropical ozone, as well as for global mean OH [e.g., *Sauvage et al.*, 2007b; *Labrador et al.*, 2004]. This leads to the question of whether lightning contributes to IAV of tropical ozone or OH. The constraint for lightning flash rates in GEOS-Chem presented in the first section of this thesis allows us to address this question for the first time with confidence.

My work addressed the following questions:

- What role does lightning play in determining IAV in tropical ozone and global mean OH?
- Can we explain the temporal behavior of OH implied from methyl chloroform?

I answered these questions by using my derived IAV constraint from the LIS within the GEOS-Chem CTM, which I compare to long-term satellite records of tropical tropospheric ozone from EPTOMS and the Aura satellite, and OH anomalies inferred from observed changes in the global methyl chloroform lifetime.

1.1.3 Glacial-interglacial variability in the oxidative capacity

Concentrations of the tropospheric oxidants may have undergone large changes since the preindustrial and the Last Glacial Maximum (LGM; 21ka) as a result of changing climate and recent human influence. Prior model studies investigating changes in tropospheric oxidant burdens have disagreed on the magnitude and even the sign of changes at the LGM and present day relative to the preindustrial (Section 4.1). These discrepancies reflect differences in the model components of the earth system allowed to vary, the differing degrees of complexity of those components, and the large uncertainties in past meteorological and biological conditions. No LGM model study to date has considered the full suite of changes in the key variables for controlling tropospheric oxidants, in particular the potentially large effect of the stratospheric ozone burden on photolysis rates in the troposphere [e.g., *Holmes et al.*, 2013]. The LGM and preindustrial are relatively well-recorded in ice-core records, but those relevant for oxidant levels are indirect proxies that require models for interpretation, including recently proposed proxies from $\Delta^{17}O$ of sulfate and nitrate aerosol in the LGM [*Wolff*, 2012; *Alexander et al.*, 2002, 2004; *Erbland et al.*, 2012]. Even with a relatively simple budget, there remains considerable uncertainty regarding the relative contribution of methane wetland emissions versus its sink with

OH in driving its large glacial-interglacial variability seen in ice-core bubbles [e.g., *Khalil and Rasmussen*, 1987; *Chappellaz et al*., 1993; *Kaplan et al*., 2006; *Valdes et al*., 2005; *Levine et al*., 2012].

My work was therefore motivated by the following questions:

- How has the oxidative capacity likely changed at the LGM and present day, relative to the preindustrial?
- What are the key parameters controlling variability in the oxidative capacity on glacial-interglacial time scales?
- What can we learn from polar ice-core records of reactive gases and proxies?
- Do sources or sinks control the glacial-interglacial variability of methane recorded in ice-core air bubbles?

I addressed these questions by developing a new capability for the GEOS-Chem CTM to be driven by output from the GISS ModelE general circulation model, and landcover products from the BIOME4-TG global equilibrium vegetation model and LMfire fire model.

1.2 Dissertation outline and major results

In Chapter 2, I use satellite observations of lightning flash rates from the Lightning Imaging Sensor (LIS) of the NASA Tropical Rainfall Monitoring Mission (TRMM) and the Optical Transient Detector with the GEOS-Chem CTM to characterize IAV in tropical lightning flash rates since 1998. I perform a hierarchical clustering technique to identify 3˜7 regions globally over which I am able to accurately constrain most of the observed spatial and seasonal variability of lightning seen by satellite in a manner that preserves coupling to deep convective transport. I find this regional constraint improves simulations of tropical tropospheric ozone columns versus

observations from the NASA Aura satellite in a statistically identical manner to using much finer spatial resolution. I find variability in NO_2 columns to be more consistent with Aura satellite observations from OMI. I demonstrate that these regions significantly reduce sampling biases associated with its orbital geometry and the strong diurnal cycle. After processing to remove the diurnal bias, I construct a monthly time series of lightning flash rates for 1998-2010 and 35°S-35°N. I find a correlation of IAV in total tropical lightning with El Niño but not with the solar cycle or the quasi-biennial oscillation. These results imply GEOS-Chem underestimates the magnitude of variability in annual mean flash rates by 50%.

In Chapter 3, I use my new lightning constraint within the GEOS-Chem CTM to identify the role of different emissions in controlling IAV in tropical ozone and OH. I perform and analyze 9-year hindcasts of the GEOS-Chem model for 1998-2006, isolating in particular the influence of time-varying satellite-constrained emissions from biomass burning and my lightning product. I find imposing IAV in lightning NO_x from LIS improves the ability of the model to reproduce observed IAV in tropical ozone from satellite and in OH inferred from the methyl chloroform lifetime. I find lightning to be far more important than biomass burning in driving the IAV of tropical ozone, even though the IAV of NO_x emissions from fires is greater than that from lightning. I find IAV in tropospheric OH to be highly sensitive to lightning relative to other emissions, and that lightning contributes an important fraction of the observed IAV in OH inferred from the methyl chloroform proxy. I demonstrate the relative sensitivity of IAV in OH to changes in lightning results from a series of positive feedbacks to ozone production, HO_x recycling, and in the OH loss frequencies. I find the model can account for the observed increase in OH in 1998-2004 and for its IAV, but that it cannot explain the OH decrease in 2004-2006. I find OH to be more strongly correlated with lightning (and tropospheric ozone) than stratospheric ozone during 1998-2006, in contrast to previous studies that examined different periods.

In Chapter 4, I introduce a new offline-coupled climate-biosphere-chemistry model framework (ICECAP) that I developed for simulating tropospheric oxidant levels in past and present

atmospheres. I coupled meteorology from the NASA Goddard Institute for Space Studies (GISS) ModelE general circulation model, land products from the BIOME4-TG global equilibrium vegetation model and LMfire model, and a linearized stratospheric ozone scheme to drive tropospheric chemistry in the GEOS-Chem CTM. I perform time-slices for the present day, preindustrial, and two different extents of cooling at the LGM. I test the sensitivity of model results to uncertainty in lightning and biomass burning emissions. Although OH is relatively well-buffered, I find reduced oxidant levels in all preindustrial and paleo climates relative to the present day, in contrast to previous work. I find global mean OH changes of -6.7 $\pm$ 11% at the LGM relative to the preindustrial, despite reductions in methane concentrations. I find a simple linear relationship between mean values of stratospheric ozone, water vapor, and total emissions of NO_x and reactive carbon that explains 69% of the variability in global mean OH in 11 different simulations across the last glacial-interglacial time interval. I identify the key variables controlling the tropospheric oxidative capacity over glacial-interglacial periods include overhead stratospheric ozone (affecting tropospheric photolysis rates), tropospheric water vapor, and lightning emissions. I find variability in global mean OH since the LGM is insensitive to large uncertainties in biomass burning emissions. Our simulations are broadly consistent with ice-core records of $\Delta^{17}O$ in sulfate and nitrate at the LGM, and CO, HCHO, and H_2O_2 in the preindustrial. The results imply that the observed variability in ice-core methane is predominantly source-driven, which I find consistent with the reductions reported in previous bottom-up estimates of LGM wetland emissions.

Chapter 2

Optimized regional and interannual variability of lightning in a global chemical transport model constrained by LIS/OTD satellite data

Abstract

Nitrogen oxides ($NO_x \equiv NO + NO_2$) produced by lightning make a major contribution to the global production of tropospheric ozone and OH. Lightning distributions inferred from standard convective parameterizations in global chemical transport models (CTMs) fail to reproduce observations from the Lightning Imaging Sensor (LIS) and the Optical Transient Detector (OTD) satellite instruments. We present an optimal regional scaling algorithm for CTMs to fit the lightning NO_x source to the satellite lightning data in a way that preserves the coupling to deep convective transport. We show that applying monthly scaling factors over 37 regions globally significantly improves the tropical ozone simulation in the GEOS-Chem CTM as compared to a simulation unconstrained by the satellite data, and performs equally well to a simulation with local scaling. The coarse regional scaling preserves sufficient statistics in the satellite data to constrain the interannual variability (IAV) of lightning. After processing the LIS data to remove its diurnal sampling bias, we construct a monthly time series of lightning flash rates for 1998-2010 and 35°S-35°N. We find a correlation of IAV in total tropical lightning with El Niño but not with the solar cycle or the quasi-biennial oscillation. The global lightning NO_x source $\pm$ IAV standard deviation in GEOS-Chem is 6.0 ± 0.5 Tg N a^{-1}, compared to 5.5 ± 0.8 Tg N a^{-1} for the biomass burning source. Lightning NO_x could have a large influence on the IAV of tropospheric ozone because it is released in the upper troposphere where ozone production is most efficient.

2.1 Introduction

The extreme heat in a lightning flash converts atmospheric N_2 and O_2 to nitrogen oxide radicals ($NO_x \equiv NO + NO_2$) that drive the formation of tropospheric ozone and OH, the principal tropospheric oxidant [*Chameides et al.*, 1977; *Logan et al.*, 1981; *Labrador et al.*, 2004]. The global source of NO_x from lightning is smaller than the source from combustion, but its impact on ozone and associated outgoing longwave radiation is disproportionately large because it is mainly released in the upper troposphere where the lifetimes of NO_x and ozone are long [*Pickering et al.*, 1990; *Hauglustaine et al.*, 1994; *Zhang et al.*, 2003; *Choi et al.*, 2009]. Lightning is the least understood of the major atmospheric NO_x sources. Global estimates range from 1-20 Tg N a^{-1}, with a most probable range of 2-8 Tg N a^{-1} [*Schumann and Huntrieser*, 2007]. Parameterizations used in global chemical transport models (CTMs) show little skill in reproducing observed lightning distributions [*Sauvage et al.*, 2007a; *Tost et al.*, 2007]. Here we develop a method for using satellite observations to constrain the lightning source in global CTMs in a way that preserves the coupling to convective transport and allows investigation of interannual variability of lightning influence. In Chapter 3, we apply this method to examine the role of lightning in driving the interannual variability of ozone and OH in the tropical troposphere.

Quantifying the source of lightning NO_x from first principles is hindered by uncertainties in the physics of lightning formation. Enormous local electric potentials of up to ±100 MV with respect to the ground develop inside thunderstorms and are subsequently dissipated in part by lightning [*Marshall and Stolzenburg*, 2001]. The most widely accepted hypothesis of cloud electrification is that charge separation occurs from collision of ice particles with supercooled water droplets [*Rakov and Uman*, 2003, and references within]. The cloud scales involved in lightning generation are therefore much smaller than the typical grid size in global models, requiring sub-grid parameterizations. Parameterization of lightning must be consistent with the convective

transport, because mixing of lightning NO_x with boundary layer gases brought up by convection greatly enhances the resulting ozone production in the upper troposphere [*Pickering et al.*, 1993; *Jaeglé et al.*, 2001]. Simply prescribing lightning in the CTM on the basis of observational data would not guarantee such consistency.

A number of lightning flash rate parameterizations for global and regional models have been developed, all based on proxies of deep convection [*Price and Rind*, 1992, 1993, 1994; *Price et al.*, 1997; *Allen et al.*, 2000; *Grewe et al.*, 2001; *Meijer et al.*, 2001; *Allen and Pickering*, 2002; *Petersen et al.*, 2005; *Jacobson and Streets*, 2009]. *Tost et al.* [2007] examined four commonly used lightning schemes within a suite of convective parameterizations, and found that all combinations failed to reproduce the observed global lightning distributions from the combined climatologies of the Optical Transient Detector (OTD) and the Lightning Imaging Sensor (LIS) satellite instruments [*Christian et al.*, 2003].

Here we explore optimal ways to use the LIS/OTD satellite observations to improve the representation of lightning in CTMs, using as testbed the GEOS-Chem CTM [*Bey et al.*, 2001]. Climatological LIS/OTD data have been used previously in CTMs to apply correction factors on various scales to the lightning flash rate parameterizations. Local correction factors [*Sauvage et al.*, 2007a; *Allen et al.*, 2010] provide maximum fidelity to the spatial and seasonal distribution of lightning observations. However, they most strongly decouple lightning frequency from simulated convective intensity, and also suffer from relatively few observations per grid cell. Correction factors applied to large regions [*Stajner et al.*, 2008; *Jourdain et al.*, 2010] have less fidelity to observations but are more statistically robust and are more consistent with the model convective transport. All studies so far have used lightning observations averaged over a number of years in order to have adequate statistics but interannual variability is then not resolved. Here we develop an optimal algorithm for selecting coherent lightning regions over which to apply correction factors, and we use an improved LIS/OTD data set to examine the sensitivity of CTM results to the scales over which the correction factors are applied. We show that adequate fidelity

to lightning observations can be achieved with regions sufficiently coarse to constrain the interannual variability in lightning and investigate the resulting impact on atmospheric chemistry.

2.2 Satellite lightning observations

We use satellite observations from the OTD instrument for May 1995 to December 2000, and its successor the LIS instrument for December 1997 to present. The two instruments detect total optical pulses from cloud-to-ground (CG) and intra-cloud (IC) lightning flashes during both day and night, with a clustering algorithm used to lump the optical pulse events into individual flashes [*Christian et al.*, 1989; *Boccippio et al.*, 2000, 2002; *Mach et al.*, 2007]. OTD flew on the Microlab I satellite with near-global coverage (75°S-75°N), and detection efficiencies (DEs) of 35-55% relative to regional ground-based detection networks. LIS is a component of the NASA Tropical Rain Measuring Mission (TRMM), with a narrower latitudinal range of 35°S-35°N, and higher DEs of about 70-90% [*Koshak et al.*, 2000; *Boccippio et al.*, 2002; *Christian et al.*, 2003; *Mach et al.*, 2007].

In this study, we use two products available from the NASA Global Hydrology and Climate Center (GHCC; http://thunder.msfc.nasa.gov/): (1) the High Resolution Monthly Climatology (HRMC) gridded product version 2.2, and (2) the LIS Science Data version 4.1. The HRMC gridded product consists of long-term monthly mean flash densities (km^{-2} d^{-1}) from OTD and LIS averaged over 1995-2005, determined by dividing the total observed flash counts in a given area by its effective view time. They are inter-calibrated and have corrections applied for their respective DEs. This product is prepared by GHCC at a resolution of $0.5° \times 0.5°$, using spatial smoothing of 2.5°. It improves over the earlier LIS/OTD gridded products from GHCC by (1) using more years of data, (2) providing monthly temporal resolution instead of seasonal, and (3) providing finer spatial resolution. The LIS Science Data product available for December 1997 to present contains the individual orbital data for lightning flashes on a 0.5° by 0.5° grid. This

product has been filtered for noise and quality assurance, and corrected for DE. We omit observations with bad data or warning flags.

2.3 GEOS-Chem chemical transport model

The GEOS-Chem global 3D CTM (version 9.01.01; http://www.geos-chem.org) simulates tropospheric ozone-NO_x-CO-hydrocarbon-aerosol chemistry with transport driven by assimilated meteorological fields from the Goddard Earth Observing System (GEOS) of the NASA Global Modeling and Assimilation Office (GMAO). Here we use archived GEOS-4 fields for 2003-2005, with 2003 used for model initialization and 2004-2005 for analysis. The meteorological data are 6 h means (3 h for surface fields and mixing depths) and have horizontal resolution of 1° latitude by 1.25° longitude with 55 layers in the vertical. We degrade the horizontal resolution to 2° by 2.5° for input to GEOS-Chem. Convective transport in GEOS-Chem mimics that in the parent GEOS general circulation model (GCM) [*Hack*, 1994; *Zhang and McFarlane*, 1995]. It uses 6 h GEOS-4 data for updraft, downdraft, and entrainment mass fluxes archived separately for deep and shallow convection [*Wu et al*., 2007a]. For this work we have updated the GEOS-Chem chemistry module in the stratosphere by archiving monthly mean production and loss frequencies of species from the NASA Global Modeling Initiative (GMI) Combo CTM Aura4 simulations using GEOS-4 meteorology [*Duncan et al*., 2007; *Considine et al*., 2008; *Allen et al*., 2010].

Table 2.1 summarizes the global NO_x sources in GEOS-Chem for 2004-2005. The lightning source is described in Section 2.4. Anthropogenic sources are from the Emission Database for Global Atmospheric Research (EDGAR) base inventory for 2000 [*Olivier and Berdowski*, 2001], overwritten with regional inventories for the United States (EPA NEI2005), Canada (CAC), Mexico (BRAVO) [*Kuhns et al*., 2003], Europe (EMEP) [*Auvray and Bey*, 2005], and South and East Asia [*Streets et al*., 2003, 2006], and scaled for each year as described by *van Donkelaar et al*. [2008]. Biofuel emissions are from *Yevich and Logan* [2003]. Biomass burning emissions

Table 2.1: Sources of Tropospheric NO_x in GEOS-Chem[a]

Source	Value (Tg N a^{-1})
Fossil fuel and biofuel combustion[b]	27.8
Lightning	5.8
Soil microbial activity[c]	5.6
Open fires	5.3
Transport from stratosphere[d]	0.8
Total	45.3

[a] Annual means for 2004-2005.
[b] Including 0.5 Tg N a^{-1} from aircraft emissions at cruise altitude.
[c] Including 0.7 Tg N a^{-1} from fertilizer application.
[d] NO_x tracked across the monthly mean tropopause.

are from the Global Fire Emissions Database (GFED v2) [*van der Werf et al.*, 2006]. Soil NO_x emissions follow the *Yienger and Levy* [1995] parameterization as implemented by *Wang et al.* [1998].

2.4 Lightning source of NO_x

2.4.1 Unconstrained parameterization

The use of a convection-based lightning parameterization in the CTM is necessary, even if it is to be subsequently corrected by lightning observations, because it allows the corrected lightning to be co-located with the convective transport in the model. We refer to a parameterization that relies solely on model convection variables as "unconstrained" since it is not constrained by the satellite lightning data. The standard GEOS-Chem model uses the Cloud Top Height (CTH) parameterization of *Price and Rind* [1992, 1993, 1994], who fit observed lightning frequency to a fifth-power function of CTH over continents and extrapolated a second-power function over oceans. The CTH in each deep convective model column is determined as the altitude where the upward convective mass flux vanishes to zero. The original *Price and Rind* [1992] parameterization treated grid cells up to 500 km from shore as continental, but here we treat grid

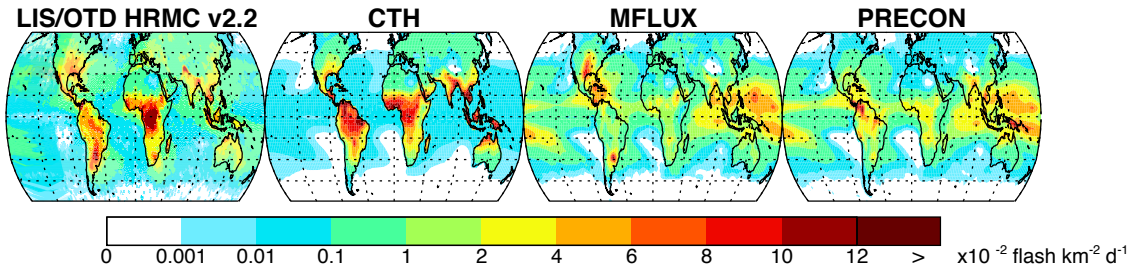

Figure 2.1: Mean observed and simulated lightning densities (flashes km^{-2} d^{-1}) for May 1995 to December 2005. LIS/OTD satellite data from the High Resolution Monthly Climatology (HRMC) v2.2 are compared to unconstrained GEOS-Chem model distributions from parameterizations based on cloud top height (CTH) [*Price and Rind*, 1992, 1993, 1994], upward mass flux (MFLUX) [*Allen et al*., 2000], and convective precipitation (PRECON) [*Allen and Pickering*, 2002].

cells as continental only if they contain over 50% land, which provides better correlation with the LIS/OTD HRMC product. We also evaluate two alternative flash rate parameterizations: the convective mass flux scheme (MFLUX) of *Allen et al*. [2000] used as the base parameterization for the GMI model [*Allen et al*., 2010], and the convective precipitation (PRECON) scheme of *Allen and Pickering* [2002]. As the latter two determine cloud-to-ground (CG) but not intra-cloud (IC) flash densities, we infer total (IC+CG) flashes locally using the IC/CG ratio parameterization from [*Price and Rind*, 1993]. Each parameterization is adjusted by a dimensionless uniform scaling parameter β, following *Tost et al*. [2007], to bring the annual average global flash rate to that of the observed LIS/OTD HRMC product, 46 flashes s^{-1} [*Christian et al*., 2003] (for GEOS-4 at $2^\circ \times 2.5^\circ$, CTH: $\beta = 0.56$; MFLUX: $\beta = 5.0$; PRECON: $\beta = 0.34$).

Any grid cell with a surface temperature less than -40°C is assumed too cold for lightning, a requirement necessary to prevent lightning in polar clouds. In addition, we assume no lightning in any convective column that does not span the full temperature range from 0° to -40°C, taken as the range of the mixed phase layer over where heterogeneous nucleation and charging can occur [*Williams*, 1985]. This effectively suppresses lightning in marine stratus clouds.

Figure 2.1 compares each of the three unconstrained lightning flash rate parameterizations in GEOS-Chem with the LIS/OTD HRMC climatology. The schemes capture less than half of the

variability of the observations at 2° × 2.5° monthly resolution (CTH: $R = 0.66$; MFLUX: $R = 0.40$; PRECON: $R = 0.41$; $n = 144$ longitudes × 91 latitudes × 12 long-term monthly means). None captures the strong maximum observed over central Africa and all have excessive lightning over Oceania. CTH overestimates lightning over Amazonia while the other two underestimate it. The MFLUX and PRECON parameterizations have spurious lightning over the tropical oceans, and their inability to reproduce the land-sea contrast is the primary reason for their lower correlation to observations. Much of the CTH error comes from underestimating the amplitude of the seasonal cycle. As the CTH scheme yields the best a priori distribution of the three approaches, we choose to use it as our unconstrained physical parameterization. *Tost et al.* [2007] also found it to be the most accurate lightning distribution model and most robust within different convective model frameworks.

2.4.2 LIS/OTD correction factors

Previous global CTMs that use the GEOS meteorological fields have constrained their flash rate parameterizations to LIS/OTD products, including GEOS-Chem [*Sauvage et al.*, 2007a; *Stajner et al.*, 2008; *Jourdain et al.*, 2010], GMI [*Allen et al.*, 2010], and the University of Maryland CTM (D. Allen, personal communication, 2007). The constraint involves correcting the unconstrained model flash rates over selected spatial and temporal domain D by a factor α to match the climatological LIS/OTD data:

$$\alpha = \beta \frac{\iint_D F_o(\vec{x}, t) d\vec{x} dt}{\iint_D F_p(\vec{x}, t) d\vec{x} dt} \tag{2.1}$$

where F_o is the observed LIS/OTD flash rate over D, F_p is the corresponding value from the unconstrained model parameterization, $\vec{x}$ is the horizontal location vector, t is time, and β was introduced previously to scale the unconstrained global flash rate to match the 46 flashes s^{-1} of

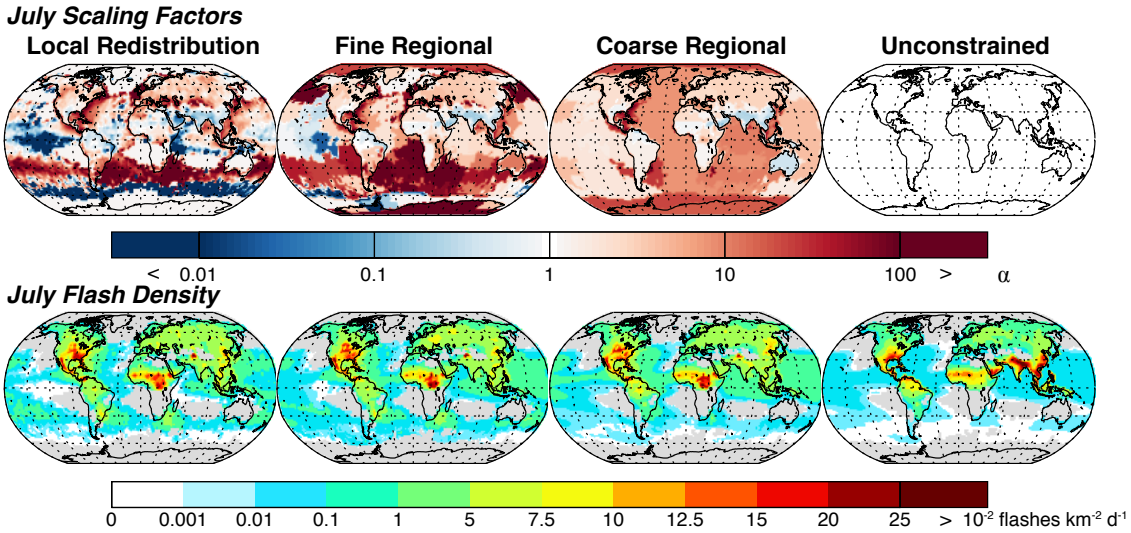

Figure 2.2: Spatial redistribution of lightning flash densities in GEOS-Chem to match the LIS/OTD HRMC data for July. Results from the local, fine regional, and coarse regional redistributions are compared and the unconstrained distribution is also shown. The top panels show the log of the scaling factors α computed from equation 2.1. The bottom panels show the corresponding July lightning flash distributions averaged over 1995-2005. The bottom left panel (local adjustment) essentially corresponds to the July LIS/OTD climatology. Gray regions have no lightning in GEOS-Chem. Statistics for the different redistributions are given in Table 2.2.

the LIS/OTD data (Section 2.4.1; $\beta = 0.56$ for GEOS-4, CTH, and $2^\circ \times 2.5^\circ$). As an example, if the model simulated uniform flash rates for a world divided into two hemispheres and correctly simulated the total flash rate (via β) but observations saw twice the lightning in one hemisphere than the other, the values of α would be respectively 1.5 and 0.75. Lightning variability within each domain D is governed by the CTM lightning parameterization (depending on CTH) to ensure that lightning NO_x emissions are coupled to deep convective transport.

Here we impose the temporal domain to be monthly and explore the sensitivity to the choice of spatial domain, which can be the grid resolution of the CTM (local scaling) as in *Sauvage et al.* [2007a] and *Allen et al.* [2010] or a larger region (regional scaling) as in *Stajner et al.* [2008] and *Jourdain et al.* [2010]. Figure 2.2 shows the resulting redistributions of lightning in GEOS-Chem for July, for both local scaling ($2^\circ \times 2.5^\circ$) and regional scaling (to be described below). Local scaling effectively forces the model to match the observed climatology. Corrections can be very

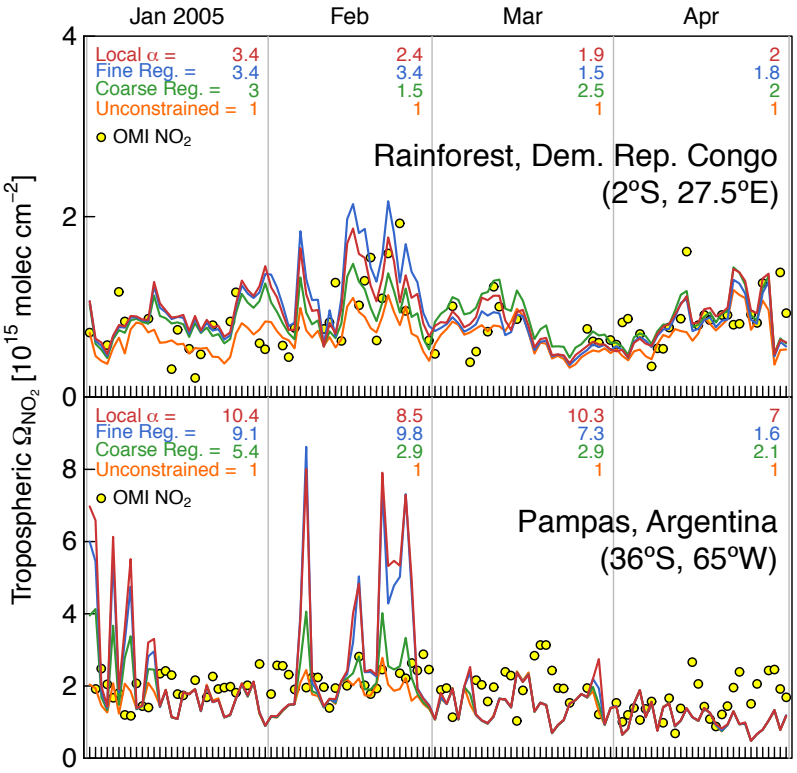

Figure 2.3: Time series of simulated and observed daily tropospheric NO_2 columns. The monthly redistribution factors α, are given for each simulation. The OMI NO_2 gridded daily global Level-3 product (OMNO2e v3) is produced by the Atmospheric Chemistry and Dynamics branch at NASA GSFC, and available online at http://disc.gsfc.nasa.gov/Aura/OMI.

large. We see for example a large upward correction over the western North Atlantic where lightning over the ocean is much higher than estimated from the CTH parameterization.

The choice of local or regional scaling can have significant implications, as noted in the Introduction. We illustrate this in Figure 2.3, which shows Jan-Apr 2005 time series of tropospheric NO_2 columns simulated by GEOS-Chem and observed by the Ozone Monitoring Instrument (OMI) on the Aura satellite [*Bucsela et al.*, 2006] for two lightning-prone $2^\circ \times 2.5^\circ$ grid squares in the Congo rainforest and the Argentina plains. We apply either local or regional scaling (see below for regional scaling definition) to the GEOS-Chem fields. The Congo grid cell is well-behaved, with scaling factors that vary moderately across scales. In that case, the local scaling captures better the observed OMI variability. The Argentina grid cell is ill-behaved, with

large variations in scaling factors across scales, and in that case the local scaling produces spurious variability compared to observations. Although local scaling maximizes fidelity to the location of lightning in the observations, the amount of lightning NO_x released per convective event may be unrealistic. In addition, the dependence of lightning on convective top height may be broken, altering the mean altitude of emission as well as the relative amount of convected surface precursors co-located with the lightning emissions.

Using regional scaling addresses these difficulties with local scaling, but the distribution of lightning within a region may then not match the observations. Here we address the latter difficulty by using hierarchical clustering [*Johnson*, 1967] as an objective data-driven aggregation technique to select coherent scaling regions in a way that tries to maximize the domain size (D) while preserving the fit to the observed global lightning distribution. The principal benefit of the hierarchical technique over other clustering algorithms is that it makes no prior assumptions about how the regions are to be clustered. The algorithm initially assigns each $2^\circ \times 2.5^\circ$ grid cell to its own region, calculates the "distance" to all other regions, and joins the two most similar; this proceeds iteratively until eventually only one region remains. We thus obtain a hierarchical tree or "dendogram" of optimally clustered regions, and can compare in the CTM the effect of choosing different levels of the dendogram (i.e., different numbers of regions).

To construct the dendogram we define the "location" for a region i by the vector $\vec{v}_i = (\vec{x}, a, b)^{\mathrm{T}}$ where $\vec{x}$ is the position of the region centroid on the sphere, a is the absolute difference between the unconstrained model and the observed monthly mean flash rates averaged over the region, and b is the logarithm of the relative difference. All variables are standardized globally to unit variance and zero mean. We then define "distance" between two regions i and j as the norm $\|\vec{v}_i - \vec{v}_j\|$. This aggregates regions that are geographically close (though not necessarily contiguous) and that match the observations similarly well or poorly. Coherent regions are calculated separately for each month of the year. We impose that the first branch separate between land and ocean because the CTH parameterization is different for these two domains.

Table 2.2: Global GEOS-Chem Lightning Redistribution Statistics[a]

Redistribution	Number of Regions[c]	Range of Scaling Factors[d]	R	Lightning Distribution (%)[b]		Global Lightning NO_x Source (Tg N a^{-1})[e]	Monthly LIS Overpasses per Region[f]
				Tropics	Northern Extratropics		
Local	13,104	10^{-11} - 10^{+4}	>0.99	65	23	6.1	67
Fine Regional	137	10^{-10} - 10^{+3}	0.93	68	22	6.0	406
Coarse Regional	37	10^{-05} - 10^{+2}	0.89	74	20	6.0	1044
Unconstrained[g]	1	1	0.66	84	13	5.6	-

[a] The redistributions constrain the lightning flash statistics in the GEOS-Chem CTM to match the monthly observed LIS/OTD HRMC v2.2 climatology over local or regional scaling domains D. The Pearson correlation coefficients R measure the fit between the resulting 1995-2005 GEOS-Chem and LIS/OTD long-term monthly mean climatologies on the $2^\circ \times 2.5^\circ$ grid of the model (n = 144 longitudes $\times$ 91 latitudes $\times$ 12 months).

[b] Redistribution affects the global lightning NO_x source because of the difference in the NO_x yield per flash between the tropics and the extratropics (Section 2.4.3)

[c] The number of regions can vary slightly from month to month with regional scaling and the values given here are annual means.

[d] Global range of scaling factors α computed from equation 2.1.

[e] Mean number of LIS orbital overpasses per region in the month of October, calculated for data from 1998 to 2006.

[f] Mean number of LIS orbital overpasses per region in the month of October, calculated for data from 1998 to 2006.

[g] Original CTH parameterization of lightning in GEOS-Chem with no redistribution (Section 2.4.1)

Figure 2.2 shows the different redistributions of lightning in GEOS-Chem for July and Table 2.2 gives the corresponding climatological redistribution statistics. We consider two levels of regional scaling, fine and coarse, corresponding to different levels of the dendogram with an average of 137 and 37 regions globally respectively per month. The regions for July are identified in Figure 2.2 by different colors. The coarse resolution is still finer than the continental scales used by *Stajner et al*. [2008] and *Jourdain et al*. [2010]. As the regions increase in size, the range of scaling factors considerably decreases as shown in Table 2.2. Correlation with the monthly LIS/OTD climatology ranges from $R = 0.66$ for the unconstrained case to $R > 0.99$ for the local redistribution. The high bias of tropical lightning in the unconstrained parameterization is corrected. Most of the improvement in fitting the LIS/OTD data is already achieved with the coarse regional scaling and its 37 regions ($R = 0.89$). We compare below the local and regional scaling approaches in terms of their effects on the GEOS-Chem simulation of ozone.

2.4.3 Converting flash rates to NO_x emissions

There is large uncertainty in relating flash rates to lightning NO_x emissions [*Schumann and Huntrieser*, 2007]. Standard practice in GEOS-Chem and other global CTMs has been to adjust the global lightning NO_x source to optimize the simulation of tropospheric ozone and nitrogen oxides. The resulting source range in global CTMs is 3-7 Tg N a^{-1} [*Denman et al.*, 2007]. *Martin et al.* [2007] derived a best estimate of 6 (4-8) Tg N a^{-1} in GEOS-Chem to match satellite estimates of the column of tropospheric ozone in the tropics.

There is evidence for higher NO_x yields per flash in the extratropics than in the tropics from aircraft campaigns [*Huntrieser et al.*, 2002, 2007, 2008], satellite observations [*Martin et al.*, 2006, 2007; *Sauvage et al.*, 2007a; *Boersma et al.*, 2008] and model studies [*Hudman et al.*, 2007]. We use here a yield of 500 mol N per flash from *Hudman et al.* [2007] for all extratropical lightning north of 23°N in America and 35°N in Eurasia. This yield is consistent with several studies of lightning NO_x production over the U.S. [*DeCaria et al.*, 2005; *Cooper et al.*, 2007; *Jourdain et al.*, 2010; *Ott et al.*, 2010]. For the rest of the world, we use the constraint of 4.4 Tg N a^{-1} for that region derived by *Martin et al.* [2006, 2007], together with the LIS/OTD climatological flash rate, to infer 260 mol N per flash. This is within the range of current literature [*Schumann and Huntrieser*, 2007].

Unlike earlier versions of GEOS-Chem going back to *Wang et al.* [1998], we do not include a dependence of the NO_x yield on the length of the flash (which is poorly constrained) or whether the flash is CG or IC. The studies by *Ott et al.* [2007, 2010] suggest no difference in yield between CG and IC flashes. A recent study for northern Alabama by *Koshak et al.* [2013] using a detailed process-based model of NO_x production finds substantially higher yields in CG than IC flashes.

The lightning NO_x emitted in the model for a given grid cell and 6 h period is distributed vertically between the surface and convective cloud top height following standard profiles for marine, tropical continental, subtropical, and mid-latitude storms simulated by *Ott et al.* [2010]

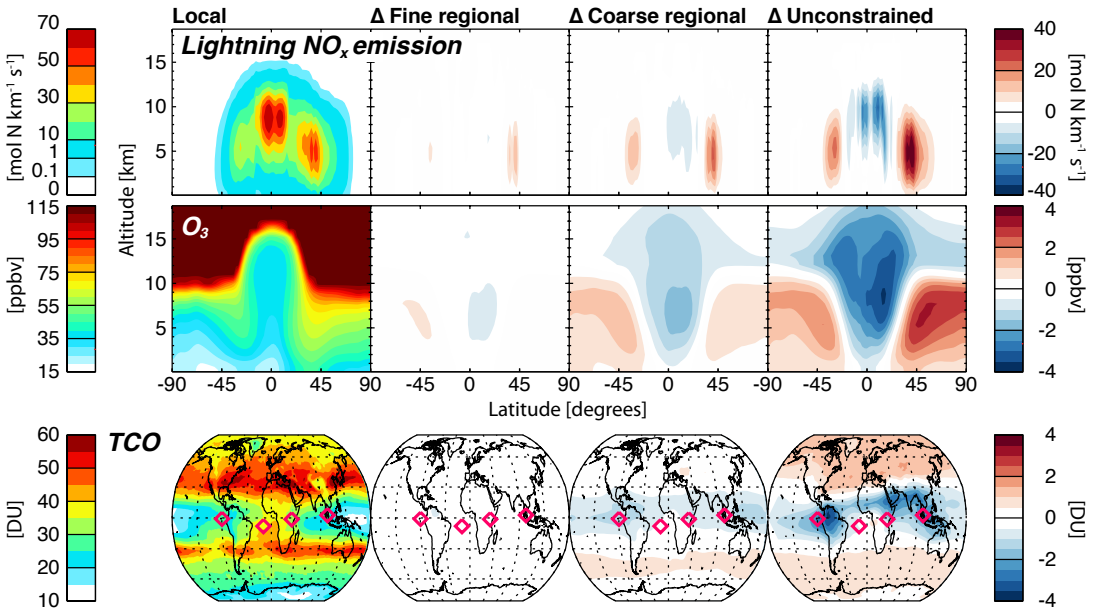

Figure 2.4: Effect of different lightning redistributions on lightning NO_x emissions and tropospheric ozone in GEOS-Chem. The left panels show annual mean results from a simulation for 2004-2005 with local redistribution based on the LIS/OTD HRMC satellite climatology: zonal mean lightning NO_x emissions (top), zonal mean ozone mixing ratio profiles (middle), and tropospheric column of ozone (TCO). The other panels show the differences (Δ) relative to that simulation when the regional redistribution is used (fine or coarse) or when no redistribution is applied (unconstrained). The diamonds show the location of stations used in Figure 2.5.

using a cloud-resolving model. This updates the vertical profiles from *Pickering et al.* [1998] used in previous versions of GEOS-Chem. The principal difference is that *Pickering et al.* [1998] release 10-20% of lightning NO_x below 2 km, as compared to 1-7% in *Ott et al.* [2010]. The newer profiles also have a lower median height of emission. The effect on simulated ozone is small, at most a few percent anywhere.

2.5 Implications for modeling tropospheric ozone

Figure 2.4 shows the impacts of the different lightning redistribution methods on the GEOS-Chem simulations of lightning NO_x emissions and zonal mean tropospheric ozone. All simulations are identical except for the lightning redistribution. The dominant effect of the

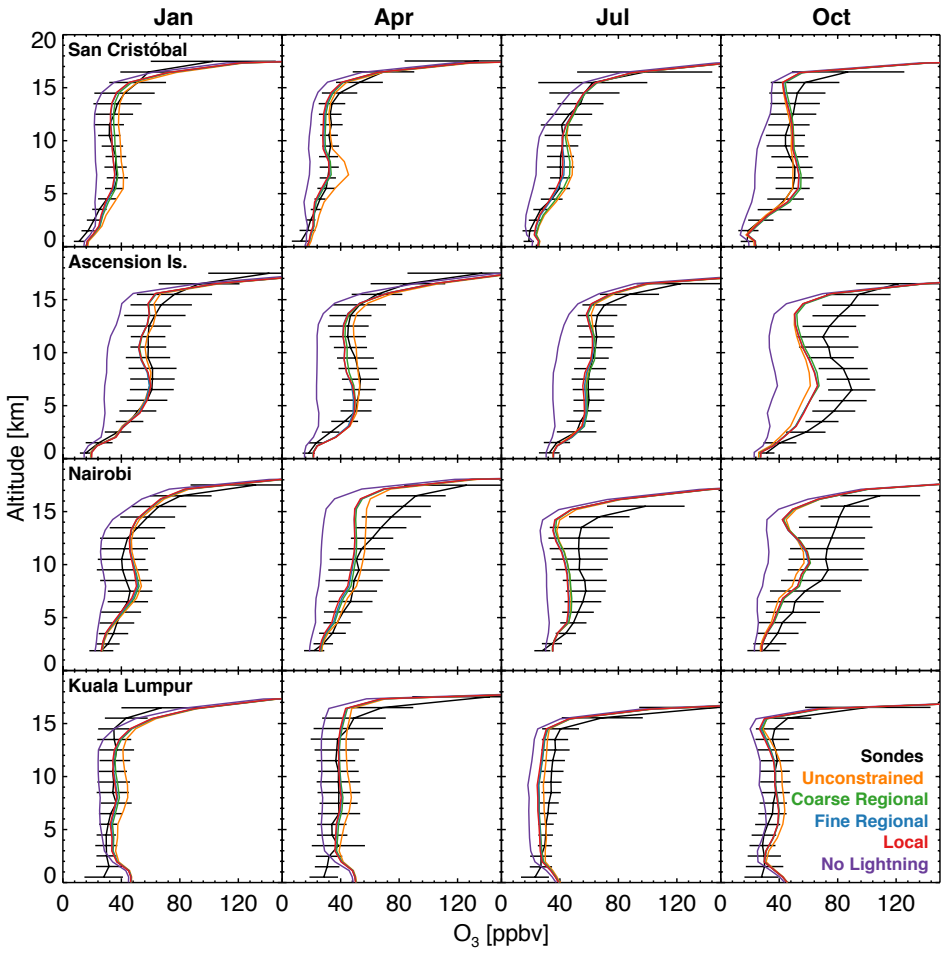

Figure 2.5: Monthly mean vertical profiles of ozone mixing ratios for four tropical stations of the SHADOZ ozonesonde network [*Thompson et al.*, 2003a]: San Cristóbal, Ecuador (0.9°S, 89.6°W), Ascension Island (8.0°S, 14.4°W), Nairobi, Kenya (1.3°S, 36.8°E), and Kuala Lumpur, Malaysia (2.7°N, 101.7°E). Plotted in black are observed mean profiles for 1998-2010 with bars indicating standard deviations of the individual profiles for 1 km vertical bins. The colored lines represent the mean daily ozone profiles for 2004-2005 simulated by GEOS-Chem using the different lightning redistributions. Also shown is a simulation without lightning NO_x (purple).

redistribution is to shift lightning flashes from the tropics to the extratropics, as previously found by *Sauvage et al.* [2007a]. This decreases tropical ozone while increasing extratropical ozone by up to 4 ppbv relative to the unconstrained simulation. Similar results are found for seasonal differences (not shown).

Figure 2.5 compares simulated ozone with climatological profiles from four representative

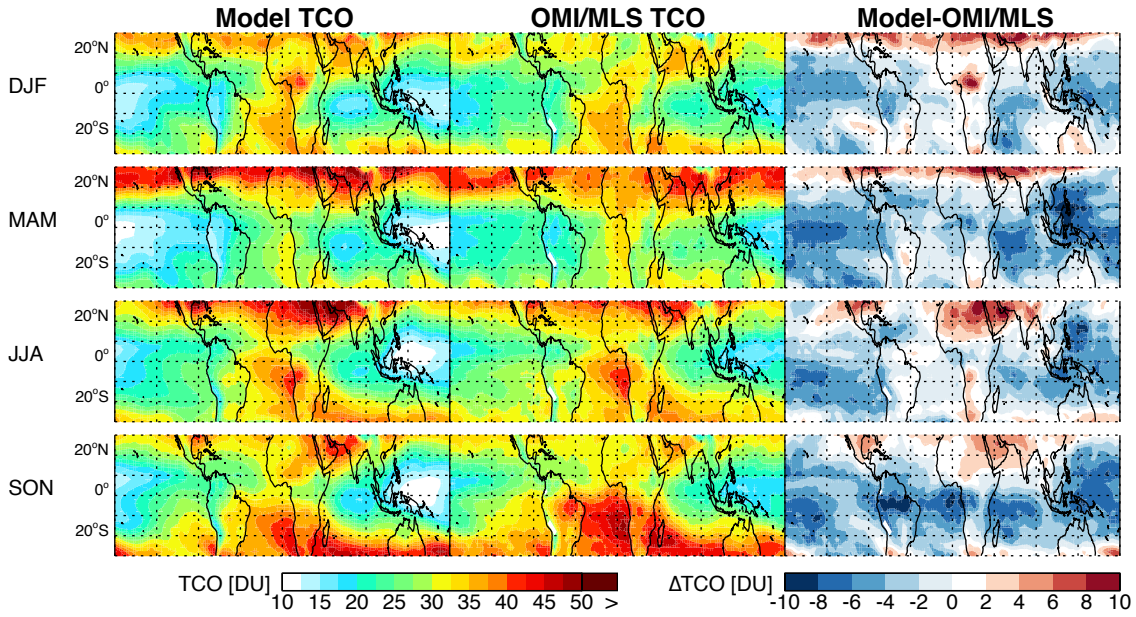

Figure 2.6: Seasonal mean tropospheric column ozone (TCO) for December 2004 to November 2005. Model results using the local lightning redistribution are compared to OMI/MLS observations [*Ziemke et al.*, 2006] from ftp://jwocky.gsfc.nasa.gov/pub/ccd/data_monthly/. The right panels show the differences between the two.

tropical stations of the SHADOZ network [*Thompson et al.*, 2003a]. Also shown is a simulation without lightning NO_x, which greatly underestimates observations and illustrates the model sensitivity to the lightning source of NO_x. The model reproduces the general vertical, zonal, and seasonal patterns in the observations, except over the South Atlantic during October and over equatorial Arica in July and October, as well as in the upper troposphere (UT) in April. We find that lightning redistribution changes ozone concentrations by typically a few ppbv relative to the unconstrained simulation, the largest effect being at San Cristóbal in April (-4.7 ppbv) due to excessive wet season lightning over Amazonia in the unconstrained simulation. The differences between the redistribution techniques are typically less than 1 ppbv. These effects are sufficiently small that no method emerges as significantly better for reproducing the observations.

High-quality satellite ozone data in the tropics provide a more sensitive test. We compared the different simulations with the OMI/MLS tropospheric column of ozone (TCO) product developed

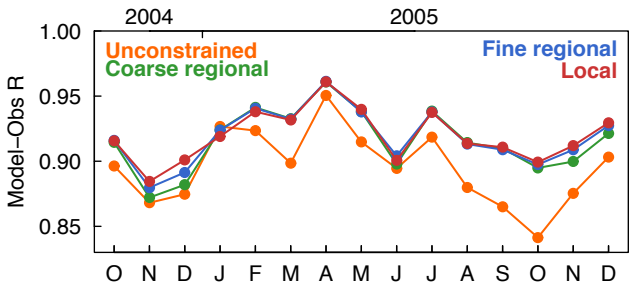

Figure 2.7: Spatial correlation coefficient *R* for GEOS-Chem versus OMI/MLS monthly mean tropospheric column ozone (TCO) on the 2°×2.5° grid of GEOS-Chem and for 23°S-23°N. Values are for October 2004 to December 2005. Results are shown for the different model lightning redistributions.

by *Ziemke et al*. [2006], who subtracted coincident measurements of stratospheric ozone made by the Microwave Limb Sounder (MLS) [*Waters et al*., 2006] from total column ozone measurements made by the Ozone Monitoring Instrument (OMI) [*Levelt et al*., 2006], both on the Aura satellite. We determined model TCO using hourly ozone profiles and the local lapse rate tropopause, and averaged over each month. Figure 2.6 compares the simulation with local redistribution to the seasonal mean observations. The model is biased low by a few DU over most of the tropics. It reproduces well the observed spatial and seasonal patterns. Figure 2.7 shows the Pearson correlation coefficient *R* for model versus observed monthly mean TCO values on the 2° × 2.5° grid for 23°S-23°N and for October 2004 to December 2005. Values are relatively high ($R = 0.84$-0.96), reflecting the dominance of large-scale variability in the TCO observations (Figure 2.6) that the model can generally simulate well. Lightning redistribution improves the simulation of ozone variability for almost every month. The improvements are statistically significant. Comparison of the three different redistributions shows slightly better results for the local scaling but the differences are not statistically significant.

There is a well-known zonal "wave one" pattern in tropical TCO [*Fishman et al*., 1990, 1991; *Shiotani*, 1992; *Thompson and Hudson*, 1999; *Thompson et al*., 2000, 2003b; *Sauvage et al*., 2006]. We illustrate this pattern in Figure 2.8 with Hovmöller plots for TCO in the latitude bands 0-23°S and 0-23°N as a function of longitude and time. In the southern tropics, the model

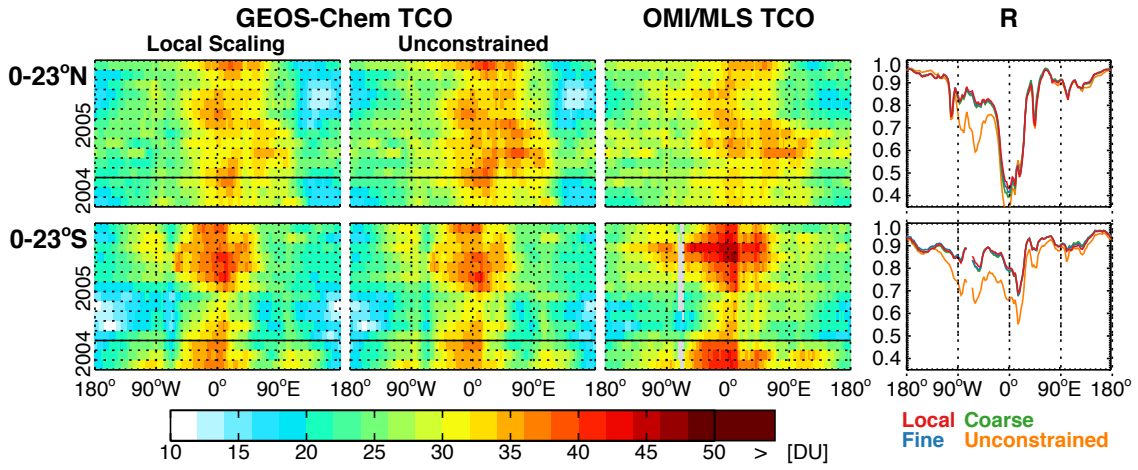

Figure 2.8: Tropospheric column ozone (TCO) in the 0-23°N and 0-23°S bands as a function of longitude and time for October 2004 to December 2005. Observations from OMI/MLS are compared to GEOS-Chem simulations with the unconstrained lightning parameterization and with local lightning redistribution based on the LIS/OTD data. The right panels show the correlation coefficients of simulated versus observed values for specified longitudes and months (n = 12 latitudes per hemisphere on the 2°×2.5° model grid × 15 months), for the simulations with unconstrained lightning and with different lightning redistributions.

reproduces the wave one pattern with a maximum over the South Atlantic and Africa (60°W to 40°E), peaking in September to November (SON), and a minimum over the Pacific (140-180°E). The maximum is driven by persistent radiative subsidence over the South Atlantic anticyclone drawing in NO_x (including from lightning) and other precursors lofted by deep convection over the continents [*Krishnamurti et al.*, 1993; *Chatfield et al.*, 1996; *Jacob et al.*, 1996; *Martin et al.*, 2002; *Sauvage et al.*, 2007b]. The unconstrained model has a relatively low correlation with observations over the South Atlantic and adjacent land masses, mainly because of underestimate of the SON seasonal maximum and a 2-month early shift in the timing of the maximum. The lightning redistributions all greatly improve the correlation with observations in that region by delaying the maximum by 1 month; there is no significant difference between the different redistributions. In the northern tropics, lightning redistribution has little effect except for a large improvement over the western North Atlantic, and a modest improvement over Africa where the

model shows low skill in reproducing ozone variability.

2.6 Interannual variability of lightning flash rates

We have shown above that the local and regional approaches for lightning redistribution using the LIS/OTD data are statistically indistinguishable in their ability to simulate tropospheric ozone, although the local redistribution may be marginally better. All improve model ozone over the unconstrained lightning simulation. An important advantage that we will demonstrate of the coarse regional over the finer redistributions is that it provides better observational statistics with which to use LIS to constrain interannual variability (IAV) in flash rates and its effects on the IAV of tropical tropospheric ozone and OH.

Here we constrain the IAV of tropical lightning using the coarse regional redistribution applied to LIS orbital data for 1998-present (Section 2.2). LIS is in inclined orbit and sweeps between 35°S and 35°N about 15 times a day. Care must be taken to correct for the interannually varying diurnal schedule of the orbit tracks as the lightning frequency varies greatly with time of day. This is illustrated in Figure 2.9 with the diurnal distribution of LIS sampling for October 2002 and 2003 at 35°N and the Equator, together with the global mean diurnal distribution of lightning observed from OTD in 1995-2000 in sun-asynchronous near-polar orbit [*Schumann and Huntrieser*, 2007]. Lightning activity is minimum at 9-10 local time (LT) and maximum at 15-16 LT. LIS observations sample this distribution very differently in October of 2002 and 2003. There is greater diurnal bias in observations at 35° than at the Equator, but observations at the Equator are ten times less frequent.

The bottom panels of Figure 2.9 show the diurnal sampling bias of LIS for October 2003 as measured by the relative departure from uniform daily sampling. The diurnal sampling bias increases from about 30% at the Equator to 60% at 35° latitude, varying little with longitude. The time required for LIS to sample all hours of day at least once ranges from about 30 days at the

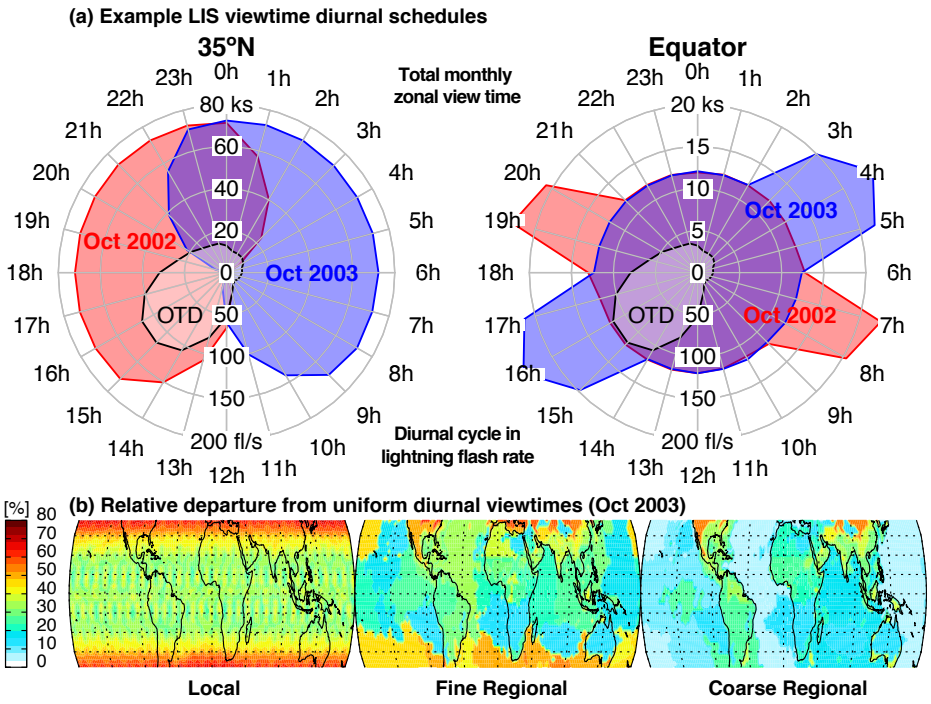

Figure 2.9: Diurnal distribution of LIS satellite observations for October 2002 and 2003. The top panel shows rose plots of the total LIS viewing times (kiloseconds or ks) at different local times of day for October 2002 (red and purple) and October 2003 (blue and purple) aggregated zonally over 2° latitudinal bands at 35°N and the Equator. Note the difference in scales for 35°N and the Equator, as 35°N is observed ten times more frequently because of the inclined satellite orbit. Also shown in the same rose plots is the climatological global frequency of lightning (flashes per second or fl/s) as a function of local time of day measured by the OTD satellite instrument in sun-asynchronous near-polar orbit. The bottom panels display the LIS diurnal sampling bias for October 2003 as the mean relative departure of hourly observation frequencies from 24-h uniform sampling. A region with uniform sampling would have a relative departure of 0%,while a region with twice as frequent sampling in the daytime than at night would show a relative departure of 33

equator to about 98 days in the subtropics, making a local redistribution inappropriate to constrain flash rates for a specific month and year. However, the bottom panels of Figure 2.9 show that regional distribution greatly reduces this diurnal bias through the merging of areas at different latitudes. This, combined with the much greater number of observations per coarse region (Table 2.2) allows an effective correction of the diurnal sampling bias.

We represent IAV in the global distribution of lightning in GEOS-Chem for the LIS observation

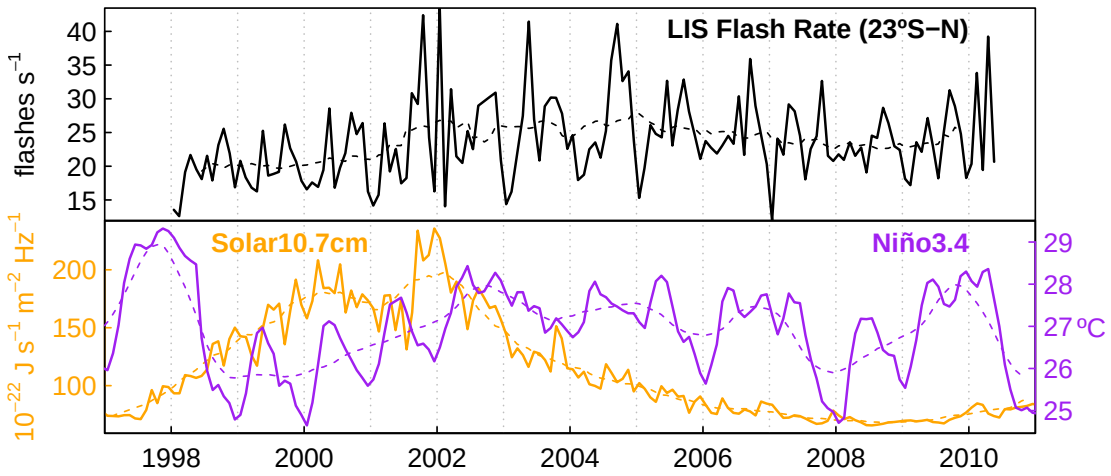

Figure 2.10: 1998-2010 interannual variability (IAV) of tropical lightning and climatological indices for 23°S-23°N. Top panel: time series of the monthly mean tropical flash rate determined from the LIS Science Data v4.1 product as described in the text. The dashed line is the 12-month running mean. Bottom panel: climatological indices available from NOAA ESRL (http://www.esrl.noaa.gov/psd/data/climateindices/), including the monthly mean Solar Flux (10.7cm; orange) provided as a service by the National Research Council of Canada, and the El Niño Region 3.4 Index (Niño3.4; purple).

domain (35°S-35°N) by first applying the local climatological scaling described in Section 2.4, and then applying the coarse regional scaling using the LIS data for individual years (1998-2010). The flash rates from the LIS Science Data 4.1 product are determined by dividing the total observed flash counts in a given area by its effective view time, and are then aggregated into 24 hourly bins (local time) for each region, month, and year. They are then adjusted with the hourly LIS detection efficiencies from *Boccippio et al*. [2002], and averaged to derive monthly regional flash rates for scaling the climatological values. In the event that any hour was not observed in a region and month, the monthly mean for 1998-2010 is used. Poleward of 35° where there are no LIS data we use the LIS/OTD climatology (effectively OTD) with local redistribution and no IAV constraint; 25% of global lightning flashes are poleward of 35° and any simulated IAV there is driven by model meteorology.

Figure 2.10 shows the resulting flash rate time series in the tropics (23°S-23°N) for the 1998-2010 period. Mean lightning activity increased slowly from 1998 until early 2002 and then

leveled off. Also shown are climatological indices for the solar flux and for the El Niño-Southern Oscillation (ENSO). We correlated the 12-month running means of tropical flash rates with those of the two indices and find little correlation with the solar flux (R = -0.21) but strong correlation with the Niño Region 3.4 index (R = 0.79). This suggests that ENSO plays an important role in driving IAV in mean tropical lightning activity. We find no correlation of lightning with the stratospheric Quasi-Biennial Oscillation (not shown), which has been previously linked to tropical deep convection [*Collimore et al*., 1998, 2003].

The positive correlation of lightning with ENSO is consistent with previous studies for Indonesia and Southeast Asia [*Hamid et al*., 2001; *Yoshida et al*., 2007; *Logan et al*., 2008] and the southeastern United States [*Goodman et al*., 2000]. However, *Yuan et al*. [2011] find that lightning IAV in the western Pacific is not correlated with ENSO but with volcanic aerosol loadings. We examined the regional patterns of lightning correlation with ENSO from our work and find results consistent with these studies. *Hamid et al*. [2001] noted that lightning frequencies in the tropics are very sensitive to small increases in surface air temperature [*Williams*, 1992] and that the surface temperature over the tropical land generally increases during the positive phase of ENSO [*Hansen and Lebedeff*, 1987].

Figure 2.11 shows the variability of the global lightning source for 1998-2006 and compares it to the other NO_x emissions in GEOS-Chem. We focus on 1998-2006 because of the common availability of LIS, GFED-2, and GEOS-4 data for this period. Local scaling to the LIS/OTD climatological data (blue line in the top panel) increases the seasonal amplitude of the global lightning source relative to the unconstrained parameterization (green line), mostly because of increased lightning at northern extratropical latitudes in summer (Table 2.2). The IAV constraint (red line) produces additional variability, including in particular the summer maximum in 2004 driven by the northern subtropics.

The middle panel of Figure 2.11 compares the local+IAV lightning NO_x source to the biomass burning source from the GFED2 inventory [*van der Werf et al*., 2006] as well as other sources.

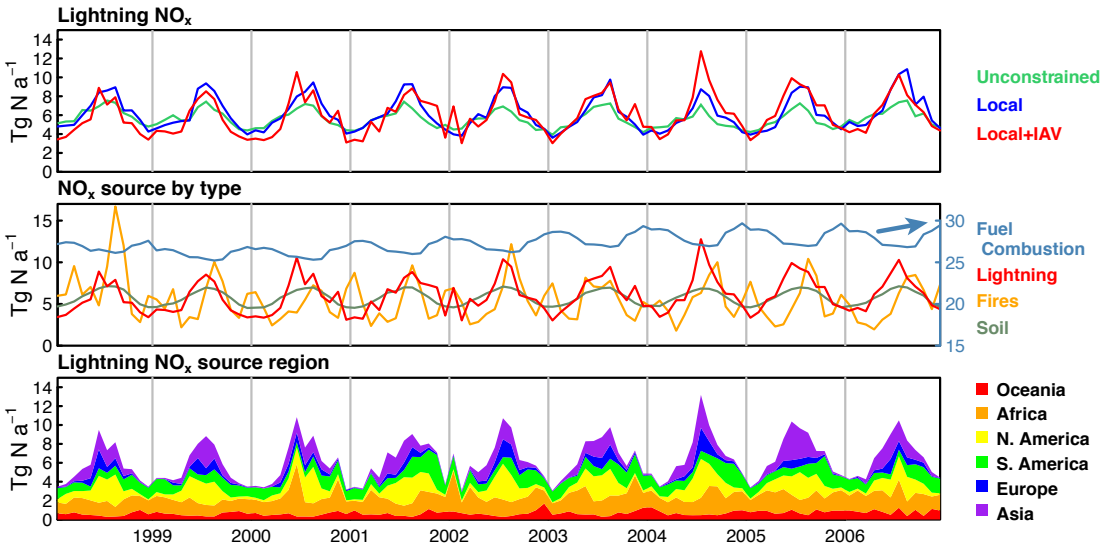

Figure 2.11: Global monthly NO_x emissions, 1998-2006. Top panel: lightning emissions computed from the unconstrained parameterization, the parameterization with local climatological scaling from the LIS/OTD data, and the simulation with local scaling and coarse regional interannual variability (IAV) from the LIS data. Middle panel: NO_x emissions by source type where lightning is from the local scaling with IAV; note different scale on the right for the anthropogenic NO_x source (fossil fuel and biofuel). Bottom panel: cumulative lightning NO_x emissions (including local scaling and IAV) by continent. The time series of lightning NO_x emissions including local scaling and IAV is reproduced in all three panels.

The mean and interannual standard deviation of the global lightning source over these 9 years is 6.0 ± 0.5 Tg N a^{-1}, as compared to 5.5 ± 0.8 Tg N a^{-1} for the global biomass burning source. The bottom panel shows the contributions of different continents to the global lightning NO_x source. The IAV in lightning flash rates is split roughly equally between the tropics (mostly Africa) and extratropics (mostly Asia). The extratropics account for two thirds of the IAV in global lightning NO_x emissions because the NO_x yield per flash is higher there than in the tropics.

2.7 Conclusions

We have explored and compared different approaches for using LIS/OTD satellite observations to constrain the lightning NO_x source in global chemical transport models, with focus on enabling simulation of tropical interannual variability (IAV) in lightning and its implications for

tropospheric chemistry. A major challenge was to effectively deal with the sparseness and sampling bias of the satellite lightning data.

The standard procedure for using satellite data to constrain the lightning source in a CTM has been to start from a parameterization of lightning (based, for example, on cloud top heights or convective mass fluxes), and then apply local or regional correction (scaling) factors from the satellite data to redistribute the model lightning. Because of the sparseness of the satellite lightning data, past studies have limited themselves to climatological scaling using multiyear data [*Sauvage et al*., 2007a; *Stajner et al*., 2008; *Allen et al*., 2010; *Jourdain et al*., 2010]. We compared the local and regional climatological approaches in the GEOS-Chem CTM, using an updated LIS/OTD data set and a hierarchical clustering algorithm to optimize the selection of regions. The local scaling maximizes fidelity to the observations but the regional scaling has better sampling statistics for LIS and yields more reasonable daily NO_2 columns. We found that local and regional (coarse or fine) redistributions of lightning yield very similar simulations of tropical tropospheric ozone in GEOS-Chem and that all improve significantly over the unconstrained parameterization.

We used the coherent lightning regions identified by our hierarchical clustering algorithm as the basis for constraining the IAV of lightning from the LIS data for 1998-2010 and 35°S-35°N, taking advantage of the better statistics afforded by scaling over coarse regions. This involved processing of the LIS data to remove the interannually varying diurnal sampling bias. The resulting time series of tropical lightning shows an interannual correlation with ENSO ($R = 0.79$) and no significant correlation with the solar cycle or the QBO. The resulting interannual variability of the global lightning NO_x source in GEOS-Chem (6.0 ± 0.5 Tg N a^{-1}) is similar to that of biomass burning from the GFED-2 inventory (5.5 ± 0.8 Tg N a^{-1}). About two thirds of the IAV in the global lightning NO_x source is contributed by the extratropics. In Chapter 3, we use these interannually varying NO_x sources in GEOS-Chem to investigate the consequences for IAV of tropospheric ozone and OH.

Chapter 3

Interannual variability in tropical tropospheric ozone and OH: the role of lightning

Abstract

Nitrogen oxide radicals (NO_x) produced by lightning are natural precursors for the production of the dominant tropospheric oxidants, OH and ozone. Observations of the interannual variability (IAV) of tropical ozone and of global mean OH (from the methyl chloroform proxy) offer a window for understanding the sensitivity of ozone and OH to environmental factors. We present the results of simulations for 1998-2006 using the GEOS-Chem chemical transport model with IAV in tropical lightning constrained by satellite observations from the Lightning Imaging Sensor (LIS). We find that this imposed IAV in lightning NO_x improves the ability of the model to reproduce observed IAV in tropical ozone and OH. Lightning is far more important than biomass burning in driving the IAV of tropical ozone, even though the IAV of NO_x emissions from fires is greater than that from lightning. Our results indicate that the IAV in tropospheric OH is highly sensitive to lightning relative to other emissions, and suggest that lightning contributes an important fraction of the observed IAV in OH inferred from the methyl chloroform proxy. Lightning affects OH through the $HO_2 + NO$ reaction, an effect compounded by positive feedback from the resulting increase in ozone production and in CO loss. We can account in the model for the observed increase in OH in 1998-2004 and for its IAV, but the model fails to explain the OH decrease in 2004-2006. We find that stratospheric ozone plays little role in driving IAV in OH during 1998-2006, in contrast to previous studies that examined different periods.

3.1 Introduction

Ozone and the hydroxyl radical (OH) play important roles in the oxidative capacity and radiative budget of the tropical troposphere. Ozone is produced by photochemical oxidation of carbon

monoxide (CO) and volatile organic compounds (VOCs) in the presence of nitrogen oxide radicals ($NO_x \equiv NO + NO_2$). In the cold upper troposphere, ozone has a potent greenhouse effect [*Lacis et al.*, 1990; *Forster and Shine*, 1997]. Photolysis of ozone in the presence of water vapor produces OH, the main tropospheric oxidant controlling the lifetime of many important climate gases including methane and hydrogenated halocarbons [*IPCC*, 2007]. Analysis of the interannual variability (IAV) of ozone and OH can provide insights into their sensitivity to environmental changes [e.g., *Ziemke and Chandra*, 1999; *Montzka et al.*, 2011]. Here we assess the ability of a global chemical transport model (the GEOS-Chem CTM) to reproduce IAV in tropical ozone and OH between 1998 and 2006, with particular focus on the role of IAV in lightning as constrained by satellite observations [*Murray et al.*, 2012] (Chapter 2).

Lightning NO_x is thought to be the most important natural ozone precursor in the tropics because it is released in the middle to upper troposphere where the lifetime of ozone is long and its production efficiency per unit NO_x is high [*Pickering et al.*, 1990; *DeCaria et al.*, 2005; *Lelieveld and Dentener*, 2000]. Subsidence of ozone produced by lightning is thought to make a major contribution to the year-round tropical maximum over the South Atlantic [*Sauvage et al.*, 2007b, 2006; *Edwards et al.*, 2003; *Moxim and Levy*, 2000]. This leads to the question of whether lightning contributes to IAV of tropical ozone. Previous studies have shown that dynamical variability makes the largest contributions to IAV over the tropical Pacific and the maritime continent, where biomass burning emissions (but not lightning) also have a large effect [e.g., *Chandra et al.*, 2002; *Nassar et al.*, 2009]. Fire emissions have a small influence on IAV in ozone over South America [*Ziemke et al.*, 2009]. *Grewe* [2007] identified lightning NO_x as the major source of IAV for ozone in a simplified chemistry-climate model, though that study lacked variability in other potentially important emissions including those from fires.

Tropospheric OH is also strongly dependent on lightning NO_x through the $HO_2 + NO$ reaction that forms OH and ultimately makes ozone [*Brune et al.*, 1999; *Logan et al.*, 1981; *Labrador et al.*, 2004]. IAV in global mean OH has been inferred from IAV in measurements of methyl

chloroform (MCF; CH_3CCl_3) which is removed by reaction with OH, and whose emissions are relatively well known [*Spivakovsky et al*., 1990, 2000; *Montzka et al*., 2000; *Lovelock*, 1977; *Prinn et al*., 2001; *Singh*, 1977]. Earlier results were strongly dependent on the reliability of year to year emissions estimates for MCF [*Bousquet et al*., 2005; *Prinn et al*., 2005, 2001; *Krol and Lelieveld*, 2003; *Krol et al*., 2003] and these studies implied larger IAV in OH than similar approaches applied to methane [*Dentener et al*., 2003], and much larger than that predicted by CTMs (1-2%) [*Duncan and Logan*, 2008; *Lelieveld et al*., 2006; *Dentener et al*., 2003; *Dalsøren and Isaksen*, 2006; *Holmes et al*., 2013]. *Montzka et al*. [2011] recently showed that the amplitude of IAV in mean OH deduced from recent data for MCF is only 2-3% now that MCF emissions are sufficiently low that they do not provide a significant source of error; MCF was regulated by the Montréal Protocol. Confidence in the OH time series deduced from recent MCF data offers a new opportunity to examine the factors controlling the IAV of OH.

In Chapter 2, we developed a 13-year (1998-2010) record of lightning IAV in the GEOS-Chem CTM constrained by satellite flash observations from the Optical Transient Detector (OTD) and Lightning Imaging Sensor (LIS) [*Christian et al*., 2003] with the CTM simulation of deep convection over coherent regions. In this work, we use the IAV constraint from LIS for 1998-2006 in GEOS-Chem simulations to examine the role of lightning in controlling IAV in tropical ozone and OH.

Section 3.2 provides a brief description of the model and simulations. Section 3.3 describes how the IAV constraint in the lightning flash rate affects tropical NO_x emissions in the model. The implications for IAV in tropical ozone and OH are discussed in Sections 3.4 and 3.5, respectively.

3.2 Model

We use the GEOS-Chem global CTM (version 9-01-01; http://www.geos-chem.org) to simulate ozone-NO_x-CO-VOC-aerosol chemistry with resolution of 4° by 5° (latitude by longitude) for

1998-2006. The model is driven by GEOS-4 assimilated meteorological data (originally at 1° by 1.25° horizontal resolution) from the NASA Global Modeling and Assimilation Office. We apply the model to study the sensitivity of tropical photochemistry to IAV in lightning constrained by the LIS satellite data ("IAV from LIS"), as compared to a base simulation without such a constraint in IAV. We focus on the tropics as the LIS data extend only from 35°S to 35°N. The OTD data poleward of 35° are too sparse to constrain IAV and ended in March 2000, and we use them only to constrain climatological monthly mean lightning. Our period of analysis (1998-2006) is selected by the availability of the LIS and GEOS-4 meteorological data sets. All simulations presented here are initialized for one year (1997).

The model treatment of the lightning NO_x source is described in detail in Chapter 2. It calculates lightning flash rates online in deep convective events as a function of the local cloud top heights following the parameterization of *Price and Rind* [1992, 1993, 1994], a commonly used scheme in atmospheric chemistry models. It then uses local (4° x 5°) or regional scaling factors to match the climatological monthly satellite distributions from LIS and OTD [*Christian et al.*, 2003]. In the base simulation without the IAV constraint, we use local correction factors to guarantee that the model's monthly mean lightning distribution for 1998-2006 matches that from LIS/OTD; IAV in flash rates in that simulation is solely determined by variability of model cloud top heights. For our improved simulation with IAV constrained by LIS, we use optimized regional scaling factors as described in Chapter 2 to exploit IAV in the LIS data. As shown in Chapter 2, regional and local scaling in GEOS-Chem yield virtually identical results for ozone when no LIS IAV constraint is applied. Thus the base and IAV from LIS simulations can be compared to diagnose the effects of constraining IAV in lightning with the LIS data.

Table 3.1 summarizes the average NO_x sources in GEOS-Chem for 1998-2006. Anthropogenic sources are from the Emission Database for Global Atmospheric Research (EDGAR) inventory for 2000 [*Olivier*, 2001], overwritten with regional inventories for the United States (EPA NEI99 and NEI2005), Canada (CAC), Mexico (BRAVO) [*Kuhns et al.*, 2003], Europe (EMEP) [*Auvray*

Table 3.1: Global and regional sources of NO_x in GEOS-Chem (Tg N a^{-1})[a]

	Global	Tropics	South America	Africa	Maritime Continent
Lightning[b]	6.1 ± 0.46 (0.33)	3.6 ± 0.37 (0.18)	1.1 ± 0.15 (0.07)	1.6 ± 0.20 (0.09)	0.9 ± 0.12 (0.05)
Open fires	5.5 ± 0.79	4.5 ± 0.51	0.8 ± 0.23	2.8 ± 0.21	0.9 ± 0.28
Biofuel and fossil fuel combustion[c]	27.3 ± 0.83	5.4 ± 0.27	1.4 ± 0.06	1.0 ± 0.06	3.0 ± 0.19
Soil microbial activity	5.8 ± 0.06	3.4 ± 0.05	1.1 ± 0.02	1.8 ± 0.02	0.6 ± 0.01
Stratospheric N_2O oxidation and downwelling	0.2 ± 0.02	-	-	-	-
Total	**44.9**	**16.4**	**4.3**	**7.1**	**5.2**

[a] 1998-2006 mean ± interannual standard deviation in annual source. Subtotals are given for the Tropics (23°S-N; 180°W-E), and are further partitioned into tropical South America (23°S-N; 180°-40°W), tropical Africa (23°S-N; 40°W-60°E), and the maritime continent (23°S-N; 60°-180°E)

[b] Values in parentheses indicate the interannual standard deviation in lightning emissions in the base simulation when IAV is not constrained by the LIS satellite data but is still present due to IAV in deep convection.

[c] Interannual standard deviation in fuel combustion solely reflects a linear increasing trend over the 1998-2006 period; cf. Figure 3.1.

and Bey, 2005] and South and East Asia [*Streets et al.*, 2003, 2006]. These inventories all have monthly variability, some with additional weekly cycles, and are scaled each year as described by *van Donkelaar et al.* [2008] to allow for trends. Biofuel emissions *Yevich and Logan* [2003] and aircraft emissions are constant. Biomass burning emissions follow the interannually-varying monthly Global Fire Emissions Database (GFED v2) driven by satellite observations of fire activity [*van der Werf et al.*, 2006]. Soil NO_x emissions follow the parameterization of *Yienger and Levy* [1995] as implemented by *Wang et al.* [1998] and are dependent on meteorological conditions. Biogenic VOC emissions follow the Model of Emissions of Gases and Aerosols from Nature (MEGAN) scheme (version 2.1) [*Guenther et al.*, 2000, 2006] and are driven by both meteorological conditions and monthly-varying satellite observations of leaf area indices from the Moderate Resolution Imaging Spectroradiometer (MODIS) satellite.

Stratospheric ozone concentrations are calculated with the Linoz linearized chemical scheme

[*McLinden et al.*, 2000]. A new development implemented in this work is the calculation of stratospheric concentrations of species other than ozone using monthly mean 3D production rates and loss frequencies from the Global Modeling Initiative (GMI) CTM also driven by GEOS-4 meteorology [*Allen et al.*, 2010; *Duncan et al.*, 2007; *Considine et al.*, 2008]. Photolysis rate calculations for the troposphere use monthly ozone columns from satellites (http://acd-ext.gsfc.nasa.gov/Data_services/merged/), thus allowing for IAV.

Chapter 2 previously evaluated the spatial and seasonal distribution of tropical tropospheric ozone in the same model version as used here at $2^\circ \times 2.5^\circ$ resolution by comparing with sonde profiles and satellite products from the Aura satellite for 2004-2005. They found that the model was generally biased low by a few Dobson Units (1 DU = 6.29×10^{20}molec m^{-2}), a smaller bias than in *Zhang et al.* [2010] using an earlier version of GEOS-Chem driven by GEOS-4. The model reproduces the dominant spatial and seasonal features of tropical tropospheric ozone including the ozone maximum over the South Atlantic although it peaks a month too early. Here we focus on the ability of the model to reproduce IAV in ozone and OH.

3.3 Interannual variability in tropical NO_x emissions

We find that the variability in the tropical lightning NO_x source constrained by LIS is twice that with no such constraint; one standard deviation (σ) in annual emissions is 0.37 Tg N a^{-1} compared to 0.18 Tg N a^{-1} (Table 3.1). Figure 3.1 (top panel) compares the time series of the interannually constrained lightning NO_x emissions to that of the base simulation, where the IAV is generated only by variability in convective cloud top heights in the model. Much of the IAV from LIS comes from a linear trend of +0.28 Tg N a^{-1} over 1998-2002; however, lightning activity is relatively constant after 2002 (Chapter 2). We note that our simulation period follows the major El Niño of 1997 that continued into early 1998.

The four major tropical sources of NO_x (lightning, biomass burning, fuel combustion, soil) are

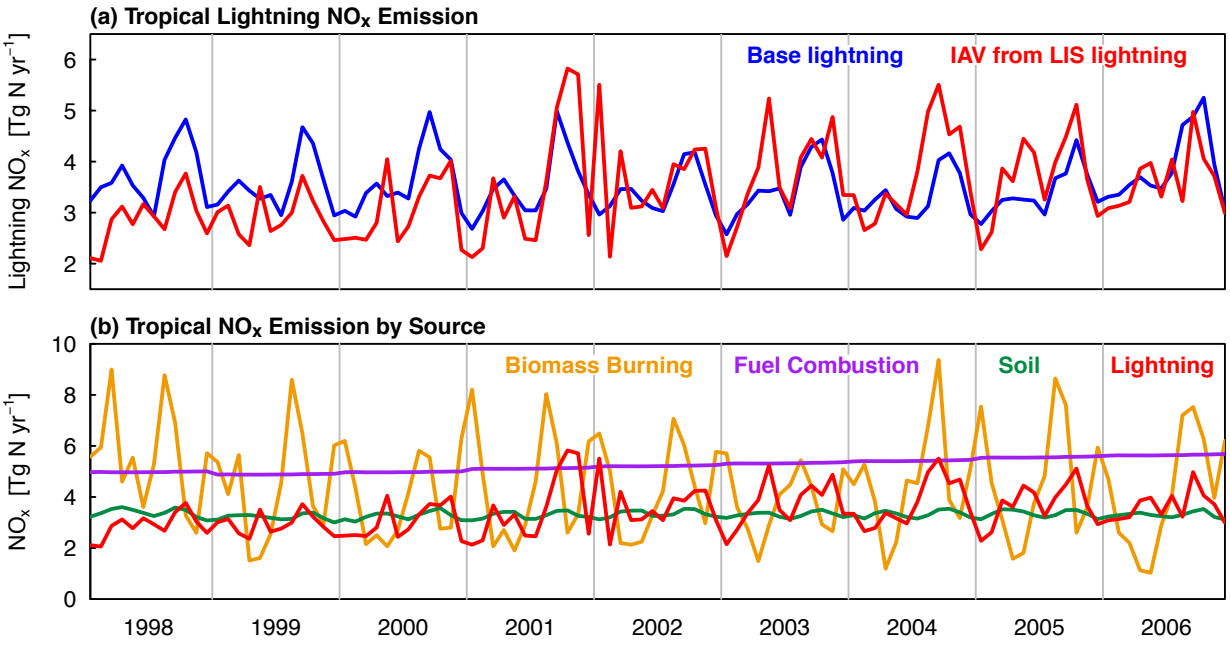

Figure 3.1: Monthly time series of tropical (23°S-23°N) NO_x emissions in GEOS-Chem. (a) Lightning NO_x emissions for the base simulation with IAV from GEOS convection (blue) and the improved simulation with IAV from LIS satellite data (red) (b) Lightning with IAV from LIS (red) is compared to other tropical NO_x emissions by source type.

roughly the same magnitude but differ greatly in variability, as shown in the second panel of Figure 3.1. Fire emissions have higher variability than lightning (σ = 0.51 Tg N a^{-1} versus σ = 0.37 Tg N a^{-1}). However, emissions from fires are released predominantly into the boundary layer, as are the other non-lightning sources. In addition, there are seasonal differences; fires occur predominantly in the dry season in each hemisphere, while lightning peaks in the wet season (Africa) or during the dry-to-wet transition (South America and the maritime continent). Soil NO_x responds to changes in precipitation and surface temperature but the corresponding IAV is low (σ = 0.05 Tg N a^{-1}).

Although our total tropical flash rate is positively correlated with El Niño, mainly because of the increase in lightning and the Niño 3.4 index in mid-1998 to 2002 (Chapter 2), individual

regions may have a more complex relationship. Comparison with previous regional analyses of lightning IAV [*Hamid et al.*, 2001; *Yoshida et al.*, 2007; *Yuan et al.*, 2011; *Satori et al.*, 2009] indicates general consistency with our results (not shown).

3.4 IAV in tropical tropospheric ozone and the role of lightning

3.4.1 IAV in ozone

We evaluate the model with the tropospheric column of ozone (TCO) product derived from EPTOMS (version 7) using the Convective Cloud Differential (CCD) method [*Ziemke et al.*, 1998] and available as gridded $5^\circ \times 5^\circ$ monthly means from 1979 to 2005 [*Ziemke et al.*, 2005]. The CCD technique is limited in its application to 15° from the equator as it assumes zonal uniformity in stratospheric ozone columns. To extend our analysis into 2006, we also use the TCO product from OMI/MLS starting in October 2004, available as gridded $1^\circ \times 1.25^\circ$ monthly means [*Ziemke et al.*, 2006]. The OMI/MLS TCO is on average 9 percent lower than the EPTOMS CCD product when they overlap. We adjust the EPTOMS product for 1998-2005 by subtracting the mean difference for each grid cell in the overlap period to eliminate the bias. The OMI/MLS and adjusted EPTOMS TCO values are then locally averaged for each month of the overlap period. Six-hour mean tropopause heights from the GEOS-4 fields (determined using the lapse rate) are used to integrate the model ozone profiles for comparison with the TCO products.

In Figure 3.2, we compare the annual average TCO for 1998-2006 in the model using the IAV from LIS lightning constraint to the merged EPTOMS and OMI/MLS TCO product. The model overestimates ozone over the South Atlantic maximum by 2-4 DU and over northern Africa by 3-6 DU; it is slightly low over the ozone minimum in the western Pacific. The mean tropical bias is small (+0.45 DU), and the spatial and seasonal variability is well reproduced ($R^2 = 0.82$; $n = 72$ longitudes $\times$ 8 latitudes $\times$ 12 months).

Figure 3.3 shows spatial patterns of IAV in tropical ozone as the standard deviations in the

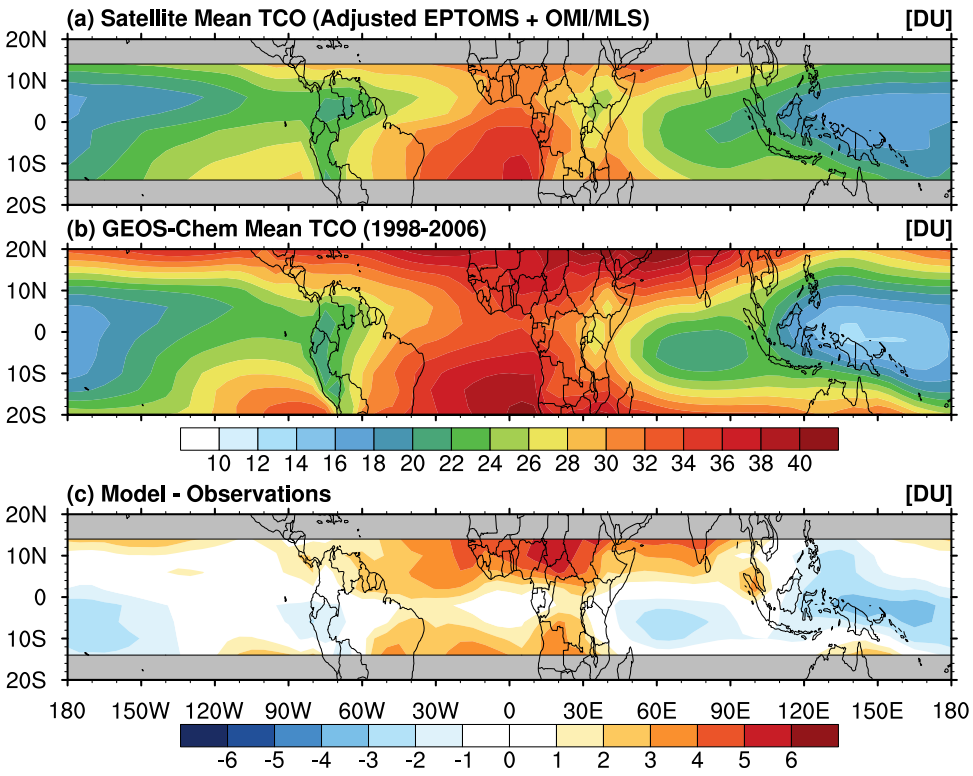

Figure 3.2: Annual average tropical tropospheric column ozone (TCO) for 1998-2006. GEOS-Chem (middle panel) is compared to observations (top panel). The observations from satellite are limited to within 15° from the equator [*Ziemke et al.*, 1998]. The bottom panel shows the difference. All units are in Dobson Units, 1 DU = 2.69×10^{20} molecules m^{-2}.

monthly anomalies of TCO for 1998-2006. The observed IAV is greatest over the maritime continent and northern Pacific and lowest over the equatorial western Pacific. The simulation using the IAV constraint has similar, if weaker, features but lacks the high variability in the northern tropics (driven almost entirely by very low ozone in early 1998). The model underestimates the observed IAV in TCO in much of the tropics outside of the maritime continent. The use of IAV in lightning NO_x significantly improves the simulation over that without such variability, particularly over South America and downwind of Africa (Figure 3.3, lower panel). The mean standard deviation of the model's monthly ozone anomalies is 2.23 DU for the LIS constraint and 1.97 DU without it, compared to 3.16 DU for the observations.

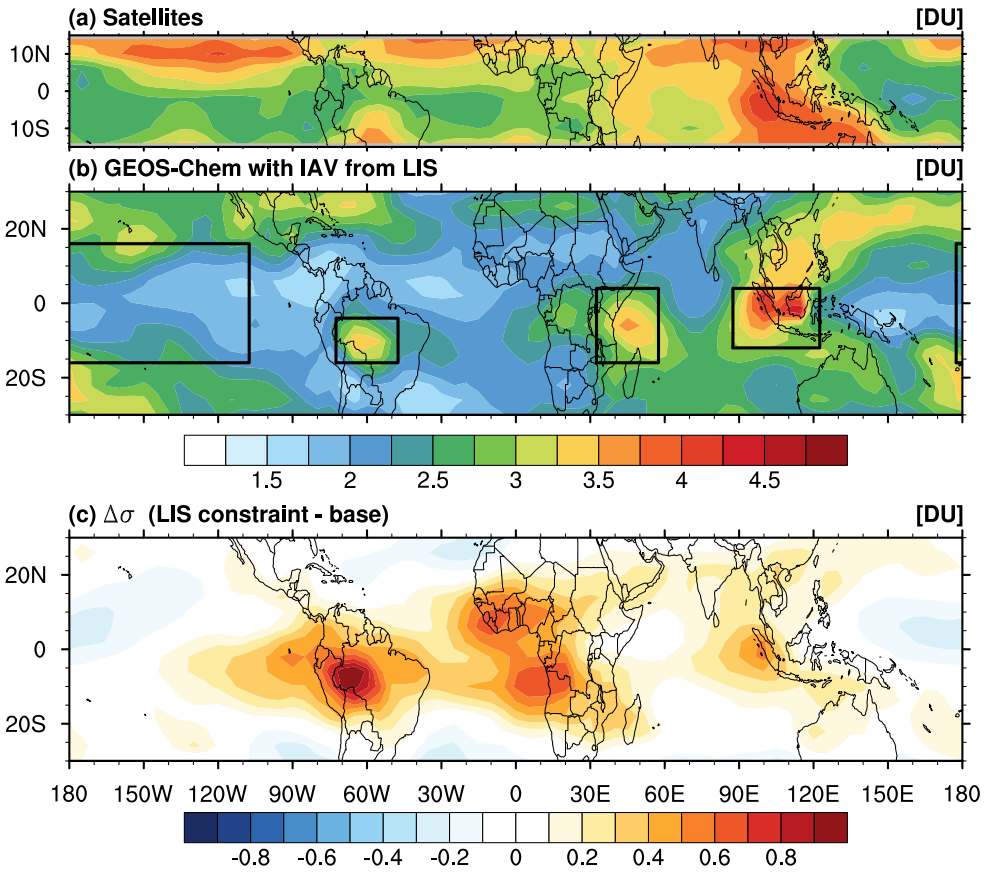

Figure 3.3: Interannual standard deviation (σ) of monthly tropospheric column ozone anomalies for 1998-2006. Observations (top panel) are compared to model results using IAV from LIS (middle panel). The bottom panel shows the difference in σ between the simulation using IAV in lightning from LIS and the base simulation with IAV only from GEOS convection. Black boxes indicate regions used in Figure 3.6.

3.4.2 Factors controlling IAV in ozone

In Figure 3.4 we use sensitivity simulations to estimate the contributions of lightning and fires to IAV in TCO. We do not explicitly test the effect of soil NO_x emissions, which have small IAV. Results show that lightning NO_x provides the greatest contribution in most of the tropics. Fire emissions dominate lightning over the maritime continent, as previously shown by *Nassar et al.* [2009]. Although fires are a greater source of IAV in emissions (Table 3.1), the larger ozone production efficiency (OPE) per unit NO_x in the remote and upper tropical troposphere results in

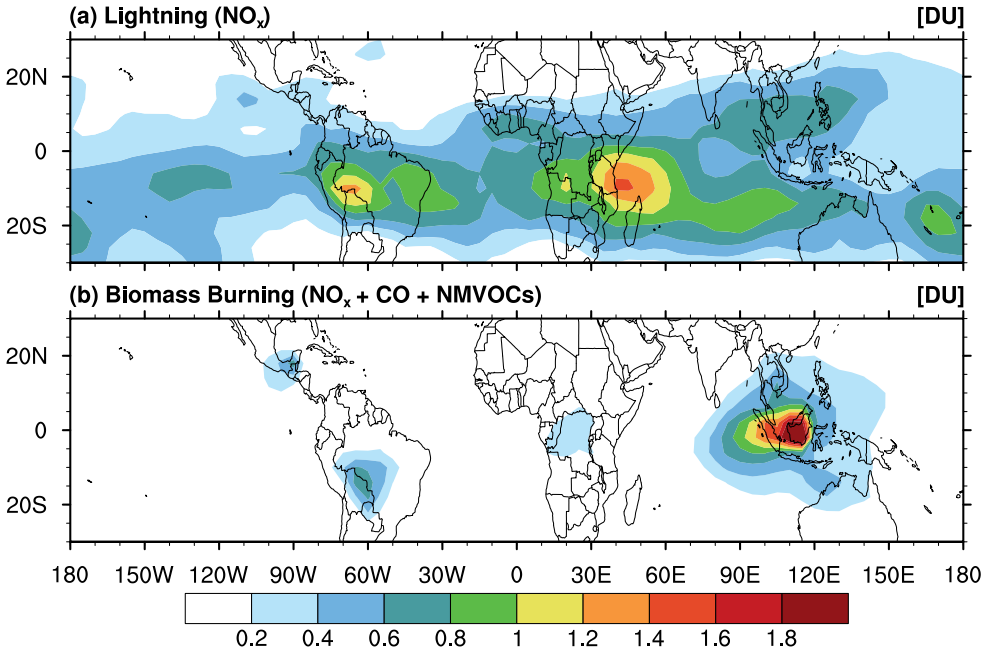

Figure 3.4: Contributions of various sources to model IAV in tropical TCO for 1998-2006, measured by the difference in the standard deviation (σ) of monthly anomalies relative to Figure 3.3b when that source is shut off.

lightning causing a greater amount of ozone variability.

In Figure 3.5 we explore the contributions of the sources of NO_x to the IAV of ozone as a function of longitude, shown in Hovmöller plots for 15°S-15°N. The satellite observations (panel a) show a general increase in tropical TCO from 1998 to 2006, with additional variability over the maritime continent. The simulation with the IAV lightning constraint (panel b) reproduces 30% of the variability in the timing and location of the observed anomalies ($R^2 = 0.30$; $n = 72$ longitudes $\times$ 12 months $\times$ 9 years), including the increasing trend. This is a significant improvement over the base case ($R^2 = 0.19$), and a simulation with no lightning ($R^2 = 0.15$). Lightning contributes to about half of total IAV in the model and drives some of the increase in ozone (panel d). Fires contribute to IAV in TCO primarily over the maritime continent during El Niño events in early 1998 and late 2002, 2004, and 2006 (panel c) in accordance with previous findings for that region [*Chandra et al.*, 2002; *Logan et al.*, 2008; *Chandra et al.*, 2009; *Nassar et al.*, 2009]. It otherwise

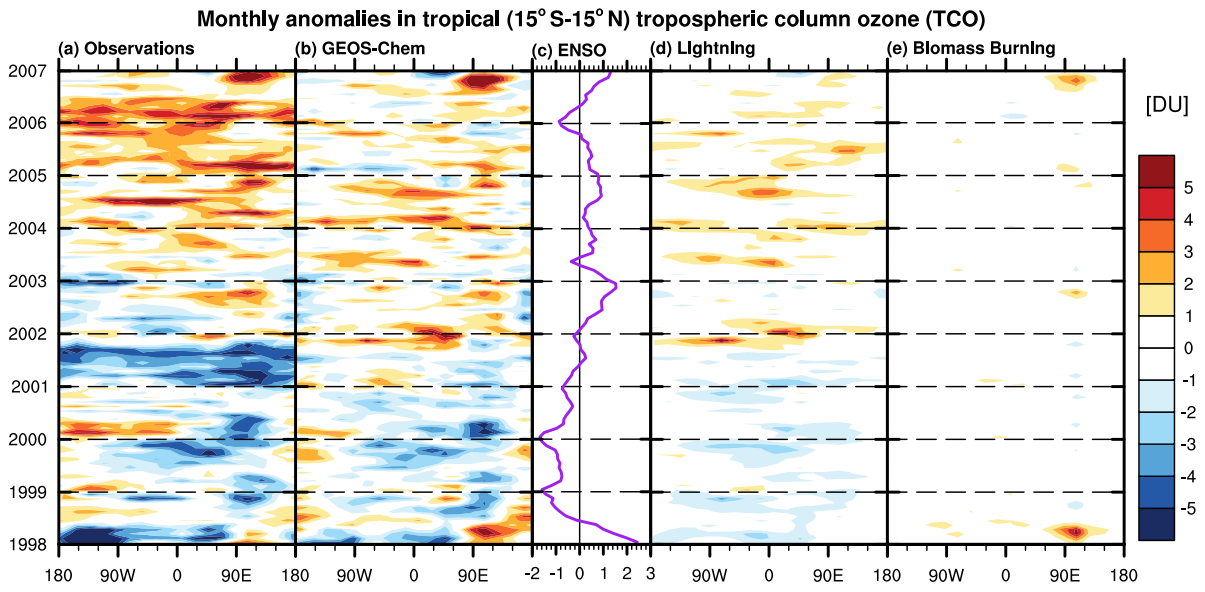

Figure 3.5: Hovmöller diagrams showing tropical (15°S-15°N) meridional mean tropospheric columns of ozone (TCO) monthly anomalies for 20° longitudinal bins versus time (1998-2006) in (a) the EPTOMS and OMI/MLS satellite observations, (b) the GEOS-Chem simulation with the interannual lightning flash constraint from LIS. (c) El Niño (Niño3.4) climate index; positive values indicate sea surface temperature anomalies (°C) in the eastern Pacific associated with an El Niño event. (d) The contribution to TCO anomalies within GEOS-Chem from lightning NO_x estimated from the difference with the simulation with lightning source removed. (e) The contribution to TCO anomalies within GEOS-Chem from biomass burning NO_x and co-products.

plays very little role.

3.4.3 Regional analysis

Figure 3.6 shows monthly mean and anomaly time series of tropospheric ozone columns in regions selected because of their high relative variability and improvement when imposing IAV in lightning from LIS (Figure 3.3). The monthly means shows that the simulations reproduce the seasonality of ozone, while the anomalies demonstrate the ability of the model to capture IAV in ozone.

The simulation with constrained IAV in lightning matches the ozone monthly means and anomalies best over the maritime continent (Figure 3.6, top row). Ozone in this region is known

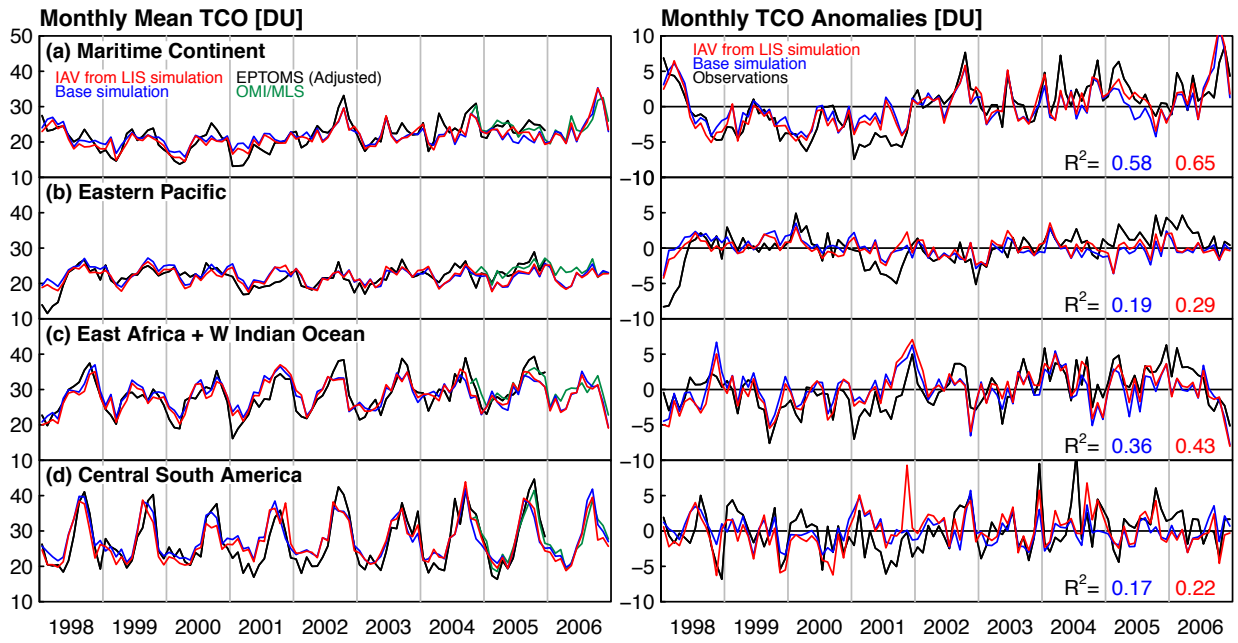

Figure 3.6: Time series of monthly TCO and their anomalies in the simulation with IAV in lightning from LIS (red line), and the base simulation (blue), and in satellite observations (black and green lines), shown by region for (a) the Maritime Continent (12°S-4°N; 87.5°-122.5°E), (b) the eastern equatorial Pacific (16°S-16°N, 177.5°E-107.5°W) (c) East Africa and the adjacent Indian Ocean (16°S-4°N; 32.5°-57.5E), (d) and central South America (16°-4°S; 72.5°-47.5°W). Regions are shown in Figure 3.3b. Pearson correlation coefficients between the observations and simulations are given.

to be influenced by ENSO related changes in convection and by major biomass burning events associated with drought induced by El Niño and the phase of the Indian Ocean dipole (IOD) [*Chandra et al*., 1998, 2007, 2002; *Nassar et al*., 2009; *Sudo and Takahashi*, 2001; *Oman et al*., 2011]. Observed and simulated TCO anomalies are well-correlated with anomalies in the El Niño 3.4 index and in outgoing long-wave radiation (OLR), a proxy for deep convection [*Liebmann and Smith*, 1996; *Chelliah and Arkin*, 1992; *Gettelman and Forster*, 2002]. Despite the decrease in convection in the region during El Niño, there is an increase in lightning frequency over Southeast Asia and Indonesia [*Hamid et al*., 2001; *Yoshida et al*., 2007] that is captured by constraining IAV with LIS. Nevertheless, changes in convection and fire emissions dominate ozone variability in the region (Figure 3.4), consistent with the model results of *Nassar et al*.

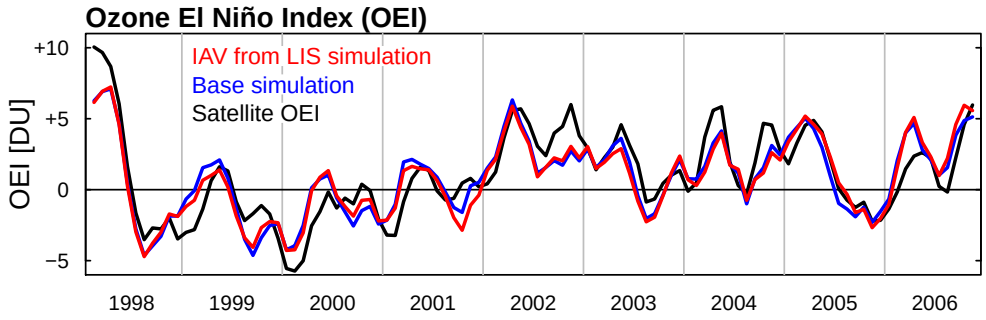

Figure 3.7: Time series of the observed and simulated Ozone El Niño Index (OEI) [*Ziemke et al*., 2010], defined as the 3-month running mean in the west-to-east difference in area-averaged TCO between two broad regions in the Indian Ocean/western Pacific and the eastern Pacific (15°S-15°N; 70°E-140°E and 180°W-110°W). The simulations reproduce the observed OEI well (IAV from LIS simulation: R^2=0.71; Base simulation: R^2=0.70; n = 12 months ×9 years), and generally reproduce the magnitude of the difference despite the model being generally biased low over the eastern domain.

[2009], who found that changing lightning NO_x made very little difference between ozone in late 2005 and the El Niño in late 2006.

During El Niño events, convection decreases over the eastern Indian Ocean and maritime continent but increases further east in the Pacific, resulting in lower ozone there [e.g., *Sudo and Takahashi*, 2001; *Ziemke and Chandra*, 2003]. The model greatly underestimates the relative variability in the latter region (almost entirely due to early 1998), although the IAV-constrained lightning improves the simulation relative to the base case, with R^2 increasing to 0.29 from 0.19 (Figure 3.6, second row). However the model reproduces the absolute difference in TCO between the two regions (Figure 3.7), defined as a new ozone ENSO index (OEI) by *Ziemke et al*. [2010].

Use of the IAV constraint from LIS also improves the IAV in TCO in two regions with relatively high observed variability (Figure 3.3), eastern equatorial Africa and the adjacent Indian Ocean, and central Brazil. In the first region (Figure 3.6, third row), the model captures the observed seasonality and almost half the variability of the monthly anomalies. The variability appears to be driven predominantly by IAV in dynamics, as imposing IAV in lightning has a small influence. *Logan et al*. [2008] noted the large changes in this region in ozone and H_2O between

late 2005 (when there was a drought in this region) and late 2006 (when there was very high rainfall), which they attributed to changes in convection, as confirmed by the model study of *Nassar et al*. [2009]. In central Brazil the model captures the observed seasonality, but less than a quarter of the variance in the monthly anomalies (Figure 3.6, bottom row). Most of the improvement by imposing IAV from LIS results from increasing the variability at the end of the dry season, from October to December; there is no correlation between the model and observed TCO in the wet season, January-April ($R^2 = 0.04$).

Figure 3.6 shows that observed TCO was anomalously low in all regions in 2001, as seen also in the Hovmöller plot for the tropics in Figure 3.5, but the simulations do not show this behavior. This year is neutral in terms of ENSO, and the causes of the 2001 anomaly are unclear. We find no evidence of such an anomaly in ozonesonde profiles from the SHADOZ network [*Thompson et al*., 2003a] (not shown).

3.5 IAV in global OH and the role of lightning

Montzka et al. [2011] inferred IAV in global mean OH from analysis of surface measurements of MCF; their time series of OH percent anomalies is reproduced in Figure 3.8a (black line). The figure also shows mean OH weighted by the loss frequency of MCF, $\overline{[OH]}_{MCF}$, calculated from the model simulations in a manner consistent with the approach of *Montzka et al*. [2011] (see Appendix A).

The simulation with IAV in lightning imposed from LIS (red line) better matches the time evolution of the $\overline{[OH]}_{MCF}$ anomalies than does the base case (blue line). The $\overline{[OH]}_{MCF}$ inferred from observations increases from 1998 to 2001 by 4% and then decreases until 2003, behavior found also in the simulation with IAV from LIS but not in the base case. Thereafter, the simulated and MCF-inferred $\overline{[OH]}_{MCF}$ time series diverge. The simulation shows an increasing trend in $\overline{[OH]}_{MCF}$ from 1998 to 2006, but the $\overline{[OH]}_{MCF}$ derived from the observations shows a decrease

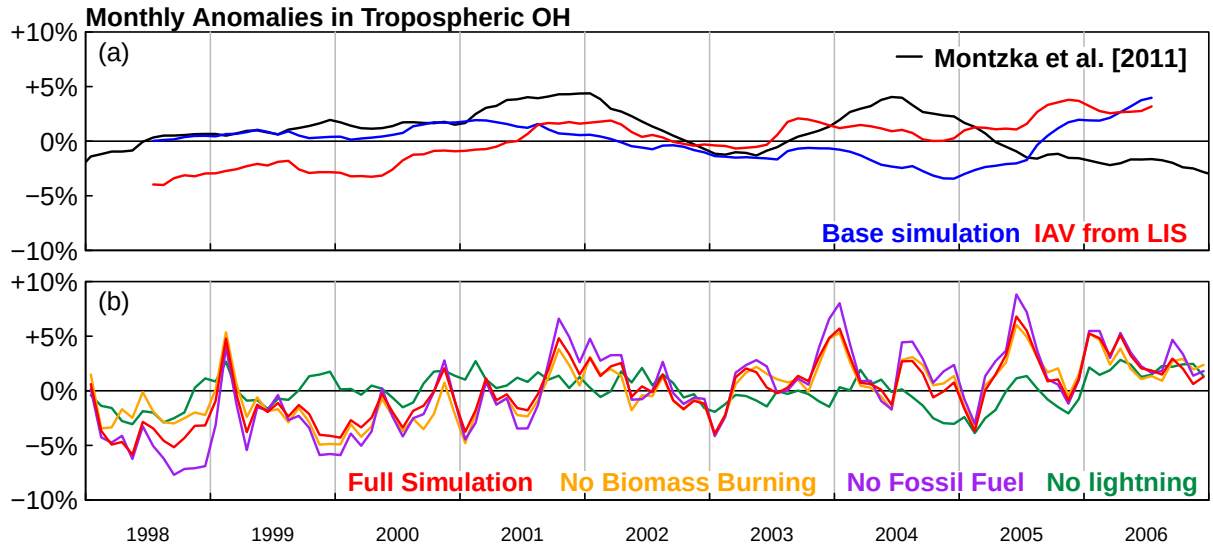

Figure 3.8: Monthly mean percent anomalies in global mean OH (a) That inferred from methyl chloroform from *Montzka et al*. [2011] (black line) and simulated by GEOS-Chem with lightning IAV from LIS (red) and for the base simulation (blue). The simulation is the tropospheric average weighted by air mass and the temperature-dependent rate constant for the oxidation of MCF by OH [*Prather and Spivakovsky*, 1990], and has a twelve-month smoothing applied to be consistent with the finite differencing of the flask technique (cf. Appendix A). (b) Monthly percent anomalies in tropospheric OH concentration weighted by air mass from GEOS-Chem simulations using lightning IAV from LIS (red). Also shown are those from sensitivity simulations containing no biomass burning emissions (orange), fossil fuel combustion (purple), or lightning (green).

from 2004 to 2006. Imposing IAV from LIS reduces the model increase from 2004 to 2006, but it is insufficient to reverse the trend to match $\overline{[OH]}_{MCF}$ inferred from MCF. Our base simulation has a similar time evolution of the $\overline{[OH]}_{MCF}$ anomalies to the hindcast for 1998-2007 shown by *Montzka et al*. [2011] using a different CTM [*Sander et al*., 2005; *Jöckel et al*., 2006] and to hindcasts shown by *Holmes et al*. [2013] for three CTMs, including GEOS-Chem driven by GEOS-5 and by MERRA meteorological fields. None of these simulations constrained IAV in lightning with LIS data.

Figure 3.8b shows that lightning has a much stronger influence than surface emissions on mean OH; here we show mass weighted OH, $\overline{[OH]}_{mass}$, without smoothing (see Appendix A). Omitting

biomass burning emissions slightly reduces IAV in $\overline{[OH]}_{mass}$ (mostly in 1998), while omitting fossil fuel emissions slightly increases the $\overline{[OH]}_{mass}$ trend. Most residual variability in the simulation with no lightning likely results from IAV in other factors such as water vapor, overhead ozone column, etc. [*Holmes et al.*, 2013; *Duncan and Logan*, 2008; *Dentener et al.*, 2003].

We analyzed the main chemical factors driving IAV in $\overline{[OH]}_{mass}$ in 1998-2006 in the model. Figure 3.9a shows the IAV in production rates of OH and in its loss frequencies (i.e., $k_{OH+X}[X]$). The anomaly in $\overline{[OH]}_{mass}$ (the black line) is determined by the competition between those from production (shown by cool colors) and those from loss (shown by warm colors). The reaction contributing the most to IAV in production is $O(^1D) + H_2O$, the primary source of HO_x, followed by the recycling reaction $HO_2 + NO$. Reaction of OH with CO contributes the most to IAV in loss.

Anomalies in both production and loss are largest in 1998, following the end of a major El Niño event, when there was enhanced loss because of the high fire emissions of CO and other species, but also enhanced water vapor; the net $\overline{[OH]}_{mass}$ anomaly was negative. During the La Niña of 1999-2000, the coincidence of relatively low tropospheric ozone (Figure 6) and water vapor and of relatively high overhead ozone columns led to low primary production of HO_x and thus negative $\overline{[OH]}_{mass}$ anomalies. Increasing lightning NO_x emissions and tropospheric water vapor slowly increased production by 2001. In 2005-2006, anomalously low CO emissions (except at the end of 2006 from Indonesian fires) and high production from reduced stratospheric ozone drive an increase in $\overline{[OH]}_{mass}$ in the model.

Figure 3.9b demonstrates how the timing of lightning emissions alters $\overline{[OH]}_{mass}$ by modulating both production and loss pathways. The difference in $\overline{[OH]}_{mass}$ anomalies between the IAV from LIS simulation and the base simulation follows the difference in lightning NO emissions (Figure 1a). Relative changes in NO alone between the two simulations would produce changes in the $\overline{[OH]}_{mass}$ anomalies via $HO_2 + NO$. However, additional NO_x increases ozone, which produces additional OH from primary production ($O(^1D) + H_2O$) and from recycling by the reaction of HO_2 with ozone and with NO itself. The NO_x-driven increases in OH also provide a

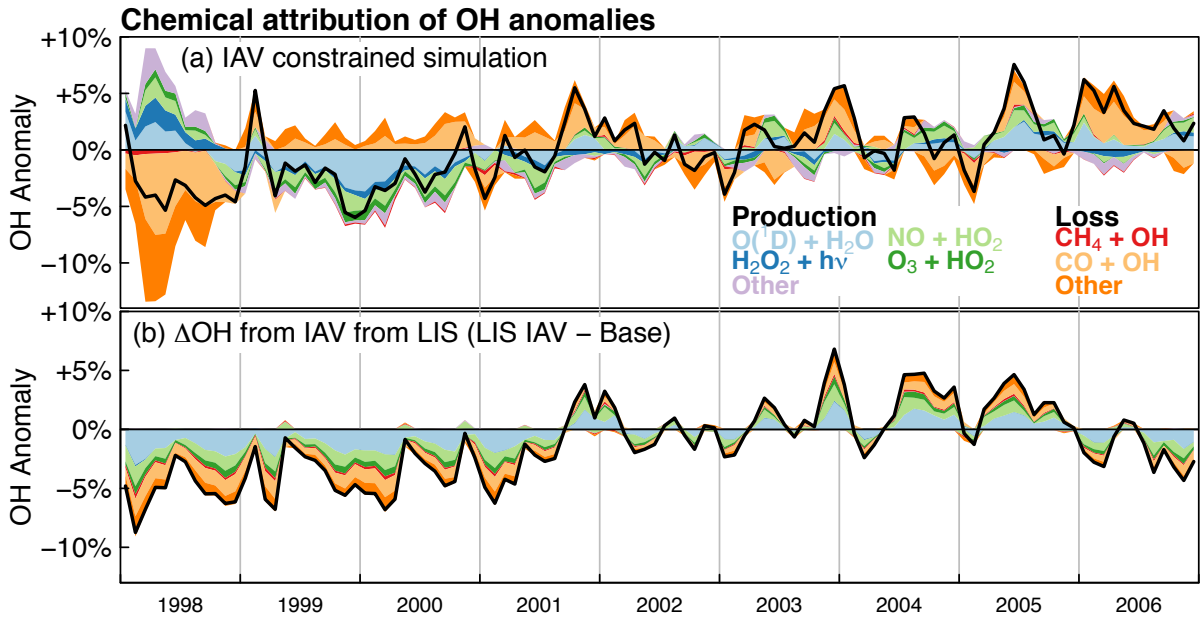

Figure 3.9: (a) Interannual variability in OH contributed from chemical sources and sinks in the simulation with lightning IAV imposed from LIS. Values are monthly anomalies in mass-weighted mean tropospheric OH resulting from production rates and loss frequencies. The net anomaly (i.e., the anomaly in OH concentrations) is shown as the black line and is the same as the red line in Figure 3.8b. (b) The difference between the standard simulation in (a) and the base simulation in which any IAV in lightning is only from GEOS convection (black line), and its components.

positive feedback on loss frequencies by suppressing CO and other reactants. Changes in lightning have greater potential than those in biomass burning or fossil fuel emissions for driving IAV in $\overline{[OH]}_{mass}$ because the feedback is much more efficient in low-NO_x environments found in much of the tropics, and also because the surface sources co-emit CO and hydrocarbons that would counteract aspects of the reinforcement. Thus, perturbations in lightning NO impart a relatively large signal on OH anomalies via reinforcing changes in both production and loss pathways (Figure 3.9b) that otherwise tend to vary independently of one another because of external factors such as water vapor, column ozone, etc. (Figure 3.9a).

Table 3.2 summarizes how our simulated $\overline{[OH]}_{mass}$ anomalies co-vary with anomalies in the various parameters that affect OH. A causal parameter will influence variability if OH has high

Table 3.2: Sensitivity of simulated IAV in OH to different reaction pathways, climate variables, and emissions

Parameter, P	R with OH anomalies[a]	Slope of $d\mathrm{OH}/dP$[b] (%/%)	σ in monthly anomalies of P[c] (%)
OH anomalies	1.00	+1.00	3.01
Production anomalies	0.32	$+0.97^{+0.17}_{-0.15}$	3.11
Primary production	0.61	$+1.06^{+0.14}_{-0.13}$	2.85
Water vapor	0.14	$+2.89^{+0.58}_{-5.85}$	1.04
Stratospheric ozone	-0.38	$-4.19^{+0.60}_{-0.71}$	0.72
Tropospheric ozone	0.54	$+1.73^{+0.26}_{-0.71}$	2.92
HO_x recycling	0.47	$+0.93^{+0.14}_{-0.12}$	3.25
Loss anomalies	-0.55	$-0.83^{+0.17}_{-0.22}$	3.64
$k_{CH_4+OH}(T)[CH_4]$	-0.63	$-3.67^{+0.53}_{-0.65}$	0.82
$k_{CO+OH}(T)[CO]$	-0.56	$-0.52^{+0.10}_{-0.12}$	5.81
Global emission rates			
Lightning	0.63	$+0.18^{+0.03}_{-0.04}$	16.4
Biomass burning[d]	-0.32	$-0.10^{+0.02}_{-0.03}$	29.5

[a] Pearson correlation coefficient, R, between time series of OH percent anomalies and the forcers.
[b] Slope of reduced major axis (RMA) regression between monthly percent anomalies in OH and the forcers. Range give 95% confidence intervals calculated from a bootstrap ensemble with 10^3 members.
[c] Standard deviation of monthly percent anomalies in tropospheric mean climate variables, reaction rates, and emissions. All values calculated from the simulation using IAV in lightning from LIS.
[d] Statistics for fire emissions are calculated using time series of NO_x emission; results are very similar for CO emissions, and negative because fires act as a net sink for OH.

sensitivity to it (second column) and/or if it has high variability itself (third column) [*Holmes et al.*, 2013]. We estimate sensitivity, i.e., the percent response in $\overline{[\mathrm{OH}]}_{\mathrm{mass}}$ to a percent change in a single parameter, with a simple regression of that relationship. These are not true sensitivities calculated with perturbation analyses as in the work of *Spivakovsky et al.* [2000] and *Holmes et al.* [2013], but may be used for a qualitative comparison. As expected from these studies, $\overline{[\mathrm{OH}]}_{\mathrm{mass}}$ anomalies in our simulation respond most sensitively to changes in the ozone column, particularly with those in the tropics [e.g., *Duncan and Logan*, 2008]. However, we find relatively small variability in column ozone in our period of analysis, and $\overline{[\mathrm{OH}]}_{\mathrm{mass}}$ is more strongly

correlated with tropospheric ozone and CO, both of which have lower sensitivity but higher variability. In contrast, earlier multi-year simulations found OH to vary most strongly with the ozone column [*Bekki et al*., 1994; *Duncan and Logan*, 2008], or that the latter was the second most important factor after water vapor [*Dentener et al*., 2003]. The variability induced in $\overline{[OH]}_{mass}$ by that in the ozone column depends on the period of analysis, and is less for 1998-2006 than for prior studies of 1979-1993 [*Bekki et al*., 1994; *Dentener et al*., 2003] and 1988-1997 [*Duncan and Logan*, 2008] simply because the observed variability of the ozone column in the tropics (where OH is highest) is less [*WMO*, 2011].

The bottom portion of Table 3.2 summarizes the relationship between anomalies in $\overline{[OH]}_{mass}$ and the lightning and biomass burning sources. Anomalies in lightning are the most strongly correlated with the $\overline{[OH]}_{mass}$ anomalies of any source ($R = 0.63$), including those not listed (e.g., anthropogenic, soil, biogenic). The estimated lightning sensitivity is very close to the values calculated for that source by *Holmes et al*. [2013]. Although variability in biomass burning emissions is relatively higher than lightning, it has lower sensitivity (reflecting its co-emissions and boundary-layer chemistry), and therefore a lower overall correlation with $\overline{[OH]}_{mass}$ ($R = -0.3$).

3.6 Conclusions

We presented results from a simulation of tropospheric oxidant chemistry for 1998-2006 including interannual variability (IAV) in tropical lightning imposed from LIS satellite data (Chapter 2). In addition to lightning, our simulation takes into account the IAV of other factors affecting oxidant chemistry including biomass burning, fossil fuel combustion, overhead ozone columns, and meteorology. Our focus was to examine the importance of lightning in driving IAV of tropical tropospheric ozone and OH, both to test our understanding of the factors controlling the oxidizing capacity of the atmosphere and to provide insight into possible effects of climate change.

In the tropics, IAV in the biomass burning source of NO_x ($\sigma = 0.51$ Tg N a^{-1}) is greater than

that from lightning (σ = 0.37 Tg N a^{-1}), yet we find lightning plays a more important role in driving IAV for tropospheric columns of ozone (TCO) in the tropics, except over the maritime continent where fires are more important. The dominance of lightning over fires in driving IAV in tropical ozone reflects the higher ozone production efficiency per unit NO_x from lightning. Imposing IAV in lightning NO_x based on the LIS observations improves the ability of the model to reproduce observed monthly anomalies in TCO in the tropics, particularly in the maritime continent, East Africa, central Brazil, and in continental outflow in the eastern Pacific and the Atlantic. However, IAV in TCO in all these regions except the first two remain poorly correlated with observations.

IAV in lightning has a much greater effect on tropospheric OH than on ozone. When we constrain IAV in lightning NO_x to LIS, simulated IAV in OH is more similar to that inferred from MCF by *Montzka et al*. [2011]. The MCF time series imply global OH increased from 1998 to the end of 2001 then decreased until 2003, behavior only reproduced in the simulation using IAV from LIS. It is not captured in our base simulation that shows similar temporal behavior in OH as other hindcasts for the same period that did not constrain IAV in lightning [e.g., *Holmes et al*., 2013; *Montzka et al*., 2011]. As with ozone, IAV in lightning causes greater IAV in OH than biomass burning, despite larger variability in the latter source.

We examined the contribution of each chemical reaction to monthly anomalies in tropospheric mean OH for 1998-2006. Anomalies from production pathways tend to be correlated in time with one another, as do anomalies in loss frequencies. Production anomalies are primarily influenced by the $O(^1D) + H_2O$ reaction, although $HO_2 + NO$ is also important; the loss anomalies are dominated by reaction with CO. The production anomalies and loss anomalies add constructively and destructively to give the net anomaly in OH. The OH increase from 1998 to 2001 is driven by high CO emissions in 1998 followed by negative production anomalies that gradually erode. Anomalies in CO loss frequencies decrease OH from late 2001 into 2003, and then low biomass burning and ozone columns drive an increase in OH not seen in that derived from MCF.

To explain the strong influence of lightning on IAV in OH, we isolated the impact of imposing additional IAV in lightning on the chemical reactions that determine the net anomalies. Perturbations in lightning NO emissions generate similarly signed anomalies in OH through a series of positive feedbacks on ozone production, HO_x recycling, and OH loss frequencies. These feedbacks impart a large lightning signal to the net anomalies similar in magnitude to the total anomalies in OH. Lightning is more efficient at inducing anomalies in OH than biomass burning or fuel combustion because the chemical feedbacks are more efficient above the boundary layer, and also because lightning does not co-emit reactive carbon species. Despite its strong sensitivity to overhead ozone, OH in our simulations is correlated more strongly with variability in lightning for 1998-2006, reflecting less variability in overhead ozone columns in our period than in those of previous studies [*Bekki et al*., 1994; *Dentener et al*., 2003; *Duncan and Logan*, 2008; *Holmes et al*., 2013].

At present, parameterizations of lightning activity commonly used by atmospheric models are incapable of reproducing even the spatial and seasonal distribution of flash rates unless locally adjusted to match climatological observations [*Tost et al*., 2007; *Murray et al*., 2012; *Sauvage et al*., 2007a; *Allen et al*., 2010]. Lightning activity has been observed to increase with increases in surface temperature on diurnal to decadal time scales. However, lightning occurs in convection, and it unclear how convection may change on longer time scales [*Williams*, 2005]. As IAV in OH is highly sensitive to IAV in lightning NO_x, development of improved parameterizations for lightning represents a critical area for future research if atmospheric models are to be able to realistically quantify chemistry-climate interactions. Until then, recently developed long-term observational networks for global lightning activity (e.g., the World Wide Lightning Location Network [*Abarca et al*., 2010], Vaisala's Global Lightning Dataset GLD360) or the next generation of satellite sensors (e.g., the Geostationary Lightning Mapper slated for GOES-R) will offer important constraints for simulating present-day lightning variability and its associated chemical influences.

Chapter 4

Variability in the oxidative capacity of the troposphere since the Last Glacial Maximum

Abstract

We present an offline-coupled climate-biosphere-chemistry framework for determining oxidant levels in the present and past troposphere. We use the GEOS-Chem chemical transport model driven by meteorological fields from the NASA Goddard Institute of Space Studies (GISS) ModelE general circulation model, with land cover variables from the BIOME4-TG global terrestrial equilibrium vegetation model, and historic fire emissions from the LMfire model. Time-slice simulations are presented for the present day, preindustrial, and two representations of the Last Glacial Maximum (LGM; 19-23ka). We test the sensitivity of model results to uncertainty in lightning and biomass burning emissions. We find reduced oxidant levels in all preindustrial and paleo climates relative to the present day. Global mean OH changes by -6.7 $\pm$ 11% at the LGM relative to the preindustrial, despite reductions in methane concentrations. We find a simple linear relationship between mean values of stratospheric ozone, water vapor, and total emissions of NO_x and reactive carbon that explains 69% of the variability in global mean OH in 11 different simulations across the last glacial-interglacial time interval. Key variables controlling the tropospheric oxidative capacity over glacial-interglacial periods include overhead stratospheric ozone, tropospheric water vapor, and lightning emissions. Variability in global mean OH since the LGM is insensitive to biomass burning emissions. Our simulations are broadly consistent with ice-core records of $\Delta^{17}O$ in sulfate and nitrate at the LGM, and CO, HCHO, and H_2O_2 in the preindustrial. Our results imply that the observed variability in ice-core methane is predominantly source-driven, consistent with the reductions reported in previous bottom-up estimates of LGM wetland emissions.

4.1 Introduction

The oxidative capacity of the troposphere—characterized by the burden of the four most abundant and reactive oxidants (OH, ozone, H_2O_2, and NO_3)—determines the lifetime of many trace gases of importance to climate and human health, including air pollutants and the greenhouse gas methane [*Fiore et al.*, 2012]. Ozone itself absorbs both longwave and shortwave radiation, and its tropospheric enhancement since the preindustrial is estimated to have contributed the third largest radiative forcing effect of any gas for that period, after CO_2 and methane [*IPCC*, 2007]. The oxidants also impact the evolution, lifetime, and physical properties of inorganic, and primary and secondary organic aerosol particles, modulating their direct and indirect radiative effects [*Liao et al.*, 2003; *Tie et al.*, 2005; *Leibensperger et al.*, 2011]. The oxidative capacity may even perturb terrestrial and marine ecosystems via oxidative stress and by altering the deposition of oxidized nutrients such as nitrate [*Sitch et al.*, 2007; *Collins et al.*, 2010]. Understanding how the oxidative capacity has changed over past time scales is critical for understanding their chemical, climatic and ecological consequences. In this work, we introduce a new model framework to improve estimates of the oxidative capacity across glacial-interglacial time scales, and we examine the implications of our results for current understanding of the observed ice-core record of methane.

Tropospheric oxidant levels respond to meteorological conditions, changes in emissions of key chemical species, and changes in surface and stratospheric boundary conditions [*Holmes et al.*, 2013; *Spivakovsky et al.*, 2000; *Lelieveld et al.*, 2002], suggesting perturbations in the oxidative capacity over long time scales. The limited observations that do exist imply that human activity has indeed substantially perturbed the tropospheric oxidants since the preindustrial [e.g., *Staffelbach et al.*, 1991; *Marenco et al.*, 1994; *Anklin and Bales*, 1997]. The Last Glacial Maximum (LGM; 19-23ka before present) is well-recorded in ice-core and sediment records, but no oxidants except for H_2O_2 are preserved in ice cores, and the H_2O_2 record is complicated by

post-depositional processes [*Hutterli et al*., 2003]. Proxies for oxidant levels have been proposed, such as those from HCHO and methane [*Staffelbach et al*., 1991] or oxygen isotope anomalies in sulfate and nitrate [e.g., *Alexander et al*., 2009, 2002], but these require models for interpretation in a global context. For methane, for example, there remains considerable uncertainty regarding the relative contributions of the wetland emissions source versus the OH sink in driving the large glacial-interglacial variability seen in ice-core bubbles [*Khalil and Rasmussen*, 1987; *Chappellaz et al*., 1993; *Crutzen and Brühl*, 1993; *Chappellaz et al*., 1997; *Martinerie et al*., 1995; *Brook et al*., 2000; *Kaplan*, 2002; *Kaplan et al*., 2006; *Valdes et al*., 2005; *Levine et al*., 2011a, 2012; *Weber et al*., 2010; *Fischer et al*., 2008; *Singarayer et al*., 2011].

Prior model studies investigating the tropospheric oxidant burden have disagreed on the magnitude and even the sign of changes, as summarized in Table 4.1. These discrepancies reflect differences in the model components of the earth system allowed to vary, the differing degrees of complexity of those components, and the large uncertainties in past meteorological and biological conditions. Contributing to the uncertainty in estimates of past oxidative capacity is the fact that the principal oxidants are strongly and non-linearly coupled to one another [*Thompson*, 1992]. Models generally agree that ozone has risen about 25-65% from the preindustrial to the present day [*Young et al*., 2013; *Lelieveld and Dentener*, 2000; *Shindell*, 2001; *Wang and Jacob*, 1998], but they have been unable to reproduce low surface concentrations of ozone implied by late 19th-century observations [*Marenco et al*., 1994; *Pavelin et al*., 1999; *Mickley et al*., 2001]. How OH has changed over this period is even more uncertain, with recent simulations from 17 state-of-the-science models of the Atmospheric Chemistry and Climate Model Intercomparison Project (ACCMIP) finding a mean change of -0.6 $\pm$ 8.8% from 1850 to 2000, even with identical anthropogenic emission inventories applied [*Naik et al*., 2012].

Table 4.1: Percent changes in tropospheric burdens of OH, ozone and H_2O_2, relative to the preindustrial, compiled from the literature

	%Δ at LGM		%Δ at present day			
Reference	OH	Ozone	OH	Ozone	H_2O_2	Method
McElroy [1989]	+56%	-	+60%	-	-	1D model
Hough and Derwent [1990]	-	-	-19%	-	-	2D model
Valentin [1990]	+23%	0%	-9%	+64%	-	2D model
Law and Pyle [1991]	-	-	-13%	+300%	-	2D model
Pinto and Khalil [1991]; *Lu and Khalil* [1991]	+15%; +26%	-17%	-4%	+57%	-	1D model; Multi 1D model
Staffelbach et al. [1991]	-	-	-23%	-	-	Ice-core HCHO
Crutzen and Zimmermann [1991]	-	-	-10% to -20%	+50%	-	3D model
Thompson et al. [1993]	+10%	-20%	-17%	+80%	-	Multi 1D model
Martinerie et al. [1995]	+20%	-30% to +30%†	+6%	Up to +250%†	-	2D model
Karol et al. [1995]	-60% to +14%*	-29% to +12%*	+9% to +12%*	+56% to +73%*	-	Multi 1D model
Levy et al. [1997]	-	-	-	+39%	-	3D model
Berntsen et al. [1997]	-	-	+6.80%	+53%	+100%	3D model
Roelofs et al. [1997]	-	-	-22%	+43%	-	3D model
Brasseur et al. [1998]	-	-	-17%	+20% to +80%†	-	3D model
Wang and Jacob [1998]	-	-	-9.60%	+63%	-	3D model
Mickley et al. [1999]	-	-	-16%	+56%	-	3D model
Lelieveld and Dentener [2000]	-	-	-	+25%	-	3D model
Grenfell et al. [2001]	-	-	-3.90%	+38%	-	3D model, no NMVOCs
Hauglustaine and Brasseur [2001]	-	-	-31%	+57%	-	3D model
Shindell et al. [2001]	-	-	-5.90%	+45%	-	3D model
Lelieveld et al. [2002]	-	-	-5%	+30%	-	3D model
Lamarque et al. [2005]	-	-	-8%	+30%	-	3D model
Valdes et al. [2005]	+25%*	-17%*	-	-	-	3D model
Kaplan et al. [2006]	+28%	-31%	-	-	-	3D model
Shindell et al. [2006b]	-	-	-16%	+11%	-	3D model
Sofen et al. [2011]	-	-	-10%	+42%	+58%	3D model
Parrella et al. [2012]	-	-	-	+47% to +48%	-	3D model
Naik et al. [2012]; *Young et al.* [2013]	-	-	-0.6 ± 8.8%	+41 ± 8.9%	-	Multi 3D model
This work, ensemble estimate[a]	-6.7 ± 11%	-12 ± 10%	+7.0 ± 4.3%	+24 ± 11%	+17 ± 22%	Multi 3D model
This work, best estimate[a]	-5.90%	-13%	+5.30%	+31%	+30%	3D model

† Represents range throughout troposphere of local percent changes relative to preindustrial, not a range in the global mean.

∗ Difference reported for mean surface concentration.

a. cf. Section 4.5 for description of ensemble and best estimates.

At the LGM, previous studies have generally found 20-30% decreases in surface or free tropospheric ozone relative to the preindustrial [*Valdes et al*., 2005; *Kaplan et al*., 2006; *Karol et al*., 1995]. Most prior model studies have concluded that OH concentrations at the LGM were about 25% higher than the preindustrial (range of 10-56%) because of lower hydrocarbon and CO concentrations [*Law and Pyle*, 1991; *Crutzen and Zimmermann*, 1991; *Pinto and Khalil*, 1991; *Lu and Khalil*, 1991; *Martinerie et al*., 1995; *Valdes et al*., 2005; *Kaplan et al*., 2006; *Thompson et al*., 1993, and references therein], although the 1D simulations by *Karol et al*. [1995] on average found 25% less OH at the surface. However, no LGM model study to date has considered the full suite of changes in the key variables for controlling tropospheric oxidants, in particular the potentially large effect of the stratospheric ozone burden on photolysis rates in the troposphere [e.g., *Holmes et al*., 2013].

This work introduces the ICE age Chemistry And Proxies (ICECAP) project, which adopts as its central component a step-wise, offline-coupled framework for simulating paleo-chemistry at and since the LGM. The primary focus of the ICECAP project is to test in a 3D model the sensitivity of tropospheric oxidants across the range of uncertainty in their controlling factors, with as much internal consistency as possible. Offline-coupling, as opposed to using an integrated earth system model, allows for rapid sensitivity tests and facilitates identification of first-order effects. To that end, we use a general circulation model to simulate meteorology for four different time slices: the present day (ca. 1990s), the preindustrial (ca. 1770s), and two different possible representations of the Last Glacial Maximum (19-23ka), one significantly colder than the other. Second, we use the simulated meteorology to determine land cover with a global vegetation model. We then apply the archived meteorology and land cover products to a detailed chemical transport model (CTM), using for upper-boundary conditions an online-coupled linearized stratospheric chemistry scheme. We allow tropospheric emissions to respond to climate within the CTM, and test the sensitivity of our results to two large sources of uncertainty, lightning and fires.

This paper focuses on the tropospheric chemistry component of the ICECAP project. In a

companion project (Sofen et al., manuscript in prep.), these oxidants and meteorological fields are used to drive an offline aerosol isotope version of GEOS-Chem [*Alexander et al*., 2005; *Sofen et al*., 2011], in order to interpret isotope signatures of $\Delta^{17}O$ of nitrate and sulfate in ice-core measurements and evaluate their use as chemical proxies for paleo-oxidant levels. In a second companion paper (Murray et al., manuscript in prep.), we evaluate the potential for chemical feedbacks on glacial-interglacial climate.

Section 4.2 describes the climate, chemistry and land models used, and the manner in which they have been coupled to one another. Section 4.3 summarizes and evaluates the four different climate simulations, focusing on the changes that are most significant for tropospheric chemistry. Section 4.4 describes how the natural emissions respond to changing climate, and scenarios to test the sensitivity to uncertainties in past lightning and fire emissions. Section 4.5 presents the resulting changes in tropospheric oxidants and identifies their controlling factors, with particular focus on OH. Section 4.6 evaluates and discusses the model results in the context of the ice-core record. Section 4.7 discusses the implications of our results for the methane record. We conclude with a summary section.

4.2 ICECAP Project and Model Description

Figure 4.1 illustrates the step-wise offline-coupling of the ICECAP project framework. Archived meteorology for multiple time-slices from the GISS ModelE general circulation model [*Schmidt et al*., 2006] are applied to the BIOME4-TG global equilibrium vegetation model [*Kaplan et al*., 2006] to determine land cover characteristics, and to the LMfire model [*Pfeiffer and Kaplan*, 2012] to calculate dry matter consumed by fires. The archived meteorology and land cover products are then used to drive the GEOS-Chem CTM of tropospheric composition [*Bey et al*., 2001], which includes online linearized stratospheric chemistry [*McLinden et al*., 2000].

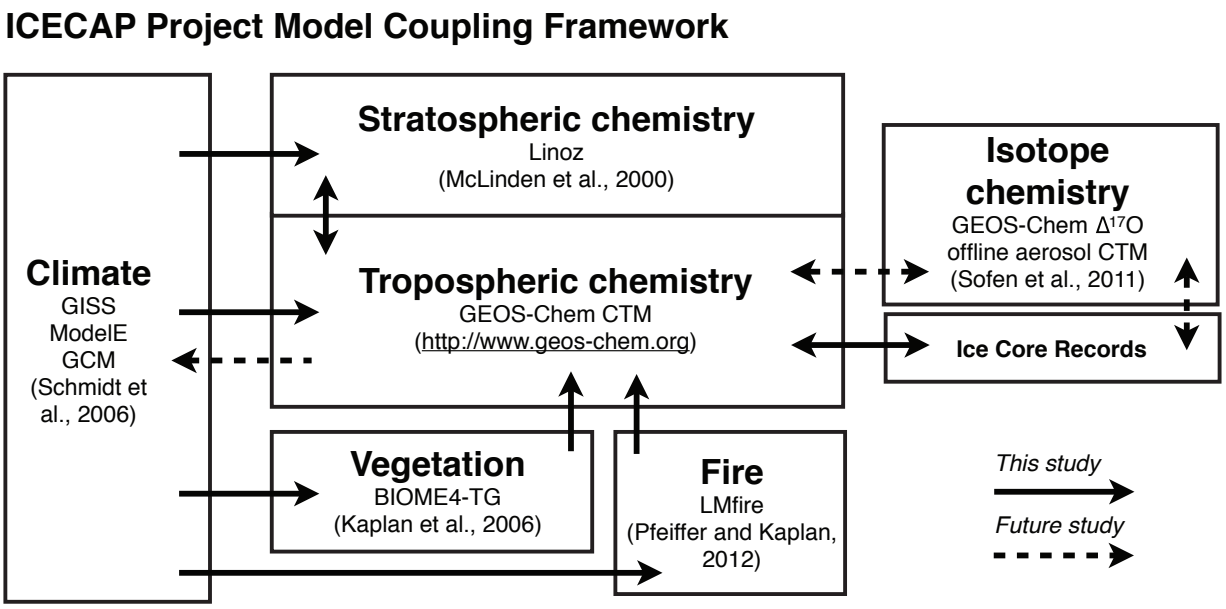

Figure 4.1: The ICE age Chemistry And Proxies (ICECAP) framework. Each box represents a separate model or measurement, except for stratospheric and tropospheric chemistry, which are online together in GEOS-Chem. Arrows indicate the coupling between models and measurements as used in this study. Dashed arrows indicate future work.

4.2.1 GISS ModelE general circulation model

The ModelE version of the GISS general circulation model (GCM) of global climate is described in detail by *Schmidt et al*. [2006]. The GISS GCM has a long history in investigations of past atmospheres [e.g., *Webb et al*., 1997; *Joussaume et al*., 1999; *Delaygue et al*., 2000; *Shindell et al*., 2003; *Schmidt and Shindell*, 2003; *LeGrande et al*., 2006; *Rind et al*., 2001, 2009]. We use here ModelE with 4° latitude by 5° longitude horizontal resolution and 23 vertical layers extended from the surface to 0.002 hPa. We archive mean meteorological fields from ModelE for input to GEOS-Chem at temporal resolution of 6 h for three-dimensional fields (e.g., winds, convective mass fluxes) and 3 h for mixing depths and surface fields (e.g., surface temperature, solar radiation, albedo). Climate in ModelE is forced by different greenhouse gas levels from ice-core measurements, orbital parameters, topography, and fixed sea ice and sea surface temperatures

Table 4.2: Climate forcings used in each climate scenario.

Simulation parameters	Last Glacial Maximum (21ka)		Preindustrial	Present Day
	Cold LGM	Warm LGM	(ca. 1770s)	(ca. 1990s)
Greenhouse gases (ppmv)				
CO_2	188	188	280	354
N_2O	0.20	0.20	0.27	0.31
CH_4	0.39	0.39	0.73	1.69
CFCs	0	0	0	1990 values
SST and sea ice	*Webb et al*. [1997]	*CLIMAP* [1976]	1880s *Rayner et al*. [2003]	1990s *Rayner et al*. [2003]
Ice sheet topography	*Licciardi et al*. [1998]	*Licciardi et al*. [1998]	Present day	Present day
Stratospheric ozone[a]	1880s values	1880s values	1880s values	1990s values
Orbital forcing[b]	2000 conditions[c]	2000 conditions[c]	1770 conditions	2000 conditions
Tropospheric aerosols and ozone[d]	1880s values	1880s values	1880s values	1990s values

[a] As used by *Hansen et al*. [2007]
[b] Calculation from *Berger* [1978]
[c] Orbital parameters for the LGM are nearly the same as they are today [*Braconnot et al*., 2007a].
[d] Aerosols from *Koch et al*. [2009]. Ozone from *Shindell et al*. [2008].

(SSTs) as summarized in Table 4.2 and discussed in Section 4.3. Each scenario is initialized over five years, with four subsequent years of meteorology archived for the terrestrial vegetation and chemical transport models. We discuss the forcings applied to the GISS climate model for each of the scenarios and the resulting climate in Section 4.3.1.

4.2.2 BIOME4-TG global terrestrial vegetation model

BIOME4-TG is a terrestrial biosphere model that calculates the equilibrium distribution of 28 biomes in response to both changing climate and atmospheric CO_2 concentrations [*Kaplan et al*., 2006]. Here the model is driven by climatological monthly mean temperature, precipitation, and solar radiation fields from the GCM. We archive for GEOS-Chem monthly mean distributions of plant functional types (PFTs), leaf area indices (LAI), and biome classification. The PFTs and LAI are used for determining terrestrial plant emissions of VOCs (Section 4.4.2); LAI and biome classes are used in calculating dry deposition velocities in a resistance-in-series model in GEOS-Chem [*Wesely*, 1989]. For anthropogenic land use change, we superimpose present-day crop fractions from the Model of Emissions of Gases and Aerosols from Nature (MEGAN)

version 2.1 [*Guenther et al*., 2012]. BIOME4-TG has previously been used for simulating past vegetation distributions and for evaluating paleoclimate simulations by GCMs [*Kaplan*, 2002; *Kaplan et al*., 2003, 2006].

4.2.3 GEOS-Chem chemical transport model

The GEOS-Chem global chemical transport model (version 9-01-03, with modifications as described; http://www.geos-chem.org) simulates tropospheric ozone-NO_x-CO-VOC-BrO_x-aerosol chemistry. Emissions and their coupling with the GCM and vegetation model outputs are the subject of Section 4.4 The original description of the chemical mechanism is by *Bey et al*. [2001]. The coupled sulfur-nitrate-ammonium aerosol simulation is described by *Park et al*. [2004], with aerosol thermodynamics computed via the ISORROPIA II model [*Fountoukis and Nenes*, 2007] as implemented by *Pye et al*. [2009]. Sea salt aerosol is described by *Jaeglé et al*. [2011], primary and secondary organic aerosol by *Heald et al*. [2011], and black carbon by *Wang et al*. [2011]. Recent updates of relevance for this study include those to oceanic sources and sinks of acetone [*Fischer et al*., 2012], sea salt aerosol emission and deposition [*Jaeglé et al*., 2011], optical properties of dust [*Ridley et al*., 2012], and snow scavenging and washout of aerosols [*Wang et al*., 2011]. We include online bromine chemistry [*Parrella et al*., 2012], whose catalytic destruction of ozone may be an important mechanism for limiting preindustrial ozone levels.

In their study of effect of climate change on surface air quality in the near future, *Wu et al*. [2007b] coupled GEOS-Chem with the GISS III version of the GISS GCM [*Rind et al*., 2007]. Here, we build upon the *Wu et al*. [2007b] framework, using meteorology from GISS ModelE to drive GEOS-Chem chemistry. Primary differences between the *Wu et al*. [2007b] implementation and this work include the prescription of land cover from an offline global terrestrial vegetation model (Sections 4.2.2 and 4.4.2), a linearized stratospheric ozone scheme, adjusted convective transport and rainout schemes to reflect the updated moist convection in ModelE [*Kim et al*.,

Table 4.3: Methane mixing ratios prescribed in GEOS-Chem [ppbv].

	90°S-30°S	30°S-0°	0°-30°N	30°N-90°N
Present Day[a]	1690	1700	1760	1810
Preindustrial[b]	710	730	730	760
LGM[b]	370	760	760	380

[a] Present-day values from flask samples of the NOAA Global Monitoring Division (GMD) database.
[b] Preindustrial and LGM are mean values from ice-core records in the NOAA National Geophysical Data Center (NGDC) Paleoclimatology Program.

2012], and implementation of the GISS quadratic upstream tracer advection scheme [*Prather*, 1986] for improved consistency with the GCM. We discuss these updates in detail below.

For this work, we prescribe methane concentrations, imposing a latitudinal gradient as summarized in Table 4.3. The preindustrial and LGM simulations use observed methane values from Antarctic, Andean, and Greenland ice cores in the NOAA National Geophysical Data Center (NGDC) Paleoclimatology Program (http://www.ncdc.noaa.gov/paleo/paleo.html). Our present-day values are from flask observations of the NOAA Global Monitoring Division database (http://www.esrl.noaa.gov/gmd/). We assume methane is uniformly mixed up to the tropopause in each latitudinal band. In the present day and preindustrial, methane increases with increasing latitude in the Northern Hemisphere, reflecting its terrestrial source. In the LGM, the maximum is instead in the tropics, and concentrations there are 4% higher than those of the preindustrial. The LGM distribution reflects changes in the latitudinal distribution of its sources and sinks relative to the preindustrial [*Kaplan et al.*, 2006].

We calculate stratospheric ozone online in GEOS-Chem following the Linoz linearized chemical scheme [*McLinden et al.*, 2000], with coefficients appropriate for stratospheric chemistry in the LGM [*Rind et al.*, 2009] and the preindustrial (C. McLinden, personal communication, 2009). GEOS-Chem typically uses satellite observations of total ozone columns to determine the attenuation of shortwave radiation in its calculation of tropospheric photolysis rates. Our use of Linoz allows for calculation of photolysis rates more consistent with changing

climate and chemical conditions. In addition to ozone, we also calculate an array of 20+ other species in the stratosphere to account for chemical fluxes across the tropopause. For example, the stratosphere is a net source of NO_x into the troposphere and a net sink of tropospheric CO. Stratospheric concentrations of these species are calculated from monthly climatological 3D production rates and loss frequencies archived from the Global Modeling Initiative (GMI) CTM driven by MERRA assimilated meteorology for 2004-2010 [*Allen et al.*, 2010; *Duncan et al.*, 2007; *Considine et al.*, 2008] and re-gridded to the ModelE grid. We approximate the paleo-stratosphere by scaling the production rates of NO_x and HNO_3 by the ratio of the primary stratospheric nitrogen precursor (N_2O) observed in NOAA/NGDC ice cores (preindustrial/present = 0.83; LGM/present = 0.77) [*Fluckiger et al.*, 2002], and similarly for CO by the ratio of ice-core methane (preindustrial/present = 0.41; LGM/present = 0.32). Bromine species are the exception to the linearized treatment, and concentrations are instead prescribed in the stratosphere as described by *Parrella et al.* [2012] and do not change between climates here.

To reach equilibrium with respect to stratosphere-troposphere exchange, each scenario was initialized over 10 years, repeatedly using the first year of archived meteorology. Simulations for analysis use the three remaining years in each climate scenario.

4.2.4 Evaluation of present-day simulation

We evaluate the ICECAP present-day simulation against a suite of sonde, aircraft, satellite, and surface measurements of trace gases, aerosols, and radionuclides, and we also compare ICECAP with the standard GEOS-Chem driven by assimilated meteorology (GEOS4 and GEOS5). We refer the reader to Appendix B for the details, and summarize here. Tropospheric vertical mixing performs better than, or on par with, the GEOS simulations compared to observed vertical profiles of ^{222}Rn and surface ratios of $^{7}Be/^{210}Pb$. Stratospheric age-of-air is longer in our simulations than either GEOS simulation, but more in agreement with observations [*Waugh and Hall*, 2002]. We find a tropospheric residence time for ^{210}Pb-containing aerosols against deposition of 7.2 d, within

the range of previous model studies: 6.5-12.5 d [*Turekian et al*., 1977; *Lambert et al*., 1982; *Balkanski et al*., 1993; *Koch et al*., 1996; *Guelle et al*., 1998a,b; *Liu et al*., 2001].

Our simulated methyl chloroform (CH_3CCl_3) lifetime against loss from tropospheric OH is 6.0 years, which matches the $6.0^{+0.5}_{-0.4}$ years inferred from observations by *Prinn et al*. [2005]. The methane lifetime against tropospheric OH is 10.4 years (cf. Section 4.7), which matches the best estimate of $10.2^{+0.9}_{-0.7}$ years from *Prinn et al*. [2005], recent multi-model estimates of 10.2 ± 1.7 [*Fiore et al*., 2009] and 9.8 ± 1.6 [*Voulgarakis et al*., 2013] years, and an observationally-derived estimate of 11.2 ± 1.3 years [*Prather et al*., 2012].

The simulated present-day stratospheric columns of ozone (SCO) in our model have a small mean bias of +1.5% versus a 2004-2010 climatology from satellite [*Ziemke et al*., 2011]. However, we overestimate SCO over the poles by 5-50% due to an overly vigorous Brewer-Dobson circulation, and particularly over Antarctica during austral spring (>100%) as our implementation of Linoz does not include the heterogeneous reactions of the ozone hole. In the troposphere, we underestimate tropical ozone columns by 20% and overestimate extratropical columns by 45% versus satellite climatologies [*Ziemke et al*., 2011]. Comparison with ozonesondes indicates that the tropical bias is in the free and upper troposphere and not at the surface, and that the extratropical bias is a springtime feature in both hemispheres, consistent with overestimated transport from the stratosphere. Overly vigorous mass fluxes from the stratosphere to the troposphere have historically been a problem with CTMs [e.g., *Liu et al*., 2001], and some models have prescribed cross tropopause fluxes of ozone [e.g., *Wu et al*., 2007b]. Here we elect to accept the bias in the cross-tropopause flux of ozone in the present day in order to examine the role of the tropical stratosphere on photochemistry in different climates.

4.3 Climate

4.3.1 Climate forcings

Table 4.2 summarizes the different greenhouse gas levels, orbital parameters, topography, and fixed sea ice and sea surface temperatures (SSTs) used to force each of our four simulations. In this section and throughout the paper, we report most changes relative to the state of the preindustrial.

Simulations of LGM climate are sensitive to assumptions about ice sheet topography and tropical SSTs [*Rind*, 2009], and these assumptions have implications for the chemical composition of the troposphere, as they affect transport, surface emissions, and the surface UV albedo. We use here the reconstruction of ice sheet thickness and extent from *Licciardi et al.* [1998]. At the LGM, large permanent land ice sheets 3-4 km thick existed over northern North America (Laurentide and Cordilleran), Greenland, and northwestern Eurasia (Fennoscandian). The accumulation of water in terrestrial ice sheets caused sea levels to drop 120 m, exposing an additional 3% of the Earth's surface as land, particularly in Southeast Asia and Oceania, the Bering Strait, and the southeastern continental shelf of South America [*Clark and Mix*, 2002].

Figure 4.2 shows the annual mean SST distribution used in each past simulation. Our preindustrial and present-day simulations use respective values from the Hadley Centre sea ice and SST version 1 (HadISST1) data set [*Rayner et al.*, 2003]. For the LGM, large uncertainty exists over the extent of cooling of tropical SSTs, which strongly affects LGM dynamics because of its influence on latitudinal temperature gradients and low latitude circulation [*Rind*, 2009]. To bound the range of likely conditions, we simulate two potential realizations of the LGM climate driven by different SSTs. For our "warm LGM" simulation, we use the SST reconstruction from Climate: Long range Investigation, Mapping, and Prediction [*CLIMAP*, 1976], with an average change in SST within 15° of the equator ($\Delta SST_{15°S-15°N}$) of -1.2°C. The CLIMAP reconstruction

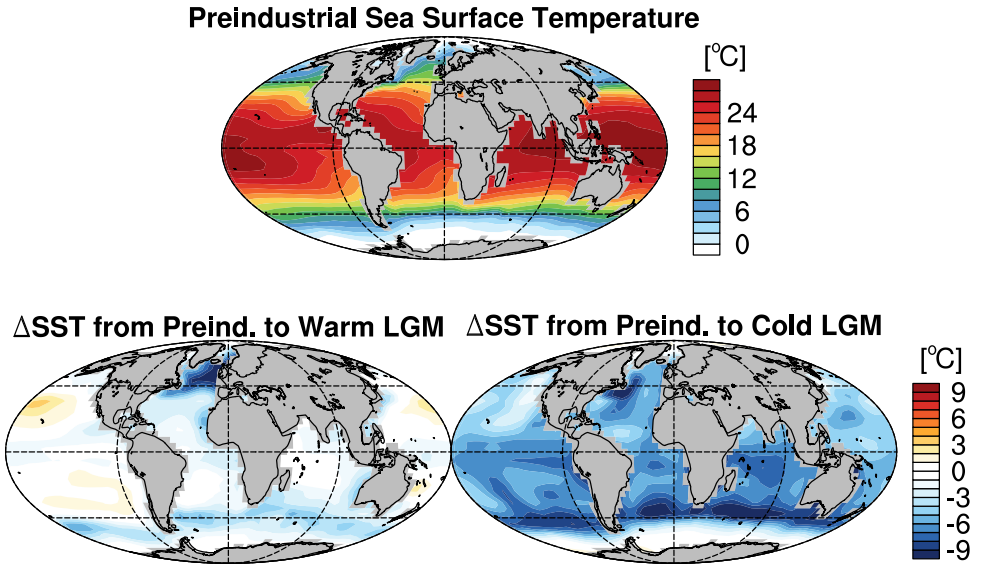

Figure 4.2: Top panel shows preindustrial sea surface temperature (SST), as reconstructed by proxies [*Rayner et al*., 2003]. Bottom two panels are the absolute changes in SST during the "warm" LGM (bottom left) [*CLIMAP*, 1976] and "cold" LGM (bottom right) [*Webb et al*., 1997] scenarios, relative to the preindustrial, with the LGM coastlines and ice sheets. The difference plots share a common colorbar. The change in SST from the preindustrial to the present day is relatively small (not shown).

indicates that much of the subtropical Pacific was warmer in the LGM than in the preindustrial, a controversial result [e.g., *Rind and Peteet*, 1985]. For our "cold LGM" simulation, we use SSTs from *Webb et al*. [1997], who achieved $\Delta SST_{15°S-15°N}$ of -6.1°C by imposing an ocean heat transport flux in the GISS GCM. The recent Multiproxy Approach for the Reconstruction of the Glacial Ocean surface [*MARGO Project Members*, 2009] concluded that the change was likely colder than that implied by the CLIMAP reconstruction ($\Delta SST_{15°S-15°N}$ = -1.7°C) with a more subdued warming of the subtropical Pacific gyres, but not as cold as in *Webb et al*. [1997].

4.3.2 Climate results

Table 4.4 shows mean values for the globe and large-zonal bands of meteorological variables in each simulated climate scenario. Surface air temperatures decrease by 1.4°C or 6.8°C in the warm and cold LGM scenarios relative to the preindustrial, driven by the decreases in greenhouse gases

Table 4.4: Climate results for the four scenarios.

	Last Glacial Maximum (21ka)															
	Cold LGM				Warm LGM				Preindustrial				Present day			
Simulated variable[a]	G	SH	T	NH	G	SH	T	NH	G	SH	T	NH	G	SH	T	NH
Surface air temperature [°C]	6.1	-3.7	19.2	-2	10.7	1.5	24.6	0.8	14.3	5.4	26	7.4	14.9	6	26.5	8
Specific humidity [g/kg]	1.8	1.3	1.8	1.8	2.6	1.7	2.6	2.6	2.9	2	2.9	2.9	3	2.1	3	3
Tropopause pressure [hPa]	151	196	98	180	135	173	80	172	126	165	75	158	123	160	73	155
Precipitation rate [mm d^{-1}]	2.4	1.6	3.5	1.7	2.8	2	4.2	1.9	3	2.3	4.3	2.1	3	2.3	4.3	2.1
Ground albedo [%]	21	29	9	28	20	26	9	30	14	18	8	20	14	17	8	19
Land coverage [%]	33	17	27	56	33	17	27	56	29	16	24	47	29	16	24	47
Land ice coverage [%]	7	9	0	16	7	9	0	16	3	9	0	2	3	9	0	2
Ocean/lake ice coverage [%]	11	31	0	7	10	24	0	9	5	8	0	8	4	7	0	7
Total cloud cover [%]	58	69	48	62	57	64	49	61	58	63	51	61	59	63	52	63
Cloud top pressure [hPa]	616	667	579	616	585	640	535	601	570	616	536	570	574	616	540	577
Elevation above sea level [m]	341	271	170	646	341	271	170	646	238	218	145	386	238	218	145	386
Surface wind speed [m s^{-1}]	5.5	6.9	5.1	4.5	5.4	7.1	4.8	4.5	5.3	6.9	4.7	4.7	5.3	6.9	4.7	4.7
Stratospheric age of air[b] [a]	1.64				1.55				1.43				1.31			

[a] Annual multi-year mean values for the globe (G), southern hemisphere (SH; 90°S-23°S), tropics (T; 23°S-23°N), and northern hemisphere (NH; 23°N-90°N).

[b] Mass-weighted mean stratospheric age of air [*Waugh and Hall*, 2002], calculated with an SF_6-like inert tracer.

and SSTs and the increase in topography (Figure 4.3, left column). The changes in surface temperature to the LGM are much greater in magnitude than the simulated 0.5°C increase from the preindustrial to the present day (not shown). Tropospheric water vapor is highly sensitive to temperature [e.g., *Held and Soden*, 2006; *Sherwood et al.*, 2010], and tropical specific humidity in our warm and cold LGM scenarios decrease by 10% and 38% relative to the preindustrial.

Figure 4.3 also shows the changing distribution of precipitation in each past scenario (right column). The decreases in greenhouse gases and water vapor increase the tropical tropospheric lapse rate at the LGM, reducing the depth and intensity of tropical deep convection [e.g., *Sherwood et al.*, 2010] and weakening the Hadley circulation. With reduced upwelling near the equator, precipitation decreases in the tropics and increases in the subtropics, especially in the warm pools of the CLIMAP reconstruction.

The residual circulation of the stratosphere also weakens with decreasing levels of greenhouse gases in our simulations. Stratospheric circulation is characterized by net ascent in the tropics and descent in the extratropics, driven by stratospheric breaking of upward-propagating planetary

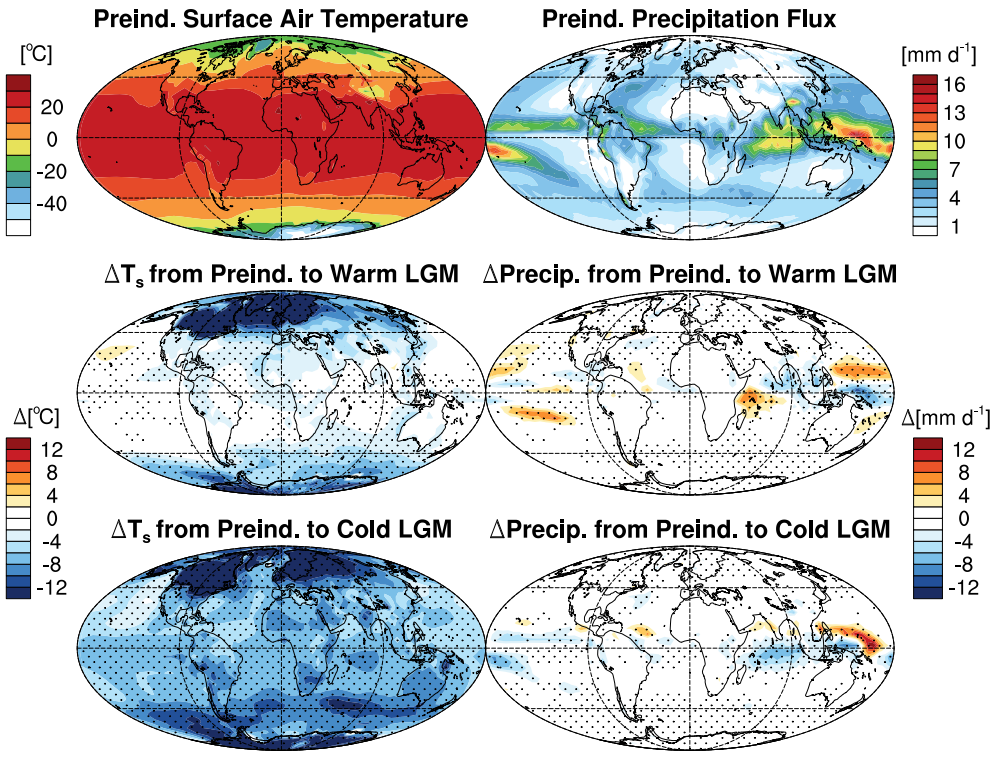

Figure 4.3: Simulated surface air temperatures (left column; °C) and precipitation fluxes (right column; mm d^{-1}). Top panels: Preindustrial conditions. Bottom panels, absolute change from preindustrial to warm LGM [middle row; *CLIMAP*, 1976] and cold LGM [bottom row; *Webb et al.*, 1997] scenarios. Both difference plots share a common colorbar for each variable. The dots indicate gridboxes with significant changes, as determined by the student's t test with degrees of freedom adjusted for autocorrelation [*Wilks*, 2011]. The changes relative to the preindustrial in present-day surface temperatures and precipitation fluxes are small, and significant only at the poles and over small areas of the tropics, respectively (not shown).

waves of tropospheric midlatitude origin [*Holton et al.*, 1995]. The vertical component of the residual circulation (w^*) weakens in magnitude relative to the preindustrial by an average of 16% and 32% in the warm and cold LGM scenarios at 50 mb in the tropics (12°S-12°N), and increases by 5% in the present day. There are corresponding changes in the extratropics. The mass-weighted mean stratospheric age of air [*Waugh and Hall*, 2002] deduced from an SF6-like tracer in GEOS-Chem is 9-15% greater in the LGM than the preindustrial, consistent with the weakening residual circulation; the present-day age of air is 8% lower than the preindustrial. That the strength of the residual circulation is correlated with greenhouse gas levels is a robust result of

GCMs [*Garcia and Randel*, 2008], including at the LGM [*Rind et al*., 2001, 2009], although not clearly supported by observations [*Engel et al*., 2008]. The decreased thermal wind shear at the LGM reduces the strength of the subtropical jet, which in turn weakens wave penetration into the stratosphere and leads to deceleration of the residual circulation relative to the preindustrial; the converse holds for the preindustrial to present [*Shepherd and McLandress*, 2011]. Weakened tropical deep convection at the LGM and increased static stability about the tropopause from stratospheric radiative warming also impedes mixing across the tropopause. In addition, the tropopause height decreases in each colder climate; in the cold LGM scenario it is 2 km lower than in the preindustrial. The slowing of the residual circulation of the stratosphere together with decreases in tropopause height during the LGM contribute toward enhancement of the SCO and have implications for photolysis rates in the tropical troposphere, as we describe in Section 4.5.1.

4.3.3 Evaluation of LGM climate changes

Figure 4.4 demonstrates that our LGM simulations are in broad agreement with other LGM model studies and an independent reconstruction of regional LGM climate from pollen records. The left panels compare the zonal mean temperature and precipitation changes of our two LGM simulations to the mean and range of those values in the models participating in the Paleoclimate Modelling Intercomparison Project Phase II (PMIP2) [*Braconnot et al*., 2007a,b]. Each of the seven models that simulated the LGM for PMIP2 had a fully-coupled ocean-atmosphere, and did not prescribe SSTs as we do here. Our LGM scenarios bound the PMIP2 ensemble mean change of -2.3°C in the tropics relative to the preindustrial. Our simulations find decreases in zonal mean precipitation of 10-50% within 10° of the equator, and of 10-90% within 40° of the poles, and little change in the midlatitudes as in the mean of the PMIP2 ensemble. Precipitation increases up to 25-33% in the tropics poleward of the equator in our simulations, where the PMIP2 ensemble mean is zero. Our zonal mean LGM precipitation changes are of greater magnitude than the range of PMIP2.

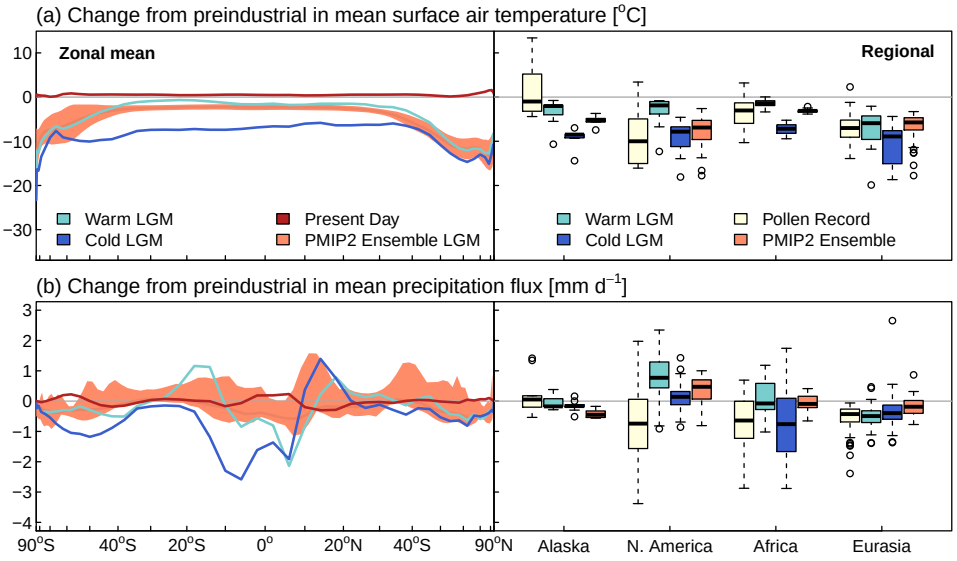

Figure 4.4: Evaluation of climate changes for (a) zonal mean surface temperature and (b) zonal mean precipitation flux. The left panels compare our ModelE simulations to the range of zonal mean changes from the preindustrial in the Paleoclimate Multimodelling Intercomparison Project Phase II [PMIP2; *Braconnot et al.*, 2007a]. The latitudinal axis is weighted by relative zonal area. The right panels compare our simulation to the pollen-based climate reconstruction from *Bartlein et al.* [2011a]. That study used the present day as its baseline, and we follow that convention here. We sample our simulations and the PMIP2 ensemble at the locations of the sediment core measurements.

Figure 4.4 also compares our modeled results and those of PMIP2 to an inverse reconstruction of regional climate using pollen data by *Bartlein et al.* [2011b]. Temperature changes in the warm LGM simulation relative to the preindustrial better match values inferred from the pollen data than do those in the cold LGM, with mean absolute biases of 4.4°C and 5.1°C, respectively (The PMIP2 bias in temperature change is 3.5°C). Both PMIP2 and our simulations have difficulty in matching the inferred changes in precipitation, except over Africa, where the cold LGM performs well. The small sample size of the pollen record (n = 98 at the LGM) and its limited geographic distribution make it challenging to draw conclusions from these comparisons.

4.4 Tropospheric emissions

Figure 4.5 summarizes the gas phase emissions and Figure 4.6 the direct and precursor aerosol emissions in our different simulations. Wherever possible, emissions respond to changing meteorology from the GCM, as described below. We test the sensitivity of our results to three different emission scenarios in the preindustrial and LGM atmospheres: a low fire and a high fire scenario which together span the range of estimated past fire magnitudes (Section 4.4.6), and a scenario in which we fix the total lightning source in all climates to compare to our other simulations in which total lightning changes with climate (Section 4.4.5).

4.4.1 Anthropogenic

Present-day anthropogenic emissions from fuel combustion, agriculture, and industry are prescribed from the Emission Database for Global Atmospheric Research (EDGAR) base inventory for 2000 [*Olivier*, 2001], overwritten with regional inventories for the United States (EPA NEI99), Canada (CAC), Mexico (BRAVO) [*Kuhns et al*., 2003], Europe (EMEP) [*Auvray and Bey*, 2005] and South and East Asia [*Streets et al*., 2003, 2006]. These inventories all have monthly variability, some with additional weekly cycles. Biofuel emissions [*Yevich and Logan*, 2003] and aircraft emissions are constant. All emissions are scaled as described by *van Donkelaar et al*. [2008] to 1995 values for our present-day simulation. Our preindustrial and LGM simulations assume no anthropogenic emissions, aside from a small biofuel burning source in the preindustrial that is 45% of the present-day value, estimated by scaling and distributing the 1850 country-level inventory from *Fernandes et al*. [2007] by the 1770/1850 local population ratios in the History Database of Global Environment (HYDE) 3.1 [*Klein Goldewijk et al*., 2011]. Anthropogenic emissions since the preindustrial yield large perturbations to the tropospheric budgets of reactive nitrogen, carbon, and sulfur (Figure 4.5 and Figure 4.6), predominantly in the northern midlatitudes.

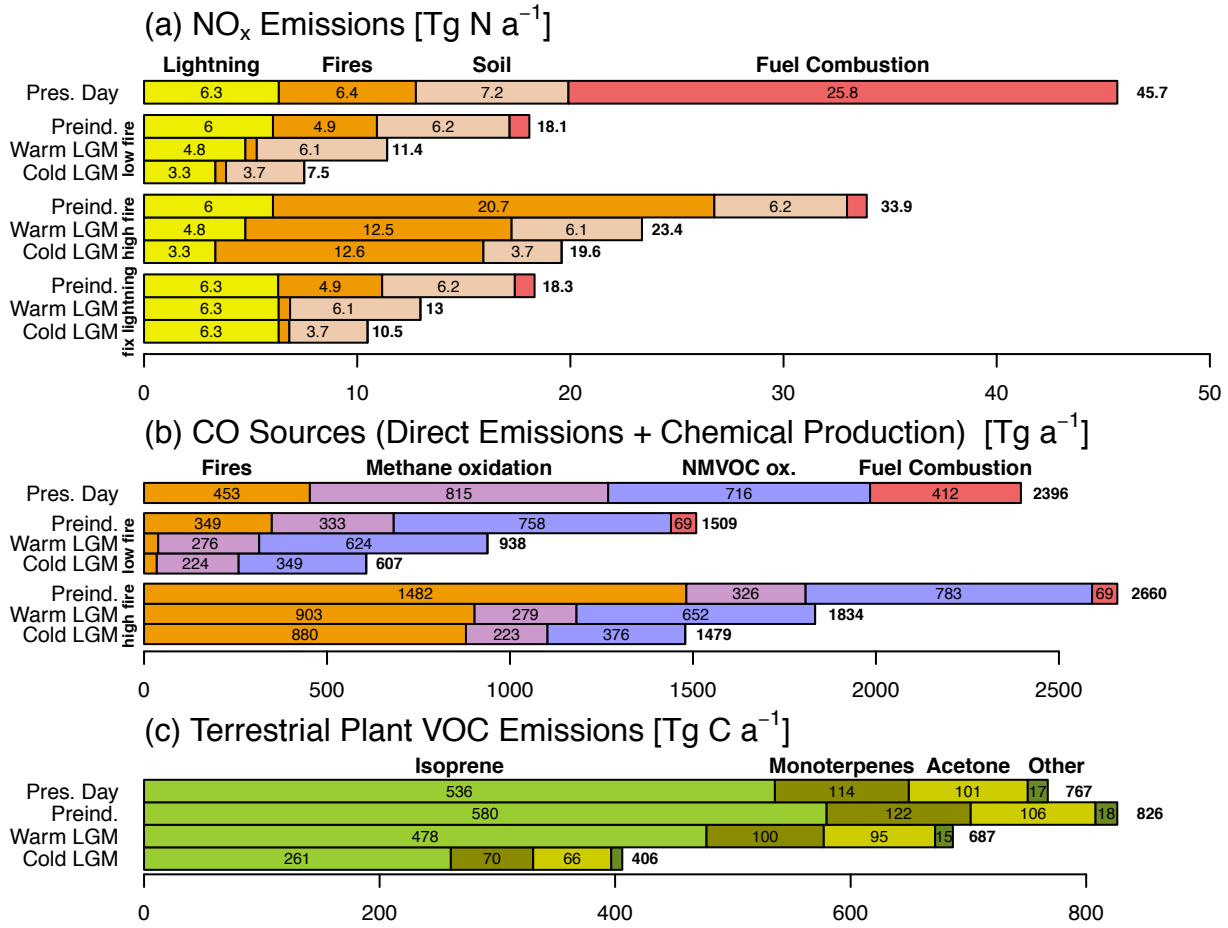

Figure 4.5: Gas phase emissions used for each climate scenario. We test two different fire emission scenarios, a "high fire" scenario with past fire emissions from the LMfire model [*Pfeiffer and Kaplan*, 2012], and a "low fire" scenario in which we scale the model output by sediment records of charcoal accumulation rates [*Power et al.*, 2008]. We also perform a "fixed lightning" suite of simulations in which we scale the total lightning NO_x source to be constant in different climates.

4.4.2 Biogenic - Land

Terrestrial plant emissions of VOCs in GEOS-Chem follow the MEGAN scheme, in which each model grid cell is assigned a base emission rate based on its local vegetation. MEGAN adjusts these local base emission rates by applying scaling factors that are time-varying functions of photosynthetically available radiation (PAR), leaf area index (LAI), and 15 d of recent surface air temperature [*Guenther et al.*, 2000, 2006, 2012, 1999, 1995]. Emissions respond positively with

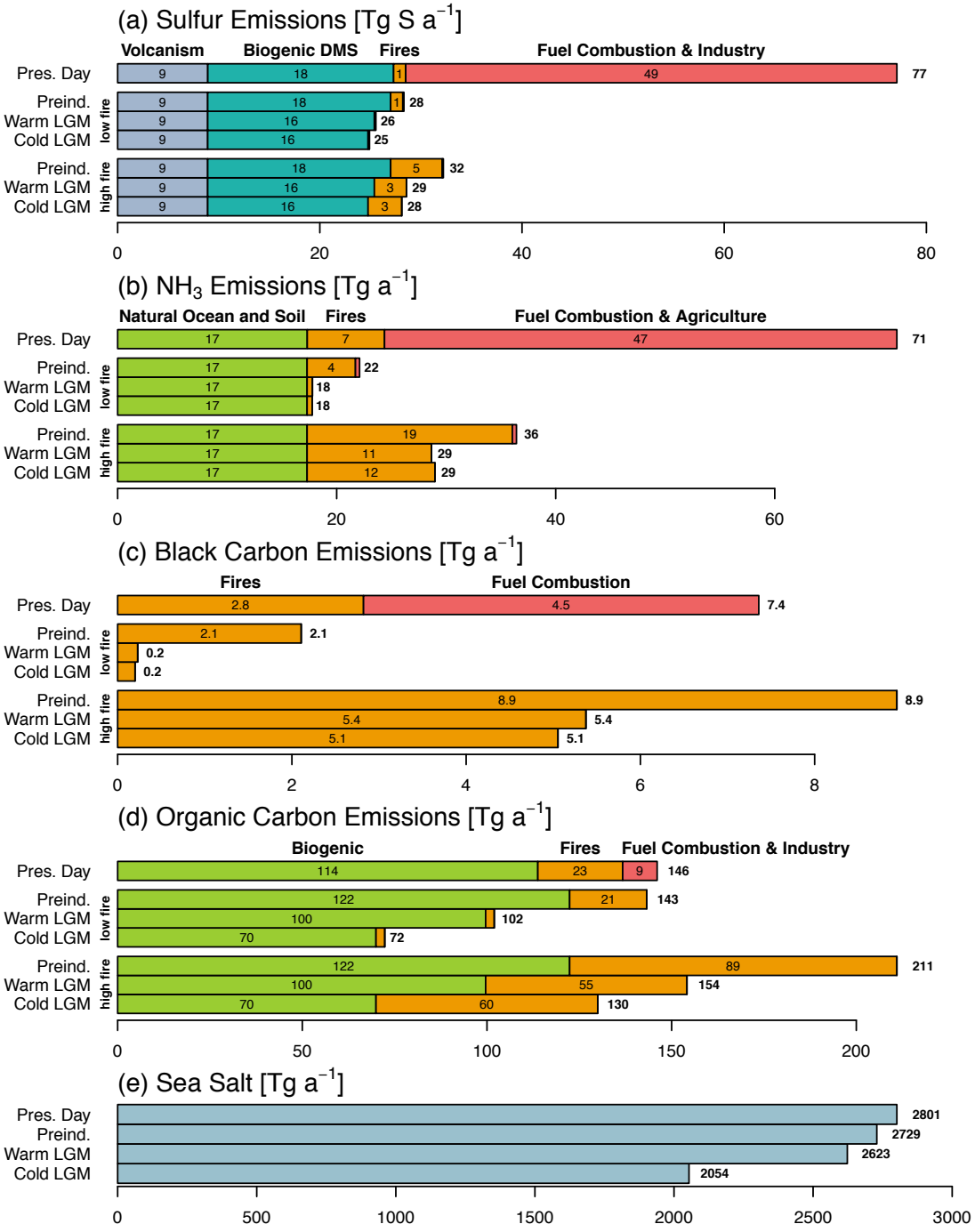

Figure 4.6: Same as Figure 4.5, but aerosol precursor emissions.

each parameter. For all scenarios in this study, we calculate the base biogenic VOC emissions using the PFT distributions from BIOME4-TG. To derive these emissions, we first perform a

Table 4.5: Biogenic emission factors used for plant functional types in the dynamic vegetation model BIOME4-TG.

BIOME4-TG PFT	Base emission factor (μg molecule m^{-2} hr^{-1}) Isoprene	Monoterpenes	Acetone
Tropical Evergreen Trees	5650	700	2.4
Tropical Drought-deciduous Trees (Raingreens)	4347	535	4.1
Temperate Broadleaved Evergreen Trees	5594	575	33
Temperate Deciduous Trees	4780	670	53
Cool Conifer Trees	3685	622	19
Boreal Evergreen Trees	3155	747	208
Boreal Deciduous Trees	3603	533	29
C3/C4 Temperate Grass Plant Type	1919	170	35
C4 Tropical Grass Plant Type	4396	475	3.9
C3/C4 Woody Desert Plant Type	2364	107	6.3
Tundra Shrub Type	3689	319	61
Cold Herbaceous Type	1677	162	24
Lichen/Forb Type	1492	111	14
Crops	407	163	0.0

multiple regression, mapping the default distribution of MEGAN version 2.1 emission factors onto the present-day PFT distribution in BIOME4-TG. We then apply the resulting emission factors, shown in Table 4.5, onto the distribution of PFTs calculated by BIOME4-TG for the preindustrial and LGM climates.

Figure 4.5c shows the resulting biogenic emissions from our approach, and Figure 4.7a the spatial distribution of changes in isoprene emissions between the different climate simulations. Global terrestrial plant emissions decrease by 7% in the present day relative to the preindustrial because of large-scale conversion of natural vegetation types to modern croplands (which have lower VOC yields), particularly over southern Brazil and northern India. In the LGM, terrestrial plant emissions decrease by 17% and 51% relative to the preindustrial in our warm and cold scenarios, predominantly driven by decreases over South America and Africa. These decreases are caused in part by a simulated reduction in tropical broadleaf forests and LAI in the colder and drier tropics (especially in the Amazon and Congo in the cold LGM scenario), but the driving factor is predominantly the leaf-temperature effect. Hence, we simulate severe reduction in plant emissions in the cold LGM scenario with its >6°C of cooling. However, additional land area

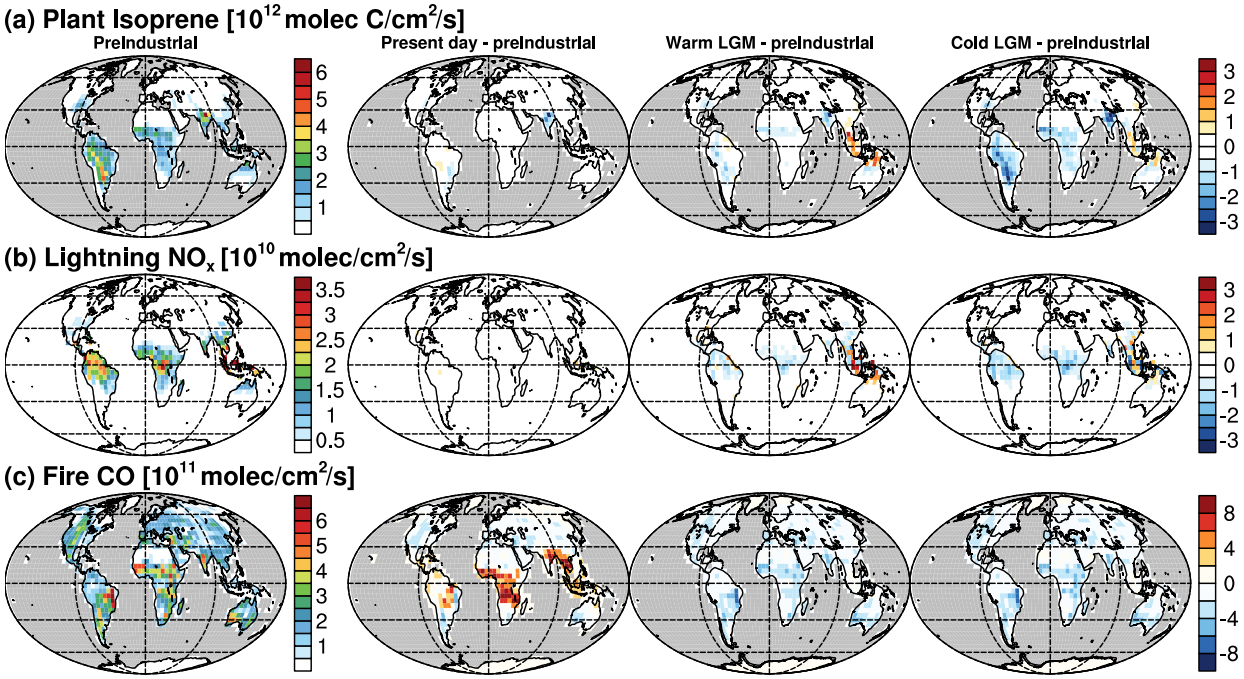

Figure 4.7: Spatial distribution of annual mean preindustrial emissions, and the present-day and LGM absolute changes in these emissions relative to the preindustrial for (a) isoprene from terrestrial plants, (b) NO_x from lightning, and (c) CO from fires in the "low fire" scenario. The difference plots share the common color bars at right.

exposed in Southeast Asia and Oceania causes a large regional increase in plant emissions that is stronger in the warm LGM scenario due to warmer temperatures and increased PAR from decreased cloud cover. Our LGM results span the range of previous estimates: *Valdes et al*. [2005] simulated a 50% reduction in biogenic VOC emissions relative to the preindustrial, *Kaplan et al*. [2006] a 33% reduction, and *Adams et al*. [2001] a 29% reduction.

Emissions of NO_x from soil microbial activity follow the parameterization of *Yienger and Levy* [1995] as implemented by *Wang et al*. [1998] and are dependent on land cover type, precipitation, and temperature. Present-day emissions are 16% higher than the preindustrial, mostly reflecting the use of fertilizers (Figure 4.5a). Soil emissions decrease in each successively colder past climate simulation, driven by the associated decreases in precipitation and surface temperature.

However, decreases in precipitation and temperature in the warm LGM scenario are offset by additional tropical land mass, and global soil emissions decrease by only 2% relative to the preindustrial. Nevertheless, large decreases in temperature and precipitation over southern Brazil in the cold LGM scenario contribute to a 40% decrease in global soil emissions relative to either the preindustrial or warm LGM.

4.4.3 Biogenic - Ocean

Phytoplankton and bacteria activity in the mixed-layer of the ocean may represent a local source or sink of acetone to the atmosphere. We assume constant ocean acetone concentrations in all climates (15 nM), but allow the sign and magnitude of the ocean-atmosphere flux to vary locally with surface temperature and atmospheric concentration as described by *Fischer et al.* [2012]. In all scenarios, the ocean acts as a net sink for acetone.

Biogenic production of dimethylsulfide (DMS) is represented in the model as the product of seawater DMS concentrations and sea-to-air transfer velocities [*Park et al.*, 2004]. We use distributions of surface ocean concentrations of DMS from *Kettle et al.* [1999] in all climates, but transfer velocities are parameterized as a function of SST and surface wind speeds [*Nightingale et al.*, 2000a,b]. At the LGM, cooler SSTs together with our assumption that no production occurs beneath sea ice yield an 11% reduction in DMS emissions relative to either the preindustrial or present-day (Figure 4.6a).

Bromocarbon emissions from oceanic macroalgae and phytoplankton are the dominant bromocarbon precursors for tropospheric Br_y [*Warwick et al.*, 2006; *Law et al.*, 2007]. Emissions are prescribed from *Liang et al.* [2010] as implemented by *Parrella et al.* [2012], and remain constant between climate scenarios.

4.4.4 Volcanic

Volcanic emissions of SO_2 are from the AEROCOM inventory [*Diehl*, 2009] as implemented by *Fisher et al*. [2011]. The emissions are released vertically into the troposphere as in *Chin et al*. [2000]. We apply emissions from a typical recent year (1995) to all scenarios, with 2.5 Tg S a^{-1} of eruptive emissions and 8.9 Tg S a^{-1} of passive outgassing. Volcanic activity may vary over glacial periods following redistribution of surface mass stresses from ice sheets [*Kutterolf et al*., 2013], but we do not examine that possibility here.

4.4.5 Lightning

Lightning is a major natural source of NO_x [*Schumann and Huntrieser*, 2007]. The standard lightning NO_x source in GEOS-Chem is described in Chapter 2. Lightning flash rates in the model follow the parameterization of *Price and Rind* [1993, 1992, 1994] and reflect changes in convective cloud top heights. We determine for the present day a uniform scaling factor (=7.0) such that the simulated global mean flash rate matches the 46 flashes s^{-1} observed by satellites [*Christian et al*., 2003]. We use the same scaling factor for all climates, but allow global mean lightning activity to change with changes in deep convection. We assume a uniform production rate of 310 mol N per all flash types (corresponding to 6.3 Tg N a^{-1} in the present day), and distribute emissions vertically following *Ott et al*. [2010].

Figure 4.7b shows changes in the lightning NO_x distribution. The *Price and Rind* [1993, 1992, 1994] formulation strongly responds to decreases in the vertical extent of deep convection, and lightning activity therefore decreases in each successively colder climate. Lightning is 5% higher in the present day and lower by 20% and 45% in the warm and cold LGM scenarios relative to the preindustrial (Figure 4.5a). The model simulates large decreases in African and South American lightning into the LGM, though there are local increases over the exposed continental margins of Southeast Asia.

Although lightning is known to be strongly correlated with surface temperatures on diurnal through decadal time scales [*Williams et al.*, 2005], how it may respond to changing meteorology on longer scales is uncertain [*Williams*, 2005]. Therefore we also perform a suite of "fixed lightning" simulations in which we uniformly scale the average NO_x yield per flash in each climate scenario such that we maintain a constant total lightning NO_x yield of 6.3 Tg N a^{-1}.

4.4.6 Fires

Both natural and human-ignited fires have likely played a large role in trace gas emissions since the LGM [*Pyne*, 2001]. For the present day, we prescribe monthly mean emissions from *Yevich and Logan* [2003]. However, there is large uncertainty in the amount of fire activity in past atmospheres. Beginning with *Crutzen and Zimmermann* [1991], many model studies have assumed that preindustrial fire emissions were 10% of present-day values and distributions. More recently, a global synthesis of charcoal accumulation rates suggests that preindustrial fire emissions were similar to or slightly higher than those in the present day [*Power et al.*, 2008], while the record of black carbon deposition at Greenland and Antarctica also implies that burning was mostly constant from the preindustrial through to the present [*McConnell et al.*, 2007; *Bisiaux et al.*, 2012]. Measurements of $\delta^{13}C$ and $\delta^{18}O$ in ice-core CO at Antarctica appear to indicate that Southern Hemispheric fire emissions were substantially higher in the preindustrial than at present [*Wang et al.*, 2010], but this view is controversial [*van der Werf et al.*, 2013]. Meanwhile, the charcoal data suggest that fire activity was at a historical minimum at the LGM [*Power et al.*, 2008]. Model representations of fire activity show large disagreements in the trends over glacial-interglacial and preindustrial to present-day time horizons [*Fischer et al.*, 2008; *Thonicke et al.*, 2005, Pfeiffer et al., manuscript in prep.]. Given the wide range of estimates for fire activity since the LGM, we test a range of emissions for each climate, as we describe below.

For all simulations, we use distributions of dry matter consumed per PFT from the LMfire model [*Pfeiffer and Kaplan*, 2012] coupled with emission factors from the Global Fire Emissions

Database version 3 (GFED3) [*van der Werf et al*., 2010] for NO_x, CO, SO_2, black carbon, OC, and 17 additional gas-phase species. LMfire simulates fire occurrence and behavior as a component of the Lena-Potsdam-Jena (LPJ) dynamic global vegetation model, taking into account both climate factors and the activities of early human populations of hunter gatherers, pastoralists, and farmers [*Pfeiffer and Kaplan*, 2012]. Here, LMfire was driven by monthly climatologies of surface temperature, diurnal temperature range, total precipitation rate, days in the month with precipitation, fraction cloud cover, and surface wind speed from our ModelE simulations. It also takes monthly mean lightning-to-ground strike rates as determined by GEOS-Chem (Section 4.4.5).

The LMfire model yields fire emissions in the preindustrial and LGM scenarios 3-4 times higher than those for the present day, primarily reflecting reductions in active fire suppression and in landscape fragmentation and livestock grazing. These results represent an upper limit of fire activity in the past atmospheres. For a lower limit, we also estimate fire emissions by scaling the LMfire total dry matter consumed to match emissions implied by the charcoal accumulation rates from the Global Charcoal Database (preindustrial = 100% and LGM = 10% of the present-day 4.2 Pg a^{-1} dry matter consumed) [*Power et al*., 2010, 2008; *van der Werf et al*., 2010]. We apply both estimates to GEOS-Chem, and refer to these simulations as the "high fire" and "low fire" scenarios in each climate. Totals for these scenarios are shown in Figure 4.5 and Figure 4.6.

Figure 4.7c shows the changing distribution of CO emissions in the low fire emissions scenario. While the total dry matter consumed is the same in the low fire preindustrial simulation and present day, there are changes in the distribution. Fire activity decreases in the present-day extratropics due to active and passive fire suppression, and increases in the tropics due to deforestation and agricultural practices. As tropical fires have higher emission factors per dry matter consumed [*van der Werf et al*., 2010], total emissions are higher in the present day by 25% relative to the preindustrial, despite dry matter consumed remaining constant. In the high fire scenario emissions decrease in the present day and almost everywhere in the LGM, relative to the

preindustrial (not shown).

4.4.7 Wind-driven

Sea salt aerosol evasion from the ocean is described by *Jaeglé et al*. [2011], and responds to SSTs and surface wind speeds. Emissions at the present day are 3% higher than the preindustrial. Emissions at the LGM are 4% and 25% lower than the preindustrial, largely reflecting SSTs and sea ice extent. Debromination of sea salt is an important source of bromine radicals to the troposphere, and responds with sea salt aerosol as described by *Parrella et al*. [2012] and has been updated with size-dependent bromine depletion factors from *Yang et al*. [2008]. The source increases by 3% at the present day and decreases by 7-9% at the LGM relative to the preindustrial. We do not consider here the possible enhancement due to increased particle acidity from present-day anthropogenic emissions, or the reduction with increased alkalinity at the LGM [*Sander et al*., 2003].

We prescribe monthly mean dust concentrations in GEOS-Chem with 3D fields taken from *Mahowald et al*. [2006], with LGM dust burdens 125% greater than in the preindustrial and present. The drier conditions of the LGM promote large increases in dust mobilized from the expanded Sahara desert and Tibetan plateau relative to the preindustrial and present, as well as from the exposed continental shelf of South America.

4.5 Changes in the tropospheric oxidants

Figure 4.8 shows the mean mass-weighted tropospheric burdens for each of the four major oxidants simulated in each of the four climates (present day, preindustrial, warm LGM, and cold LGM), and three sensitivity studies for the past climates (high fire, low fire, and fixed lightning). For comparison, we also show a present-day simulation driven by assimilated GEOS-4 meteorology for 1994-1996 instead of ModelE meteorology. Anthropogenic emissions in the two

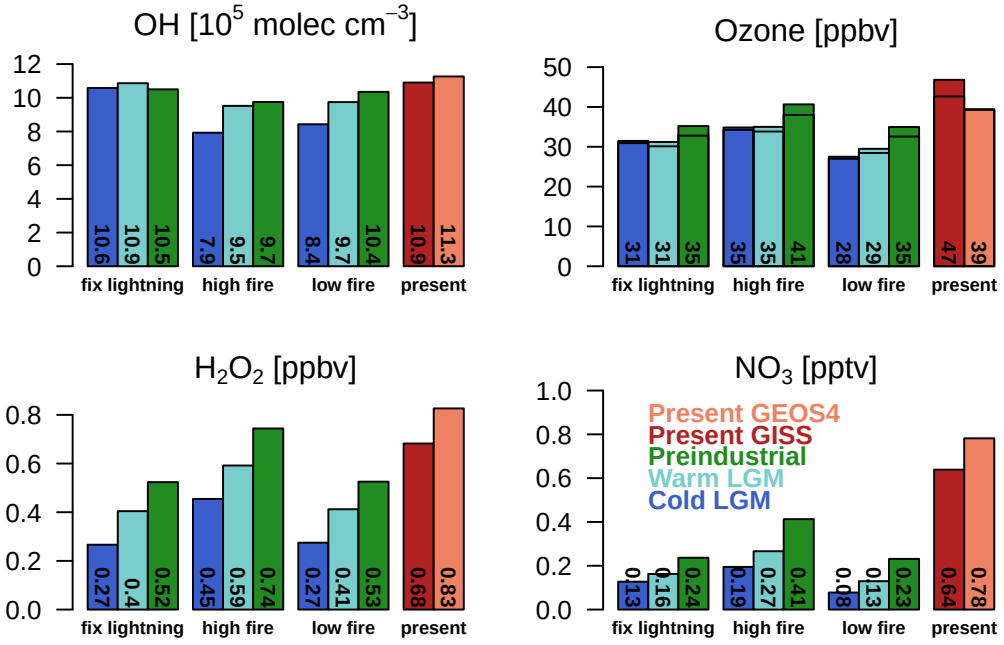

Figure 4.8: Tropospheric mean mass-weighted oxidant burdens, calculated with the tropopause determined from the thermal lapse rate. For comparison with ACCMIP [*Young et al.*, 2013], the horizontal black lines for ozone show the tropospheric burden calculated using a 150 ppb chemical tropopause.

present-day simulations are identical. We find reduced oxidative capacity relative to the present day in all climates, except for H_2O_2 in the preindustrial high fire scenario. In general, oxidant burdens decrease with decreasing surface temperature, and changes in OH are well-buffered compared to the other oxidants. We discuss these changes in oxidants in more detail below. Unless otherwise indicated, all changes are reported as the mean percent change $\pm$ standard deviation in the 18 pairwise combinations of the 6 LGM relative to the 3 preindustrial simulations, and the 3 pairwise combinations of the ModelE present day vs. 3 preindustrial. Comparison with the PMIP2 ensemble and with reconstructions of LGM climate from pollen records (Section 4.3) and ice-core records (Section 4.6) suggest that the low-fire scenarios and the warm LGM climate are the most likely representations of the past atmospheres; we refer to these

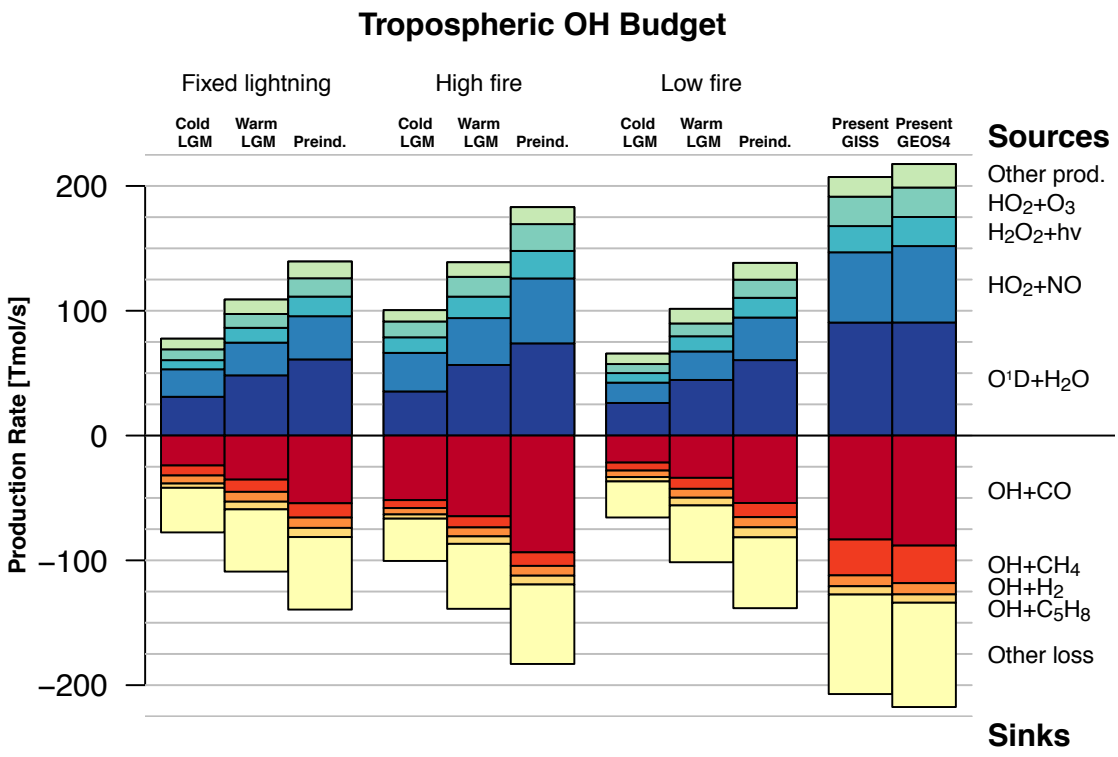

Figure 4.9: Global annually averaged chemical production and loss rates of OH in each simulation, by contributing reaction.

scenarios as our "best estimate."

4.5.1 Hydroxyl radical

Global mean OH decreases in each successively colder climate scenario, except for the fixed lightning scenario in which it remains roughly constant (Figure 4.8, top left panel). OH burdens in our ModelE-driven simulations increase by +7.0 $\pm$ 4.3% in the present and decrease by -6.7 $\pm$ 11% at the LGM, relative to the preindustrial (+5.3% and -5.9% in our best estimate). OH is largely insensitive to variations in fire emissions. We diagnose these changes below.

Figure 4.9 shows the global chemical budget for OH in each simulation. The non-linear reactions controlling OH are complicated, but well-known [e.g., *Logan et al.*, 1981; *Spivakovsky et al.*, 2000; *Lelieveld et al.*, 2002]. Primary production is by photolysis of tropospheric ozone in

the presence of water vapor, with secondary production from rapid chemical cycling of the HO_x family ($HO_x \equiv OH + RO_2$; $RO_2 \equiv HO_2$ + organic peroxy radicals). Loss is primarily via reaction with CO in all climates, but reaction with methane, other VOCs, and their degradation products (which include CO) are also important. Absolute production and loss rates consistently decrease in each successively colder climate, and do so mostly independently of our different emission scenarios, implying the changes are primarily driven by meteorology. However, the response of mean OH as seen in Figure 4.8 is more buffered than the overall rates of its production and loss reactions.

Global mean OH in the present day increases +7.0 ± 4.3% relative to preindustrial levels, which is much less than the perturbations to emissions — e.g., the 35-52% increase in NO_x. Our results are consistent with the recent multi-model ACCMIP study, which reported a mean ΔOH of -0.6 ± 8.8% for 1850-2000 [*Naik et al.*, 2012]. To understand the relatively small impact of anthropogenic emissions on OH, we follow the approach of *Wang and Jacob* [1998], who derived a linear relationship between OH and emissions using the steady state equations of the NO_x-HO_x-CO-ozone system. They found that mean OH varies with the ratio $S_N/(S_C^{3/2})$, where S_N represents total NO_x emissions (mol a^{-1}) and S_C represents the source of reactive carbon (CO and hydrocarbons; mol a^{-1}). We also find a linear relationship between OH and $S_N/(S_C^{3/2})$ in our preindustrial and present-day simulations ($R^2 = 0.77$; $n = 2$ present day + 3 preindustrial simulations). ΔOH is small because $S_N/(S_C^{3/2})$ has changed little from the preindustrial to the present, as human activity has increased both S_N and S_C [*Thompson et al.*, 1993].

The dependence of OH on $S_N/(S_C^{3/2})$ alone cannot explain the simulated variability across glacial-interglacial timescales ($R^2 = 0.00$; $n = 11$ simulations). Instead, we find linear dependence by including two quantities that *Wang and Jacob* [1998] had assumed remained constant in their derivation: the mean tropospheric ozone photolysis frequency, J_{O_3} (s^{-1}), and specific humidity, q (g H_2O/kg air), i.e.,

$$[OH] \propto J_{O_3} q S_N/(S_C^{3/2}) \tag{4.1}$$

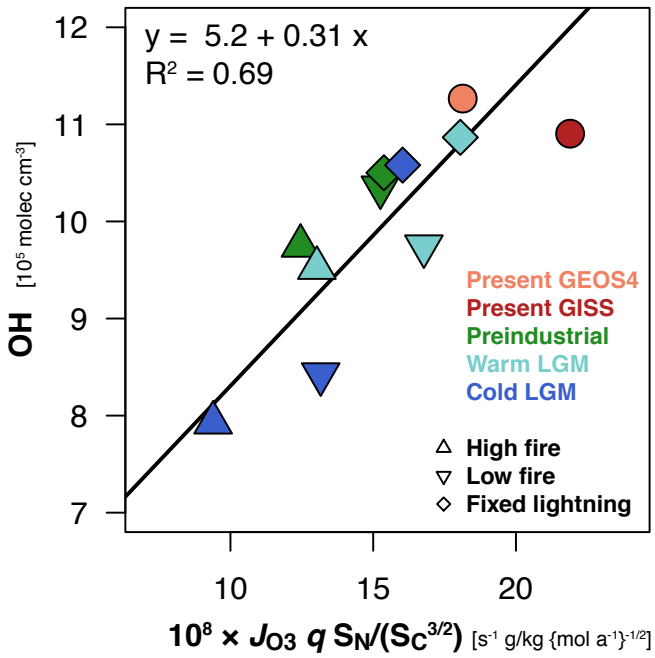

Figure 4.10: Global mean OH concentration in each simulation as a function of $J_{O_3} q S_N/(S_C^{3/2})$, where J_{O_3} is the mean tropospheric ozone photolysis frequency (s^{-1}), q is the tropospheric mean specific humidity (g/kg), and S_N and S_C are the tropospheric sources of reactive nitrogen (mol N a^{-1}) and reactive carbon (mol C a^{-1}). The line shows a reduced major axis regression fit. S_C is calculated as the sum of direct emission of CO and its chemical production from VOC oxidation, an implied source of methane equal to its loss rate, and the emissions of NMVOCs, as in *Wang and Jacob* [1998]. Each molecule of isoprene yields an average 2.6 carbons that react within the gas-phase mechanism; the other NMVOCs have negligible global impact.

This linear relationship explains 69% of the simulated variability in global mean OH across our 11 simulations (Figure 4.10). Our simulations indicate that J_{O_3} and q are sufficiently variable across glacial time scales to effect changes greater than those from emissions. To first order, $J_{O_3} q$ may be thought of as controlling the variability in primary production of HO_x, and $S_N/(S_C^{3/2})$ in regulating HO_x equilibrium partitioning between OH and RO_2, which taken together determine mean OH (although, the ratio $S_N/(S_C^{3/2})$ also influences ozone production and therefore HO_x production).

Mean OH varies most in our simulations with the photolysis component (J_{O_3}) of Equation 4.1

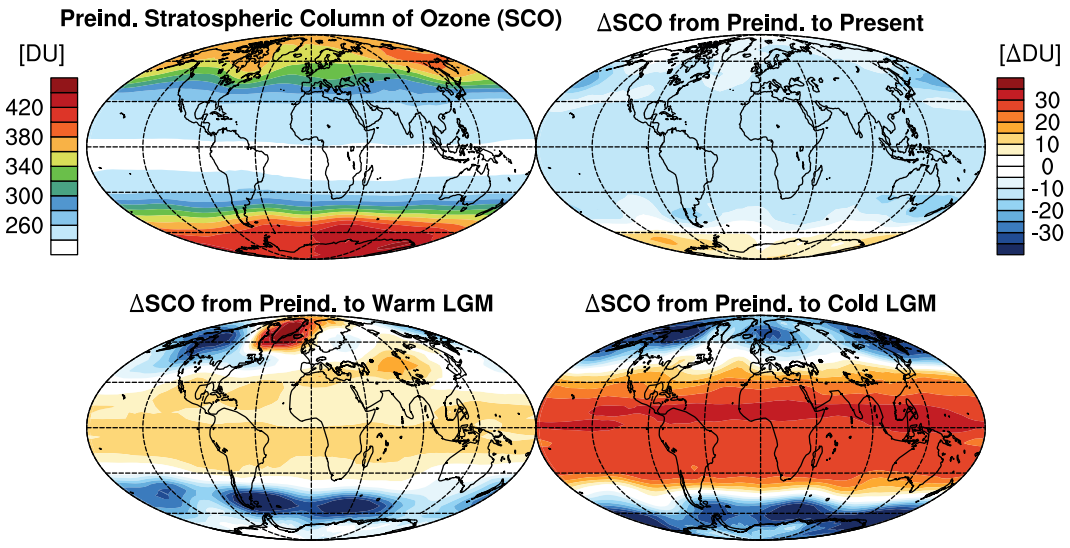

Figure 4.11: Preindustrial simulated zonal mean stratospheric ozone columns [DU], and the change in ozone in the present-day relative to the preindustrial (top panels). Also shown are the changes during the "warm" and "cold" simulations of the LGM, relative to the preindustrial (bottom panels). The difference plots share a common color bar.

($R^2 = 0.41$, $n = 11$ simulations). Both J_{O_3} and OH show reductions in successively colder climates; J_{O_3} decreases by 0.4-0.5% in the warm LGM and 10-12% in the cold LGM simulations relative to the preindustrial. Changes in J_{O_3} reflect changes in amount of shortwave radiation attenuated through overhead ozone columns, aerosol concentrations, and clouds; overhead ozone accounts for most of the change (J_{O_3} vs. SCO: $R^2 = 0.88$). Total cloud cover does not change sufficiently in our simulations to have a significant impact on global photolysis rates. There is an effect on photolysis rates from increased UV surface albedos at the LGM (resulting from increased snow and ice cover over both land and ocean) that is relatively important in high latitudes during summer, but inconsequential for the global OH budget. Specific humidity q is a strong function of temperature [*Sherwood et al.*, 2010], decreasing by 23% in the warm LGM scenario and 50% in the cold LGM scenario.

Figure 4.11 shows the absolute changes in stratospheric columns of ozone in our simulations. Relative to the preindustrial simulation, tropical stratospheric ozone columns have decreased

4-6% (10-12 DU) in the present day, and have increased 3-6% (10-12 DU) in the warm LGM and 10-13% (26-30 DU) in the cold LGM simulations. The increases in tropical ozone at the LGM are driven in the model by: (a) reduced catalytic destruction of ozone from reduced stratospheric halogen and NO_x burdens, (b) the deceleration of the residual stratospheric circulation (cf. Section 4.3.2), which slows the transport of ozone away from the region of net photochemical production in the tropics to the polar stratosphere, and (c) decreases in the tropical tropopause height, which increases stratospheric mass, especially in the cold LGM scenario. These increases in stratospheric ozone are slightly offset by the influence of warmer stratospheric temperatures at the LGM. The converse holds true for explaining the preindustrial to present-day changes. Our results are consistent with *Rind et al*. [2009], who also simulated increases in stratospheric ozone at the LGM using Linoz online within the GISS III GCM., and with climate-driven changes in stratospheric ozone seen in satellite observations (Neu et al., submitted) and model studies [*Hsu and Prather*, 2009; *Hegglin and Shepherd*, 2009] for the present day and near future.

The dependence of OH on $S_N/(S_C^{3/2})$ explains why the global OH burden is insensitive to fire emissions but highly sensitive to lightning. The model emits NO, CO, and VOCs using fixed emission factors per dry matter consumed [*van der Werf et al*., 2010], so large absolute differences in burning yield relatively small changes in $S_N/(S_C^{3/2})$. In contrast, lightning and soil microbial activity are large sources of NO_x with potentially large changes on glacial-interglacial time scales and so can strongly alter $S_N/(S_C^{3/2})$. Large changes in emissions of biogenic VOCs could also potentially perturb the $S_N/(S_C^{3/2})$ ratio. However, we find interglacial changes in biogenic VOCs are strongly correlated to soil NO_x emissions ($R^2 = 0.92$), muting the impact of either on OH.

That we generally find reduced OH at the LGM is contrary to most earlier studies (Table 4.1). *Valdes et al*. [2005] and *Kaplan et al*. [2006] simulated 25-28% increases in OH at the LGM driven by reductions in biogenic emissions. These two studies favored the influence of biogenic emissions in the context of Equation 4.1 by calculating little or no change in S_N across climates, by having smaller values of S_N but simulating slightly larger changes in biogenic emissions than

we do at the LGM, and by assuming present-day stratospheric conditions in all climates. *Levine et al*. [2011a] recently concluded that the temperature effects on OH loss rates and on specific humidity q are sufficient to cancel out the effects of biogenic NMVOC on OH across glacial time scales, more in keeping with our results. Previous LGM studies have neglected the possible influence of the stratosphere, except *Karol et al*. [1995] who also simulated decreases at the LGM. Equation 4.1 indicates OH will increase at the LGM only if the source of NO_x from lightning (or potentially soils) increases relative to the reference period (as in four of our LGM-preindustrial pairs), or if biogenic VOC emissions decrease sufficiently such that the increase in $S_N/(S_C^{3/2})$ can overcome the counter-effects of reduced water vapor and increased overhead ozone.

Figure 4.12 shows the modeled spatiotemporal distribution of OH concentrations in the preindustrial scenario and the absolute changes in the present-day and LGM scenarios relative to the preindustrial. Only results from the low fire scenarios are shown, as the other emission scenarios have similar spatiotemporal patterns. Most of the change from the preindustrial to present occurs in the boundary layer over northern midlatitude in summer, reflecting the rise of anthropogenic emissions. At the LGM, the changes in overhead ozone and water vapor decrease OH relatively uniformly throughout the tropics, with maximum decreases occurring over the land regions where lightning NO_x decreases the most (Figure 4.7b). Decreased production rates in the tropics outweigh the reduction in loss frequencies from reduced CO, methane, and NMVOCs, driving net negative anomalies in most regions in all simulations. One exception is over South Asia, where increased lightning NO_x enhances OH. In the polar regions, where OH production is relatively slow, OH increases in response to reductions in polar methane concentrations (Table 4.3) and in reactive carbon transported from lower latitudes. The increase is greatest in LGM summer over regions with enhanced snow and ice cover (e.g., the Southern Ocean and the Laurentide ice sheet) and thus higher UV surface albedos relative to the preindustrial or present day. The polar changes are inconsequential for global OH, but are of potential interest for the interpretation of trace gas measurements from ice cores.

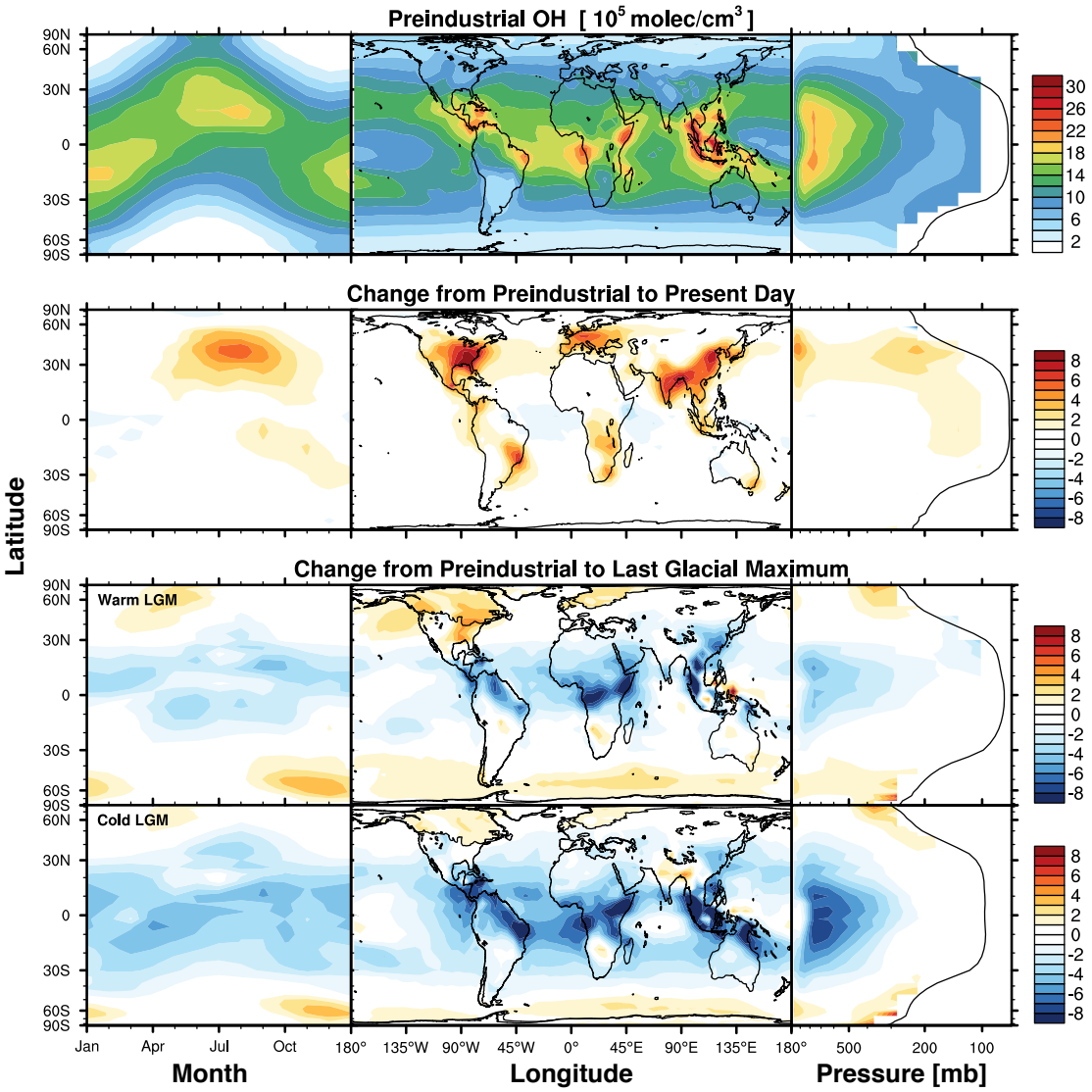

Figure 4.12: Spatiotemporal distribution of OH concentrations (10^5 molec cm^{-3}) in the preindustrial simulation (top row), and absolute changes in the present day (second row) and LGM (third and fourth rows) relative to the preindustrial. Each row contains three plots sharing a common ordinate axis (area-weighted latitude) and presents mass-weighted tropospheric OH concentrations averaged across different dimensions. From left to right, a Hovmöller plot shows seasonality in zonal mean column densities, a map shows the horizontal distribution of the tropospheric mean columns, and an altitude plot shows the zonal mean vertical distribution. Mean tropopause pressure is shown as the black line in the rightmost column. All difference plots share a common colorbar.

4.5.2 Tropospheric ozone

Like global mean OH, the tropospheric ozone burden decreases in each progressively colder scenario (Figure 4.8). Relative to the preindustrial, present-day ozone increases +24 ± 11%

(+31% best estimate), somewhat less than the mean change of +41 ± 9% from 1850 to 2000 in the ACCMIP ensemble [*Young et al*., 2013] or the +40-48% changes simulated by changing emissions in GEOS-Chem by *Sofen et al*. [2011] and *Parrella et al*. [2012]. Our more tempered response likely reflects the relatively high cross-tropopause flux of ozone in our model, and in the case of *Sofen et al*. [2011] and *Parrella et al*. [2012], our much higher fire emissions in the preindustrial. Our simulated changes of -12 ± 10% (-13% best estimate) in the LGM tropospheric ozone burden relative to the preindustrial are consistent with previous estimates (Table 4.1).

To understand these changes, we examine the ozone budget in each simulation (Figure 4.13). Photochemical production increases in the present day, relative to the preindustrial, but decreases in the two LGM scenarios in response to reductions in photolysis rates and in emissions of NO_x, CO and VOCs. Ozone production efficiencies (OPE) per molecule NO_x emitted [*Liu et al*., 1987], as shown in the middle panel of Figure 4.13, have decreased in the present day by 6% to 35%, and are nearly the same to 16% higher in the LGM relative to the preindustrial. Progressing through each successively colder climate scenario has a similar effect on OPE as increasing in altitude [*Sauvage et al*., 2007b] in that NO_x concentrations are lower and NO_x lifetimes are increased from reduced temperatures and decreased water vapor.

The cross-tropopause ozone flux decreases in each colder climate in response to the deceleration of the stratospheric circulation (Section 4.3.2) together with decreases in extratropical lower stratospheric ozone (Section 4.5.1 and Figure 4.11) where most stratosphere-to-troposphere transport occurs. Nonetheless, transport of ozone from the stratosphere becomes an increasingly important fraction of total ozone sources in each colder climate, increasing from 17% in the present-day to 32% in the cold LGM.

The bottom panel of Figure 4.13 gives the lifetime of tropospheric ozone in each simulation. Loss is primarily by photolysis in the presence of water vapor (i.e., primary production of OH), but also by reaction with HO_x radicals; both decrease in each cold climate as described in Section 4.5.1 and Section 4.5.3. The lifetimes of the present-day simulation driven by ModelE (23 d) is

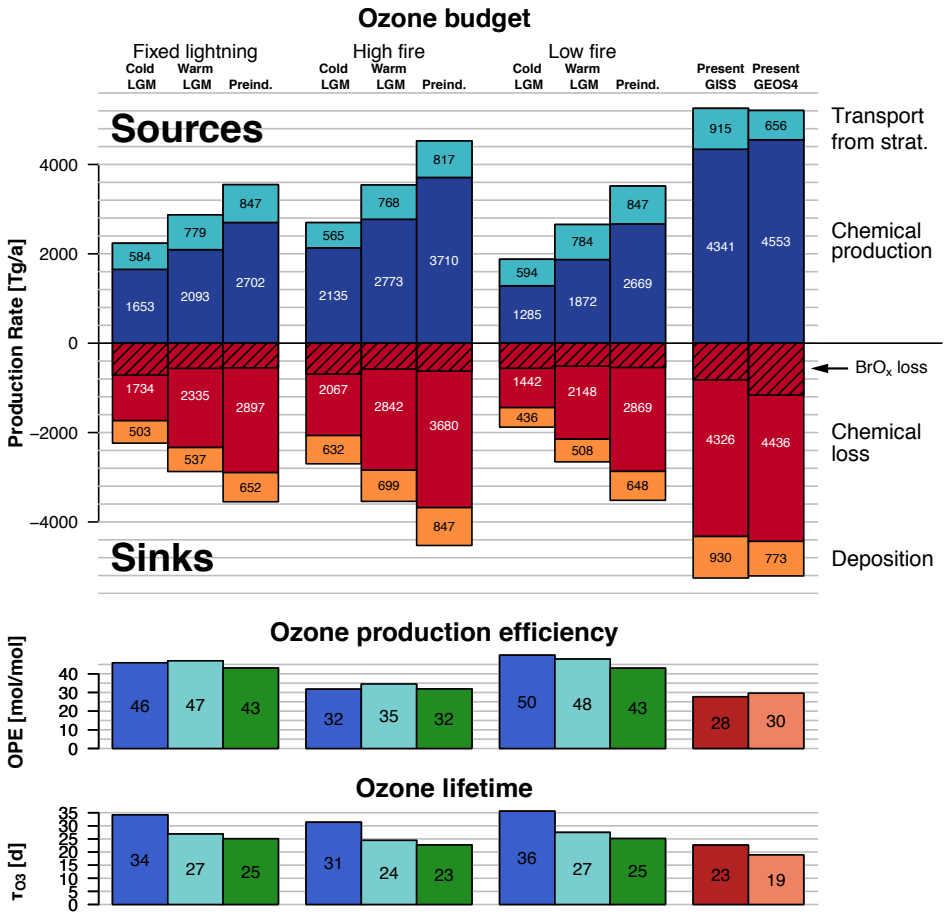

Figure 4.13: Top panel: Budget of tropospheric ozone in each simulation. Production and loss rates are for the odd oxygen family ($O_x \equiv O_3 + O + NO_2 + 2NO_3$ + organic nitrates + $HNO_4 + 3N_2O_5 + HNO_3$ + BrO + HOBr + $BrNO_2 + 2BrNO_3$). Transport from the stratosphere is inferred by mass balance in the troposphere with chemical production, loss and deposition. Tropopause calculated with thermal lapse rate definition. Diagonal hatching indicates net magnitude of ozone destroyed by $BrO + h\nu \longrightarrow O_3 + Br$ and $Br + O_3 \longrightarrow BrO + O_2$. Middle panel: O_x production efficiency per unit NO_x emitted. Bottom panel: Lifetime of tropospheric ozone against chemical loss and deposition.

comparable to that of the multi-model ensemble of *Stevenson et al*. [2006] (22 ± 2 d).

Bromine represents an increasingly important component (19-41%) of the total loss rates in each successively colder climate, as the net loss of ozone from the cycling of BrO_x radicals (shown as hatching in the top panel of Figure 4.13) remains relatively constant between simulations. This reflects the nearly constant emissions of Br_y. The depositional loss frequencies

decrease in each successively colder climate scenario reflecting decreases in LAIs and total vegetated area (despite the exposed continental margins), and to lesser extent, decreases in surface friction velocities.

The multi-model comparisons by *Stevenson et al*. [2006] and *Young et al*. [2013] show a tight linear relationship between ozone burdens and NO_x emissions. Our simulations extend the relationship of the tropospheric ozone burden with NO_x into the different climate and emission scenarios of the Last Glacial Maximum, with an almost identical slope to *Young et al*. [2013]. In the 10 simulations driven by ModelE meteorology, 96% of the variability in tropospheric ozone is explained by differences in NO_x emissions alone (O_3 = [172 Tg] + [3.0Tg/TgN] S_N), likely reflecting that the majority of the atmosphere is NO_x-limited [*Sillman et al*., 1990].

Figure 4.14 shows the changes in the temporal and spatial distribution of ozone relative to the preindustrial in our low fire simulations, which have similar patterns to the other emissions scenarios. In the preindustrial simulations, tropospheric ozone columns peak at the poles during their respective spring months due to transport from the stratosphere, consistent with *Mickley et al*. [2001]. In the present day, ozone increases everywhere due to anthropogenic precursor emissions, particularly in the northern midlatitudes. Extratropical ozone also increases in both hemispheres because of enhanced transport from the stratosphere, especially at the poles. Most of the LGM troposphere has reduced ozone relative to the preindustrial driven by the changes in climate and emissions. Greenland experiences local enhancements in stratospheric downwelling at the LGM, likely due to the presence of the Laurentide and Fennoscandian ice sheets [*Pausata et al*., 2011].

Despite inclusion of bromine chemistry, our simulated reduction in global ozone at the preindustrial is not sufficient to explain the low concentrations derived from surface air measurements taken in the late 19th century [e.g., *Pavelin et al*., 1999]. Reproduction of these low values remains a long-standing issue in the modeling of past changes in tropospheric ozone [*Wang and Jacob*, 1998; *Mickley et al*., 2001; *Shindell et al*., 2003; *Lamarque et al*., 2005; *Horowitz*, 2006; *Parrella et al*., 2012; *Young et al*., 2013].

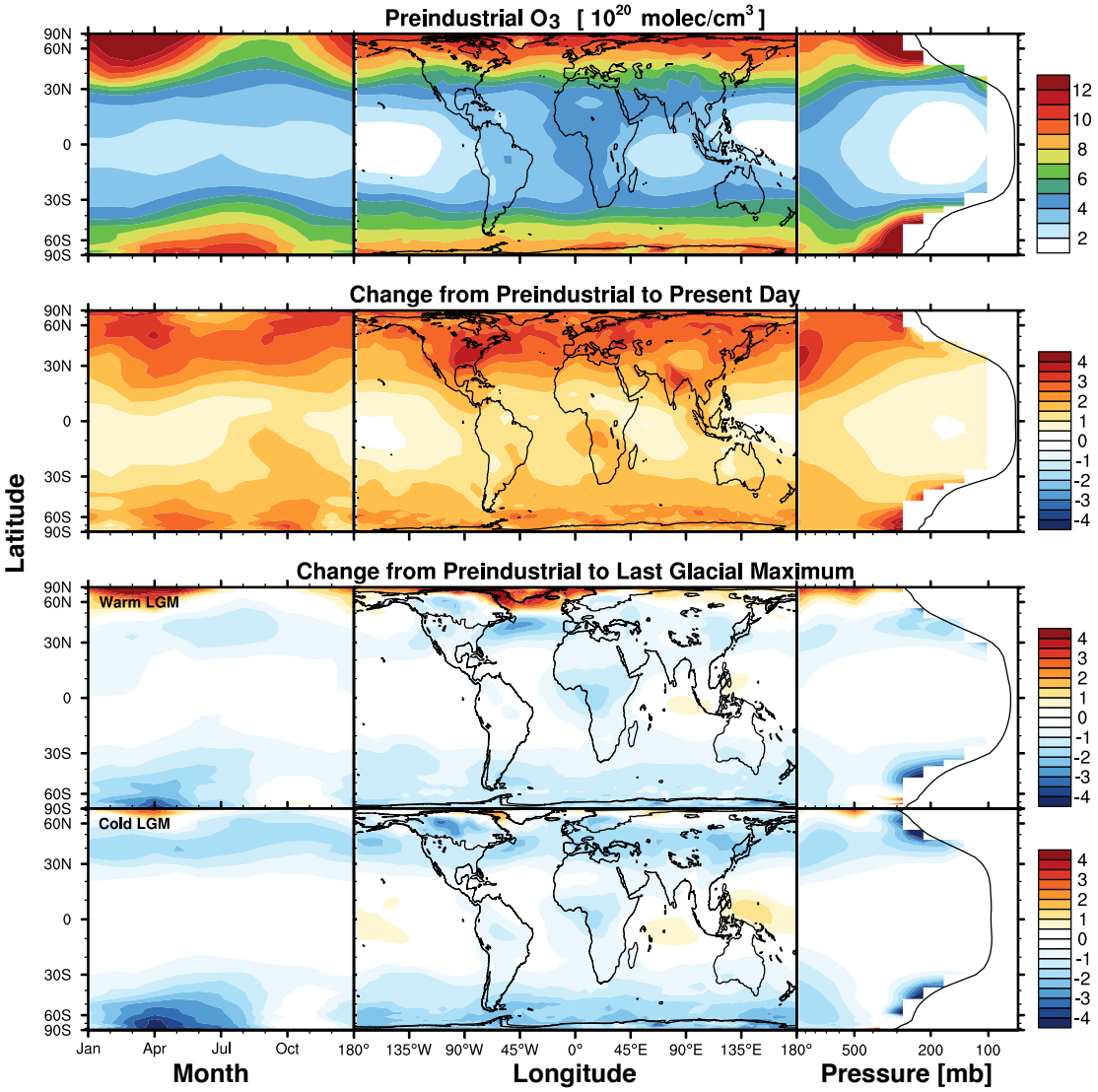

Figure 4.14: Same as Figure 4.12, but for tropospheric ozone concentrations (10^{20} molec cm^{-3}).

4.5.3 Hydrogen peroxide

H_2O_2 responds sensitively to different climates and emission scenarios (Figure 4.8), changing by +17 ± 22% in the present day and by -31 ± 23% at the LGM relative to the preindustrial (+30% and -22% best estimate). Its tropospheric budget is given in Table 4.6. H_2O_2 is both a reservoir species for HO_x and the dominant HO_x sink. The main loss mechanism for H_2O_2, and thus HO_x,

Table 4.6: Global sources, sinks, and lifetimes for tropospheric H_2O_2

Emissions	Fixed lightning			High fire			Low fire				
Climate	LGM		Preind.	LGM		Preind.	LGM		Preind.	Present	
	Cold	Warm		Cold	Warm		Cold	Warm		ModelE	GEOS4
Burden (Tmol)	0.04	0.06	0.08	0.06	0.08	0.11	0.04	0.06	0.08	0.10	0.12
Sources (Tmol a^{-1})											
Chemical production	11	17	23	17	24	33	10	17	23	32	33
Sinks (Tmol a^{-1})											
Chemical loss	6	10	14	10	14	19	6	10	14	19	22
Dry deposition	1	2	2	2	2	3	1	2	2	3	4
Wet deposition	3	5	8	5	8	11	3	5	8	10	7
Lifetime (hr)	31	29	29	33	30	29	33	30	29	28	32

is via uptake by cloud droplets and subsequent deposition. Despite reductions in precipitation in each successively colder climate that increase the H_2O_2 lifetime against deposition, we find that the decline in HO_x production in the colder climates (Section 4.5.1) governs the changes in H_2O_2. Our simulations indicate that H_2O_2, unlike OH, is very sensitive to changing fire emissions, with H_2O_2 levels in the high fire scenarios 40-70% greater than in the low fire scenarios. Fire emissions generate peroxy radicals (RO_2) and therefore can enhance total HO_x (although not OH, for reasons described in Section 4.5.1). The sensitivity of H_2O_2 to fire emissions but not to lightning make ice-core measurements of this molecule a potentially useful proxy for paleo fire abundance. H_2O_2 could also reflect changes in biogenic VOC emissions, as they also generate RO_2.

Figure 4.15 shows the spatiotemporal distribution of H_2O_2 and its changes in our low fire simulations. Production of H_2O_2 is greatest in the tropics, coincident with maximum production of OH, and therefore HO_x. However, the solubility of H_2O_2 causes high loss in the inter-tropical convergence zone, leading to the maxima in H_2O_2 concentrations in the subtropical lower free troposphere. At the LGM, precipitation increases in the subtropics and decreases in the tropics relative to the preindustrial in our simulations (Figure 4.3), but these changes are not enough to offset reductions in primary production, and H_2O_2 decreases almost everywhere. The exception is over Southeast Asia in the warm LGM, where enhanced reactive carbon emissions from biogenics and fires over the exposed continental shelves (Figure 4.7) promote RO_2 production. In the

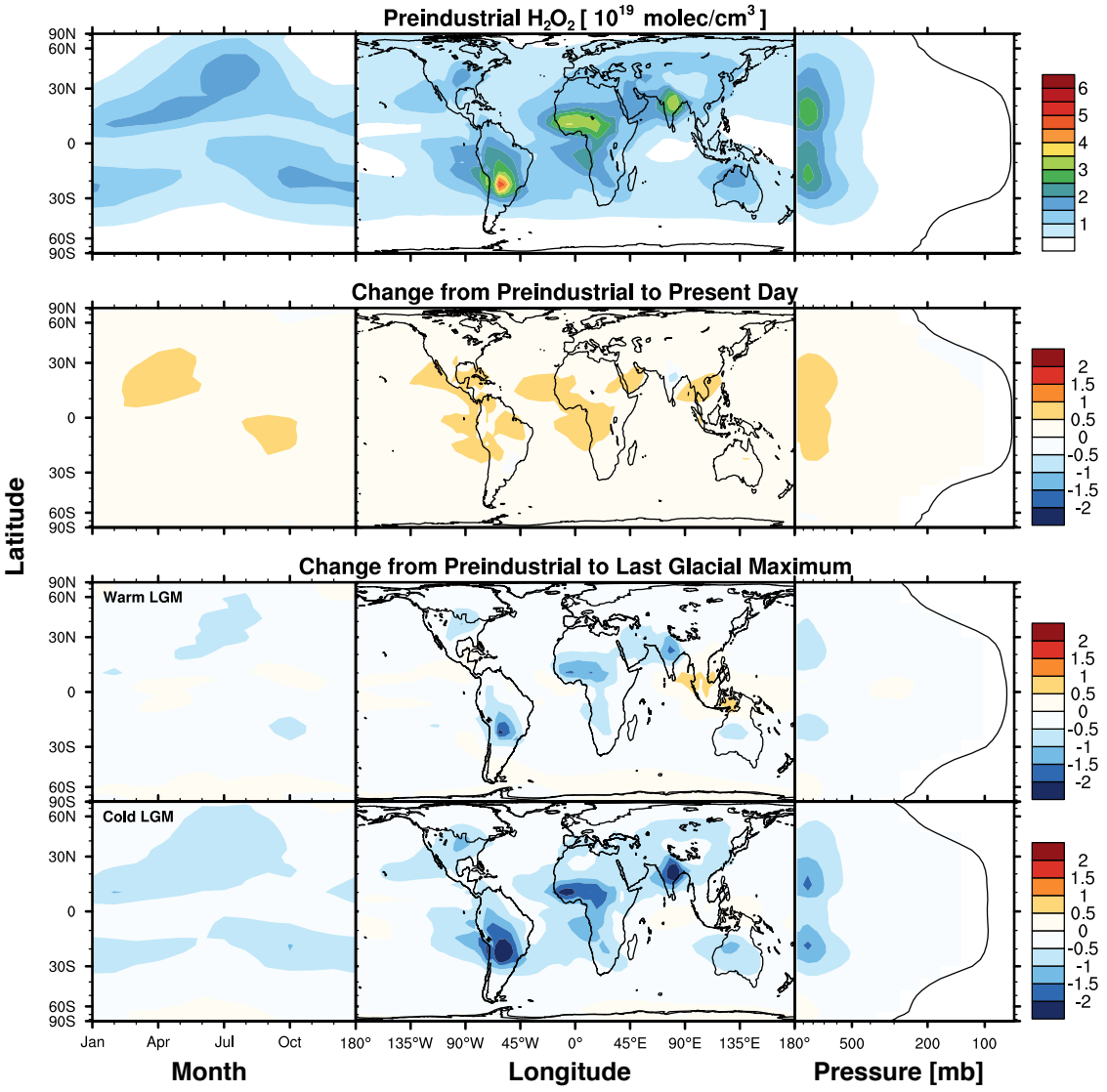

Figure 4.15: Same as Figure 4.12, but for H_2O_2 (10^{19} molec cm^{-3}).

present day relative to the low fire preindustrial scenario, H_2O_2 increases everywhere.

The overall decrease in H_2O_2 levels has implications for the oxidation pathways of SO_2, which is primarily oxidized to sulfate in the aqueous phase by H_2O_2 within cloud droplets. If a greater fraction of SO_2 is instead oxidized by OH in the gas phase, it would lead to additional particle formation with associated direct and indirect climate effects.

4.5.4 Nitrate radical

The chemistry of the nighttime troposphere is dominated by the nitrate radical (NO_3) [*Wayne et al.*, 1991]. In the absence of solar radiation, almost all NO_x is converted to NO_2, which may react with ozone to produce NO_3. The tropospheric burden changes by +130 $\pm$ 70 % at the present day and -42 $\pm$ 27 % at the LGM, relative to the preindustrial (+180% and -44% best estimate). The tropospheric burden of NO_3 (X_{NO_3}) in each of the 11 simulations shown in the bottom right panel of Figure 4.8 almost exactly follows the total source of reactive nitrogen ($\Delta X_{NO_3} = \Delta S_N \times 0.0140$ ppt/Tg N a^{-1}; $R^2 = 0.94$). How NO_3 changes in different climates is therefore sensitive to assumptions made about lightning, fire and soil emissions.

4.6 Comparison with ice-core record

Observations of reactive species in ice cores are limited for the preindustrial, and even more so for the LGM [*Wolff*, 2012], but offer our only constraints for past atmospheres. Comparison of our model simulations with the ice-core record is important for both evaluation of the model, and for interpretation of the observations, particularly for placing polar observations in the context of the entire troposphere. However, many reactive species are suspected or known to undergo post-depositional changes [e.g., *Hutterli et al.*, 2002, 2003; *Haan et al.*, 1996], which complicates interpretation.

Formaldehyde (HCHO) undergoes substantial post-depositional processing via evaporation followed by photolysis. The degree of post-depositional processing is strongly influenced by local temperature and the snow accumulation rate [*Hutterli et al.*, 2002, 2003]. The available HCHO data have not been corrected since that realization, though our simulations qualitatively match measurements from Greenland [*Staffelbach et al.*, 1991] and Antarctica [*Gillett et al.*, 2000], which indicate that HCHO was relatively stable through the past 1000 years and then increased in the 20th century following increases in VOC precursors (70% simulated vs. 100% observed

increases at Greenland; +40% vs. +40-100% at Antarctica). At the LGM, however, the Antarctic ice core indicates a 100% increase relative to the preindustrial, while we simulate 78-86% decreases in deposition fluxes. This discrepancy may be due to the expected increase in ice-core HCHO preserved at the very cold temperatures of the LGM [*Hutterli et al*., 2003].

The ratio of HCHO to methane in ice cores has been identified as a potential proxy for polar OH abundance, as production of HCHO in the remote atmosphere results primarily from methane oxidation [*Staffelbach et al*., 1991]. Given the large uncertainty in ice-core HCHO [*Hutterli et al*., 2002, 2003], it is unclear what to make of uncorrected HCHO/methane ratios. However, our simulations, like those of *Levine et al*. [2011b] show that this ratio at most offers local information, and only in the polar regions where methane is the dominant source of HCHO. Global tropospheric mean OH is strongly correlated with tropospheric mean ratio of HCHO/methane in the preindustrial and present-day simulations ($R^2 = 0.79$; $n = 5$ simulations). The relationship is weaker if we include the warm LGM ($R^2 = 0.56$; $n = 8$ simulations) and is uncorrelated if we include the cold LGM scenario. The erosion of the correlation between tropospheric mean OH and HCHO/methane over interglacial time scales may reflect variability in NMVOC precursors to HCHO, strong sensitivity of the CH_4^+OH reaction to temperature relative to other NMVOCs, changes in the meridional distribution of methane, and/or changes in photolysis loss frequency of HCHO.

Hydrogen peroxide is the only oxidant directly preserved in ice cores, but like HCHO it undergoes post-depositional processing that should be considered [*Hutterli et al*., 2003]. Ice cores from the West Antarctic Ice Sheet (WAIS) considered representative of surface air concentrations indicate H_2O_2 was relatively constant over the past 500 years, but has at least doubled since 1950 [*Frey et al*., 2006]; uncorrected data from Greenland cores also show a large 20th century increase [*Fuhrer et al*., 1993; *Anklin and Bales*, 1997]. Compared to our preindustrial low-fire scenario, deposition of H_2O_2 increases by 31% over Greenland in the present day, consistent with the ice-core record. However, although surface concentrations increase by 5% over the WAIS divide,

deposition shows no significant change due to decreases in precipitation in our model here. The preindustrial high fire simulation is inconsistent with the ice-core data, as it implies lower H_2O_2 surface concentrations and deposition everywhere in the present day relative to the preindustrial. For the LGM, uncorrected measurements from Law Dome in East Antarctica imply decreases in H_2O_2 relative to the preindustrial [*vanOmmen and Morgan*, 1996], generally matched by reduced deposition fluxes in our simulations despite enhanced surface concentrations. Surface concentrations over East Antarctica generally increase relative to the preindustrial in our various LGM simulations because of enhanced polar OH production (Section 4.5.1) and decreased precipitation (Section 4.3.2), with large variability reflecting the wide spread in the LGM fire emissions as HO_x precursors.

Our present-day simulation matches the mean CO concentration of 49 ppbv measured at the South Pole by NOAA CMDL for the 1990s, as well as the Southern Hemispheric gradient in CO. Carbon monoxide has been recorded in ice-core air bubbles over the past two millennia. *Wang et al*. [2010] measured ice-core concentrations of CO at the South Pole of 47 $\pm$ 4 ppbv for 1770. Our low fire preindustrial scenario yields 35 ppbv surface CO at the South Pole, consistent with *Wang et al*. [2010], given that as much as 10 ppbv of CO in Antarctic ice cores may derive from situ production [*Haan and Raynaud*, 1998]. Our high fire simulations yield much higher surface concentrations of 63 ppbv at the preindustrial, a value that is greater than any over the entire CO ice-core record at Antarctica.

Black carbon deposited in Greenland ice cores increased from 1850-1950 due to human industrial activity, but then declined to the 1800 values by the 1950s [*McConnell et al*., 2007]. Records of black carbon deposition to Antarctica for 1850-2000 imply mostly constant deposition rates [*Bisiaux et al*., 2012]. Squaring these records of black carbon deposition with our model results is challenging. Our high fire scenario for the preindustrial implies 40-50% decreases in black carbon deposition to both Greenland and Antarctica from the 1770s to the present day, not consistent with observations. Our low fire preindustrial scenario yields a better match with the

observations over Antarctica, with similar rates of deposition in the 1770s and the present-day. But this same scenario indicates large, 40-500% increases in black carbon deposited to Greenland in the present-day relative to the 1770s. Reconciling both the black carbon and CO ice-core records with current understanding of trends in biomass burning is a direction for future research.

Antarctic ice cores show increased sea salt aerosol deposition during cold periods, perhaps as a result of enhanced sea salt emission from frost flowers across the greater expanse of sea ice [*Wolff et al.*, 2010; *Wolff*, 2003; *Wolff et al.*, 2006; *Fischer et al.*, 2007; *Rothlisberger et al.*, 2008; *Röthlisberger et al.*, 2010]. GEOS-Chem assumes no source of sea salt from sea ice (Figure 4.6e) [*Jaeglé et al.*, 2011], and therefore predicts 70-90% decreases in sea salt deposition to Antarctica in the LGM climate relative to the preindustrial.

The $\Delta^{17}O$ of ice-core sulfate measures the departure from mass-dependent fractionation in its oxygen isotopes [*Thiemens*, 2006]. It provides a constraint for assessing the relative importance of different sulfate chemical production pathways — i.e., gas-phase oxidation by OH versus aqueous phase production via H_2O_2 or ozone, as the latter imparts a large $\Delta^{17}O$ signature [*Savarino et al.*, 2000]. Measurements from the Vostok ice core in Antarctica imply that gas-phase oxidation by OH contributed up to 40% more to sulfate production during the LGM relative to the interglacial periods that came before or after [*Alexander et al.*, 2002]. Our results appear consistent with these measurements of $\Delta^{17}O$ of sulfate. In our LGM scenarios, surface concentrations of OH at the poles increase driven primarily by the reduction in methane, CO, and overhead ozone, and increases in surface UV albedo. In addition, the fraction of SO_2 oxidized in the gas phase by OH increases throughout the LGM troposphere, reflecting a global decrease in aqueous-phase chemistry in the drier climate. An extensive interpretation of the measurements of $\Delta^{17}O$ of sulfate using an isotope aerosol chemistry version of the model, and determining the suitability of $\Delta^{17}O$ as proxy for oxidant variability (which has been recently questioned [*Levine et al.*, 2011b]), is the subject of a companion paper (E. Sofen, manuscript in preparation).

Unlike sulfate, nitrate aerosol undergoes substantial post-depositional photochemical

processing via evaporation of HNO_3 [*Rothlisberger et al.*, 2002] and photolysis to produce NO_x [*Honrath et al.*, 1999, 2000]. Photolysis of snow nitrate to produce NO_x it thought to be dominant [*Davis et al.*, 2008; *Erbland et al.*, 2012]. The degree of post-depositional processing depends mainly on snow accumulation rate. In East Antarctica where the snow accumulation rate is low, it is thought that all of the nitrate originally deposited to the snow is photolyzed to NO_x during austral spring and summer [*Erbland et al.*, 2012]. This NO_x is released to the boundary layer where it is re-oxidized locally and redeposited to the snow surface as nitrate. The $\Delta^{17}O$ signature in East Antarctic ice-core nitrate thus reflects the relative abundance of local atmospheric oxidants ozone and RO_2. At locations with higher snow accumulation rates such as Greenland and West Antarctica, the $\Delta^{17}O$ of nitrate may reflect a combination of the local summertime and ozone/RO_2 ratio and that ratio in the NO_x source regions. For the present day, our low fire simulations yield 10-20% decreases in the ozone/RO_2 ratio over Greenland and 20-30% decreases over the WAIS relative to the preindustrial, consistent with the expected sign change from ice-core measurements of $\Delta^{17}O$ of nitrate [*Alexander et al.*, 2004]. For the LGM, we calculate 35-65% increases in the ozone/RO_2 ratio over East Antarctica relative to the preindustrial, and up to a 50% increase over Greenland. Over Greenland, the increases result from increases in both tropospheric ozone from local enhanced stratospheric downwelling (Figure 4.14) and reductions in RO_2. Over Antarctica, ozone decreases in both LGM scenarios, so decreases in RO_2 largely dominate the response. Observations of nitrate $\Delta^{17}O$ in the LGM are not yet published, but are currently being collected.

4.7 Implications for the methane budget

Table 4.7 shows the methane lifetime against OH oxidation in the troposphere for each simulation, calculated as the integrated atmospheric burden (Tg) divided by the total loss rate in the troposphere (Tg a^{-1}). We determine the global methane burden from mean surface concentration using a conversion factor of 2.75 Tg $ppbv^{-1}$ for all simulations as in *Prather et al.* [2012]. We

Table 4.7: Global methane burden, and loss rate and lifetime (τ) against tropospheric oxidation by OH

Emissions	Fixed lightning			High fire			Low fire			Present Day		
Climate	Cold LGM	Warm LGM	Preind.	Cold LGM	Warm LGM	Preind.	Cold LGM	Warm LGM	Preind.	ModelE	GEOS4	Literature
CH_4 surface concentration [ppbv]	570		730	570		730	570		730	1740		1745[a]
CH_4 burden [Tg][b]	1570		2010	1570		2010	1570		2010	4790		4850[a]
Loss by OH in troposphere [Tg a^{-1}]	128	157	184	102	143	174	102	141	181	460	481	512[c]
OH, mass-weighted[d]	10.6	10.9	10.5	7.9	9.5	9.7	8.4	9.7	10.4	10.9	11.3	
OH, k_{CH_4+OH}-weighted[e]	12.6	13.2	12.3	10.0	12.0	11.6	10.1	11.8	12.1	12.7	13.0	
CH_4 τ against tropospheric OH [a]	12.2	10.0	10.9	15.4	11.0	11.5	15.4	11.1	11.1	10.4	9.9	$10.2^{+0.9}_{-0.7}$[f]

[a] *IPCC* [2001]. Global burden calculated with 2.78 Tg $ppbv^{-1}$.
[b] Global burden calculated from mean surface concentration using conversion factor of 2.75 Tg CH_4 $ppbv^{-1}$ [*Prather et al.*, 2012].
[c] *IPCC* [2007].
[d] Tropospheric mean OH, weighted by air mass.
[e] Tropospheric mean OH, weighted by $k_{CH_4+OH}(T)M_{CH_4}$, where $k_{CH_4+OH}(T)$ is the temperature-dependent rate coefficient for reaction of CH_4 with OH and M_{CH_4} is the mass of CH_4 in the grid box.
[f] *Prinn et al.* [2005], inferred from methyl chloroform observations.

find that the present-day methane lifetime in our simulations decreases by $9 \pm 3\%$, relative to the preindustrial. The lifetime in the warm LGM decreases by $5 \pm 5\%$, but increases by $27 \pm 14\%$ at the cold LGM. In our most likely representation of change across the glacial-interglacial period (low fire and warm LGM), the methane lifetime is the same at the LGM as in the preindustrial.

The lifetime of global methane against reaction with tropospheric OH reflects changes in both mean OH and the tropospheric distribution of methane, as well as the strong temperature kinetic effect on the reaction rate constant (2.4% K^{-1} at 273K) [*Lawrence et al.*, 2001; *Sander et al.*, 2011; *John et al.*, 2012]. The temperature changes alone would cause the methane lifetime to increase by 6.5% and 19% in the warm and cold LGM scenarios relative to the preindustrial, and decrease by 1.4% at the present day. The kinetic effect is then offset or enhanced by changes in OH responding to the factors as outlined in Section 4.5.1, convolved with changes in the methane distribution. For the present day, the kinetic effect is augmented by the increase in global mean OH, and the lifetime decreases relative to the preindustrial. In the warm LGM, both temperature and global mean OH decrease relative to the preindustrial, but the fraction of methane located

within 30° of the equator (where most OH is located) increases by 33%. The methane lifetime therefore remains either nearly constant or actually decreases. In the cold LGM, however, the greater OH changes and especially the temperature kinetic effect guarantee that the methane lifetime increases relative to the preindustrial.

That the methane lifetime remains nearly constant or increases at the LGM in most of our simulations puts a higher burden on sources in explaining the ice-core methane glacial-interglacial record. And the few simulations in which the methane lifetime decreased at the LGM did so in spite of global mass-weighted mean OH, as a result of the shifting meridional distribution. In their model study, which did not include a paleo-stratosphere, *Levine et al*. [2011a] concluded that the effects of temperature and biogenic VOCs cancel out each other such that observed changes in ice-core methane must be driven primarily by sources. Our findings confirm those of *Levine et al*. [2011a], and imply that even when changes in overhead ozone, tropospheric water vapor, and lightning NO_x reduce OH concentrations, the global methane burden can still decrease as a result of changing wetlands emissions and the shifting source distribution..

Assuming no large changes occurred in the minor loss mechanisms for methane (soils and stratospheric OH [*IPCC*, 2007]), the source of methane emissions scales as its loss by OH in the troposphere (Table 4.7 and Figure 4.9). We estimate the methane loss frequency in the stratosphere to change by less than 1% since the LGM in our simulations; the effect of reduced stratospheric water vapor at the LGM is largely offset by temperature increases. Our simulations therefore imply that relative to the preindustrial, total methane emissions are 170% higher in the present, and were reduced by 10-40% at the LGM, with a 22% reduction our best estimate. These estimated reductions at the LGM are consistent with the 29-42% decrease in wetland emissions simulated by the PMIP2 ensemble members [*Weber et al*., 2010], as well as the 16% and 23% decreases in natural methane emissions simulated by *Kaplan et al*. [2006] and *Valdes et al*. [2005] over the same period.

4.8 Conclusions

We present a step-wise, offline-coupled modeling framework for simulating paleo-oxidant levels since the Last Glacial Maximum. Our goal is to test within a 3D model framework the sensitivity of tropospheric oxidants over a range of likely forcings from climate-driven and anthropogenic changes. Archived meteorology from the GISS ModelE GCM is used to drive the BIOME4-TG global equilibrium terrestrial vegetation model and the LMfire fire model. We also apply the ModelE meteorology to the GEOS-Chem CTM, together with the BIOME4-TG vegetation structure and LM fire emissions. We then perform detailed simulations of tropospheric composition with an online-coupled linearized stratospheric chemistry scheme.

We simulate four different time slices with the GCM: the present day (ca. 1990s), preindustrial (ca. 1770s), and two possible realizations of the Last Glacial Maximum (LGM; 21ka), one significantly colder than the other reflecting uncertainty in the extent of tropical cooling at the LGM. The climate simulations are forced by prescribing greenhouse gas levels, orbital parameters, SSTs, sea ice extent, and ice sheet topography. Reductions in greenhouse gases drive decreases in tropospheric temperatures and water vapor, and decelerate the stratospheric residual circulation, consistent with earlier work [*Braconnot et al.*, 2007a; *Bartlein et al.*, 2011b; *Rind et al.*, 2009]. Tropical surface air temperatures change by -1.4°C in the warm LGM scenario and by -6.8°C in the cold LGM scenario relative to the preindustrial; the preindustrial to present-day change is +0.5°C. Reduced stratospheric circulation leads to an increase in tropical stratospheric ozone columns, which strongly affect tropospheric photolysis rates.

Tropospheric emissions respond to climate, and we simulate reductions in most trace gas emissions in cooler climates. Terrestrial plant VOC emissions are influenced by both land cover and meteorology, however, and decrease in the present day relative to the preindustrial because of expansions in cropland. In the LGM, the cooler temperatures ultimately drive decreases in plant VOC emissions. Soil microbial emissions of NO_x decrease with reduced temperatures and

precipitation fluxes at the LGM. Lightning responds with vertical extent of deep convection, and therefore decreases at the LGM, especially in the cold LGM scenario. We also test a scenario in which we fix total lightning emissions. Estimates of fire emissions in past atmospheres are highly uncertain; we test the extremes in the range of estimates at the LGM (10% and 200% of present) and the preindustrial (100% and 320% of present), using distributions of dry matter burned from the LMfire model.

We find net reductions in all oxidants in past atmospheres relative to the present day, except for H_2O_2 in the high fire preindustrial simulation. OH is relatively well-buffered in comparison with the other oxidants. It is relatively insensitive to changes in anthropogenic and fire emissions, but sensitive to lightning trends. In our simulations, OH increases at the present day by $+7.0 \pm 4.3\%$, and OH likely decreases at the LGM by $6.7 \pm 11\%$, both relative to the preindustrial. A linear relationship with $J_{O_3} q S_N/(S_C^{3/2})$ explains 67% of the total variability seen in the mean OH burdens of our 11 simulations. J_{O_3} and q largely regulate primary production of HO_x, whereas $S_N/(S_C^{3/2})$ largely influences HO_x partitioning between OH and RO_2 (but also primary production). Most previous studies lacked realistic paleo-stratospheres and simulated increases in OH at the LGM (cf. Table 4.1). Our work suggests that increased OH during the LGM is unlikely. Only a significant increase in LGM lightning emissions of NO_x could enhance OH in this time period. Of the various emission sources, lightning is most capable of perturbing $S_N/(S_C^{3/2})$, as it makes up a relatively large fraction of S_N ($37 \pm 16\%$ of S_N in past atmospheres; 14% in the present day), and $S_N \ll S_C$. Unlike anthropogenic or fire emissions, NO_x from lightning also lacks any co-emissions of reactive carbon, and it is uncorrelated with a competing emission source, as soil NO_x emissions are with those of biogenic VOCs. Therefore, we conclude that the three factors OH is most sensitive on glacial-interglacial time scales are overhead ozone, tropospheric water vapor, and lightning emissions. These factors should be given particular attention in future studies.

Ozone in our simulations increases from the preindustrial to the present by $24 \pm 11\%$, and decreases by $12 \pm 10\%$ to the LGM. Our changes are consistent with prior studies but more

tempered, likely reflecting the high bias in the source of ozone transported from the stratosphere. That source decreases in magnitude in the colder climates following the deceleration of the stratospheric circulation, but nevertheless becomes an increasingly large fraction of the total source. We extend to LGM conditions the finding that global mean ozone from 1850 through 2100 depends strongly on S_N [*Stevenson et al.*, 2006; *Young et al.*, 2013]. Ozone production efficiencies per unit NO_x emitted increase in each successively colder atmosphere.

H_2O_2 responds to changes in both climate and emissions, varying more strongly in its production pathways across the different scenarios than in its loss rates via wet deposition. We find that H_2O_2 abundance is very sensitive to fire emissions, as these emissions generate HO_x. Ice-core H_2O_2 may therefore act as a useful proxy for paleo fire emissions as well as for biogenic emissions, another HO_x source. Nitrate radical is directly related to the total source of reactive nitrogen, S_N ($R^2 = 0.94$).

Our simulations are broadly consistent with ice-core records of $\Delta^{17}O$ in sulfate and nitrate at the LGM, and CO, HCHO, black carbon, and H_2O_2 in the preindustrial. Comparison with black carbon, CO and H_2O_2 preserved in ice cores indicate that fire emissions during the preindustrial and LGM likely fall closer to the lower end of the estimated range. Our simulations indicate that the HCHO/methane ratio cannot serve as a proxy for global OH variability.

Prior studies have disagreed as to the relative role of sources versus sinks in explaining the large glacial-interglacial variability in atmospheric methane concentrations recorded in ice cores. We simulate nearly constant or increased methane lifetimes at the LGM relative to the preindustrial, implying that the large glacial-interglacial variability seen in ice-core methane is predominantly driven by changing methane sources. If the fraction of the methane burden contained in the tropics increases at the LGM as implied by ice cores, the reduced oxidative capacity at the LGM that we calculate here is nonetheless consistent with the smaller tropospheric methane burden. Unlike previous studies [e.g., *Kaplan et al.*, 2006; *Valdes et al.*, 2005], we do not need to invoke a greater oxidation capacity at the LGM to reconcile the ice-core methane record

with bottom-up estimates of wetland emissions.

Appendices

Appendix A

Definition of global mean OH

Mean hydroxyl radical concentrations $\overline{[OH]}$ are determined from models by integrating OH concentrations over a domain of interest and weighting by some averaging kernel, W.

$$\overline{[OH]} = \Sigma(W\overline{[OH]})/\Sigma W \tag{A.1}$$

The definition and physical interpretation of $\overline{[OH]}$ is therefore sensitive to the selection of the weighting factor [*Prather and Spivakovsky*, 1990; *Lawrence et al.*, 2001]. Comparison of model output to $\overline{[OH]}$ inferred from methyl chloroform (MCF) observations requires that the weighting factor $W = k_{OH+MCF}X_{MCF}M$, where k_{OH+MCF} is the rate constant for reaction of OH with MCF, X_{MCF} is the molar mixing ratio of MCF, and M is the air mass in a grid box. This rate constant k_{OH+MCF} has a strong temperature dependence (2.1% K^{-1} at 273K) [*Sander et al.*, 2011]. Thus $\overline{[OH]}$ inferred from changes in the MCF burden will intrinsically reflect OH weighted by this rate constant and the mass of MCF in a grid cell, which we refer to as $\overline{[OH]}_{MCF}$. It is standard to assume that MCF is uniformly mixed in the troposphere and therefore X_{MCF} drops out of the calculation.

Montzka et al. [2011] inferred IAV in $\overline{[OH]}_{MCF}$ using a global mass balance approach, equating the rate of change in the global MCF burden (G), dG/dt to the difference between its global emissions rate E and its loss rate k^1G, where k^1 is the temperature dependent pseudo-first order rate constant for oxidation. Thus

$$dG/dt = E - k^1 G \tag{A.2}$$

Percent anomalies were then calculated for k^1, as a proxy for $\overline{[OH]}_{MCF}$. They inferred G from surface flask measurements of MCF, and approximated the differential by finite differencing over twelve month intervals. They showed their results to be insensitive to assumptions about E since 1997. Their use of k^1 as a proxy for $\overline{[OH]}_{MCF}$ is equivalent to using $W = k_{OH^+MCF}M$ in the numerator of equation A.1 and assuming that the denominator, which contributes little to total variability, is constant.

To compare our model simulations to their $\overline{[OH]}_{MCF}$, we directly calculate monthly anomaly time series of the mass-weighted tropospheric mean k^1 values for MCF in each simulation, and apply a 12 month smoothing filter to be consistent with the inherent smoothing of the finite differencing approach. *Montzka et al*. [2011] assigned the results of their finite differencing to the first month; we shift their flask time series six months forward to assign it to the midpoint. The reference period over which monthly anomalies were determined from the flask data is slightly longer (1997-2007) than our period (1998-2006).

Except for the comparison to the results of *Montzka et al*. [2011], we report anomalies determined from integrating monthly mean tropospheric OH concentrations weighted by the air mass, M, in each grid cell, which we denote $\overline{[OH]}_{mass}$. This value is linearly proportional to the global oxidizing efficiency of a uniformly distributed gas with no temperature or pressure dependence in its reaction with OH.

Appendix B

Evaluation of present-day ICECAP simulation

B.1 Description of simulations used for evaluation

Chapter 4 introduces the model framework for ICE age Chemistry And Proxies (ICECAP), a project focused on paleo-chemistry at and since the Last Glacial Maximum. The framework includes the GEOS-Chem 3D global chemical transport model (CTM; http://www.geos-chem.org), driven by archived meteorology from the NASA Goddard Institute for Space Sciences (GISS) ModelE general circulation model (GCM). Here we evaluate the performance of the present-day ModelE-driven simulation versus a standard suite of observations used to test chemical and physical processes (e.g., transport, convection, and wet deposition). We also compare our results with state-of-the-science GEOS-Chem simulations driven by two different assimilated meteorological products from the Goddard Earth Observing System (GEOS) of the NASA Global Modeling and Assimilation Office. The GEOS4 product consists of 6 h means for most fields and 3 h means for surface fields, with a horizontal resolution of 1° latitude by 1.25° longitude and with 55 layers in the vertical. The GEOS5 product (version 5.1.0) has the same temporal resolution as GEOS4 and a horizontal resolution of 0.5° latitude by 0.667° longitude with 72 layers in the vertical. For this evaluation, the GEOS4 and GEOS5 products are upscaled to 4° latitude by 5° longitude, and to 30 and 47 vertical layers, respectively.

B.1.1 SF_6 simulation

Sulfur hexafluoride (SF_6) is a trace gas of industrial origin that is chemically and physically inert on human time scales, with an atmospheric lifetime of 3200 years [*Maiss and Brenninkmeijer*, 1998]. It is emitted primarily over industrialized regions of the northern hemisphere, and its meridional gradient is a useful test for meridional mixing [*Rigby et al.*, 2010; *Hall et al.*, 2011]. It is also used with other long-lived gases to infer mean age of air in the stratosphere [*Waugh and Hall*, 2002]. We perform three 43-year simulations of SF_6 in GEOS-Chem, each using a single year of present-day ModelE, GEOS4 (1993), and GEOS5 (2005) meteorology and emissions from the Emissions Database for Global Atmospheric Research (EDGAR) version 4.0 (http://edgar.jrc.ec.europa.eu, 2009) for 1970-2012.

B.1.2 Radionuclide simulation

Radon-222, lead-210, and beryllium-7 comprise the standard set of radionuclides used for evaluation of global atmospheric chemistry and climate models.

Terrigenic ^{222}Rn is an inert, insoluble, short-lived (half-life 3.8 d) noble gas produced from the slow decay of ^{226}Ra (half-life 1600 a) found in uranium ores. Its evasion from surface soils is relatively uniform and constant, but reduced when the surface is frozen. Its insolubility and time scale of decay make it a useful tracer for diagnosing quick vertical mixing within atmospheric models from moist convection and boundary layer mixing and ventilation [e.g., *Allen et al.*, 1996; *Brost and Chatfield*, 1989; *Considine et al.*, 2005; *Feichter and Crutzen*, 1990; *Hauglustaine et al.*, 2004; *Jacob*, 1990; *Jacob et al.*, 1997; *Lambert et al.*, 1982; *Mahowald et al.*, 1995; *Stockwell et al.*, 1998].

Radiogenic ^{210}Pb is the chemically-inert decay daughter of ^{222}Rn. It is readily taken up by submicron aerosol particles and subsequently removed from the atmosphere by deposition or decay [*Bondietti et al.*, 1988; *Maenhaut et al.*, 1979; *Preiss et al.*, 1996; *Sanak et al.*, 1981].

Table B.1: Global budgets of radionuclides in GEOS-Chem simulations using different meteorology [a]

		GEOS4	GEOS5	ModelE
Rn-222				
Global Burden, g		193	192	188
Troposphere		193 (99.8%)	192 (99.8%)	188 (100.%)
Stratosphere		0.43 (0.2%)	0.45 (0.2%)	0.02 (0.0%)
Tropospheric residence time, d		5.5	5.5	5.5
Sources, g d^{-1}		35	35	34
Sinks, g d^{-1}		35	35	34
Pb-210				
Global Burden, g		323	383	257
Troposphere		285 (88%)	322 (84%)	216 (84%)
Stratosphere		38 (12%)	61 (16%)	41 (16%)
Tropospheric residence time, d		8.6	9.7	6.7
Sources, g d^{-1}		33	33	32
Sinks, g d^{-1}		33	33	32
Radioactive Decay	Tropospheric	0.02 (0%)	0.03 (0%)	0.02 (0%)
	Stratospheric	0 (0%)	0.01 (0%)	0 (0%)
Dry Deposition		4 (11%)	3 (11%)	2 (7%)
Wet Deposition	Stratiform	10 (30%)	10 (31%)	12 (36%)
	Convective	20 (59%)	19 (59%)	18 (56%)
Be-7				
Global Burden, g		16	16	15
Troposphere		3.8 (25%)	4.4 (27%)	5.5 (36%)
Stratosphere		11.7 (75%)	12 (73%)	9.6 (64%)
Tropospheric residence time, d		21.1	24.8	25.7
Sources, g d^{-1}		0.33	0.33	0.33
Cosmogenic	Tropospheric	0.14 (41%)	0.13 (40%)	0.15 (44%)
	Stratospheric	0.2 (59%)	0.2 (60%)	0.19 (56%)
Sinks, g d^{-1}		0.33	0.33	0.34
Radioactive Decay	Tropospheric	0.05 (15%)	0.06 (17%)	0.07 (21%)
	Stratospheric	0.15 (46%)	0.16 (47%)	0.13 (37%)
Dry Deposition		0.01 (3%)	0.01 (3%)	0 (1%)
Wet Deposition	Stratiform	0.04 (12%)	0.04 (11%)	0.04 (12%)
	Convective	0.08 (24%)	0.07 (22%)	0.1 (29%)

[a] Parentheses give percentage of total global burden, source, or sink

Because of its relatively long lifetime (half-life 22.2 a), nearly all ^{210}Pb is removed via deposition. As its source from ^{222}Rn is relatively well known and there exists a global and long-term surface deposition flux and concentration inventory [*Preiss et al.*, 1996], it is the standard test for modeled wet deposition. The source of ^{210}Pb is evaluated in Section B.2.3.

Cosmogenic ^{7}Be is produced by the cosmic ray spallation of N_2 and O_2, predominantly in the

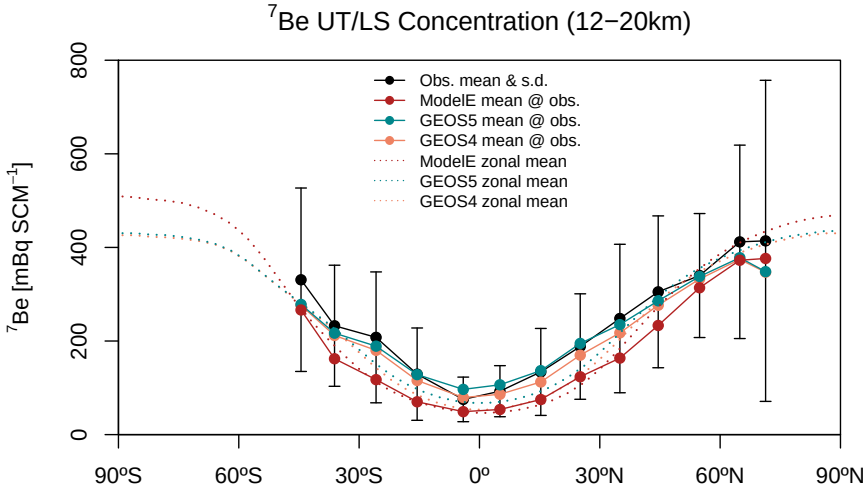

Figure B.1: Comparison of model ^{7}Be source parameterization with UT/LS aircraft observations from the DOE RAdioNuclide DAtaBase (RANDAB) from 1957-1983. The data are from the Oak Ridge National Laboratory Carbon Dioxide Information Analysis Center (http://cdiac.ornl.gov/; doi: 10.3334/CDIAC/atg.db1019) and have been linearly adjusted for solar activity using *Usoskin et al.* [2005].

polar upper troposphere and lower stratosphere (UT/LS) [*Lal et al.*, 1958]. Like ^{210}Pb, it is rapidly taken up by submicron aerosol particles [*Bondietti et al.*, 1988; *Maenhaut et al.*, 1979; *Papastefanou*, 2009; *Papastefanou and Ioannidou*, 1996; *Sanak et al.*, 1981]. It is subsequently transported until removal by rainout or surface deposition in the troposphere, or by radioactive decay (half-life 53.3 d). ^{7}Be has been used to constrain vertical transport, wet deposition fluxes, and stratosphere-troposphere exchange (STE) in models [e.g., *Allen et al.*, 2003; *Brost et al.*, 1991; *Koch et al.*, 1996; *Liu et al.*, 2001, in review; *Barrett et al.*, 2012].

Table B.1 gives the atmospheric budget of simulations in GEOS-Chem of these three radionuclides driven by meteorology from ModelE (4 years of present-day meteorology), and the GEOS4 (2004-2006) and GEOS5 (2004-2006) assimilated products. Emissions of ^{222}Rn within GEOS-Chem are those of *Jacob et al.* [1997]. We simulate the source of ^{7}Be using the parameterization of *Usoskin and Kovaltsov* [2008] for mean solar activity, which leads to an average production of 0.064 atoms cm^{-2} s^{-1}; about 60% in the stratosphere and 40% in the

troposphere. Figure B.1 evaluates the source of ^{7}Be in the model by showing concentrations of UT/LS ^{7}Be in the model versus aircraft observations for 1957-1983 from the Department of Energy RAdioNuclide DAtaBase (RANDAB). The model distributions match those of the RANDAB dataset (R^2 = 0.48-0.53). In the the region of greatest production, the extratropical lower stratosphere, the models are all biased low by 10-13% relative to the observations, although well within the range of observed variability.

B.1.3 Full chemistry simulation

We also analyze the present-day ozone-NO_x-CO-VOC-BrO_x-aerosol simulation as described in the main text driven by ModelE (using three years of 1990s meteorology) and GEOS4 meteorology (1994-1996). Both simulations have identical anthropogenic emissions. We use identical treatment of natural emissions, and modify the standard GEOS4 simulation to be consistent with the ModelE-driven simulation (e.g., lightning uses a global NO_x yield per flash, and is not constrained to satellite observations). Total emissions and their distribution therefore differ with the different meteorology.

B.2 Evaluation

B.2.1 Horizontal Mixing

Figure B.2 shows the observed meridional gradient of SF_6 in monthly mean flask samples of surface air from NOAA, relative to the concentration at American Samoa (SMO) in the remote tropical southern Pacific. Also shown is each simulation sampled as in the observations, and the zonal mean gradient. In all simulations, GEOS-Chem overestimates the meridional gradient in SF_6 by 60-100%. This suggests that the inter-hemispheric mixing rate in the model is too slow, and/or that the EDGAR inventory overestimates the emissions growth rate in the northern hemisphere relative to the southern hemisphere. However, the difference between the ModelE

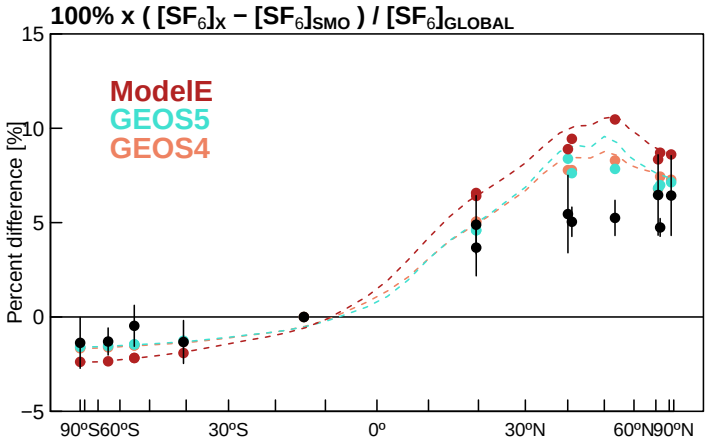

Figure B.2: Meridional gradient of SF_6 in flask samples for 1995-2005 at 13 flask sites in the NOAA Earth System Research Laboratory (ESRL) Global Monitoring Division (GMD; http://www.esrl.noaa.gov/gmd). All values are shown as percent differences relative to American Samoa (SMO). Vertical bars show the standard deviation in the observations. Also shown are the values from the CTM driven by different meteorology products, sampled at the observations (filled circles), and the zonal mean (dashed lines).

and GEOS simulations with identical emissions indicates that GEOS-Chem driven by ModelE has about a 25% slower rate of meridional mixing than by the GEOS simulations.

B.2.2 Vertical Mixing

Troposphere

We assess vertical mixing within the troposphere using vertical profiles of ^{222}Rn, and ratios of $^{7}Be/^{210}Pb$ in surface air.

Figure B.3 shows simulated climatological ^{222}Rn profiles sampled at the month and location of available observations, also plotted. Observations are scarce and available only at northern extratropical continental locations. In an overly-convective atmosphere, the vertical gradient of ^{222}Rn would disappear. In all of our simulations, there is a slight overestimate within the boundary layer and underestimate above, implying a small underestimate in boundary layer ventilation. Our results are comparable to or better than other CTMs/GCMs [e.g., *Considine et al.*, 2005]. All three simulations represent the climatological median of the measurements well, especially above

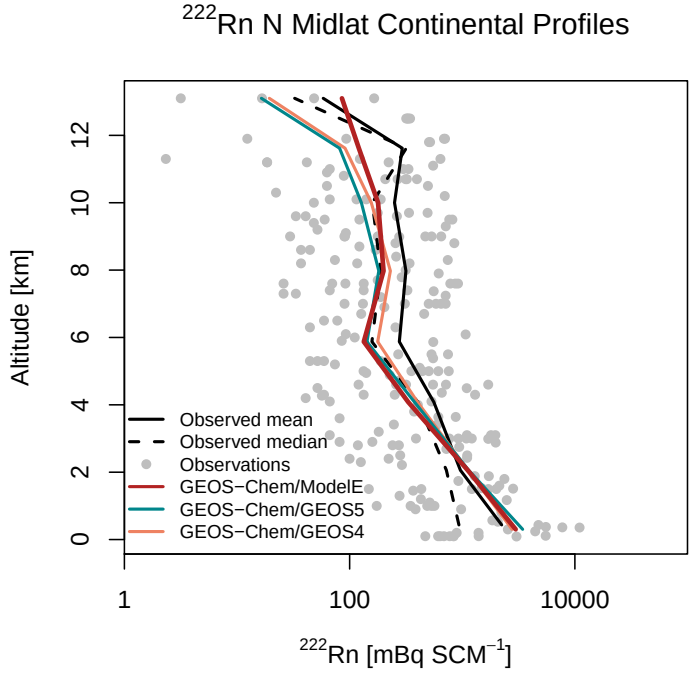

Figure B.3: Mean observed vertical profile of ^{222}Rn compared with GEOS-Chem sampled at month and location of observations [*Bradley and Pearson*, 1970; *Nazarov et al*., 1970; *Wilkening*, 1970; *Moore et al*., 1973; *Kritz et al*., 1998]. The units are mBq per standard cubic meter at 0°C and 1 atm, calculated with a linear transformation of the molar mixing ratio (5.637 mBq SCM^{-1} = 1.0 $\times 10^{-22}$ mol ^{222}Rn / mol air).

the boundary layer. ModelE reproduces the ^{222}Rn distribution the best of the three models (ModelE R^2 = 0.46; GEOS5 = 0.34; GEOS4 = 0.42), particularly in the upper troposphere.

Figure B.4 shows the annual mean surface concentration of ^{7}Be simulated with mean solar activity, surface ^{210}Pb, and their ratio. Given the difference in the source regions for the two molecules, and that the ratio of ^{7}Be/^{210}Pb is unaffected by deposition, the ratio serves as a useful measure of vertical mixing in the troposphere [*Koch et al*., 1996]. A persistent high bias would indicate excessive downward transport and/or insufficient upward transport, assuming no bias in either source. The filled circles represent measurements from surface monitoring stations of the DOE Environmental Measurements Laboratory (EML) Surface Air Sampling Program (SASP) (http://www.nbl.doe.gov/htm/EML_Legacy_Website/). SASP recorded the spatial and temporal

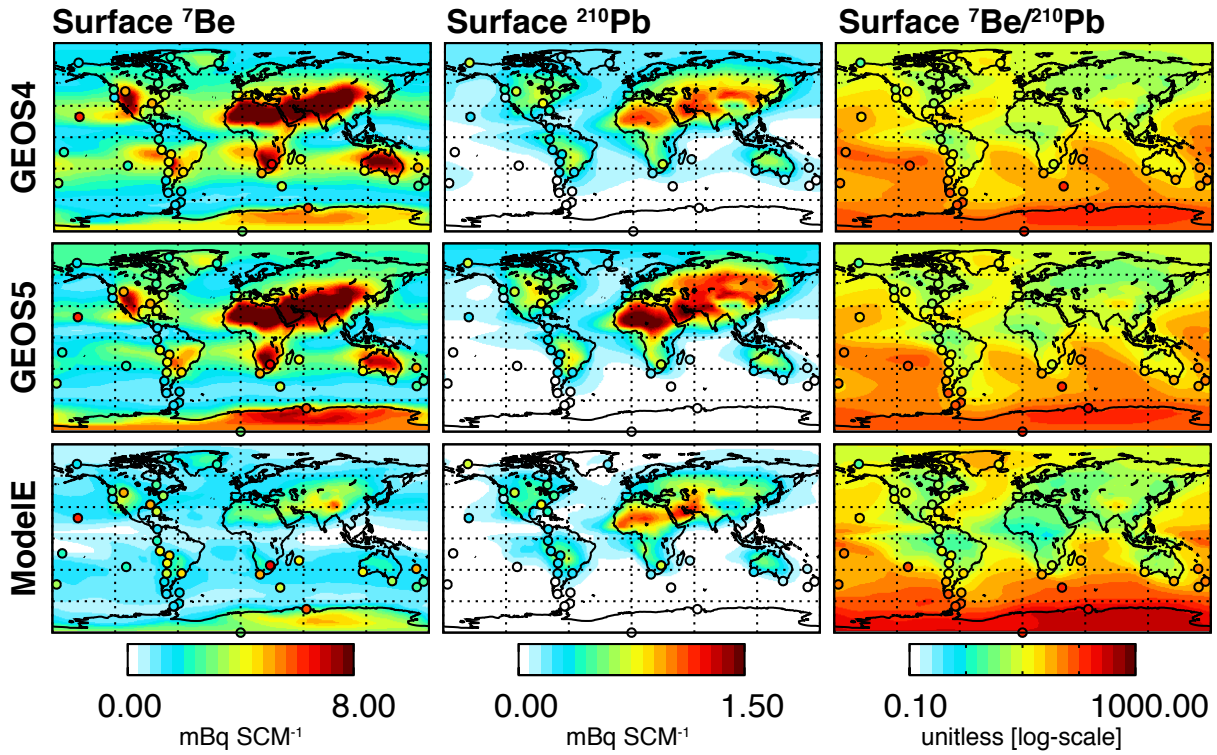

Figure B.4: Mean GEOS-Chem surface concentrations of ^{7}Be (left column) and ^{210}Pb (center column), and the ^{7}Be/^{210}Pb ratio (right column). Filled circles show the long-term mean observations from the DOE SASP network. The ^{7}Be observations have been selected for periods of average solar activity.

distribution of various radionuclides in surface ambient air from 1957 until 1999, including ^{7}Be and ^{210}Pb. For comparison with our simulations, we select data from periods of average solar activity (solar modulation potential $\Phi = 670 \pm 50$ MV from the *Usoskin et al.* [2005] reconstruction). Surface concentrations of both ^{7}Be and ^{210}Pb are lower in the ModelE simulation, consistent with the shorter lifetime against deposition. The ^{7}Be/^{210}Pb ratio is higher in the polar regions and lower in the tropics than in the GEOS simulations, which imply less tropical mixing and more polar vertical mixing in the ModelE simulations.

Stratosphere

Figure B.5 shows the simulated zonal distributions of the annual mean age of air in the stratosphere, which is defined as the mean time since air at a particular point in the stratosphere

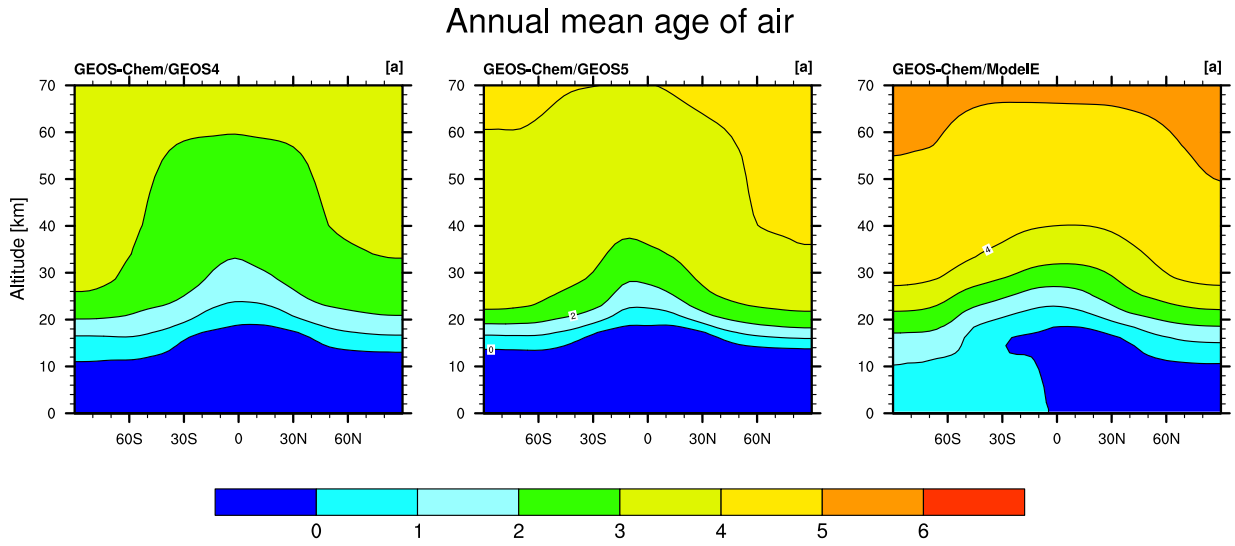

Figure B.5: Average age of air in the stratosphere in GEOS-Chem simulations driven by GEOS4, GEOS5 and GISS ModelE, using as a chronological tracer the temporal lag in the simulated 1995-2012 time series of SF_6 relative to the tropical tropopause [*Waugh and Hall*, 2002].

was last in the troposphere [*Hall and Waugh*, 2000]. Age of air increases away from the tropopause and equator, where most tropospheric air enters the stratosphere [*Holton et al.*, 1995]. We determine age of air by using SF_6 as a chronological tracer [*Waugh and Hall*, 2002] to determine the average temporal lag between a concentration at given location in the stratosphere relative to the tropical upper troposphere. We use the period 1995-2012, in which the atmospheric burden of SF_6 grew linearly in our simulations.

Most models underestimate the stratospheric age of air implied by observations of CO_2, SF_6, and HF, which increases up to 7 years by 35 km in the poles [*Waugh and Hall*, 2002]. GEOS-Chem using ModelE is most accurate in reproducing the average age of air implied from the observations. However, the shallower meridional gradient of ModelE indicates a stronger "leaky pipe" [e.g., *Ray et al.*, 2010] and more poleward flow in the lower tropical stratosphere than in either GEOS model. Coupled with an overly vigorous stratosphere-troposphere exchange (next section), this apparently allows for more efficient transport from the tropical to the Antarctic troposphere via the lower stratosphere, and leads to an overestimate of stratospheric ozone

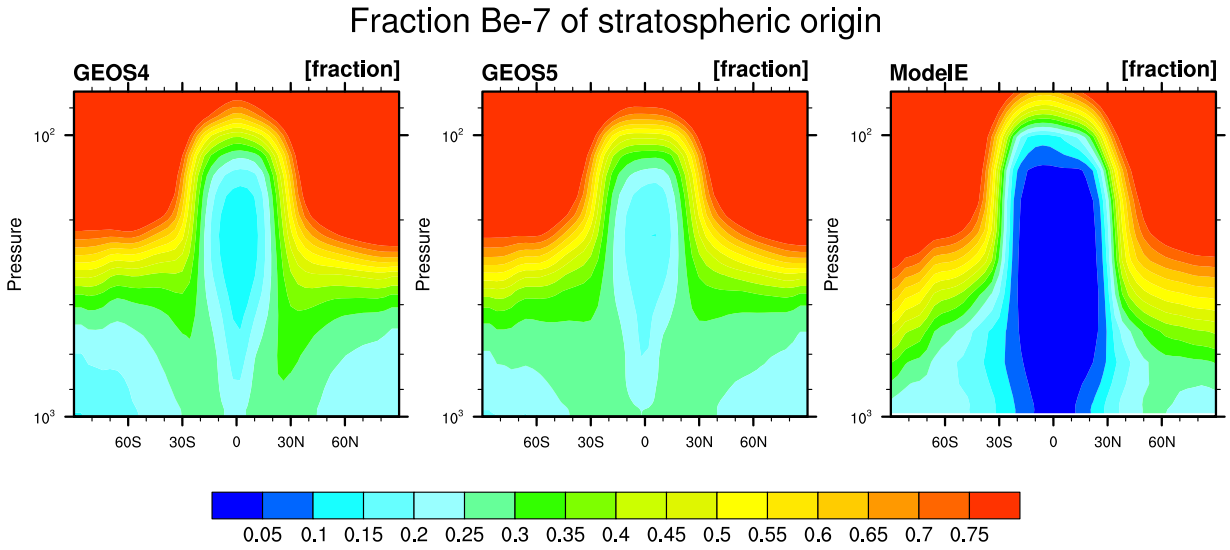

Figure B.6: Zonal annual mean fraction ^{7}Be of stratospheric origin in GEOS-Chem driven by different meteorology. Tropopause determined using local lapse rate.

concentrations in the extratropical lower stratosphere.

Stratosphere-Troposphere Exchange

Beryllium-7 has often been used as a tracer of downward transport from the stratosphere [*Dibb et al.*, 1992, 1994; *Husain et al.*, 1977; *Rehfeld and Heimann*, 1995; *Sanak et al.*, 1985; *Viezee and Singh*, 1980] and as an indicator of STE performance within global atmospheric models [*Allen et al.*, 2003; *Liu et al.*, 2001, in review; *Barrett et al.*, 2012].

Figure B.6 shows the annual zonal fraction of ^{7}Be of stratospheric origin in each simulation. Using GEOS4 and GEOS5 meteorology, we find that 24-26% of annual average surface midlatitude concentrations of ^{7}Be is of stratospheric origin, consistent with the *Dutkiewicz and Husain* [1985] constraint of 25% from ^{7}Be/^{90}Sr for 38-51°N. For ModelE using QUS, we find a slight underestimate of 20-25%. However, the fraction throughout the polar free troposphere in the ModelE-driven simulation is much higher than in the GEOS simulations, implying a larger stratosphere-to-troposphere mass flux. The amount of ^{7}Be over Antarctica in ModelE of

stratospheric origin is roughly double that of either GEOS simulation. Our results are similar to the NASA Global Modeling Initiative (GMI) CTM driven by GISS Model II' meteorology [*Liu et al.*, in review].

We found that application of the GISS QUS winds to the standard TPCORE advection scheme in GEOS-Chem originally lead to much larger overestimates in stratosphere-troposphere mixing, as small inconsistencies in the the horizontal mass fluxes manifest as large vertical fluxes. This problem was apparent in earlier GEOS-Chem simulations using GISS Model III meteorology, especially at the poles, [e.g., *Wu et al.*, 2007b], but as the cross-tropopause flux of ozone in those simulations was prescribed, it was less of an issue in those studies. To allow for online stratospheric chemistry in this study, we found it necessary to implement the QUS advection scheme within GEOS-Chem.

B.2.3 Wet Deposition

Figure B.7 (right column) compares the mean ^{210}Pb wet deposition flux in each simulation with that of the long-term mean aggregated from rainfall collectors, soil cores, and snow samples by *Preiss et al.* [1996] aggregated to the model resolutions. GEOS-Chem captures the magnitude and global spatial distribution of the ^{210}Pb deposition flux, with the exception of the East Asian outflow. Wet deposition of ^{210}Pb in the GEOS simulations is biased by -16% and -26%, and by -16% in the ModelE simulation versus the observations. If we neglect the observations over the Japanese archipelago, which may reflect in situ production of ^{210}Pb on mineral dust aerosol [*Fukuda and Tsunogai*, 1975] that we do not simulate, the GEOS simulations remain similarly biased (-13 to -28%), but ModelE is now positively biased by +7%. Altogether, these results imply a small low bias in the ^{210}Pb source (and therefore ^{222}Rn emission), although the results are clearly sensitive to precipitation distributions.

We find a tropospheric residence time for ^{210}Pb-containing aerosols against deposition in our ModelE-driven simulation of 7.2 d, shorter than than with GEOS4 (9.5 d) or GEOS5 (11 d)

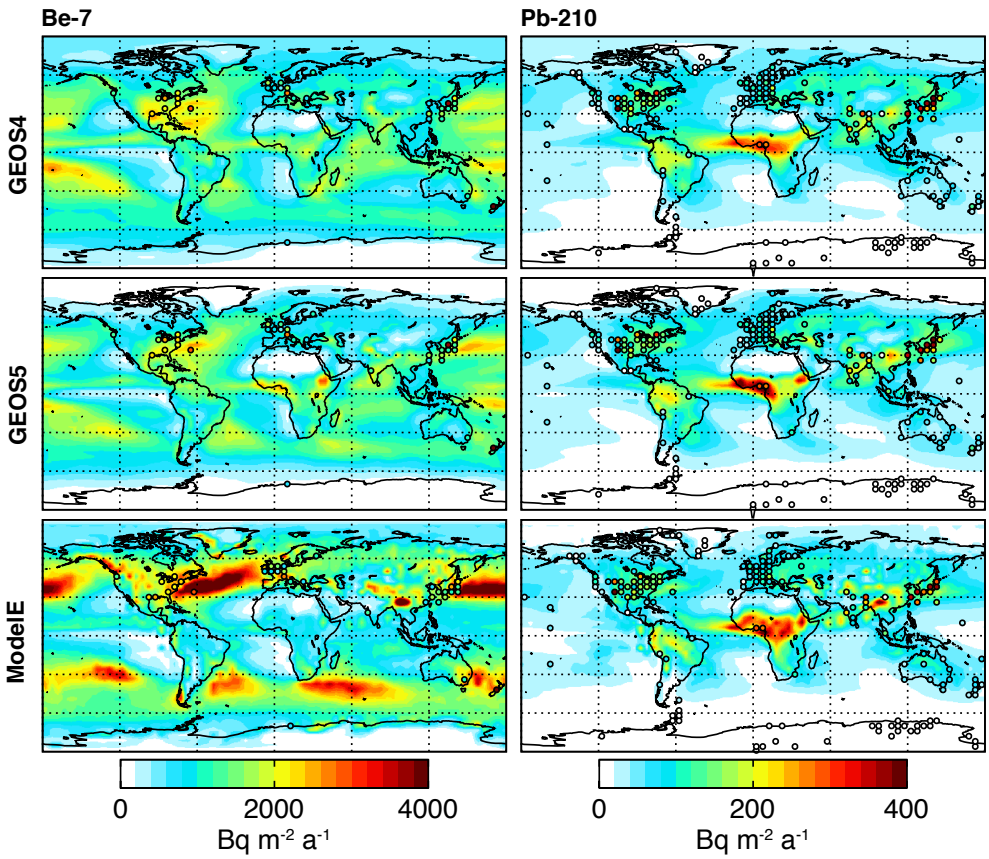

Figure B.7: GEOS-Chem annual average aerosol wet deposition flux for ^{7}Be (left column) and ^{210}Pb (right column). Each row uses different meteorology. The filled circles show observed values aggregated to the model resolution.

meteorology for 2004-2006, but within the range of previous estimates, 6.5-12.5 d [*Turekian et al.*, 1977; *Lambert et al.*, 1982; *Balkanski et al.*, 1993; *Koch et al.*, 1996; *Guelle et al.*, 1998a,b; *Liu et al.*, 2001].

Figure B.7 (left column) examines the modeled ^{7}Be wet deposition fluxes, compared against the few available observations [*Baskaran et al.*, 1993; *Bleichrodt*, 1978; *Brown et al.*, 1989; *Dibb*, 1989; *Du et al.*, 2008; *Harvey and Matthews*, 1989; *Hasebe et al.*, 1981; *Hirose et al.*, 2004; *Igarashi et al.*, 1998; *Narazaki and Fujitaka*, 2010; *Nijampurkar and Rao*, 1993; *Olsen et al.*, 1985; *Papastefanou et al.*, 1995; *Schuler et al.*, 1991; *Turekian et al.*, 1983; *Wallbrink and Murray*, 1994, and references therein]. The wet deposition flux is increased in our ModelE

simulation relative to the GEOS simulations, particularly over the midlatitude oceans. This result reflects the higher stratosphere-to-troposphere mass flux in ModelE, which increases the fraction of the ^{7}Be burden in the troposphere relative to the stratosphere. It also derives from greater precipitation in regions of stratospheric downwelling, which increases the fraction of ^{7}Be lost by deposition rather than by radioactive decay. Compared to observed values of ^{7}Be, the ModelE-driven simulation shows a bias of +33% while GEOS4 and GEOS5 yield biases of -22% and -26%. The spread in biases shows the difficulty in modeling precipitation accurately, as well as large variability in the observed fluxes induced by the solar cycle.

We find a lifetime of tropospheric ^{7}Be against wet deposition of 40 d in our ModelE simulation, which is consistent with our GEOS5 simulation, and longer than our GEOS4 simulation (32 d). These lifetimes are all longer than prior findings, e.g., 23 d [*Koch et al.*, 1996] and 21 d [*Liu et al.*, 2001], but within the variability expected from the sensitivity of the calculation to model vertical resolution and tropopause definition, as the ^{7}Be burden straddles the tropopause.

B.2.4 Hydroxyl Radical

To assess OH concentrations in the model, we examine the lifetime and/or distributions of relatively long-lived molecules whose main sink in the troposphere is OH. We find that the lifetime of methyl chloroform (MCF) against tropospheric OH is 6.0 years in the CTM driven by present-day meteorology from ModelE, matching the observed constraint of $6.0^{+0.5}_{-0.4}$ years from *Prinn et al.* [2005]. The simulated methane lifetime against loss by tropospheric OH is 10.4 years, which agrees with the best estimate of $10.2^{+0.9}_{-0.7}$ years derived from the MCF data [*Prinn et al.*, 2005], recent multi-model estimates of 10.2 ± 1.7 [*Fiore et al.*, 2009] and 9.8 ± 1.6 [*Voulgarakis et al.*, 2013] years, and an estimate of 11.2 ± 1.3 years derived from methane observations [*Prather et al.*, 2012]. The present-day simulation captures the observed meridional gradient of CO in the southern hemisphere. Like most other models [*Shindell et al.*, 2006a], our simulations underestimate the CO gradient in the northern hemisphere by about a third, for reasons that are

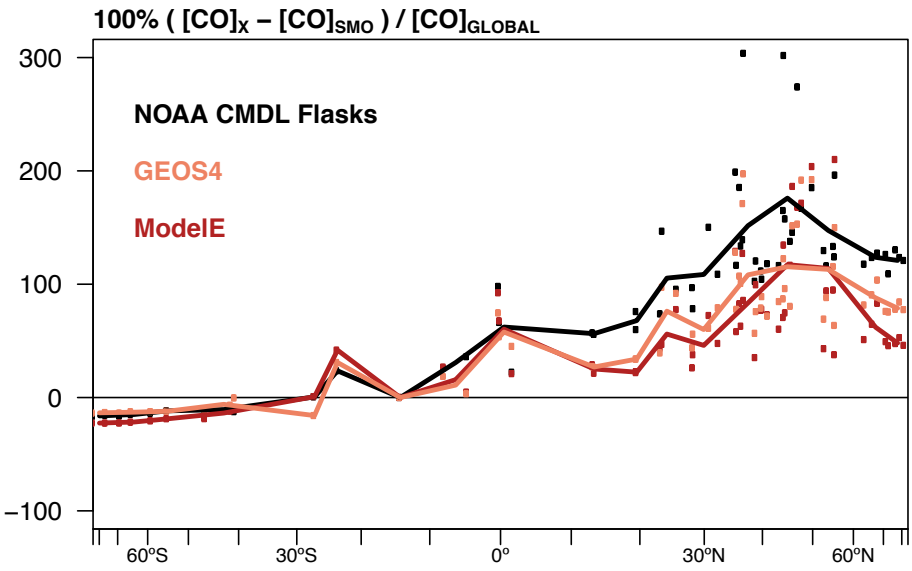

Figure B.8: Meridional gradient of CO in flask samples for 1990-2010 at sites in the NOAA Global Monitoring Division, relative to American Samoa (SMO; 14°S). Also shown are the values from GEOS-Chem driven by ModelE and GEOS4 meteorology sampled at the month and location of the observations (filled circles). The solid lines show the mean for 20 equal-area latitudinal bins.

uncertain (Figure B.8).

B.2.5 Ozone

Figure B.9a shows that total ozone columns (TOC) over the tropics (30°S-30°N) in the ModelE-driven simulations have a small bias (+1.5%) against 1990-1999 mean TOC from the TOMS/SBUV merged total ozone data set, version 8, revision 3 (available online at http://acd-ext.gsfc.nasa.gov/Data_services/merged/). Data from the Aura satellite allow for isolating the stratospheric and tropospheric contributions to TOC [*Ziemke et al.*, 2011]. Figure B.9b shows that over the tropics (30°S-30°N), where the stratosphere has its greatest influence on tropospheric photochemistry, the simulated stratospheric columns of ozone (SCO) agree within 5% of the *Ziemke et al.* [2011] satellite climatology (mean bias ModelE: +0.2%; GEOS4: +4.8%). Extratropical SCO is overestimated by up to 100% in both simulations, particularly over the southern hemisphere, resulting from overly strong meridional air mass fluxes

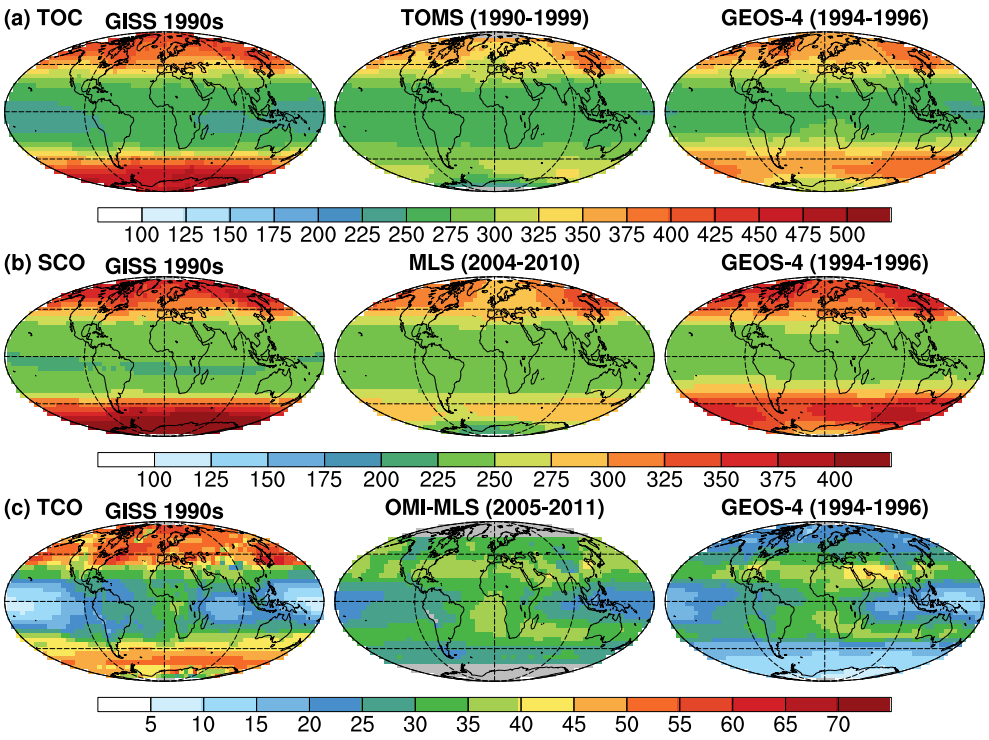

Figure B.9: Annual average total ozone columns (TOC; top panel), stratospheric columns of ozone (SCO; middle panel), and tropospheric columns of ozone (TCO; bottom panel). The left column shows ozone columns determined from GEOS-Chem driven by three years of present-day GISS ModelE meteorology. The center column shows satellite climatologies of TOC in the 1990s from the TOMS/SBUV TOMS/SBUV merged data, the 2004-2010 SCO climatology from the Microwave Limb Sounder (MLS) [*Ziemke et al*., 2011], and the 2005-2011 TCO climatology from OMI/MLS [*Ziemke et al*., 2006]. The right column shows ozone columns in GEOS-Chem driven by GEOS4 meteorology for 1993-1996. All units are Dobson Units (DU). Tropopause determined in the simulations using thermal lapse rate for comparison with satellite stratospheric and tropospheric products.

in the lower stratosphere from the tropical regions of net photochemical production (Section S2.2.2 and S2.2.3). Figure B.9c shows tropospheric columns of ozone (TCO). ModelE and GEOS4 are biased low by 20% and 9% in the tropics versus the 2000s TCO climatology from OMI/MLS [*Ziemke et al*., 2006]. The overly vigorous stratospheric-troposphere exchange in ModelE leads to a cross-tropopause flux of ozone from the stratosphere that is approximately 40% higher in the CTM driven by ModelE than GEOS4. This causes large overestimates in tropospheric ozone in the extratropics (+46% from 60°S-30°S and +44% from 30°N-60°N),

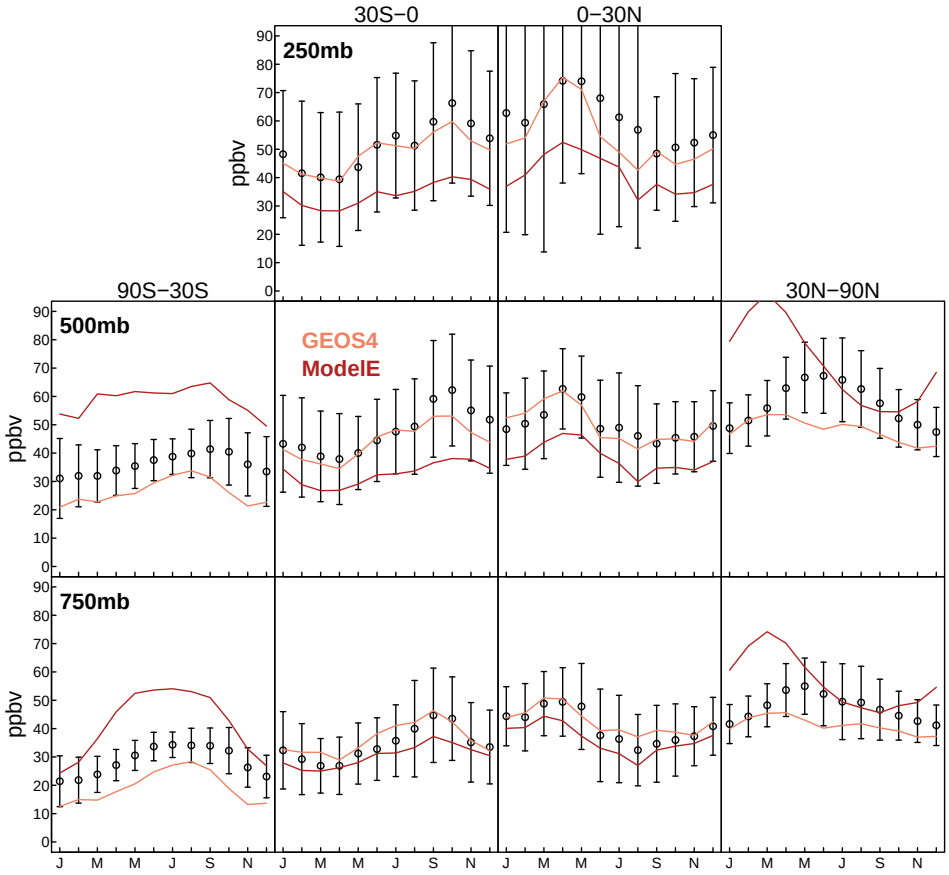

Figure B.10: Comparison of the annual cycle of ozone observations (black dots) and model results (colored lines), sampled for different latitude bands (90°S–30°S, 30°S to equator; equator to 30°N, and 30°N–90°N) and different pressure levels (750, 500, and 250 hPa). The models are sampled at the same sites and with the same frequency as the observations. The bars for each observation are the average of the interannual standard deviations at each station.

particularly during the spring months. On the other hand, GEOS4 is biased low in the extratropics (-32% from 60°S-30°S and -12% from 30°N-60°N) due to the recent inclusion of bromine chemistry in the model. Figure B.10 compares the modeled ozone profiles against all available ozonesondes for the 1990s from the World Ozone and Ultraviolet Radiation Data Center (WOUDC; http://www.woudc.org), using the zonal bands and pressure levels from *Stevenson et al*. [2006]. Most of the tropical bias occurs in the free and upper troposphere, and is within the range of observed variability. GEOS4 is biased low in the extratropics with the recent inclusion of

bromine chemistry in the model. The ModelE biases in the extratropics are again consistent with the overestimate of stratosphere-troposphere exchange.

In summary, GEOS-Chem driven by ModelE for the ICECAP project recreates the global lifetimes of MCF and methane against oxidation by tropospheric OH implied by observation (better than GEOS simulations), and has very small bias in its tropical overhead stratospheric ozone columns. Its greatest limitation is in an overly vigorous mass flux from the stratosphere, which creates large biases in extratropical tropospheric ozone. It also underestimates the ozone burden in the tropical upper troposphere. Future projects using the ICECAP framework will increase the resolution of the GCM to improve mass transport.

References

Abarca, S. F., K. L. Corbosiero, and T. J. J. Galarneau (2010), An evaluation of the Worldwide Lightning Location Network (WWLLN) using the National Lightning Detection Network (NLDN) as ground truth, *J Geophys Res-Atmos*, *115*.

Adams, J. M., J. V. H. Constable, A. B. Guenther, and P. Zimmerman (2001), An estimate of natural volatile organic compound emissions from vegetation since the last glacial maximum, *Atmos Environ*, *3*(1), 73--91.

Alexander, B., J. Savarino, N. Barkov, R. Delmas, and M. H. Thiemens (2002), Climate driven changes in the oxidation pathways of atmospheric sulfur, *Geophys Res Lett*, *29*(14).

Alexander, B., J. Savarino, K. Kreutz, and M. H. Thiemens (2004), Impact of preindustrial biomass-burning emissions on the oxidation pathways of tropospheric sulfur and nitrogen, *J Geophys Res-Atmos*, *109*(D8), D08,303.

Alexander, B., R. Park, D. J. Jacob, Q. Li, R. Yantosca, J. Savarino, C. Lee, and M. H. Thiemens (2005), Sulfate formation in sea-salt aerosols: Constraints from oxygen isotopes, *J Geophys Res-Atmos*, *110*.

Alexander, B., M. G. Hastings, D. J. Allman, J. Dachs, J. A. Thornton, and S. A. Kunasek (2009), Quantifying atmospheric nitrate formation pathways based on a global model of the oxygen isotopic composition ($\Delta^{17}O$) of atmospheric nitrate, *Atmos Chem Phys*, *9*(14), 5043--5056.

Allen, D., K. Pickering, G. Stenchikov, A. M. Thompson, and Y. Kondo (2000), A three-dimensional total odd nitrogen (NOy) simulation during SONEX using a stretched-grid chemical transport model, *J Geophys Res-Atmos*, *105*, 3851--3876.

Allen, D. J., and K. Pickering (2002), Evaluation of lightning flash rate parameterizations for use in a global chemical transport model, *J Geophys Res-Atmos*, *107*.

Allen, D. J., R. Rood, A. M. Thompson, and R. Hudson (1996), Three-dimensional radon 222 calculations using assimilated meteorological data and a convective mixing algorithm, *J Geophys Res-Atmos*, *101*, 6871--6881.

Allen, D. J., J. Dibb, B. Ridley, K. Pickering, and R. Talbot (2003), An estimate of the stratospheric contribution to springtime tropospheric ozone maxima using TOPSE measurements and beryllium-7 simulations, *J Geophys Res-Atmos*, *108*.

Allen, D. J., K. Pickering, B. Duncan, and M. Damon (2010), Impact of lightning NO emissions on North American photochemistry as determined using the Global Modeling Initiative (GMI) model, *J Geophys Res-Atmos*, *115*.

Anklin, M., and R. C. Bales (1997), Recent increase in H2O2 concentration at Summit, Greenland, *J Geophys Res-Atmos*, *102*(D15), 19,099--19,104.

Auvray, M., and I. Bey (2005), Long-range transport to Europe: Seasonal variations and implications for the European ozone budget, *J Geophys Res-Atmos*, *110*.

Balkanski, Y., D. J. Jacob, G. Gardner, W. Graustein, and K. Turekian (1993), Transport and Residence Times of Tropospheric Aerosols Inferred From a Global 3-Dimensional Simulation of Pb-210, *J Geophys Res-Atmos*, *98*, 20,573--20,586.

Barrett, S. R. H., S. H. L. Yim, C. K. Gilmore, L. T. Murray, S. R. Kuhn, A. P. K. Tai, R. M. Yantosca, D. W. Byun, F. Ngan, X. Li, J. I. Levy, A. Ashok, J. Koo, H. M. Wong, O. Dessens, S. Balasubramanian, G. G. Fleming, M. N. Pearlson, C. Wollersheim, R. Malina, S. Arunachalam, F. S. Binkowski, E. M. Leibensperger, D. J. Jacob, J. I. Hileman, and I. A. Waitz (2012), Public Health, Climate, and Economic Impacts of Desulfurizing Jet Fuel, *Environ Sci Technol*, *46*(8), 4275--4282.

Bartlein, P. J., S. P. Harrison, S. Brewer, S. Connor, B. A. Davis, K. Gajewski, J. Guiot, T. I. Harrison-Prentice, A. Henderson, O. Peyron, I. C. Prentice, M. Scholze, H. Seppa, B. Shuman, S. Sugita, R. S. Thompson, A. E. Viau, J. Williams, and H. Wu (2011a), Pollen-based continental climate reconstructions at 6 and 21 ka: a global synthesis, *Climate Dynamics*, *37*(3), 775--802.

Bartlein, P. J., S. P. Harrison, S. Brewer, S. Connor, B. A. S. Davis, K. Gajewski, J. Guiot, T. I. Harrison-Prentice, A. Henderson, O. Peyron, I. C. Prentice, M. Scholze, H. Seppa, B. Shuman, S. Sugita, R. S. Thompson, A. E. Viau, J. Williams, and H. Wu (2011b), Pollen-based continental climate reconstructions at 6 and 21 ka: a global synthesis, *Climate Dynamics*, *37*(3), 775--802.

Baskaran, M., C. Coleman, and P. Santschi (1993), Atmospheric Depositional Fluxes of Be-7 and Pb-210 at Galveston and College-Station, Texas, *J Geophys Res-Atmos*, *98*, 20,555--20,571.

Bekki, S., K. S. Law, and J. A. Pyle (1994), Effect of Ozone Depletion on Atmospheric CH4 and CO Concentrations, *Nature*, *371*(6498), 595--597.

Berger, A. L. (1978), Long-term variations of daily insolation and Quaternary climatic changes, *J Atmos Sci*, *35*(12), 2362--2367.

Berntsen, T. K., I. S. A. Isaksen, G. Myhre, J. S. Fuglestvedt, F. Stordal, T. A. Larsen, R. S. Freckleton, and K. P. Shine (1997), Effects of anthropogenic emissions on tropospheric ozone and its radiative forcing, *J Geophys Res*, *102*(D23), 28,101.

Bey, I., D. J. Jacob, R. Yantosca, J. A. Logan, B. Field, A. Fiore, Q. Li, H. Liu, L. Mickley, and M. Schultz (2001), Global modeling of tropospheric chemistry with assimilated meteorology: Model description and evaluation, *J Geophys Res-Atmos*, *106*, 23,073--23,095.

Bisiaux, M. M., R. Edwards, J. R. McConnell, M. A. J. Curran, T. D. Van Ommen, A. M. Smith, T. A. Neumann, D. R. Pasteris, J. E. Penner, and K. Taylor (2012), Changes in black carbon deposition to Antarctica from two high-resolution ice core records, 1850-2000 AD, *Atmos Chem Phys*, *12*(9), 4107--4115.

Bleichrodt, J. (1978), Mean Tropospheric Residence Time of Cosmic-Ray-Produced Beryllium-7 at North Temperate Latitudes, *J Geophys Res-Oc Atm*, *83*, 3058--3062.

Boccippio, D., W. Koshak, R. Blakeslee, K. Driscoll, D. Mach, D. Buechler, W. Boeck, H. Christian, and S. Goodman (2000), The Optical Transient Detector (OTD): Instrument characteristics and cross-sensor validation, *J Atmos Ocean Tech*, *17*(4), 441--458.

Boccippio, D., W. Koshak, and R. Blakeslee (2002), Performance assessment of the Optical Transient Detector and Lightning Imaging Sensor. Part I: Predicted diurnal variability, *J Atmos Ocean Tech*, *19*(9), 1318--1332.

Boersma, K. F., D. J. Jacob, H. J. Eskes, R. W. Pinder, J. Wang, and R. J. van der A (2008), Intercomparison of SCIAMACHY and OMI tropospheric NO2 columns: Observing the diurnal evolution of chemistry and emissions from space, *J Geophys Res-Atmos*, *113*.

Bondietti, E., J. Brantley, and C. Rangarajan (1988), Size Distributions and Growth of Natural and Chernobyl-Derived Sub-Micron Aerosols in Tennessee, *J Environ Radioactiv*, *6*(2), 99--120.

Bousquet, P., D. Hauglustaine, P. Peylin, C. Carouge, and P. Ciais (2005), Two decades of OH variability as inferred by an inversion of atmospheric transport and chemistry of methyl chloroform, *Atmos Chem Phys*, *5*, 2635--2656.

Braconnot, P., B. Otto-Bliesner, S. Harrison, S. Joussaume, J. Y. Peterchmitt, A. Abe-Ouchi, M. Crucifix, E. Driesschaert, T. Fichefet, C. D. Hewitt, M. Kageyama, A. Kitoh, A. Laîné, M. F. Loutre, O. Marti, U. Merkel, G. Ramstein, P. Valdes, S. L. Weber, Y. Yu, and Y. Zhao (2007a), Results of PMIP2 coupled simulations of the Mid-Holocene and Last Glacial Maximum -- Part 1: experiments and large-scale features, *Clim. Past*, *3*(2), 261--277.

Braconnot, P., B. Otto-Bliesner, S. Harrison, S. Joussaume, J. Y. Peterchmitt, A. Abe-Ouchi, M. Crucifix, E. Driesschaert, T. Fichefet, C. D. Hewitt, M. Kageyama, A. Kitoh, M. F. Loutre, O. Marti, U. Merkel, G. Ramstein, P. Valdes, L. Weber, Y. Yu, and Y. Zhao (2007b), Results of PMIP2 coupled simulations of the Mid-Holocene and Last Glacial Maximum -- Part 2: feedbacks with emphasis on the location of the ITCZ and mid- and high latitudes heat budget, *Clim. Past*, *3*(2), 279--296.

Bradley, W., and J. Pearson (1970), Aircraft Measurements of Vertical Distribution of Radon in Lower Atmosphere, *J Geophys Res*, *75*(30), 5890.

Brasseur, G., J. Kiehl, J. Muller, T. Schneider, C. Granier, X. Tie, and D. Hauglustaine (1998), Past and future changes in global tropospheric ozone: Impact on radiative forcing, *Geophys Res Lett*, *25*(20), 3807--3810.

Brook, E. J., S. Harder, J. Severinghaus, E. J. Steig, and C. M. Sucher (2000), On the origin and timing of rapid changes in atmospheric methane during the Last Glacial Period, *Global Biogeochem Cy*, *14*(2), 559--572.

Brost, R., and R. Chatfield (1989), Transport of Radon in a 3-Dimensional, Subhemispheric Model, *J Geophys Res-Atmos*, *94*, 5095--5119.

Brost, R., J. Feichter, and M. Heimann (1991), 3-Dimensional Simulation of Be-7 in a Global Climate Model, *J Geophys Res-Atmos*, *96*, 22,423--22,445.

Brown, L., G. Stensland, J. Klein, and R. Middleton (1989), Atmospheric Deposition of Be-7 and Be-10, *Geochim Cosmochim Ac*, *53*(1), 135--142.

Brune, W., D. Tan, I. Faloona, L. Jaeglé, D. J. Jacob, B. Heikes, J. Snow, Y. Kondo, R. Shetter, G. Sachse, B. Anderson, G. Gregory, S. Vay, H. Singh, D. Davis, J. Crawford, and D. Blake (1999), OH and HO_2 chemistry in the North Atlantic free troposphere, *Geophys Res Lett*, *26*(20), 3077--3080.

Bucsela, E. J., E. A. Celarier, M. O. Wenig, J. F. Gleason, J. P. Veefkind, K. F. Boersma, and E. J. Brinksma (2006), Algorithm for NO_2 vertical column retrieval from the ozone monitoring instrument, *Geoscience and Remote Sensing, IEEE Transactions on*, *44*(5), 1245--1258.

Chameides, W., D. Stedman, R. Dickerson, D. Rusch, and R. Cicerone (1977), NOx Production in Lightning, *J Atmos Sci*, *34*(1), 143--149.

Chandra, S., J. R. Ziemke, W. Min, and W. Read (1998), Effects of 1997-1998 El Nino on tropospheric ozone and water vapor, *Geophys Res Lett*, *25*(20), 3867--3870.

Chandra, S., J. R. Ziemke, P. Bhartia, and R. Martin (2002), Tropical tropospheric ozone: Implications for dynamics and biomass burning, *J Geophys Res-Atmos*, *107*.

Chandra, S., J. R. Ziemke, M. R. Schoeberl, L. Froidevaux, W. G. Read, P. F. Levelt, and P. K. Bhartia (2007), Effects of the 2004 El Nino on tropospheric ozone and water vapor, *Geophys Res Lett*, *34*(6).

Chandra, S., J. R. Ziemke, B. N. Duncan, T. L. Diehl, N. J. Livesey, and L. Froidevaux (2009), Effects of the 2006 El Nino on tropospheric ozone and carbon monoxide: implications for dynamics and biomass burning, *Atmos Chem Phys*, *9*(13), 4239--4249.

Chappellaz, J., T. Bluniert, D. Raynaud, J. M. Barnola, J. Schwander, and B. Stauffert (1993), Synchronous changes in atmospheric CH4 and Greenland climate between 40 and 8 kyr BP, *Nature*, *366*(6454), 443--445.

Chappellaz, J., T. Blunier, S. Kints, A. Dällenbach, J.-M. Barnola, J. Schwander, D. Raynaud, and B. Stauffer (1997), Changes in the atmospheric CH4 gradient between Greenland and Antarctica during the Holocene, *J Geophys Res*, *102*(D13), 15,987.

Chatfield, R., J. Vastano, H. Singh, and G. Sachse (1996), A general model of how fire emissions and chemistry produce African/oceanic plumes (O3, CO, PAN, smoke) in TRACE A, *J Geophys Res*, *101*(D19), 24,279--24,306.

Chelliah, M., and P. Arkin (1992), Large-Scale Interannual Variability of Monthly Outgoing Longwave Radiation Anomalies Over the Global Tropics, *Journal of Climate*, *5*(4), 371--389.

Chin, M., R. B. Rood, S. J. Lin, J.-F. Muller, and A. M. Thompson (2000), Atmospheric sulfur cycle simulated in the global model GOCART- Model description and global properties, *J Geophys Res*, *105*(D20), 24--671--24--687.

Choi, Y., J. Kim, A. Eldering, G. Osterman, Y. L. Yung, Y. Gu, and K. N. Liou (2009), Lightning and anthropogenic NOx sources over the United States and the western North Atlantic Ocean: Impact on OLR and radiative effects, *Geophys Res Lett*, *36*.

Christian, H., R. Blakeslee, and S. Goodman (1989), The Detection of Lightning From Geostationary Orbit, *J Geophys Res-Atmos*, *94*, 13,329--13,337.

Christian, H., R. Blakeslee, D. Boccippio, W. Boeck, D. Buechler, K. Driscoll, S. Goodman, J. Hall, W. Koshak, D. Mach, and M. Stewart (2003), Global frequency and distribution of lightning as observed from space by the Optical Transient Detector, *J Geophys Res-Atmos*, *108*.

Clark, P. U., and A. C. Mix (2002), Ice sheets and sea level of the Last Glacial Maximum, *Quaternary Science Reviews*, *21*, 1--7.

CLIMAP (1976), Surface of Ice-Age Earth, *Science*, *191*(4232), 1131--1137.

Collimore, C., M. Hitchman, and D. Martin (1998), Is there a quasi-biennial oscillation in tropical deep convection?, *Geophys Res Lett*, *25*(3), 333--336.

Collimore, C., D. Martin, M. Hitchman, A. Huesmann, and D. Waliser (2003), On the relationship between the QBO and tropical deep convection, *Journal of Climate*, *16*(15), 2552--2568.

Collins, W. J., S. Sitch, and O. Boucher (2010), How vegetation impacts affect climate metrics for ozone precursors, *J Geophys Res*, *115*(D23), D23,308.

Considine, D., D. Bergmann, and H. Liu (2005), Sensitivity of Global Modeling Initiative chemistry and transport model simulations of radon-222 and lead-210 to input meteorological data, *Atmos Chem Phys*, *5*, 3389--3406.

Considine, D. B., J. A. Logan, and M. A. Olsen (2008), Evaluation of near-tropopause ozone distributions in the Global Modeling Initiative combined stratosphere/troposphere model with ozonesonde data, *Atmos Chem Phys*, *8*(9), 2365--2385.

Cooper, O. R., M. Trainer, A. M. Thompson, S. J. Oltmans, D. W. Tarasick, J. C. Witte, A. Stohl, S. Eckhardt, J. Lelieveld, M. J. Newchurch, B. J. Johnson, P. R. W, L. Kalnajs, M. K. Dubey, T. Leblanc, I. S. McDermid, G. Forbes, D. Wolfe, T. Carey-Smith, G. A. Morris, B. Lefer, B. Rappengluck, E. Joseph, F. Schmidlin, J. Meagher, F. C. Fehsenfeld, T. J. Keating, R. A. Van Curen, and K. Minschwaner (2007), Evidence for a recurring eastern North America upper tropospheric ozone maximum during summer, *J Geophys Res-Atmos*, *112*.

Crutzen, P. J., and C. Brühl (1993), A model study of atmospheric temperatures and the concentrations of ozone, hydroxyl, and some other photochemically active gases during the glacial, the pre-industrial Holocene and the present, *Geophys Res Lett*, *20*(11), 1047--1050.

Crutzen, P. J., and P. H. Zimmermann (1991), The changing photochemistry of the troposphere, *Tellus B*, *43*(4), 136--151.

Dalsøren, S. B., and I. S. A. Isaksen (2006), CTM study of changes in tropospheric hydroxyl distribution 1990-2001 and its impact on methane, *Geophys Res Lett*, *33*(23).

Davis, D., J. Seelig, G. Huey, J. Crawford, G. Chen, Y. Wang, M. Buhr, D. Helmig, W. Neff, and D. Blake (2008), A reassessment of Antarctic plateau reactive nitrogen based on ANTCI 2003 airborne and ground based measurements, *Atmos Environ*, *42*(12), 2831--2848.

DeCaria, A., K. Pickering, G. Stenchikov, and L. Ott (2005), Lightning-generated NOX and its impact on tropospheric ozone production: A three-dimensional modeling study of a Stratosphere-Troposphere Experiment: Radiation, Aerosols and Ozone (STERAO-A) thunderstorm, *J Geophys Res-Atmos*, *110*.

Delaygue, G., V. Masson, J. Jouzel, R. D. Koster, and R. J. Healy (2000), The origin of Antarctic precipitation: a modelling approach, *Tellus B*, *52*(1), 19--36.

Denman, K. L., G. Brasseur, A. Chidthaisong, P. Ciais, P. M. Cox, R. E. Dickinson, D. Hauglustaine, C. Heinze, E. Holland, D. J. Jacob, U. Lohmann, S. Ramachandran, P. L. da Silva Dias, S. C. Wofsy, and X. Zhang (2007), Couplings Between Changes in the Climate System and Biogeochemistry, in *Climate Change 2007: The Physical Science Basis*, edited by S. Solomon, D. Qin, M. Manning, Z. Chen, M. Marquis, K. Averyt, M. Tignor, and H. Miller, Cambridge University Press, Cambridge, United Kingdom and New York, NY, USA.

Dentener, F., W. Peters, M. Krol, M. van Weele, P. Bergamaschi, and J. Lelieveld (2003), Interannual variability and trend of CH4 lifetime as a measure for OH changes in the 1979-1993 time period, *J Geophys Res-Atmos*, *108*.

Dibb, J. (1989), Atmospheric Deposition of Beryllium-7 in the Chesapeake Bay Region, *J Geophys Res-Atmos*, *94*, 2261--2265.

Dibb, J., R. Talbot, and G. Gregory (1992), Beryllium-7 and Pb-210 in the Western-Hemisphere Arctic Atmosphere - Observations From Three Recent Aircraft-Based Sampling Programs, *J Geophys Res-Atmos*, *97*, 16,709--16,715.

Dibb, J., L. Meeker, R. Finkel, J. Southon, M. Caffee, and L. Barrie (1994), Estimation of Stratospheric Input to the Arctic Troposphere - Be-7 and Be-10 in Aerosols at Alert, Canada, *J Geophys Res-Atmos*, *99*, 12,855--12,864.

Diehl, T. (2009), A Global Inventory of Volcanic SO_2Emissions for Hindcast Scenarios, http://www-lscedods.cea.fr/aerocom/AEROCOM_HC/volc.

Du, J., J. Zhang, J. Zhang, and Y. Wu (2008), Deposition patterns of atmospheric Be-7 and Pb-210 in coast of East China Sea, Shanghai, China, *Atmos Environ*, *42*(20), 5101--5109.

Duncan, B. N., and J. A. Logan (2008), Model analysis of the factors regulating the trends and variability of carbon monoxide between 1988 and 1997, *Atmos Chem Phys*, *8*(24), 7389--7403.

Duncan, B. N., J. A. Logan, I. Bey, I. A. Megretskaia, R. M. Yantosca, Novelli, P. C., N. B. Jones, and C. P. Rinsland (2007), Global budget of CO, 1988-1997: Source estimates and validation with a global model, *J Geophys Res-Atmos*, *112*.

Dutkiewicz, V., and L. Husain (1985), Stratospheric and Tropospheric Components of Be-7 in Surface Air, *J Geophys Res-Atmos*, *90*, 5783--5788.

Edwards, D., J. Lamarque, J. Attie, L. Emmons, A. Richter, J. Cammas, J. Gille, G. Francis, M. Deeter, J. Warner, D. Ziskin, L. Lyjak, J. Drummond, and J. Burrows (2003), Tropospheric ozone over the tropical Atlantic: A satellite perspective, *J Geophys Res-Atmos*, *108*.

Ehhalt, D. H. (1999), Photooxidation of trace gases in the troposphere Plenary Lecture, *Phys Chem Chem Phys*, *1*(24), 5401--5408.

Engel, A., T. Möbius, H. Bönisch, U. Schmidt, R. Heinz, I. Levin, E. Atlas, S. Aoki, T. Nakazawa, S. Sugawara, F. Moore, D. Hurst, J. Elkins, S. Schauffler, A. Andrews, and K. Boering (2008), Age of stratospheric air unchanged within uncertainties over the past 30□years, *Nature*, *2*(1), 28--31.

EPA (2006), Air Quality Criteria for Ozone and Related Photochemical Oxidants (2006 Final), *Tech. Rep. EPA/600/R-05/004aF-cF*, Washington, DC.

Erbland, J., W. C. Vicars, J. Savarino, S. Morin, M. M. Frey, D. Frosini, E. Vince, and J. M. F. Martins (2012), Air-snow transfer of nitrate on the East Antarctic Plateau -- Part 1: Isotopic evidence for a photolytically driven dynamic equilibrium, *Atmos Chem Phys Disc*, *12*(10), 28,559--28,608.

Feichter, J., and P. Crutzen (1990), Parameterization of vertical tracer transport due to deep cumulus convection in a global transport model and its evaluation with ^{222}Radon measurements, *Tellus B*, *42*, 100--117.

Fernandes, S. D., N. M. Trautmann, D. G. Streets, C. A. Roden, and T. C. Bond (2007), Global biofuel use, 1850-2000, *Global Biogeochem Cy*, *21*(2).

Fiore, A. M., F. J. Dentener, O. Wild, C. Cuvelier, M. G. Schultz, P. Hess, C. Textor, M. Schulz, R. M. Doherty, L. W. Horowitz, I. A. MacKenzie, M. G. Sanderson, D. T. Shindell, D. S. Stevenson, S. Szopa, R. Van Dingenen, G. Zeng, C. Atherton, D. Bergmann, I. Bey, G. Carmichael, W. J. Collins, B. N. Duncan, G. Faluvegi, G. Folberth, M. Gauss, S. Gong, D. Hauglustaine, T. Holloway, I. S. A. Isaksen, D. J. Jacob, J. E. Jonson, J. W. Kaminski, T. J. Keating, A. Lupu, E. Marmer, V. Montanaro, R. J. Park, G. Pitari, K. J. Pringle, J. A. Pyle, S. Schroeder, M. G. Vivanco, P. Wind, G. Wojcik, S. Wu, and A. Zuber (2009), Multimodel estimates of intercontinental source-receptor relationships for ozone pollution, *J Geophys Res-Atmos*, *114*.

Fiore, A. M., V. Naik, D. V. Spracklen, A. Steiner, N. Unger, M. Prather, D. Bergmann, P. J. Cameron-Smith, I. Cionni, W. J. Collins, S. Dalsoren, V. Eyring, G. A. Folberth, P. Ginoux, L. W. Horowitz, B. Josse, J.-F. Lamarque, I. A. MacKenzie, T. Nagashima, F. M. O'Connor, M. Righi, S. T. Rumbold, D. T. Shindell, R. B. Skeie, K. Sudo, S. Szopa, T. Takemura, and G. Zeng (2012), Global air quality and climate, *Chem. Soc. Rev.*

Fischer, E. V., D. J. Jacob, D. B. Millet, R. M. Yantosca, and J. Mao (2012), The role of the ocean in the global atmospheric budget of acetone, *Geophys Res Lett*, *39*(1), L01,807.

Fischer, H., F. Fundel, U. Ruth, B. Twarloh, A. Wegner, R. Udisti, S. Becagli, E. Castellano, A. Morganti, M. Severi, E. Wolff, G. C. Littot, R. Rothlisberger, R. Mulvaney, M. A. Hutterli, P. Kaufmann, U. Federer, F. Lambert, M. Bigler, M. Hansson, U. Jonsell, M. De Angelis, C. F. Boutron, M. L. Siggaard-Andersen, J. P. Steffensen, C. Barbante, V. Gaspari, P. Gabrielli, and D. Wagenbach (2007), Reconstruction of millennial changes in dust emission, transport and regional sea ice coverage using the deep EPICA ice cores from the Atlantic and Indian Ocean sector of Antarctica, *Earth Planet Sc Lett*, *260*(1), 340--354.

Fischer, H., M. Behrens, M. Bock, U. Richter, J. Schmitt, L. Loulergue, J. Chappellaz, R. Spahni, T. Blunier, M. Leuenberger, and T. F. Stocker (2008), Changing boreal methane sources and constant biomass burning during the last termination, *Nature*, *452*(7189), 864--867.

Fisher, J. A., D. J. Jacob, Q. Wang, R. Bahreini, C. C. Carouge, M. J. Cubison, J. E. Dibb, T. Diehl, J. L. Jimenez, E. M. Leibensperger, Z. Lu, M. B. J. Meinders, H. O. T. Pye, P. K. Quinn, S. Sharma, D. G. Streets, A. van Donkelaar, and R. M. Yantosca (2011), Sources, distribution, and acidity of sulfate-ammonium aerosol in the Arctic in winter-spring, *Atmos Environ*, *45*(39), 7301--7318.

Fishman, J., C. Watson, J. Larsen, and J. A. Logan (1990), Distribution of Tropospheric Ozone Determined From Satellite Data, *J Geophys Res-Atmos*, *95*, 3599--3617.

Fishman, J., K. Fakhruzzaman, B. Cros, and D. Nganga (1991), Identification of Widespread Pollution in the Southern-Hemisphere Deduced From Satellite Analyses, *Science*, *252*(5013), 1693--1696.

Fluckiger, J., E. Monnin, B. Stauffer, J. Schwander, T. Stocker, J. Chappellaz, D. Raynaud, and J. Barnola (2002), High-resolution Holocene N2O ice core record and its relationship with CH4 and CO2, *Global Biogeochem Cy*, *16*(1).

Forster, P., and K. Shine (1997), Radiative forcing and temperature trends from stratospheric ozone changes, *J Geophys Res-Atmos*, *102*, 10,841--10,855.

Fountoukis, C., and A. Nenes (2007), ISORROPIA II: a computationally efficient thermodynamic equilibrium model for K^+--Ca^{2+}--Mg^{2+}--NH_4^+--Na^+--SO_4^{2-}--NO_3^---Cl^---H_2O aerosols, *Atmos Chem Phys*, *7*(17), 4639--4659.

Frey, M. M., R. C. Bales, and J. R. McConnell (2006), Climate sensitivity of the century-scale hydrogen peroxide (H2O2) record preserved in 23 ice cores from West Antarctica, *J Geophys Res*, *111*(D21), D21,301.

Fuhrer, K., A. Neftel, M. Anklin, and V. Maggi (1993), Continuous measurements of hydrogen peroxide, formaldehyde, calcium and ammonium concentrations along the new grip ice core from summit, Central Greenland, *Atmos Environ*, *27*(12), 1873--1880.

Fukuda, K., and S. Tsunogai (1975), Pb-210 in Precipitation in Japan and Its Implication for Transport of Continental Aerosols Across Ocean, *Tellus*, *27*(5), 514--521.

Garcia, R. R., and W. J. Randel (2008), Acceleration of the Brewer-Dobson circulation due to increases in greenhouse gases, *J Atmos Sci*, *65*(8), 2731--2739.

Gettelman, A., and P. Forster (2002), A climatology of the tropical tropopause layer, in *J Meteorol Soc Jpn*, pp. 911--924, Natl Ctr Atmospher Res, Boulder, CO 80307 USA.

Gillett, R. W., T. D. Van Ommen, A. V. Jackson, and G. P. Ayers (2000), Formaldehyde and peroxide concentrations in Law Dome (Antarctica) firn and ice cores, *Journal of Glaciology*, *46*(152), 15--19.

Goodman, S., D. Buechler, K. Knupp, K. Driscoll, and E. McCaul (2000), The 1997-98 El Nino event and related wintertime lightning variations in the southeastern United States, *Geophys Res Lett*, *27*(4), 541--544.

Grenfell, J. L., D. T. Shindell, D. Koch, and D. Rind (2001), Chemistry-climate interactions in the Goddard Institute for Space Studies general circulation model: 2. New insights into modeling the preindustrial atmosphere, *J Geophys Res*, *106*(D24), 33,435.

Grewe, V. (2007), Impact of climate variability on tropospheric ozone, *Sci Total Environ*, *374*(1), 167--181.

Grewe, V., D. Brunner, M. Dameris, J. Grenfell, R. Hein, D. T. Shindell, and J. Staehelin (2001), Origin and variability of upper tropospheric nitrogen oxides and ozone at northern mid-latitudes, *Atmos Environ*, *35*(20), 3421--3433.

Guelle, W., Y. Balkanski, M. Schulz, F. Dulac, and P. Monfray (1998a), Wet deposition in a global size-dependent aerosol transport model - 1. Comparison of a 1 year Pb-210 simulation with ground measurements, *J Geophys Res-Atmos*, *103*, 11,429--11,445.

Guelle, W., Y. Balkanski, J. Dibb, M. Schulz, and F. Dulac (1998b), Wet deposition in a global size-dependent aerosol transport model 2. Influence of the scavenging scheme on Pb-210 vertical profiles, surface concentrations, and deposition, *J Geophys Res-Atmos*, *103*, 28,875--28,891.

Guenther, A., C. N. Hewitt, D. Erickson, R. Fall, C. Geron, T. Graedel, P. Harley, L. Klinger, M. Lerdau, W. A. Mckay, T. Pierce, B. Scholes, R. Steinbrecher, R. Tallamraju, J. Taylor, and P. Zimmerman (1995), A global model of natural volatile organic compound emissions, *J Geophys Res*, *100*(D5), 8873.

Guenther, A., W. M. Baugh, G. P. Brasseur, J. Greenberg, P. Harley, L. F. Klinger, D. Serça, L. A. Vierling, and e. al (1999), Isoprene emission estimates and uncertainties for the Central African EXPRESSO study domain, *J Geophys Res-Atmos*, *104*, 30,625--30,639.

Guenther, A., C. Geron, T. Pierce, B. Lamb, P. Harley, and R. Fall (2000), Natural emissions of non-methane volatile organic compounds; carbon monoxide, and oxides of nitrogen from North America, *Atmos Environ*, *34*, 2205--2230.

Guenther, A., T. Karl, P. Harley, C. Wiedinmyer, P. I. Palmer, and C. Geron (2006), Estimates of global terrestrial isoprene emissions using MEGAN (Model of Emissions of Gases and Aerosols from Nature), *Atmos Chem Phys*, *6*, 3181--3210.

Guenther, A., X. Jiang, C. L. Heald, T. Sakulyanontvittaya, T. Duhl, L. K. Emmons, and X. Wang (2012), The Model of Emissions of Gases and Aerosols from Nature version 2.1 (MEGAN2. 1): an extended and updated framework for modeling biogenic emissions, *Geosci Model Dev*, *5*, 1471--1492.

Haan, D., and D. Raynaud (1998), Ice core record of CO variations during the last two millennia: atmospheric implications and chemical interactions within the Greenland ice, *Tellus B*, *50*(3), 253--262.

Haan, D., P. Martinerie, and D. Raynaud (1996), Ice core data of atmospheric carbon monoxide over Antarctica and Greenland during the last 200 years, *Geophys Res Lett*, *23*(17), 2235--2238.

Hack, J. J. (1994), Parameterization of moist convection in the National Center for Atmospheric Research community climate model (CCM2), *J Geophys Res-Atmos*, *99*, 5551--5568.

Hall, B. D., G. S. Dutton, D. J. Mondeel, J. D. Nance, M. Rigby, J. H. Butler, F. L. Moore, D. F. Hurst, and J. W. Elkins (2011), Improving measurements of SF_6 for the study of atmospheric transport and emissions, *Atmos. Meas. Tech.*, *4*(11), 2441--2451.

Hall, T. M., and D. W. Waugh (2000), Stratospheric residence time and its relationship to mean age, *J Geophys Res*, *105*(D5), 6773.

Hamid, E., Z. Kawasaki, and R. Mardiana (2001), Impact of the 1997-98 El Nino event on lightning activity over Indonesia, *Geophys Res Lett*, *28*(1), 147--150.

Hansen, J., and S. Lebedeff (1987), Global Trends of Measured Surface Air-Temperature, *J Geophys Res-Atmos*, *92*, 13,345--13,372.

Hansen, J., M. Sato, R. Ruedy, P. Kharecha, A. Lacis, R. Miller, L. Nazarenko, K. Lo, G. A. Schmidt, G. Russell, I. Aleinov, S. Bauer, E. Baum, B. Cairns, V. Canuto, M. Chandler, Y. Cheng, A. Cohen, A. Del Genio, G. Faluvegi, E. Fleming, A. Friend, T. Hall, C. Jackman, J. Jonas, M. Kelley, N. Y. Kiang, D. Koch, G. Labow, J. Lerner, S. Menon, T. Novakov, V. Oinas, J. Perlwitz, J. Perlwitz, D. Rind, A. Romanou, R. Schmunk, D. T. Shindell, P. Stone, S. Sun, D. Streets, N. Tausnev, D. Thresher, N. Unger, M. Yao, and S. Zhang (2007), Climate simulations for 1880-2003 with GISS modelE, *Climate Dynamics*, *29*(7-8), 661--696.

Harvey, M., and K. Matthews (1989), Be-7 Deposition in a High-Rainfall Area of New-Zealand, *J Atmos Chem*, *8*(4), 299--306.

Hasebe, N., T. Doke, J. Kikuchi, Y. Takeuchi, and T. Sugiyama (1981), Observation of Fallout Rates of Atmospheric Be-7 and Na-22 Produced by Cosmic-Rays Concerning Estimation of the Fallout Rate of Atmospheric Al-26, *J Geophys Res-Space*, *86*, 520--524.

Hauglustaine, D., and G. Brasseur (2001), Evolution of tropospheric ozone under anthropogenic activities and associated radiative forcing of climate, *J Geophys Res-Atmos*, *106*, 32,337--32,360.

Hauglustaine, D., C. Granier, G. Brasseur, and G. Megie (1994), Impact of Present Aircraft Emissions of Nitrogen-Oxides on Tropospheric Ozone and Climate Forcing, *Geophys Res Lett*, *21*(18), 2031--2034.

Hauglustaine, D., F. Hourdin, L. Jourdain, M. Filiberti, S. Walters, J. Lamarque, and E. Holland (2004), Interactive chemistry in the Laboratoire de Meteorologie Dynamique general circulation model: Description and background tropospheric chemistry evaluation, *J Geophys Res-Atmos*, *109*.

Heald, C. L., H. Coe, J. L. Jimenez, R. J. Weber, R. Bahreini, A. M. Middlebrook, L. M. Russell, M. Jolleys, T. M. Fu, J. D. Allan, K. N. Bower, G. Capes, J. Crosier, W. T. Morgan, N. H. Robinson, P. I. Williams, M. J. Cubison, P. F. DeCarlo, and E. J. Dunlea (2011), Exploring the vertical profile of atmospheric organic aerosol: comparing 17 aircraft field campaigns with a global model, *Atmos Chem Phys*, *11*(24), 12,673--12,696.

Hegglin, M. I., and T. G. Shepherd (2009), Large climate-induced changes in ultraviolet index and stratosphere-to-troposphere ozone flux, *Nat Geosci*, *2*(10), 687--691.

Held, I. M., and B. J. Soden (2006), Robust responses of the hydrological cycle to global warming, *Journal of Climate*, *19*(21), 5686--5699.

Hirose, K., T. Honda, S. Yagishita, Y. Igarashi, and M. Aoyama (2004), Deposition behaviors of Pb-210, Be-7 and thorium isotopes observed in Tsukuba and Nagasaki, Japan, *Atmos Environ*, *38*(38), 6601--6608.

Holmes, C. D., M. J. Prather, O. A. Søvde, and G. Myhre (2013), Future methane, hydroxyl, and their uncertainties: key climate and emission parameters for future predictions, *Atmos Chem Phys*, *13*(1), 285--302.

Holton, J., P. Haynes, M. Mcintyre, A. Douglass, R. Rood, and L. Pfister (1995), Stratosphere-Troposphere Exchange, *Rev Geophys*, *33*(4), 403--439.

Honrath, R. E., M. C. Peterson, S. Guo, J. E. Dibb, P. B. Shepson, and B. Campbell (1999), Evidence of NO xproduction within or upon ice particles in the Greenland snowpack, *Geophys Res Lett*, *26*(6), 695--698.

Honrath, R. E., S. Guo, M. C. Peterson, M. P. Dziobak, J. E. Dibb, and M. A. Arsenault (2000), Photochemical production of gas phase NOx from ice crystal NO3−, *J Geophys Res*, *105*(D19), 24,183.

Horowitz, L. W. (2006), Past, present, and future concentrations of tropospheric ozone and aerosols: Methodology, ozone evaluation, and sensitivity to aerosol wet removal, *J Geophys Res*, *111*(D22), D22,211.

Hough, A. M., and R. G. Derwent (1990), Changes in the global concentration of tropospheric ozone due to human activities, *Nature*, *344*(6267), 645--648.

Hsu, J., and M. J. Prather (2009), Stratospheric variability and tropospheric ozone, *J Geophys Res-Atmos*, *114*.

Hudman, R. C., D. J. Jacob, S. Turquety, E. M. Leibensperger, L. T. Murray, S. Wu, A. B. Gilliland, M. Avery, T. H. Bertram, W. Brune, R. C. Cohen, J. E. Dibb, F. M. Flocke, A. Fried, J. Holloway, J. A. Neuman, R. Orville, A. Perring, X. Ren, G. W. Sachse, H. B. Singh, A. Swanson, and P. J. Wooldridge (2007), Surface and lightning sources of nitrogen oxides over the United States: Magnitudes, chemical evolution, and outflow, *J Geophys Res-Atmos*, *112*.

Huntrieser, H., C. Feigl, H. Schlager, F. Schroder, C. Gerbig, P. van Velthoven, F. Flatoy, C. Thery, A. Petzold, H. Holler, and U. Schumann (2002), Airborne measurements of NOx, tracer species, and small particles during the European lightning nitrogen oxides experiment, *J Geophys Res-Atmos*, *107*.

Huntrieser, H., H. Schlager, A. Roiger, M. Lichtenstern, U. Schumann, C. Kurz, D. Brunner, C. Schwierz, A. Richter, and A. Stohl (2007), Lightning-produced NOx over Brazil during TROCCINOX: airborne measurements in tropical and subtropical thunderstorms and the importance of mesoscale convective systems, *Atmos Chem Phys*, *7*(11), 2987--3013.

Huntrieser, H., U. Schumann, H. Schlager, H. Hoeller, A. Giez, H. D. Betz, D. Brunner, C. Forster, O. J. Pinto, and R. Calheiros (2008), Lightning activity in Brazilian thunderstorms during TROCCINOX: implications for NOx production, *Atmos Chem Phys*, *8*(4), 921--953.

Husain, L., P. Coffey, R. Meyers, and R. Cederwall (1977), Ozone Transport From Stratosphere to Troposphere, *Geophys Res Lett*, *4*(9), 363--365.

Hutterli, M. A., R. C. Bales, J. R. McConnell, and R. W. Stewart (2002), HCHO in Antarctic snow: Preservation in ice cores and air-snow exchange, *Geophys Res Lett*, *29*(8), 1235.

Hutterli, M. A., J. R. McConnell, R. C. Bales, and R. W. Stewart (2003), Sensitivity of hydrogen peroxide (H2O2) and formaldehyde (HCHO) preservation in snow to changing environmental conditions: Implications for ice core records, *J Geophys Res*, *108*(D1), 4023.

Igarashi, Y., I. Hirose, and M. Otsuji-Hatori (1998), Beryllium-7 deposition and its relation to sulfate deposition, *J Atmos Chem*, *29*(3), 217--231.

IPCC (2001), *Climate Change 2001: The Scientific Basis*, Contribution of Working Group I to the Third Assessment Report of the Intergovernmental Panel on Climate Change, Cambridge University Press, Cambridge, UK.

IPCC (2007), *Climate Change 2007: The Physical Science Basis*, Contribution of Working Group I to the Fourth Assessment Report of the Intergovernmental Panel on Climate Change, Cambridge University Press, Cambridge, United Kingdom and New York, NY, USA.

Jacob, D. J. (1990), Radon-222 as a test of convective transport in a general circulation model, *Tellus B*, *42*(1), 118--134.

Jacob, D. J., B. Heikes, S. Fan, J. A. Logan, D. Mauzerall, J. Bradshaw, H. Singh, G. Gregory, R. Talbot, D. Blake, and G. Sachse (1996), Origin of ozone and NOx in the tropical troposphere: A photochemical analysis of aircraft observations over the South Atlantic basin, *J Geophys Res-Atmos*, *101*, 24,235--24,250.

Jacob, D. J., M. Prather, P. Rasch, R. Shia, Y. Balkanski, S. Beagley, D. Bergmann, W. Blackshear, M. Brown, M. Chiba, M. Chipperfield, J. deGrandpre, J. Dignon, J. Feichter, C. Genthon, W. Grose, P. Kasibhatla, I. Kohler, M. Kritz, K. Law, J. PENNER, M. Ramonet, C. Reeves, D. Rotman, D. Stockwell, P. VanVelthoven, G. Verver, O. Wild, H. Yang, and P. Zimmermann (1997), Evaluation and intercomparison of global atmospheric transport models using Rn-222 and other short-lived tracers, *J Geophys Res-Atmos*, *102*, 5953--5970.

Jacobson, M. Z., and D. G. Streets (2009), Influence of future anthropogenic emissions on climate, natural emissions, and air quality, *J Geophys Res-Atmos*, *114*.

Jaeglé, L., D. J. Jacob, W. Brune, and P. Wennberg (2001), Chemistry of HOx radicals in the upper troposphere, *Atmos Environ*, *35*(3), 469--489.

Jaeglé, L., P. K. Quinn, T. S. Bates, B. Alexander, and J. T. Lin (2011), Global distribution of sea salt aerosols: new constraints from in situ and remote sensing observations, *Atmos Chem Phys*, *11*(7), 3137--3157.

Jöckel, P., H. Tost, A. Pozzer, C. Bruehl, J. Buchholz, L. Ganzeveld, P. Hoor, A. Kerkweg, M. G. Lawrence, R. Sander, B. Steil, G. Stiller, M. Tanarhte, D. Taraborrelli, J. Van Aardenne, and J. Lelieveld (2006), The atmospheric chemistry general circulation model ECHAM5/MESSy1: consistent simulation of ozone from the surface to the mesosphere, *Atmos Chem Phys*, *6*, 5067--5104.

John, J. G., A. M. Fiore, V. Naik, L. W. Horowitz, and J. P. Dunne (2012), Climate versus emission drivers of methane lifetime against loss by tropospheric OH from 1860-2100, *Atmos Chem Phys*, *12*(24), 12,021--12,036.

Johnson, S. (1967), Hierarchical Clustering Schemes, *Psychometrika*, *32*(3), 241--254.

Jourdain, L., S. S. Kulawik, H. M. Worden, K. E. Pickering, J. Worden, and A. M. Thompson (2010), Lightning NOx emissions over the USA constrained by TES ozone observations and the GEOS-Chem model, *Atmos Chem Phys*, *10*(1), 107--119.

Joussaume, S., K. E. Taylor, P. Braconnot, J. F. B. Mitchell, J. E. Kutzbach, S. P. Harrison, I. C. Prentice, A. J. Broccoli, A. Abe-Ouchi, P. J. Bartlein, C. Bonfils, B. Dong, J. Guiot, K. Herterich, C. D. Hewitt, D. Jolly, J. W. Kim, A. Kislov, A. Kitoh, M. F. Loutre, V. Masson, B. McAvaney, N. McFarlane, N. de Noblet, W. R. Peltier, J. Y. Peterschmitt, D. Pollard, D. Rind, J. F. Royer, M. E. Schlesinger, J. Syktus, S. Thompson, P. Valdes, G. Vettoretti, R. S. Webb, and U. Wyputta (1999), Monsoon changes for 6000 years ago: Results of 18 simulations from the Paleoclimate Modeling Intercomparison Project (PMIP), *Geophys Res Lett*, *26*(7), 859--862.

Kaplan, J., N. Bigelow, I. Prentice, S. Harrison, P. Bartlein, T. Christensen, W. Cramer, N. Matveyeva, A. McGuire, D. Murray, V. Razzhivin, B. Smith, D. Walker, P. Anderson, A. Andreev, L. Brubaker, M. Edwards, and A. Lozhkin (2003), Climate change and Arctic ecosystems: 2. Modeling, paleodata-model comparisons, and future projections, *J Geophys Res-Atmos*, *108*.

Kaplan, J. O. (2002), Wetlands at the Last Glacial Maximum: Distribution and methane emissions, *Geophys Res Lett*, *29*(6), 1079.

Kaplan, J. O., G. Folberth, and D. A. Hauglustaine (2006), Role of methane and biogenic volatile organic compound sources in late glacial and Holocene fluctuations of atmospheric methane concentrations, *Global Biogeochem Cy*, *20*(2).

Karol, I., V. Frolkis, and A. Kiselev (1995), Radiative-Photochemical Modeling of the Annually Averaged Composition and Temperature of the Global Atmosphere During the Last Glacial and Interglacial Periods, *J Geophys Res-Atmos*, *100*, 7291--7301.

Kettle, A., M. Andreae, D. Amouroux, T. Andreae, T. Bates, H. Berresheim, H. Bingemer, R. Boniforti, M. Curran, G. DiTullio, G. Helas, G. Jones, M. Keller, R. Kiene, C. Leck, M. Levasseur, G. Malin, M. Maspero, P. Matrai, A. McTaggart, N. Mihalopoulos, B. Nguyen, A. Novo, J. Putaud, S. Rapsomanikis, G. Roberts, G. Schebeske, S. Sharma, R. Simo, R. Staubes, S. Turner, and G. Uher (1999), A global database of sea surface dimethylsulfide (DMS) measurements and a procedure to predict sea surface DMS as a function of latitude, longitude, and month, *Global Biogeochem Cy*, *13*(2), 399--444.

Khalil, M. A. K., and R. A. Rasmussen (1987), Atmospheric methane: Trends over the last 10,000 years, *Atmos Environ*, *21*(11), 2445--2452.

Kim, D., A. H. Sobel, A. D. Del Genio, Y. Chen, S. J. Camargo, M.-S. Yao, M. Kelley, and L. Nazarenko (2012), The Tropical Subseasonal Variability Simulated in the NASA GISS General Circulation Model, *Journal of Climate*, *25*(13), 4641--4659.

Klein Goldewijk, K., A. Beusen, G. Van Drecht, and M. De Vos (2011), The HYDE 3.1 spatially explicit database of human-induced global land-use change over the past 12,000 years, *Global Ecol Biogeogr*, *20*(1), 73--86.

Koch, D., D. J. Jacob, and W. Graustein (1996), Vertical transport of tropospheric aerosols as indicated by Be-7 and Pb-210 in a chemical tracer model, *J Geophys Res-Atmos*, *101*, 18,651--18,666.

Koch, D., S. Menon, A. Del Genio, R. Ruedy, I. Alienov, and G. A. Schmidt (2009), Distinguishing aerosol impacts on climate over the past century, *Journal of Climate*, *22*(10), 2659--2677.

Koshak, W., M. Stewart, H. Christian, J. Bergstrom, J. Hall, and R. Solakiewicz (2000), Laboratory calibration of the optical transient detector and the lightning imaging sensor, *J Atmos Ocean Tech*, *17*(7), 905--915.

Koshak, W., H. Peterson, A. Biazar, M. Khan, and L. Wang (2013), The NASA Lightning Nitrogen Oxides Model (LNOM): Application to air quality modeling, *Atmos Res*.

Krishnamurti, T., H. Fuelberg, M. Sinha, D. Oosterhof, E. Bensman, and V. Kumar (1993), The Meteorological Environment of the Tropospheric Ozone Maximum Over the Tropical South-Atlantic Ocean, *J Geophys Res-Atmos*, *98*, 10,621--10,641.

Kritz, M., S. Rosner, and D. Stockwell (1998), Validation of an off-line three-dimensional chemical transport model using observed radon profiles - 1. Observations, *J Geophys Res-Atmos*, *103*, 8425--8432.

Krol, M., and J. Lelieveld (2003), Can the variability in tropospheric OH be deduced from measurements of 1,1,1-trichloroethane (methyl chloroform)?, *J Geophys Res-Atmos*, *108*.

Krol, M., J. Lelieveld, D. Oram, G. Sturrock, S. Penkett, C. Brenninkmeijer, V. Gros, J. Williams, and H. Scheeren (2003), Continuing emissions of methyl chloroform from Europe, *Nature*, *421*(6919), 131--135.

Kuhns, H., M. Green, and V. Etyemezian (2003), Big Bend Regional Aerosol and Visibility Observational (BRAVO) Study Emissions Inventory.

Kutterolf, S., M. Jegen, J. X. Mitrovica, T. Kwasnitschka, A. Freundt, and P. J. Huybers (2013), A detection of Milankovitch frequencies in global volcanic activity, *Geology*, *41*(2), 227--230.

Labrador, L., R. von Kuhlmann, and M. Lawrence (2004), Strong sensitivity of the global mean OH concentration and the tropospheric oxidizing efficiency to the source of NOx from lightning, *Geophys Res Lett*, *31*(6).

Lacis, A. A., D. J. Wuebbles, and J. A. Logan (1990), Radiative forcing of climate by changes in the vertical distribution of ozone, *J Geophys Res*, *95*(D7), 9971.

Lal, D., P. Malhotra, and B. Peters (1958), On the Production of Radioisotopes in the Atmosphere by Cosmic Radiation and Their Application to Meteorology, *J Atmos Terr Phys*, *12*(4), 306--328.

Lamarque, J. F., P. Hess, L. Emmons, L. Buja, W. Washington, and C. Granier (2005), Tropospheric ozone evolution between 1890 and 1990, *J Geophys Res*, *110*(D8), D08,304.

Lambert, G., G. Polian, J. Sanak, B. Ardouin, A. Buisson, A. Jegou, and J. Leroulley (1982), Cycle du radon et de ses descendants: application à l'étude des échanges troposphère-stratosphère, *Ann Geophys*, *38*(4), 497--531.

Law, K. S., and J. A. Pyle (1991), Modelling the response of tropospheric trace species to changing source gas concentrations, *Atmos Environ*, *25*(9), 1863--1871.

Law, K. S., W. T. Sturges, D. R. Blake, J. B. Burkholder, J. H. Butler, R. A. Cox, P. H. Haynes, M. K. W. Ko, K. Kreher, C. Mari, K. Pfeilsticker, J. M. C. Plane, R. J. Salawitch, C. Schiller, B. M. Sinnhuber, R. von Glasow, N. J. Warwick, D. J. Wuebbles, and S. A. Yvon-Lewis (2007), Chapter 2, Halogenated Very Short-Lived Substances, in *Scientific Assessment of Ozone Depletion: 2006, Global Ozone Research and Monitoring Project - Report No. 50*, World Meteorological Organization, Geneva, Switzerland.

Lawrence, M. G., P. Jöckel, and R. von Kuhlmann (2001), What does the global mean OH concentration tell us?, *Atmos Chem Phys*, *1*(1), 37--49.

LeGrande, A. N., G. A. Schmidt, D. T. Shindell, C. V. Field, R. L. Miller, D. M. Koch, G. Faluvegi, and G. Hoffmann (2006), Consistent simulations of multiple proxy responses to an abrupt climate change event, *P Natl Acad Sci USA*, *103*(4), 837--842.

Leibensperger, E. M., L. J. Mickley, D. J. Jacob, and S. R. H. Barrett (2011), Intercontinental influence of NOx and CO emissions on particulate matter air quality, *Atmos Environ*, *45*(19), 3318--3324.

Lelieveld, J., and F. Dentener (2000), What controls tropospheric ozone?, *J Geophys Res-Atmos*, *105*, 3531--3551.

Lelieveld, J., W. Peters, F. Dentener, and M. Krol (2002), Stability of tropospheric hydroxyl chemistry, *J Geophys Res-Atmos*, *107*.

Lelieveld, J., C. A. M. Brenninkmeijer, P. Joeckel, I. S. A. Isaksen, M. C. Krol, J. E. Mak, E. Dlugokencky, S. A. Montzka, Novelli, P. C., W. Peters, and P. P. Tans (2006), New Directions: Watching over tropospheric hydroxyl (OH), *Atmos Environ*, *40*(29), 5741--5743.

Levelt, P., G. Van den Oord, M. Dobber, A. Malkki, H. Visser, J. de Vries, P. Stammes, J. Lundell, and H. Saari (2006), The Ozone Monitoring Instrument, *IEEE T Geosci Remote*, *44*(5), 1093--1101.

Levine, J. G., E. W. Wolff, A. E. Jones, L. C. Sime, P. J. Valdes, A. T. Archibald, G. D. Carver, N. J. Warwick, and J. A. Pyle (2011a), Reconciling the changes in atmospheric methane sources and sinks between the Last Glacial Maximum and the pre-industrial era, *Geophys Res Lett*, *38*(23), L23,804.

Levine, J. G., E. W. Wolff, A. E. Jones, M. A. Hutterli, O. Wild, G. D. Carver, and J. A. Pyle (2011b), In search of an ice core signal to differentiate between source-driven and sink-driven changes in atmospheric methane, *J Geophys Res*, *116*(D5), D05,305.

Levine, J. G., E. W. Wolff, P. O. Hopcroft, and P. J. Valdes (2012), Controls on the tropospheric oxidizing capacity during an idealized Dansgaard-Oeschger event, and their implications for the rapid rises in atmospheric methane during the last glacial period, *Geophys Res Lett*, *39*(12), n/a--n/a.

Levy, H., II, P. S. Kasibhatla, W. J. Moxim, A. A. Klonecki, A. I. Hirsch, S. J. Oltmans, and W. L. Chameides (1997), The global impact of human activity on tropospheric ozone, *Geophys Res Lett*, *24*(7), 791--794.

Liang, Q., R. S. Stolarski, S. R. Kawa, J. E. Nielsen, A. R. Douglass, J. M. Rodriguez, D. R. Blake, E. L. Atlas, and L. E. Ott (2010), Finding the missing stratospheric Br_y: a global modeling study of $CHBr_3$ and CH_2Br_2, *Atmos Chem Phys*, *10*(5), 2269--2286.

Liao, H., P. Adams, S. Chung, J. Seinfeld, L. Mickley, and D. J. Jacob (2003), Interactions between tropospheric chemistry and aerosols in a unified general circulation model, *J Geophys Res-Atmos*, *108*.

Licciardi, J. M., P. U. Clark, J. W. Jenson, and D. R. Macayeal (1998), Deglaciation of a Soft-Bedded Laurentide Ice Sheet, *Atmos Environ*, *17*(4-5), 427--448.

Liebmann, B., and C. Smith (1996), Description of a complete (interpolated) outgoing longwave radiation dataset, *Bulletin of the American Meteorological Society*, *77*(6), 1275--1277.

Liu, H., D. J. Jacob, I. Bey, and R. Yantosca (2001), Constraints from Pb-210 and Be-7 on wet deposition and transport in a global three-dimensional chemical tracer model driven by assimilated meteorological fields, *J Geophys Res-Atmos*, *106*, 12,109--12,128.

Liu, H., D. B. Considine, L. W. Horowitz, J. H. Crawford, S. E. Strahan, M. Damon, J. M. Rodriguez, X. Xu, C. C. Carouge, and R. M. Yantosca (in review), Using beryllium-7 to assess cross-tropopause transport in global models, *J Geophys Res-Atmos*.

Liu, S. C., M. Trainer, F. C. Fehsenfeld, D. D. Parrish, E. J. Williams, D. W. Fahey, G. Hubler, and P. C. Murphy (1987), Ozone production in the rural troposphere and the implications for regional and global ozone distributions, *J Geophys Res*, *92*(D4), 4191.

Logan, J. A., M. Prather, S. C. Wofsy, and M. McElroy (1981), Tropospheric Chemistry - a Global Perspective, *J Geophys Res-Oc Atm*, *86*, 7210--7254.

Logan, J. A., I. A. Megretskaia, R. Nassar, L. T. Murray, L. Zhang, K. W. Bowman, H. M. Worden, and M. Luo (2008), Effects of the 2006 El Nino on tropospheric composition as revealed by data from the Tropospheric Emission Spectrometer (TES), *Geophys Res Lett*, *35*(3).

Lovelock, J. E. (1977), Methyl Chloroform in Troposphere as an Indicator of OH Radical Abundance, *Nature*, *267*(5606), 32--32.

Lu, Y., and M. Khalil (1991), Tropospheric OH: model calculations of spatial, temporal, and secular variations, *Chemosphere*, *23*(3), 397--444.

Mach, D. M., H. J. Christian, R. J. Blakeslee, D. J. Boccippio, S. J. Goodman, and W. L. Boeck (2007), Performance assessment of the Optical Transient Detector and Lightning Imaging Sensor, *J Geophys Res-Atmos*, *112*.

Maenhaut, W., W. Zoller, and D. Coles (1979), Radionuclides in the South Pole Atmosphere, *J Geophys Res-Oc Atm*, *84*, 3131--3138.

Mahowald, N., P. Rasch, and R. Prinn (1995), Cumulus parameterizations in chemical transport models, *J Geophys Res-Atmos*, *100*, 26,173--26,189.

Mahowald, N. M., M. Yoshioka, W. D. Collins, A. J. Conley, D. W. Fillmore, and D. B. Coleman (2006), Climate response and radiative forcing from mineral aerosols during the last glacial maximum, pre-industrial, current and doubled-carbon dioxide climates, *Geophys Res Lett*, *33*(20).

Maiss, M., and C. A. M. Brenninkmeijer (1998), Atmospheric SF 6: Trends, Sources, and Prospects, *Environ Sci Technol*, *32*(20), 3077--3086.

Marenco, A., H. Gouget, P. Nedelec, J. P. Pages, and F. Karcher (1994), Evidence of a Long-Term Increase in Tropospheric Ozone From Pic Du Midi Data Series - Consequences - Positive Radiative Forcing, in *J Geophys Res-Atmos*, pp. 16,617--16,632, Ctr Natl Rech Meteorol, F-31057 Toulouse, France.

MARGO Project Members (2009), Constraints on the magnitude and patterns of ocean cooling at the Last Glacial Maximum, *Nat Geosci*, *2*(2), 127--132.

Marshall, T., and M. Stolzenburg (2001), Voltages inside and just above thunderstorms, *J Geophys Res-Atmos*, *106*, 4757--4768.

Martin, R., D. J. Jacob, J. A. Logan, I. Bey, R. Yantosca, A. Staudt, Q. Li, A. Fiore, B. Duncan, H. Liu, P. Ginoux, and V. Thouret (2002), Interpretation of TOMS observations of tropical tropospheric ozone with a global model and in situ observations, *J Geophys Res-Atmos*, *107*.

Martin, R. V., C. E. Sioris, K. Chance, T. B. Ryerson, T. H. Bertram, P. J. Wooldridge, R. C. Cohen, J. A. Neuman, A. Swanson, and F. M. Flocke (2006), Evaluation of space-based constraints on global nitrogen oxide emissions with regional aircraft measurements over and downwind of eastern North America, *J Geophys Res-Atmos*, *111*.

Martin, R. V., B. Sauvage, I. Folkins, C. E. Sioris, C. Boone, P. Bernath, and J. R. Ziemke (2007), Space-based constraints on the production of nitric oxide by lightning, *J Geophys Res-Atmos*, *112*.

Martinerie, P., G. Brasseur, and C. Granier (1995), The Chemical-Composition of Ancient Atmospheres - a Model Study Constrained by Ice Core Data, *J Geophys Res-Atmos*, *100*, 14,291--14,304.

McConnell, J. R., R. Edwards, G. L. Kok, M. G. Flanner, C. S. Zender, E. S. Saltzman, J. R. Banta, D. R. Pasteris, M. M. Carter, and J. D. W. Kahl (2007), 20th-Century Industrial Black Carbon Emissions Altered Arctic Climate Forcing, *Science*, *317*(5843), 1381--1384.

McElroy, M. B. (1989), Studies of Polar Ice: Insights for Atmospheric Chemistry, in *Report of the Dahlem Workshop on The Environmental Record in Glaciers and Ice Sheets*, edited by H. Oeschger and C. C. Langway, Jr, p. 363, John Wiley and Sons.

McLinden, C., S. Olsen, B. Hannegan, O. Wild, M. Prather, and J. Sundet (2000), Stratospheric ozone in 3-D models: A simple chemistry and the cross-tropopause flux, *J Geophys Res-Atmos*, *105*, 14,653--14,665.

Meijer, E., P. van Velthoven, D. Brunner, H. Huntrieser, and H. Kelder (2001), Improvement and evaluation of the parameterisation of nitrogen oxide production by lightning, *Phys Chem Earth Pt C*, *26*(8), 577--583.

Mickley, L., P. Murti, D. J. Jacob, J. A. Logan, D. Koch, and D. Rind (1999), Radiative forcing from tropospheric ozone calculated with a unified chemistry-climate model, *J Geophys Res-Atmos*, *104*, 30,153--30,172.

Mickley, L., D. J. Jacob, and D. Rind (2001), Uncertainty in preindustrial abundance of tropospheric ozone: Implications for radiative forcing calculations, *J Geophys Res-Atmos*, *106*, 3389--3399.

Montzka, S., C. Spivakovsky, J. Butler, J. Elkins, L. Lock, and D. Mondeel (2000), New observational constraints for atmospheric hydroxyl on global and hemispheric scales, *Science*, *288*(5465), 500--503.

Montzka, S. A., M. Krol, E. Dlugokencky, B. Hall, P. Joeckel, and J. Lelieveld (2011), Small Interannual Variability of Global Atmospheric Hydroxyl, *Science*, *331*(6013), 67--69.

Moore, H., S. Poet, and E. Martell (1973), Rn-222, Pb-210, Bi-210, and Po-210 Profiles and Aerosol Residence Times Versus Altitude, *J Geophys Res*, *78*(30), 7065--7075.

Moxim, W. J., and H. Levy, II (2000), A model analysis of the tropical South Atlantic Ocean tropospheric ozone maximum: The interaction of transport and chemistry, *J Geophys Res*, *105*(D13), 17,393--17--415.

Murray, L. T., D. J. Jacob, J. A. Logan, R. C. Hudman, and W. J. Koshak (2012), Optimized regional and interannual variability of lightning in a global chemical transport model constrained by LIS/OTD satellite data, *J Geophys Res-Atmos*, *117*(D20307).

Naik, V., A. Voulgarakis, A. M. Fiore, L. W. Horowitz, J. F. Lamarque, M. Lin, M. J. Prather, P. J. Young, D. Bergmann, P. J. Cameron-Smith, I. Cionni, W. J. Collins, S. B. Dalsøren, R. Doherty, V. Eyring, G. Faluvegi, G. A. Folberth, B. Josse, Y. H. Lee, I. A. MacKenzie, T. Nagashima, van Noije, T. P. C., D. A. Plummer, M. Righi, S. T. Rumbold, R. Skeie, D. T. Shindell, D. S. Stevenson, S. Strode, K. Sudo, S. Szopa, and G. Zeng (2012), Preindustrial to present day changes in tropospheric hydroxyl radical and methane lifetime from the Atmospheric Chemistry and Climate Model Intercomparison Project (ACCMIP), *Atmos Chem Phys Disc*, *12*(11), 30,755--30,804.

Narazaki, Y., and K. Fujitaka (2010), The Geographical Distribution and Features of 7Be Deposition in Japan, *Japan Health Physics Society*, *37*(4), 317--324.

Nassar, R., J. A. Logan, I. A. Megretskaia, L. T. Murray, L. Zhang, and D. B. A. Jones (2009), Analysis of tropical tropospheric ozone, carbon monoxide, and water vapor during the 2006 El Nino using TES observations and the GEOS-Chem model, *J Geophys Res-Atmos*, *114*.

Nazarov, L., A. Kuzenkov, S. Malakhov, L. Volokitina, Y. Gaziyev, and A. Vasilyev (1970), Radioactive Aerosol Distribution in Middle and Upper Troposphere Over Ussr in 1963-1968, *J Geophys Res*, *75*(18), 3575.

Nightingale, P. D., G. Malin, C. S. Law, A. J. Watson, P. S. Liss, M. I. Liddicoat, J. Boutin, and R. C. Upstill-Goddard (2000a), In situ evaluation of air-sea gas exchange parameterizations using novel conservative and volatile tracers, *Global Biogeochem Cy*, *14*(1), 373.

Nightingale, P. D., P. S. Liss, and P. Schlosser (2000b), Measurements of air-sea gas transfer during an open ocean algal bloom, *J Geophys Res*, *27*(14), 2117--2120.

Nijampurkar, V., and D. Rao (1993), Polar Fallout of Radionuclides Si-32, Be-7 and Pb-210 and Past Accumulation Rate of Ice at Indian Station, Dakshin Gangotri, East Antarctica, *J Environ Radioactiv*, *21*(2), 107--117.

Olivier, J. G. (2001), *Global emissions sources and sinks*, The Climate System, A. A. Balkema Publishers/Swets & Zeitlinger Publishers, Lisse, Netherlands.

Olivier, J. G. J., and J. J. M. Berdowski (2001), *Global Emissions sources and sinks*, The Climate System, A A Balkema Publishers/Swets & Zeitlinger Publishers, Lisse, The Netherlands.

Olsen, C., I. Larsen, P. Lowry, N. Cutshall, J. Todd, G. Wong, and W. Casey (1985), Atmospheric Fluxes and Marsh-Soil Inventories of Be-7 and Pb-210, *J Geophys Res-Atmos*, *90*, 10,487--10,495.

Oman, L. D., J. R. Ziemke, A. R. Douglass, D. W. Waugh, C. Lang, J. M. Rodriguez, and J. E. Nielsen (2011), The response of tropical tropospheric ozone to ENSO, *Geophys Res Lett*, *38*.

Ott, L. E., K. E. Pickering, G. L. Stenchikov, H. Huntrieser, and U. Schumann (2007), Effects of lightning NOx production during the 21 July European Lightning Nitrogen Oxides Project storm studied with a three-dimensional cloud-scale chemical transport model, *J Geophys Res-Atmos*, *112*.

Ott, L. E., K. E. Pickering, G. L. Stenchikov, D. J. Allen, A. J. DeCaria, B. Ridley, R.-F. Lin, S. Lang, and W.-K. Tao (2010), Production of lightning NOx and its vertical distribution calculated from three-dimensional cloud-scale chemical transport model simulations, *J Geophys Res-Atmos*, *115*.

Papastefanou, C. (2009), Beryllium-7 Aerosols in Ambient Air, *Aerosol Air Qual Res*, *9*(2), 187--197.

Papastefanou, C., and A. Ioannidou (1996), Beryllium-7 aerosols in ambient air, in *Environ Int*, pp. S125--S130.

Papastefanou, C., A. Ioannidou, S. Stoulos, and M. Manolopoulou (1995), Atmospheric Deposition of Cosmogenic Be-7 and Cs-137 From Fallout of the Chernobyl Accident, *Sci Total Environ*, *170*, 151--156.

Park, R., D. J. Jacob, B. Field, R. Yantosca, and M. Chin (2004), Natural and transboundary pollution influences on sulfate-nitrate-ammonium aerosols in the United States: Implications for policy, *J Geophys Res-Atmos*, *109*.

Parrella, J. P., D. J. Jacob, Q. Liang, Y. Zhang, L. J. Mickley, B. Miller, M. Evans, X. Yang, J. A. Pyle, N. Theys, and M. Van Roozendael (2012), Tropospheric bromine chemistry: implications for present and pre-industrial ozone and mercury, *Atmos Chem Phys*, *12*, 6723--6740.

Pausata, F. S. R., C. Li, J. J. Wettstein, M. Kageyama, and K. H. Nisancioglu (2011), The key role of topography in altering North Atlantic atmospheric circulation during the last glacial period, *Clim. Past*, *7*(4), 1089--1101.

Pavelin, E. G., C. E. Johnson, S. Rughooputh, and R. Toumi (1999), Evaluation of pre-industrial surface ozone measurements made using Schönbein's method, *Atmos Environ*, *33*(6), 919--929.

Petersen, W., H. Christian, and S. Rutledge (2005), TRMM observations of the global relationship between ice water content and lightning, *Geophys Res Lett*, *32*(14).

Pfeiffer, M., and J. O. Kaplan (2012), SPITFIRE-2: an improved fire module for Dynamic Global Vegetation Models.

Pickering, K., A. M. Thompson, R. Dickerson, W. Luke, D. Mcnamara, J. Greenberg, and P. Zimmerman (1990), Model-Calculations of Tropospheric Ozone Production Potential Following Observed Convective Events, *J Geophys Res-Atmos*, *95*, 14,049--14,062.

Pickering, K., A. M. Thompson, W. Tao, and T. Kucsera (1993), Upper Tropospheric Ozone Production Following Mesoscale Convection During STEP/EMEX, *J Geophys Res-Atmos*, *98*, 8737--8749.

Pickering, K., Y. Wang, W. Tao, C. Price, and J. Muller (1998), Vertical distributions of lightning NOx for use in regional and global chemical transport models, *J Geophys Res-Atmos*, *103*, 31,203--31,216.

Pinto, J. P., and M. Khalil (1991), The stability of tropospheric OH during ice ages, inter□glacial epochs and modern times, *Tellus B*, *43*(5), 347--352.

Power, M. J., J. Marlon, N. Ortiz, P. J. Bartlein, S. P. Harrison, F. E. Mayle, A. Ballouche, R. H. W. Bradshaw, C. Carcaillet, C. Cordova, S. Mooney, P. I. moreno, I. C. Prentice, K. Thonicke, W. Tinner, C. Whitlock, Y. Zhang, Y. Zhao, A. A. Ali, R. S. Anderson, R. Beer, H. Behling, C. Briles, K. J. Brown, A. Brunelle, M. Bush, P. Camill, G. Q. Chu, J. Clark, D. Colombaroli, S. Connor, A. L. Daniau, M. Daniels, J. Dodson, E. Doughty, M. E. Edwards, W. Finsinger, D. Foster, J. Frechette, M. J. Gaillard, D. G. Gavin, E. Gobet, S. Haberle, D. J. Hallett, P. Higuera, G. Hope, S. Horn, J. Inoue, P. Kaltenrieder, L. Kennedy, Z. C. Kong, C. Larsen, C. J. Long, J. Lynch, E. A. Lynch, M. McGlone, S. Meeks, S. Mensing, G. Meyer, T. Minckley, J. Mohr, D. M. Nelson, J. New, R. Newnham, R. Noti, W. Oswald, J. Pierce, P. J. H. Richard, C. Rowe, M. F. Sanchez Goñi, B. N. Shuman, H. Takahara, J. Toney, C. Turney, D. H. Urrego-Sanchez, C. Umbanhowar, M. Vandergoes, B. Vanniere, E. Vescovi, M. Walsh, X. Wang, N. Williams, J. Wilmshurst, and J. H. Zhang (2008), Changes in fire regimes since the Last Glacial Maximum: an assessment based on a global synthesis and analysis of charcoal data, *Climate Dynamics*, *30*(7-8), 887--907.

Power, M. J., J. R. Marlon, P. J. Bartlein, and S. P. Harrison (2010), Fire history and the Global Charcoal Database: A new tool for hypothesis testing and data exploration, *Atmos Environ*, *291*(1-2), 52--59.

Prather, M. (1986), Numerical Advection by Conservation of 2nd-Order Moments, *J Geophys Res-Atmos*, *91*, 6671--6681.

Prather, M., and C. Spivakovsky (1990), Tropospheric OH and the Lifetimes of Hydrochlorofluorocarbons, *J Geophys Res-Atmos*, *95*, 18,723--18,729.

Prather, M. J., C. D. Holmes, and J. Hsu (2012), Reactive greenhouse gas scenarios: Systematic exploration of uncertainties and the role of atmospheric chemistry, *Geophys Res Lett*, *39*(9), L09,803.

Preiss, N., M. Melieres, and M. Pourchet (1996), A compilation of data on lead 210 concentration in surface air and fluxes at the air-surface and water-sediment interfaces, *J Geophys Res-Atmos*, *101*, 28,847--28,862.

Price, C., and D. Rind (1992), A Simple Lightning Parameterization for Calculating Global Lightning Distributions, *J Geophys Res-Atmos*, *97*, 9919--9933.

Price, C., and D. Rind (1993), What Determines the Cloud-to-Ground Lightning Fraction in Thunderstorms, *Geophys Res Lett*, *20*(6), 463--466.

Price, C., and D. Rind (1994), Modeling Global Lightning Distributions in a General-Circulation Model, *Mon Weather Rev*, *122*(8), 1930--1939.

Price, C., J. Penner, and M. Prather (1997), NOx from lightning .1. Global distribution based on lightning physics, *J Geophys Res-Atmos*, *102*, 5929--5941.

Prinn, R., J. Huang, R. Weiss, D. Cunnold, P. Fraser, P. Simmonds, A. McCulloch, C. Harth, P. Salameh, S. O'Doherty, R. Wang, L. Porter, and B. Miller (2001), Evidence for substantial variations of atmospheric hydroxyl radicals in the past two decades, *Science*, *292*(5523), 1882--1888.

Prinn, R., J. Huang, R. Weiss, D. Cunnold, P. Fraser, P. Simmonds, A. McCulloch, C. Harth, S. Reimann, P. Salameh, S. O'Doherty, R. Wang, L. Porter, B. Miller, and P. Krummel (2005), Evidence for variability of atmospheric hydroxyl radicals over the past quarter century, *Geophys Res Lett*, *32*(7).

Pye, H., H. Liao, S. Wu, L. J. Mickley, D. J. Jacob, D. K. Henze, and J. H. Seinfeld (2009), Effect of changes in climate and emissions on future sulfate-nitrate-ammonium aerosol levels in the United States, *J Geophys Res*, *114*(D1), D01,205.

Pyne, S. (2001), *Fire: A Brief History*, University of Washington Press.

Rakov, V. A., and M. A. Uman (2003), *Lightning Physics and Effects*, Cambridge University Press, Cambridge, United Kingdom.

Ray, E. A., F. L. Moore, K. H. Rosenlof, S. M. Davis, H. Boenisch, O. Morgenstern, D. Smale, E. Rozanov, M. Hegglin, G. Pitari, E. Mancini, P. Braesicke, N. Butchart, S. Hardiman, F. Li, K. Shibata, and D. A. Plummer (2010), Evidence for changes in stratospheric transport and mixing over the past three decades based on multiple data sets and tropical leaky pipe analysis, *J Geophys Res*, *115*(D21), D21,304.

Rayner, N. A., D. E. Parker, E. B. Horton, C. K. Folland, L. V. Alexander, D. P. Rowell, E. C. Kent, and A. Kaplan (2003), Global analyses of sea surface temperature, sea ice, and night marine air temperature since the late nineteenth century, *J Geophys Res*, *108*(D14), 4407.

Rehfeld, S., and M. Heimann (1995), Three dimensional atmospheric transport simulation of the radioactive tracers Pb-210, Be-7, Be-10, and Sr-90, *J Geophys Res-Atmos*, *100*, 26,141--26,161.

Ridley, D. A., C. L. Heald, and B. Ford (2012), North African dust export and deposition: A satellite and model perspective, *J Geophys Res*, *117*(D2), D02,202.

Rigby, M., J. Mühle, B. R. Miller, R. G. Prinn, P. B. Krummel, L. P. Steele, P. J. Fraser, P. K. Salameh, C. M. Harth, R. F. Weiss, B. R. Greally, S. O'Doherty, P. G. Simmonds, M. K. Vollmer, S. Reimann, J. Kim, K. R. Kim, H. J. Wang, J. G. J. Olivier, E. J. Dlugokencky, G. S. Dutton, B. D. Hall, and J. W. Elkins (2010), History of atmospheric SF_6 from 1973 to 2008, *Atmos Chem Phys*, *10*(21), 10,305--10,320.

Rind, D. (2009), Atmospheric circulation during the Last Glacial Maximum, in *Encyclopedia of Paleoclimatology and Ancient Environments*, pp. 57--61, Springer.

Rind, D., and D. Peteet (1985), Terrestrial conditions at the Last Glacial Maximum and CLIMAP sea-surface temperature estimates: Are they consistent?, *Atmos Environ*, *24*(1), 1--22.

Rind, D., M. Chandler, P. Lonergan, and J. Lerner (2001), Climate change and the middle atmosphere 5. Paleostratosphere in cold and warm climates, *J Geophys Res*, *106*(D17), 20,195--20,212.

Rind, D., J. Lerner, J. Jonas, and C. McLinden (2007), Effects of resolution and model physics on tracer transports in the NASA Goddard Institute for Space Studies general circulation models, *J Geophys Res-Atmos*, *112*(D9), D09,315.

Rind, D., J. Lerner, C. McLinden, and J. Perlwitz (2009), Stratospheric ozone during the Last Glacial Maximum, *Geophys Res Lett*, *36*.

Roelofs, G.-J., J. Lelieveld, and R. van Dorland (1997), A three-dimensional chemistry/general circulation model simulation of anthropogenically derived ozone in the troposphere and its radiative climate forcing, *J Geophys Res*, *102*(D19), 23,389.

Rothlisberger, R., M. Hutterli, E. W. Wolff, R. Mulvaney, H. Fischer, M. Bigler, K. Goto-Azuma, M. E. Hansson, U. Ruth, M. L. Siggaard-Andersen, and J. P. Steffensen (2002), Nitrate in Greenland and Antarctic ice cores: a detailed description of post-depositional processes, *Annals of Glaciology*, *35*, 210--216.

Rothlisberger, R., M. Mudelsee, M. Bigler, M. De Angelis, H. Fischer, M. Hansson, F. Lambert, V. Masson-Delmotte, L. Sime, R. Udisti, and E. W. Wolff (2008), The Southern Hemisphere at glacial terminations: insights from the Dome C ice core, *Clim. Past*, *4*(4), 345--356.

Röthlisberger, R., X. Crosta, N. J. Abram, L. Armand, and E. W. Wolff (2010), Potential and limitations of marine and ice core sea ice proxies: an example from the Indian Ocean sector, *Quaternary Science Reviews*, *29*(1-2), 296--302.

Sanak, J., A. Gaudry, and G. Lambert (1981), Size Distribution of Pb-210 Aerosols Over Oceans, *Geophys Res Lett*, *8*(10), 1067--1069.

Sanak, J., G. Lambert, and B. Ardouin (1985), Measurement of Stratosphere-to-Troposphere Exchange in Antarctica by Using Short-Lived Cosmonuclides, *Tellus B*, *37*(2), 109--115.

Sander, R., W. C. Keene, A. A. P. Pszenny, R. Arimoto, G. P. Ayers, E. Baboukas, J. M. Cainey, P. J. Crutzen, R. A. Duce, G. Hönninger, B. J. Huebert, W. Maenhaut, N. Mihalopoulos, V. C. Turekian, and R. Van Dingenen (2003), Inorganic bromine in the marine boundary layer: a critical review, *Atmos Chem Phys*, *3*(5), 1301--1336.

Sander, R., A. Kerkweg, P. Jöckel, and J. Lelieveld (2005), Technical note: The new comprehensive atmospheric chemistry module MECCA, *Atmos Chem Phys*, *5*, 445--450.

Sander, S. P., R. R. Friedl, J. P. D. Abbatt, J. R. Barker, J. B. Burkholder, D. M. Golden, C. E. Kolb, M. J. Kurylo, G. K. Moortgat, P. H. Wine, R. E. Huie, and V. L. Orkin (2011), Chemical Kinetics and Photochemical Data for Use in Atmospheric Studies, *Tech. rep*.

Satori, G., E. Williams, and I. Lemperger (2009), Variability of global lightning activity on the ENSO time scale, in *Atmos Res*, pp. 500--507, HAS, Geodet & Geophys Res Inst, H-9401 Sopron, Hungary.

Sauvage, B., V. Thouret, A. M. Thompson, J. Witte, J. Cammas, P. Nedelec, and G. Athier (2006), Enhanced view of the "tropical Atlantic ozone paradox" and "zonal wave one" from the in situ MOZAIC and SHADOZ data, *J Geophys Res-Atmos*, *111*.

Sauvage, B., R. V. Martin, A. van Donkelaar, X. Liu, K. Chance, L. Jaeglé, P. I. Palmer, S. Wu, and T. M. Fu (2007a), Remote sensed and in situ constraints on processes affecting tropical tropospheric ozone, *Atmos Chem Phys*, *7*, 815--838.

Sauvage, B., R. V. Martin, A. van Donkelaar, and J. R. Ziemke (2007b), Quantification of the factors controlling tropical tropospheric ozone and the South Atlantic maximum, *J Geophys Res-Atmos*, *112*.

Savarino, J., C. Lee, and M. H. Thiemens (2000), Laboratory oxygen isotopic study of sulfur (IV) oxidation: Origin of the mass-independent oxygen isotopic anomaly in atmospheric sulfates and sulfate mineral deposits on Earth, *J Geophys Res-Atmos*, *105*, 29,079--29,088.

Schmidt, G. A., and D. T. Shindell (2003), Atmospheric composition, radiative forcing, and climate change as a consequence of a massive methane release from gas hydrates, *Paleoceanography*, *18*(1), 1004.

Schmidt, G. A., R. Ruedy, J. Hansen, I. Aleinov, N. Bell, M. Bauer, S. Bauer, B. Cairns, V. Canuto, Y. Cheng, A. Del Genio, G. Faluvegi, A. Friend, T. Hall, Y. Hu, M. Kelley, N. Kiang, D. Koch, A. Lacis, J. Lerner, K. Lo, R. Miller, L. Nazarenko, V. Oinas, J. Perlwitz, J. Perlwitz, D. Rind, A. Romanou, G. Russell, M. Sato, D. T. Shindell, P. Stone, S. Sun, N. Tausnev, D. Thresher, and M. Yao (2006), Present-day atmospheric simulations using GISS ModelE: Comparison to in situ, satellite, and reanalysis data, *Journal of Climate*, *19*(2), 153--192.

Schuler, C., E. Wieland, P. Santschi, M. Sturm, A. Lueck, S. Bollhalder, J. Beer, G. Bonani, H. Hofmann, M. Suter, and W. Wolfli (1991), A Multitracer Studyof Radionuclides in Lake Zurich, Switzerland .1. Comparison of Atmospheric and Sedimentary Fluxes of Be-7, Be-10, Pb-210, Po-210, and Cs-137, *J Geophys Res-Oceans*, *96*, 17,051--17,065.

Schumann, U., and H. Huntrieser (2007), The global lightning-induced nitrogen oxides source, *Atmos Chem Phys*, *7*(14), 3823--3907.

Shepherd, T. G., and C. McLandress (2011), A Robust Mechanism for Strengthening of the Brewer-Dobson Circulation in Response to Climate Change: Critical-Layer Control of Subtropical Wave Breaking, *J Atmos Sci*, *68*(4), 784--797.

Sherwood, S. C., R. Roca, T. M. Weckwerth, and N. G. Andronova (2010), Tropospheric water vapor, convection, and climate, *Rev Geophys*, *48*(2), RG2001.

Shindell, D. T. (2001), Solar Forcing of Regional Climate Change During the Maunder Minimum, *Science*, *294*(5549), 2149--2152.

Shindell, D. T., J. Grenfell, D. Rind, V. Grewe, and C. Price (2001), Chemistry-climate interactions in the Goddard Institute for Space Studies general circulation model 1. Tropospheric chemistry model description and evaluation, *J Geophys Res-Atmos*, *106*, 8047--8075.

Shindell, D. T., G. Faluvegi, and N. Bell (2003), Preindustrial-to-present-day radiative forcing by tropospheric ozone from improved simulations with the GISS chemistry-climate GCM, *Atmos Chem Phys*, *3*(5), 1675--1702.

Shindell, D. T., G. Faluvegi, D. S. Stevenson, M. C. Krol, L. K. Emmons, J. F. Lamarque, G. Petron, F. J. Dentener, K. Ellingsen, M. G. Schultz, O. Wild, M. Amann, C. S. Atherton, D. J. Bergmann, I. Bey, T. Butler, J. Cofala, W. J. Collins, R. G. Derwent, R. M. Doherty, J. Drevet, H. J. Eskes, A. M. Fiore, M. Gauss, D. A. Hauglustaine, L. W. Horowitz, I. S. A. Isaksen, M. G. Lawrence, V. Montanaro, J. F. Mueller, G. Pitari, M. J. Prather, J. A. Pyle, S. Rast, J. M. Rodriguez, M. G. Sanderson, N. H. Savage, S. E. Strahan, K. Sudo, S. Szopa, N. Unger, van Noije, T. P. C., and G. Zeng (2006a), Multimodel simulations of carbon monoxide: Comparison with observations and projected near-future changes, *J Geophys Res-Atmos*, *111*.

Shindell, D. T., G. Faluvegi, N. Unger, E. Aguilar, G. A. Schmidt, D. M. Koch, S. E. Bauer, and R. L. Miller (2006b), Simulations of preindustrial, present-day, and 2100 conditions in the NASA GISS composition and climate model G-PUCCINI, *Atmos Chem Phys*, *6*, 4427--4459.

Shindell, D. T., G. Faluvegi, S. E. Bauer, D. M. Koch, N. Unger, S. Menon, R. L. Miller, G. A. Schmidt, and D. G. Streets (2007), Climate response to projected changes in short-lived species under an A1B scenario from 2000-2050 in the GISS climate model, *J Geophys Res-Atmos*, *112*.

Shindell, D. T., H. I. Levy, M. D. Schwarzkopf, L. W. Horowitz, J.-F. Lamarque, and G. Faluvegi (2008), Multimodel projections of climate change from short-lived emissions due to human activities, *J Geophys Res-Atmos*, *113*.

Shiotani, M. (1992), Annual, Quasi-Biennial, and El Niño-Southern Oscillation (ENSO) Time-Scale Variations in Equatorial Total Ozone, *J Geophys Res-Atmos*, *97*, 7625--7633.

Sillman, S., J. A. Logan, and S. C. Wofsy (1990), The Sensitivity of Ozone to Nitrogen-Oxides and Hydrocarbons in Regional Ozone Episodes, *J Geophys Res-Atmos*, *95*, 1837--1851.

Singarayer, J. S., P. J. Valdes, P. Friedlingstein, S. Nelson, and D. J. Beerling (2011), Late Holocene methane rise caused by orbitally controlled increase in tropical sources, *Nature*, *470*(7332), 82--85.

Singh, H. (1977), Preliminary Estimation of Average Tropospheric HO Concentrations in Northern and Southern Hemispheres, *Geophys Res Lett*, *4*(10), 453--456.

Sitch, S., P. M. Cox, W. J. Collins, and C. Huntingford (2007), Indirect radiative forcing of climate change through ozone effects on the land-carbon sink, *Nature*, *448*(7155), 791--794.

Sofen, E. D., B. Alexander, and S. A. Kunasek (2011), The impact of anthropogenic emissions on atmospheric sulfate production pathways, oxidants, and ice core $\Delta^{17}O(SO_4^{2-})$, *Atmos Chem Phys*, *11*(7), 3565--3578.

Spivakovsky, C., R. Yevich, J. A. Logan, S. C. Wofsy, M. McElroy, and M. Prather (1990), Tropospheric OH in a Three-Dimensional Chemical Tracer Model - An Assessment Based on Observations of CH_3CCl_3, *J Geophys Res-Atmos*, *95*, 18,441--18,471.

Spivakovsky, C., J. A. Logan, S. Montzka, Y. Balkanski, M. Foreman-Fowler, D. Jones, L. Horowitz, A. Fusco, C. Brenninkmeijer, M. Prather, S. C. Wofsy, and M. McElroy (2000), Three-dimensional climatological distribution of tropospheric OH: Update and evaluation, *J Geophys Res-Atmos*, *105*, 8931--8980.

Staffelbach, T., A. Neftel, B. Stauffer, and D. J. Jacob (1991), A Record of the Atmospheric Methane Sink From Formaldehyde in Polar Ice Cores, *Nature*, *349*(6310), 603--605.

Stajner, I., K. Wargan, S. Pawson, H. Hayashi, L.-P. Chang, R. C. Hudman, L. Froidevaux, N. Livesey, P. F. Levelt, A. M. Thompson, D. W. Tarasick, R. Stuebi, S. B. Andersen, M. Yela, G. Koenig-Langlo, F. J. Schmidlin, and J. C. Witte (2008), Assimilated ozone from EOS-Aura: Evaluation of the tropopause region and tropospheric columns, *J Geophys Res-Atmos*, *113*.

Stevenson, D., F. Dentener, M. Schultz, K. Ellingsen, T. van Noije, O. Wild, G. Zeng, M. Amann, C. Atherton, N. Bell, D. Bergmann, I. Bey, T. Butler, J. Cofala, W. Collins, R. Derwent, R. Doherty, J. Drevet, H. Eskes, A. Fiore, M. Gauss, D. Hauglustaine, L. Horowitz, I. Isaksen, M. Krol, J. Lamarque, M. Lawrence, V. Montanaro, J. Muller, G. Pitari, M. Prather, J. Pyle, S. Rast, J. Rodriguez, M. Sanderson, N. Savage, D. T. Shindell, S. Strahan, K. Sudo, and S. Szopa (2006), Multimodel ensemble simulations of present-day and near-future tropospheric ozone, *J Geophys Res-Atmos*, *111*.

Stockwell, D., M. Kritz, M. Chipperfield, and J. Pyle (1998), Validation of an off-line three-dimensional chemical transport model using observed radon profiles - 2. Model results, *J Geophys Res-Atmos*, *103*, 8433--8445.

Streets, D., T. Bond, G. Carmichael, S. Fernandes, Q. Fu, D. He, Z. Klimont, S. Nelson, N. Tsai, M. Wang, J. Woo, and K. Yarber (2003), An inventory of gaseous and primary aerosol emissions in Asia in the year 2000, *J Geophys Res-Atmos*, *108*.

Streets, D. G., Q. Zhang, L. Wang, K. He, J. Hao, Y. Wu, Y. Tang, and G. R. Carmichael (2006), Revisiting China's CO emissions after the Transport and Chemical Evolution over the Pacific (TRACE-P) mission: Synthesis of inventories, atmospheric modeling, and observations, *J Geophys Res-Atmos*, *111*.

Sudo, K., and M. Takahashi (2001), Simulation of tropospheric ozone changes during 1997-1998 El Nino: Meteorological impact on tropospheric photochemistry, *Geophys Res Lett*, *28*(21), 4091--4094.

Thiemens, M. H. (2006), History and applications of mass-independent isotope effects, *Annu Rev Earth Planet Sci*, *34*, 217--262.

Thompson, A. M. (1992), The Oxidizing Capacity of the Earths Atmosphere - Probable Past and Future Changes, *Science*, *256*(5060), 1157--1165.

Thompson, A. M., and R. Hudson (1999), Tropical tropospheric ozone (TTO) maps from Nimbus 7 and Earth Probe TOMS by the modified-residual method: Evaluation with sondes, ENSO signals, and trends from Atlantic regional time series, in *J Geophys Res-Atmos*, pp. 26,961--26,975, Univ Maryland, Dept Meteorol, College Pk, MD 20742 USA.

Thompson, A. M., J. Chappellaz, I. Y. Fung, and T. Kucsera (1993), The atmospheric CH4 increase since the Last Glacial Maximum. (2). Interactions with oxidants, *Tellus B*, *45*(3), 242--257.

Thompson, A. M., B. Doddridge, J. Witte, R. Hudson, W. Luke, J. Johnston, B. Johnston, S. Oltmans, and R. Weller (2000), A tropical Atlantic paradox: Shipboard and satellite views of a tropospheric ozone maximum and wave-one in January-February 1999., *Geophys Res Lett*, *27*(20), 3317--3320.

Thompson, A. M., J. Witte, R. McPeters, S. Oltmans, F. Schmidlin, J. A. Logan, M. Fujiwara, V. Kirchhoff, F. Posny, G. Coetzee, B. Hoegger, S. Kawakami, T. Ogawa, B. Johnson, H. Vomel, and G. Labow (2003a), Southern Hemisphere Additional Ozonesondes (SHADOZ) 1998-2000 tropical ozone climatology - 1. Comparison with Total Ozone Mapping Spectrometer (TOMS) and ground-based measurements, *J Geophys Res-Atmos*, *108*.

Thompson, A. M., J. Witte, S. Oltmans, F. Schmidlin, J. A. Logan, M. Fujiwara, V. Kirchhoff, F. Posny, G. Coetzee, B. Hoegger, S. Kawakami, T. Ogawa, J. Fortuin, and H. Kelder (2003b), Southern Hemisphere Additional Ozonesondes (SHADOZ) 1998-2000 tropical ozone climatology - 2. Tropospheric variability and the zonal wave-one, *J Geophys Res-Atmos*, *108*.

Thonicke, K., I. C. Prentice, and C. Hewitt (2005), Modeling glacial-interglacial changes in global fire regimes and trace gas emissions, *Global Biogeochem Cy*, *19*(3), n/a--n/a.

Tie, X., S. Madronich, S. Walters, D. P. Edwards, P. Ginoux, N. Mahowald, R. Y. Zhang, C. Lou, and G. Brasseur (2005), Assessment of the global impact of aerosols on tropospheric oxidants, *J Geophys Res*, *110*(D3), D03,204.

Tost, H., P. J. Joeckel, and J. Lelieveld (2007), Lightning and convection parameterisations - uncertainties in global modelling, *Atmos Chem Phys*, *7*(17), 4553--4568.

Turekian, K., Y. Nozaki, and L. Benninger (1977), Geochemistry of Atmospheric Radon and Radon Products, *Annu Rev Earth Planet Sci*, *5*, 227--255.

Turekian, K., L. Benninger, and E. DION (1983), Be-7 and Pb-210 Total Deposition Fluxes at New-Haven, Connecticut and at Bermuda, *J Geophys Res-Oc Atm*, *88*, 5411--5415.

Usoskin, I., K. Alanko-Huotari, G. Kovaltsov, and K. Mursula (2005), Heliospheric modulation of cosmic rays: Monthly reconstruction for 1951-2004, *J Geophys Res-Space*, *110*.

Usoskin, I. G., and G. A. Kovaltsov (2008), Production of cosmogenic Be-7 isotope in the atmosphere: Full 3-D modeling, *J Geophys Res-Atmos*, *113*.

Valdes, P., D. Beerling, and C. Johnson (2005), The ice age methane budget, *Geophys Res Lett*, *32*(2).

Valentin, M. K. (1990), Numerical modeling of the climatological and anthropogenic influences on the chemical composition of the troposphere since the Last Glacial Maximum, Ph.D. thesis, Johannes Gutenburg Univ., Mainz, Germany.

van der Werf, G. R., J. T. Randerson, L. Giglio, G. J. Collatz, P. S. Kasibhatla, and A. F. J. Arellano (2006), Interannual variability in global biomass burning emissions from 1997 to 2004, *Atmos Chem Phys*, *6*, 3423--3441.

van der Werf, G. R., J. T. Randerson, L. Giglio, G. J. Collatz, M. Mu, P. S. Kasibhatla, D. C. Morton, R. S. DeFries, Y. Jin, and T. T. van Leeuwen (2010), Global fire emissions and the contribution of deforestation, savanna, forest, agricultural, and peat fires (1997-2009), *Atmos Chem Phys*, *10*(23), 11,707--11,735.

van der Werf, G. R., W. Peters, T. T. van Leeuwen, and L. Giglio (2013), What could have caused pre-industrial biomass burning emissions to exceed current rates?, *Clim. Past*, *9*(1), 289--306.

van Donkelaar, A., R. V. Martin, W. R. Leaitch, A. M. Macdonald, T. W. Walker, D. G. Streets, Q. Zhang, E. J. Dunlea, J. L. Jimenez, J. E. Dibb, L. G. Huey, R. Weber, and M. O. Andreae (2008), Analysis of aircraft and satellite measurements from the Intercontinental Chemical Transport Experiment (INTEX-B) to quantify long-range transport of East Asian sulfur to Canada, *Atmos Chem Phys*, *8*(11), 2999--3014.

vanOmmen, T., and V. Morgan (1996), Peroxide concentrations in the Dome Summit South ice core, Law Dome, Antarctica, *J Geophys Res-Atmos*, *101*, 15,147--15,152.

Viezee, W., and H. Singh (1980), The Distribution of Beryllium-7 in the Troposphere - Implications on Stratospheric-Tropospheric Air Exchange, *Geophys Res Lett*, *7*(10), 805--808.

Voulgarakis, A., V. Naik, J. F. Lamarque, D. T. Shindell, P. J. Young, M. J. Prather, O. Wild, R. D. Field, D. Bergmann, P. Cameron-Smith, I. Cionni, W. J. Collins, S. B. Dalsøren, R. M. Doherty, V. Eyring, G. Faluvegi, G. A. Folberth, L. W. Horowitz, B. Josse, I. A. MacKenzie, T. Nagashima, D. A. Plummer, M. Righi, S. T. Rumbold, D. S. Stevenson, S. A. Strode, K. Sudo, S. Szopa, and G. Zeng (2013), Analysis of present day and future OH and methane lifetime in the ACCMIP simulations, *Atmos Chem Phys*, *13*(5), 2563--2587.

Wallbrink, P., and A. Murray (1994), Fallout of Be-7 in South Eastern Australia, *J Environ Radioactiv*, *25*(3), 213--228.

Wang, Q., D. J. Jacob, J. A. Fisher, J. Mao, E. M. Leibensperger, C. C. Carouge, P. Le Sager, Y. Kondo, J. L. Jimenez, M. J. Cubison, and S. J. Doherty (2011), Sources of carbonaceous aerosols and deposited black carbon in the Arctic in winter-spring: implications for radiative forcing, *Atmos Chem Phys*, *11*(23), 12,453--12,473.

Wang, Y., and D. J. Jacob (1998), Anthropogenic forcing on tropospheric ozone and OH since preindustrial times, *J Geophys Res-Atmos*, *103*, 31,123--31,135.

Wang, Y., D. J. Jacob, and J. A. Logan (1998), Global simulation of tropospheric O3-NOx-hydrocarbon chemistry 1. Model formulation, *J Geophys Res-Atmos*, *103*, 10,713--10,725.

Wang, Z., J. Chappellaz, K. Park, and J. E. Mak (2010), Large variations in Southern Hemisphere biomass burning during the last 650 years, *Science*, *330*(6011), 1663--1666.

Warwick, N. J., J. A. Pyle, G. D. Carver, X. Yang, N. H. Savage, F. M. O'Connor, and R. A. Cox (2006), Global modeling of biogenic bromocarbons, *J Geophys Res*, *111*(D24), D24,305.

Waters, J., L. Froidevaux, R. Harwood, R. Jarnot, H. Pickett, W. Read, P. Siegel, R. Cofield, M. Filipiak, D. Flower, J. Holden, G. Lau, N. Livesey, G. Manney, H. Pumphrey, M. Santee, D. Wu, D. Cuddy, R. Lay, M. Loo, V. Perun, M. Schwartz, P. Stek, R. Thurstans, M. Boyles, K. Chandra, M. Chavez, G. Chen, Chudasama, BV, R. Dodge, R. Fuller, M. Girard, J. Jiang, Y. Jiang, B. Knosp, R. LaBelle, J. Lam, K. Lee, D. Miller, J. Oswald, N. Patel, D. Pukala, O. Quintero, D. Scaff, W. Van Snyder, M. Tope, P. Wagner, and M. Walch (2006), The Earth Observing System Microwave Limb Sounder (EOS MLS) on the Aura satellite, *IEEE T Geosci Remote*, *44*(5), 1075--1092.

Waugh, D. W., and T. M. Hall (2002), Age of stratospheric air: Theory, observations, and models, *Rev Geophys*, *40*(4), 1010.

Wayne, R. P., I. Barnes, P. Biggs, J. P. Burrows, C. E. Canosa-Mas, J. Hjorth, G. Le Bras, G. K. Moortgat, D. Perner, G. Poulet, G. Restelli, and H. Sidebottom (1991), The nitrate radical: Physics, chemistry, and the atmosphere, *Atmos Environ*, *25*(1), 1--203.

Webb, R., D. Rind, S. Lehman, R. Healy, and D. Sigman (1997), Influence of ocean heat transport on the climate of the Last Glacial Maximum, *Nature*, *385*(6618), 695--699.

Weber, S. L., A. J. Drury, W. H. J. Toonen, and M. van Weele (2010), Wetland methane emissions during the Last Glacial Maximum estimated from PMIP2 simulations: Climate, vegetation, and geographic controls, *J Geophys Res*, *115*(D6), D06,111.

Wesely, M. (1989), Parameterization of Surface Resistances to Gaseous Dry Deposition in Regional-Scale Numerical-Models, *Atmos Environ*, *23*(6), 1293--1304.

Wilkening, M. (1970), Rn-222 Concentrations in Convective Patterns of a Mountain Environment, *J Geophys Res*, *75*(9), 1733.

Wilks, D. S. (2011), *Statistical Methods in the Atmospheric Sciences*, *International Geophysics Series*, vol. 100, 3 ed., Elsevier Academic Press, Oxford, UK.

Williams, E. (1985), Large-Scale Charge Separation in Thunderclouds, *J Geophys Res-Atmos*, *90*, 6013--6025.

Williams, E. (1992), The Schumann Resonance - a Global Tropical Thermometer, *Science*, *256*(5060), 1184--1187.

Williams, E. (2005), Lightning and climate: A review, in *Atmos Res*, pp. 272--287, MIT, Cambridge, MA 02139 USA.

Williams, E., V. Mushtak, D. Rosenfeld, S. Goodman, and D. Boccippio (2005), Thermodynamic conditions favorable to superlative thunderstorm updraft, mixed phase microphysics and lightning flash rate, in *Atmos Res*, pp. 288--306, MIT, Cambridge, MA 02139 USA.

WMO (2011), *Scientific Assessment of Ozone Depletion: 2010, Global Ozone Research and Monitoring Project - Report No. 52*, World Meteorological Organization.

Wolff, E. W. (2003), An ice core indicator of Antarctic sea ice production?, *Geophys Res Lett*, *30*(22), 2158.

Wolff, E. W. (2012), Chemical signals of past climate and environment from polar ice cores and firn air, *Chem. Soc. Rev.*, *41*(19), 6247--6258.

Wolff, E. W., H. Fischer, F. Fundel, U. Ruth, B. Twarloh, G. C. Littot, R. Mulvaney, R. Röthlisberger, M. De Angelis, C. F. Boutron, M. Hansson, U. Jonsell, M. Hutterli, F. Lambert, A. J. Kaufmann, B. Stauffer, M. Severi, D. Wagenbach, C. Barbante, P. Gabrielli, and V. Gaspari (2006), Southern Ocean sea-ice extent, productivity and iron flux over the past eight glacial cycles, *Nature*, *440*(7083), 491--496.

Wolff, E. W., C. Barbante, S. Becagli, M. Bigler, C. F. Boutron, E. Castellano, M. De Angelis, U. Federer, H. Fischer, F. Fundel, M. Hansson, M. A. Hutterli, U. Jonsell, T. Karlin, P. Kaufmann, F. Lambert, G. C. Littot, R. Mulvaney, R. Rothlisberger, U. Ruth, M. Severi, M. L. Siggaard-Andersen, L. C. Sime, J. P. Steffensen, T. Stocker, R. Traversi, B. Twarloh, R. Udisti, D. Wagenbach, and A. Wegner (2010), Changes in environment over the last 800,000 years from chemical analysis of the EPICA Dome C ice core, *Quaternary Science Reviews*, *29*(1), 285--295.

Wu, H., J. Guiot, S. Brewer, and Z. Guo (2007a), Climatic changes in Eurasia and Africa at the last glacial maximum and mid-Holocene: reconstruction from pollen data using inverse vegetation modelling, *Climate Dynamics*, *29*(2), 211--229.

Wu, S., L. J. Mickley, D. J. Jacob, J. A. Logan, R. M. Yantosca, and D. Rind (2007b), Why are there large differences between models in global budgets of tropospheric ozone?, *J Geophys Res-Atmos*, *112*.

Yang, X., J. A. Pyle, and R. A. Cox (2008), Sea salt aerosol production and bromine release: Role of snow on sea ice, *Geophys Res Lett*, *35*(16), L16,815.

Yevich, R., and J. A. Logan (2003), An assessment of biofuel use and burning of agricultural waste in the developing world, *Global Biogeochem Cy*, *17*(4).

Yienger, J., and H. Levy (1995), Empirical-Model of Global Soil-Biogenic NOx Emissions, *J Geophys Res-Atmos*, *100*, 11,447--11,464.

Yoshida, S., T. Morimoto, T. Ushio, and Z. Kawasaki (2007), ENSO and convective activities in Southeast Asia and western Pacific, *Geophys Res Lett*, *34*(21).

Young, P. J., A. T. Archibald, K. W. Bowman, J. F. Lamarque, V. Naik, D. S. Stevenson, S. Tilmes, A. Voulgarakis, O. Wild, D. Bergmann, P. Cameron-Smith, I. Cionni, W. J. Collins, S. B. Dalsøren, R. M. Doherty, V. Eyring, G. Faluvegi, L. W. Horowitz, B. Josse, Y. H. Lee, I. A. MacKenzie, T. Nagashima, D. A. Plummer, M. Righi, S. T. Rumbold, R. B. Skeie, D. T. Shindell, S. A. Strode, K. Sudo, S. Szopa, and G. Zeng (2013), Pre-industrial to end 21st century projections of tropospheric ozone from the Atmospheric Chemistry and Climate Model Intercomparison Project (ACCMIP), *Atmos Chem Phys*, *13*(4), 2063--2090.

Yuan, T., L. A. Remer, K. E. Pickering, and H. Yu (2011), Observational evidence of aerosol enhancement of lightning activity and convective invigoration, *Geophys Res Lett*, *38*.

Zhang, G., and N. McFarlane (1995), Sensitivity of Climate Simulations to the Parameterization of Cumulus Convection in the Canadian Climate Center General-Circulation Model, *Atmos Ocean*, *33*(3), 407--446.

Zhang, L., D. J. Jacob, X. Liu, J. A. Logan, K. Chance, A. Eldering, and B. R. Bojkov (2010), Intercomparison methods for satellite measurements of atmospheric composition: application to tropospheric ozone from TES and OMI, *Atmos Chem Phys*, *10*(10), 4725--4739.

Zhang, X., J. Helsdon, and R. Farley (2003), Numerical modeling of lightning-produced NOx using an explicit lightning scheme: 2. Three-dimensional simulation and expanded chemistry, *J Geophys Res-Atmos*, *108*, A21--A37.

Ziemke, J. R., and S. Chandra (1999), Seasonal and interannual variabilities in tropical tropospheric ozone, *J Geophys Res-Atmos*, *104*, 21,425--21,442.

Ziemke, J. R., and S. Chandra (2003), La Nina and El Nino-induced variabilities of ozone in the tropical lower atmosphere during 1970-2001, *Geophys Res Lett*, *30*(3).

Ziemke, J. R., S. Chandra, and P. Bhartia (1998), Two new methods for deriving tropospheric column ozone from TOMS measurements: Assimilated UARS MLS/HALOE and convective-cloud differential techniques, *J Geophys Res-Atmos*, *103*, 22,115--22,127.

Ziemke, J. R., S. Chandra, and P. Bhartia (2001), "Cloud slicing": A new technique to derive upper tropospheric ozone from satellite measurements, *J Geophys Res-Atmos*, *106*, 9853--9867.

Ziemke, J. R., S. Chandra, and P. Bhartia (2005), A 25-year data record of atmospheric ozone in the Pacific from Total Ozone Mapping Spectrometer (TOMS) cloud slicing: Implications for ozone trends in the stratosphere and troposphere, *J Geophys Res-Atmos*, *110*.

Ziemke, J. R., S. Chandra, B. N. Duncan, L. Froidevaux, P. K. Bhartia, P. F. Levelt, and J. W. Waters (2006), Tropospheric ozone determined from aura OMI and MLS: Evaluation of measurements and comparison with the Global Modeling Initiative's Chemical Transport Model, *J Geophys Res-Atmos*, *111*.

Ziemke, J. R., S. Chandra, B. N. Duncan, M. R. Schoeberl, O. Torres, M. R. Damon, and P. K. Bhartia (2009), Recent biomass burning in the tropics and related changes in tropospheric ozone, *Geophys Res Lett*, *36*.

Ziemke, J. R., S. Chandra, L. D. Oman, and P. K. Bhartia (2010), A new ENSO index derived from satellite measurements of column ozone, *Atmos Chem Phys*, *10*(8), 3711--3721.

Ziemke, J. R., S. Chandra, G. J. Labow, P. K. Bhartia, L. Froidevaux, and J. C. Witte (2011), A global climatology of tropospheric and stratospheric ozone derived from Aura OMI and MLS measurements, *Atmos Chem Phys*, *11*(17), 9237--9251.